Measuring the Electron Bunch Timing with Femtosecond Resolution at FLASH

Dissertation

zur Erlangung des Doktorgrades
des Fachbereichs Physik
der Universität Hamburg

vorgelegt von

Dipl.-Phys. Marie Kristin Bock
aus Preetz (Schleswig-Holstein)

Hamburg
2012

“BAM Sweet BAM”

Gutachter der Dissertation	Prof. Dr. Eckhard Elsen Prof. Dr. Jörg Rossbach
Gutachter der Disputation	Prof. Dr. Eckhard Elsen PD Dr. Bernhard Schmidt
Datum der Disputation	14. März 2012
Vorsitzender des Prüfungsausschusses	Dr. Michael Martins
Vorsitzender des Promotionsausschusses	Prof. Dr. Peter Hauschildt
Dekan der Fakultät für Mathematik, Informatik und Naturwissenschaften	Prof. Dr. Heinrich Graener

Abstract

Bunch arrival time monitors (BAMs) are an integral part of the laser-based synchronisation system which is being developed at the Free Electron Laser in Hamburg (FLASH). The operation principle comprises the measurement of the electron bunch arrival time relative to the optical timing reference, which is provided by actively length-stabilised fibre-links of the synchronisation system. The monitors are foreseen to be used as a standard diagnostic tool, not only for FLASH but also for the future European X-Ray Free-Electron Laser (European XFEL). The present bunch arrival time monitors have evolved from proof-of-principle experiments to beneficial diagnostic devices, which are almost permanently available during standard machine operation. This achievement has been a major objective of this thesis. The developments went in parallel to improvements in the reliable and low-maintenance operation of the optical synchronisation system. The key topics of this thesis comprised the characterisation and optimisation of the opto-mechanical front-ends of both, the fibre-links and the BAMs. The extent of applications involving the bunch arrival time information has been enlarged, providing automated measurements for properties of the RF acceleration modules, for instance, the RF on-crest phase determination and the measurement of energy fluctuations. Furthermore, two of the currently installed BAMs are implemented in an active phase and gradient stabilisation of specific modules in order to minimise the arrival time jitter of the electron bunches at the location of the FEL undulators, which is crucial for a high timing resolution of pump-probe experiments.

Kurzdarstellung

Ankunftszeitmonitore für Elektronenpakete sind ein wesentlicher Bestandteil des laserbasierten Synchronisationssystems, welches derzeit am Freie-Elektronenlaser in Hamburg (FLASH) entwickelt wird. Das Funktionsprinzip umfasst die Messung der Ankunftszeit von Elektronenpaketen relativ zu der optischen Zeitreferenz, welche über aktiv längenstabilisierte Faserlinks des Synchronisationssystems zur Verfügung gestellt wird. Die Monitore dienen der standardmäßigen Strahldiagnose und werden nicht nur bei FLASH sondern auch beim künftigen Europäischen Freie-Elektronenlaser (European XFEL) eingesetzt. Die jetzigen Ankunftszeitmonitore haben sich von einfachen Prototypen für Machbarkeitsstudien hin zu nützlichen Strahldiagnosegeräten entwickelt. Sie stehen nahezu permanent während des normalen Maschinenbetriebs zur Verfügung, wobei diese Errungenschaft eine Hautpzielsetzung dieser Arbeit war. Die Entwicklungsschritte verliefen parallel zu Verbesserungen des Synchronisationssystems zum Erreichen eines zuverlässigen und wartungsarmen Betriebes. Die Schwerpunkte dieser Arbeit umfassten eine genaue Charakterisierung und die Verbesserung der optomechanischen Baugruppen von sowohl Faserlinks als auch BAMs. Darüberhinaus hat sich der Umfang an Anwendungen der Ankunftszeitinformation enorm erweitert, so dass nun automatisierte Messungen von Eigenschaften der HF-Beschleunigungsmodule zur Verfügung stehen, wie beispielsweise die Bestimmung der Scheitelpunktphase und die Messung von Energiefluktuationen. Desweiteren sind zwei der derzeitig installierten BAMs in einem System zur aktiven Stabilisierung von Phasen und Amplituden bestimmter Beschleunigungsmodule eingebunden, um schnelle Ankunftszeitsfluktuationen der Elektronenpakete am Ort der FEL Undulatoren zu minimieren, welches unabdingbar für eine präzise Zeitauflösung von Pump-Probe Experimenten ist.

Contents

List of Figures

List of Tables

Introduction

The Free-Electron Laser in Hamburg (FLASH) evolved from the TESLA project, which started in 2004 and has been the very first demonstrated free-electron laser (FEL) facility delivering soft X-ray radiation. Today, the linear accelerator (linac) of FLASH is capable of accelerating electron bunches to an energy of up to 1.2 GeV, generating FEL pulses in a self-amplified spontaneous emission (SASE) process with wavelengths ranging from 60 nm down to 4.5 nm, thus reaching the carbon edge and water window.

From the very first beginning, the number of demonstrated and planned free-electron laser facilities has grown continuously. According to [BBC+10b], in 2010 about 30 FELs have been in operation or demonstrated, making use of accelerators, which operate at relativistic energies. At least eight facilities out of those comprise a high gain FEL like FLASH, compare illustration 1.

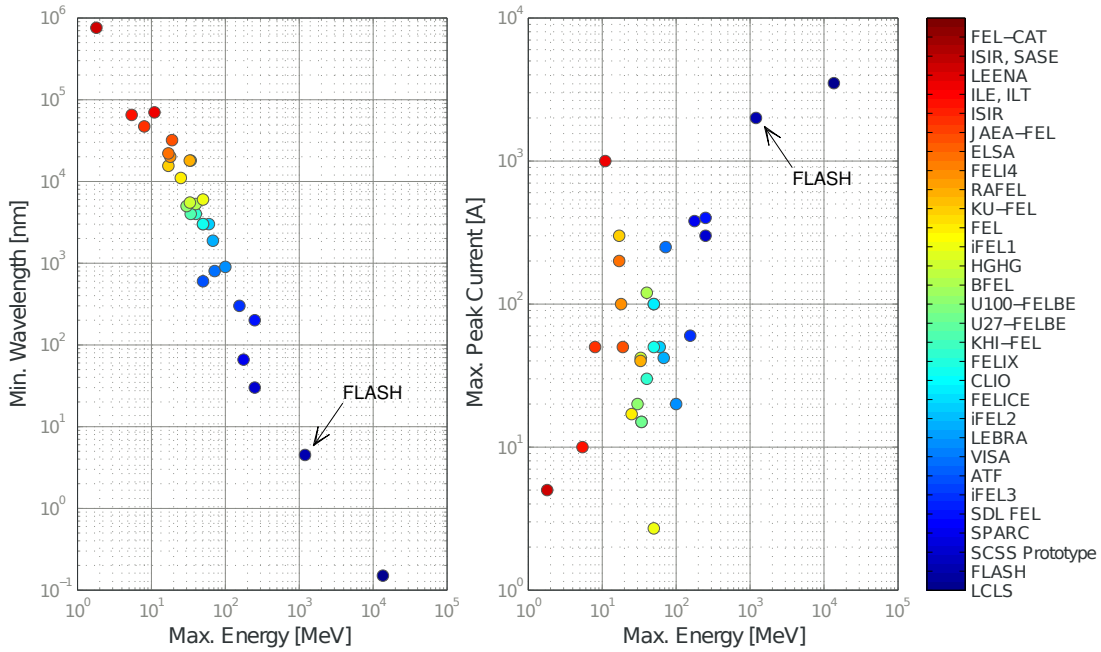

Figure 1: Demonstrated Free-Electron Lasers in 2010 (only relativistic RF linear accelerators are regarded). The plot on the left-hand side shows the lowest radiation wavelengths achieved in comparison to the maximum electron beam kinetic energy, whereas the plot on the right-hand side compares the peak currents to the maximum kinetic energy. The facilities are sorted by achieved wavelength, starting with longer wavelengths at FEL-CAT (dark red) down to the lowest wavelength at LCLS (dark blue). Eight out of the thirty facilities mentioned here are not FEL oscillators: ISIR, VISA, SDL FEL, SPARC, SCSS, FLASH and LCLS (SASE FELs) and HGHG (FEL Amplifier) [BBC+10b].

Depending on the compression factor in the magnetic chicanes of the FLASH linac, the FEL pulses can be as short as 10 fs, with a high transverse coherence and peak brilliances of about 10^{29} to 10^{30} photons /s/mrad^2/mm^2/ (0.1 % bandwidth), being several orders of magnitude higher than those achieved at the best synchrotron radiation storage rings. Chapter 1 of this thesis provides a brief description of FLASH, with special regard to specific subsystems, which have been relevant for studies performed in the course of this thesis.

For achieving increasingly high spatial and temporal resolution in pump-probe (PP) experiments the demands on the time structure and especially the timing stability of the FEL pulses are increasing, as well. This includes the precise knowledge of the timing between both the external laser systems being employed in the experimental set-ups and the FEL pulses. The latter is equivalent to the demand of a highly resolved measurement of the arrival time of the electron bunches at the undulators. In addition to the monitoring of the timing behaviour, an active stabilisation of either the external laser system, the electron beam or both can in principle substantially increase the precision of pump-probe experiments. For this purpose a laser-based synchronisation (LbSyn) system is being developed at FLASH, based on the distribution of a pulsed optical reference, being capable of reaching point-to-point timing stabilities of below 10 fs (RMS) [SWB+10]. The distribution is accomplished by actively length-stabilised fibre links, which connect several different types of end-stations with the optical master in a star topology. All key components of the LbSyn system have evolved during the past few years to become sophisticated and mechanically stable engineered versions. Currently, seven fibre-links of different design stages are installed and in operation. One of the key objectives of this thesis has been the further development of the opto-mechanical design, as it is used for the links, in order to enhance their performance. In this regard, major improvements have been accomplished, which are described in detail in chapter 2.

The utilisation of a pulsed timing system opens the opportunity to employ a large variety of end-stations, for example

- an optical-to-RF conversion, generating an RF comb spectrum for picking out any harmonic of the fundamental frequency from the laser pulse repetition rate. This signal can be used for phase-locking external laser systems to the optical reference.
- the development of a phase-locking scheme, which incorporates a direct all-optical measurement of the timing delay between the reference laser pulses and and an external laser system, like the *pump-probe* laser.
- the direct usage of the laser pulses for electron bunch and photon pulse diagnostics.

The latter category comprises in particular the bunch arrival time monitors (BAMs), which utilise a commercial, electro-optic modulator (EOM) in order to measure the electron bunch arrival times relative to the optical timing reference. Button-type RF pick-ups, which are installed at five locations of FLASH, provide a bipolar voltage signal. The time of arrival of the voltage zero-crossing marks the arrival time of the centre of bunch charge. The RF signal transfer line, as well as the EOMs are rated for bandwidths of up to 12 GHz. It has been shown earlier, that the intrinsic resolution of the BAMs can be better than 10 fs [LAF+10].

The bunch arrival time monitors are an integral part of the laser-based synchronisation system and deliver valuable information on the electron bunch arrival time at different locations of FLASH.

For the operation of the FEL it is necessary to not only have a thorough knowledge, but to achieve an improvement of the timing stability of the electron bunches, and therefore of the FEL pulses. The main objective is to achieve a sub-10 fs resolution in pump-probe experiments, requiring a high quality synchronisation between the FEL pulses and external laser sources [Fel10]. There are different approaches to meet this demand. Those include:

- reduction of timing jitter and drifts of the external laser system. This goal can be reached on long-term time scales through a low-jitter lock of the laser to the optical synchronisation system.
- reduction of the timing jitter and drift of the FEL beam, and hence of the electron bunches. This is related to improvements in the LLRF system, since phase and gradient fluctuations of the RF field directly generate timing jitter of the electron bunches. Furthermore, the improvement of the timing stability can be achieved through an active timing stabilisation by use of feedback implementations.

Besides using actively stabilised systems, the knowledge of the actual timing behaviour of both the FEL beam and the external laser pulses can be used for a post-sorting of the experimental data in order to achieve a higher measurement accuracy in the PP set-up. Afterwards, the resolution in principle only depends on the accuracy of the timing measurement. There are three diagnostic tools available, which are suitable for this purpose:

- the long-term drift behaviour of the external laser system can be monitored with a streak camera in the experimental hall, near the PP set-up.
- a measurement of the relative timing by electro-optical sampling (TEO) between the FEL pulse and the external laser pulse [RASA+11].
- the online and bunch resolved monitoring of the electron bunch arrival time near the undulator, as a measure for the timing of the FEL pulses at the location of the PP experimental set-up.

The latter measurement makes use of a BAM and is the only diagnostic tool of all mentioned above, which is capable of delivering a detection resolution in the order of 10 fs and below.

Among other approaches, the synchronisation accuracy between the *pump*-laser and *probe*-laser pulses can also be increased by an external seeding of the FEL radiation process, while using a single laser source for both the seeding and as an optical pump in the pump-probe experiments. This system also relies on a precise knowledge of the electron timing behaviour, with a precision of a few ten femtoseconds, since the seeding process requires both, a precise spatial and temporal overlap of the seed laser pulses and the electron bunches.

In parallel to the continuous upgrades of the LbSyn system, an intense further development and enhancement of the bunch arrival time monitors has been required. Hence, in addition to the improvement of the timing stability of the reference laser pulses delivered to the monitor system, one of the main objectives of this thesis has been the optimisation of the opto-mechanical front-end of the BAM, which is described in detail in chapter 3. The progressive design revisions improved the stability and reliability of the arrival time measurement to a large extent. Furthermore, the transition of the

BAM from a prototype to a standard diagnostic tool, integrated into the accelerator's control system, is nearly accomplished. A considerable contribution to this task has been the vast amount on experience, which has been gathered during the commissioning and maintenance of the four currently installed BAMs.

Apart from the improvement of the opto-mechanics and the long-term stability of the BAMs, their performance has been studied systematically, evaluating the dependence of the arrival time detection on the bunch charge and on position deviations of the electron bunches from the design orbit. The measurement results are presented in chapter 4 of this thesis. All of this information has been used to promote the further development of a new BAM layout, which will be capable of measuring even at very low bunch charges of a few ten pico-coulomb with high precision, as required for planned projects like the 2nd FEL beam line of FLASH (FLASH II) and the European X-Ray Free-Electron Laser (European XFEL).

Especially the two newest BAMs, which have been installed in the course of this work, allow for intense studies on the performance of the injector and the first acceleration module of FLASH. The accumulated bunch arrival time jitter up to the point before the first bunch compressing magnetic chicane mainly results from arrival time variations of the photo-injector laser and from phase variations of the RF gun. In this regard, the influence of the first acceleration module can typically be neglected, although an unexpected correlation between the tuning of the first RF cavity and arrival time changes at the exit of this module has been observed. Furthermore, the determination of fluctuations in the time-of-flight (ToF) through the magnetic chicane allow for a precise determination of energy fluctuations in the preceding acceleration module. Finally, two of the four installed BAMs are already employed in a beam-based feedback system, which is currently under development, in order to achieve the projected long-term arrival time stabilisation of below 20 fs at the end of the linac. In chapter 5, not only important applications, but also a selection of mission-critical arrival time data is discussed. The latter has been analysed under two aspects, namely to evaluate the performance of the current BAMs and to evaluate the long-term timing behaviour of the electron bunches under combinations of different slow and fast feedback systems.

The appendices of this thesis comprise a detailed explanation of the incorporated electron bunch dynamics, which lead to arrival time fluctuations and jitter. In addition, the electro-optic modulator as central component for the arrival time detection is briefly discussed, providing complementary information to the explanation on the commissioning process of a BAM, given in chapter 4. At large user facilities like FLASH and the European XFEL the cost-benefit calculation with regard to the installation of subsystems cannot be disregarded. Therefore, an overview on the opto-mechanical and electric components, which are employed in the current designs of the fibre-links and bunch arrival time monitors, and a specification of the total costs are given in the appendix.

Glossary

Terms

ACC1	first acceleration module at FLASH, in front of BC2.
ACC23	two coupled acceleration modules in front of BC3.
ACC39	decelerating module behind ACC1, operated at the third harmonic of the fundamental RF frequency of 1.3 GHz.
ACC45	two coupled acceleration modules behind BC3.
ACC67	two coupled acceleration modules at the end of the FLASH linac.
BAM.1UBC2	BAM in section UBC2 of FLASH at longitudinal position 20.6 m; also named BAM No.1.
BAM.18ACC7	BAM in warm section of ACC7 at longitudinal position 142.7 m; also named BAM No.4.
BAM.3DBC2	BAM in section DBC2 at longitudinal position 27.6 m; also named BAM No.2.
BAM.4DBC3	BAM in section DBC3 at longitudinal position 84.5 m; also named BAM No.3.
BC2	first bunch compressing magnetic chicane of FLASH.
BC3	second bunch compressing magnetic chicane of FLASH.
INCOUPLING EFFICIENCY	the efficiency of coupling light into an optical fibre using an appropriate lens or lens system; qualitatively, the ratio between the initial optical power and the one measured at the exit of the fibre.
LINK	short name for length-stabilised fibre links as part of the Laser-based Synchronisation System.
WAVEPLATE	usually quarter or half waveplate: birefringent plate retarding one direction of polarisation of light passing through it; the magnitude of retardation is given in fractions of the specified wavelength.

Acronyms

ACB	advanced carrier board.
ACCT	AC current transformer.
ADC	analogue-to-digital converter.
Al	Aluminium.
BAM	bunch arrival time monitor.
BBF	beam based feedback.
BC	bunch compressor.
BCM	bunch compression monitor.
BPM	beam position monitor.
C1.ACC1	first cavity of module ACC1.
CCD	charge-coupled device.
Cs_2Te	Caesium Telluride.
CSR	coherent synchrotron radiation.
Cu	Copper.
cw	continuous wave.
DAC	digital-to-analogue converter.
DAQ	data acquisition.
DC	direct current.
DCF	dispersion compensating fibre.
DESY	Deutsches Elektronen-Synchrotron.
DOOCS	distributed object-oriented control system.
DSP	digital signal processor.
EBPM	large horizontal aperture beam position monitor.
EDFA	erbium-doped fibre amplifier.
EM	electro-magnetic.
EMI	electro-magnetic interference.
EO	electro-optic.
EOM	electro-optic modulator.
European XFEL	European X-Ray Free-Electron Laser.
FB	feedback.
FEL	free-electron laser.
FLASH	Free-Electron Laser in Hamburg.

FLASH II	2nd FEL beam line of FLASH.
FRM	FARADAY rotating mirror.
FSD	free-space distribution unit.
FWHM	full width at half maximum.
GDD	group delay dispersion.
GUI	graphical user interface.
GVD	group velocity dispersion.
HHG	high-harmonic generation.
IL2	photo injector laser system.
ILC	International Linear Collider.
IR	infra-red.
ISR	incoherent synchrotron radiation.
L2L	laser-to-laser.
L2RF	laser-to-RF.
LBSYN	laser-based synchronisation.
LD	laser diode.
LDD	laser diode driver.
LFF	learning feed forward.
LINAC	linear accelerator.
$LiNbO_3$	Lithium Niobate.
LLRF	low-level radio frequency.
LMS	linear motor stage.
LNA	low-noise amplifier.
LO	local oscillator.
MIMO	multiple input multiple output.
MLO	master laser oscillator.
MO	RF master oscillator.
MPS	machine protection system.
NB	Niobium.
ND:YLF	Neodymium-doped Yttrium Lithium Fluoride.
ODL	optical delay line.

OIC	optical integrated circuit.
OTR	optical transition radiation.
OXC	optical cross-correlator.
P	proportional.
PBC	polarising beam cube.
PBS	polarising beam splitter.
PCA	principal component analysis.
PCB	printed circuit board.
PD	photodiode.
PER	polarisation extinction ratio.
PLL	phase-locked loop.
PM	polarisation maintaining.
PMF	polarisation maintaining fibre.
PMT	photomultiplier tube.
PP	pump-probe.
PPKTP	periodically poled Potassium Titanyl Phosphate.
PSOF	phase-stable optical fibre.
PZT	piezoelectric transducer.
RBV	read-back value.
RF	radio frequency.
RIN	relative intensity noise.
RMS	root mean square.
ROI	region of interest.
SASE	self-amplified spontaneous emission.
SESAM	semiconductor saturable absorber mirror.
sFLASH	seeding experiment at FLASH.
SMF	single mode fibre.
SNR	signal-to-noise ratio.
SOP	state of polarisation.
SRM	synchrotron radiation monitor.
SSA	signal-source analyser.
SSB	single side band.
TDS	transverse deflecting structure.
TE	transverse electric.

TEC	thermo-electric cooler.
TEO	timing by electro-optical sampling.
Ti	Titanium.
TM	transverse magnetic.
ToF	time-of-flight.
TPS	toroid protection system.
TTF	TESLA Test Facility.
uTCA	Micro Telecommunications Computing Architecture.
UV	ultraviolet.
VM	vector modulator.
VME	Versa Module Eurocard.
XUV	extreme ultraviolet.

Symbols

α_{G}	a measure for the divergence of a GAUSSian beam.
BD	beam diameter.
β_{G}	a measure for the cross-sectional area of a GAUSSian beam.
c_0	speed of light in vacuum (2.99792458×10^8 m/s).
CA	clear aperture.
e_0	elementary charge ($1.602176565(35) \times 10^{-19}$ C).
ε_{G}	emittance of a GAUSSian beam.
η	modulation depth.
$\eta_{\max}$	extinction ratio of a modulator.
f_{RF}	fundamental mode of the RF cavities.
γ_{G}	measure for the radius of a GAUSSian beam at the RAYLEIGH range.
Γ_m	intensity modulation index.
G_{gun}	weighting factor defining the contribution of the RF gun to the arrival time jitter.
G_{laser}	weighting factor defining the contribution of the photo-injector laser to the arrival time jitter.
IL	insertion loss.
Λ	transfer matrix connecting RF amplitude and phase errors with bunch arrival time and compression variations.
MF	mismatch factor.
n_e	refractive index of the extraordinary beam.
NA	numerical aperture.
n_o	refractive index of the ordinary beam.
R_{16}	horizontal dispersion parameter of a magnetic chicane.
R_{36}	vertical dispersion parameter of a magnetic chicane.
R_{56}	longitudinal dispersion parameter of a magnetic chicane.
ROC	radius of curvature.
R_{rep}	repetition rate.

θ_{DA}	full angular divergence of a GAUSSian beam.
θ_{G}	half angle of divergence and convergence respectively.
T_{rep}	time interval as inverse repetition rate.
V_{π}	half-wave voltage.
w_{G}	$1/e^2$ radius of a GAUSSian beam.

1 FLASH & Optical Timing System

Contents

1.1 FLASH Accelerator Facility

The Free-Electron Laser in Hamburg (FLASH) at the Deutsches Elektronen-Synchrotron (DESY) has evolved from the TESLA Test Facility (TTF) project which started in 2004. In the subsequent years, the performance of the TTF accelerator and the extent of its applications had been increased successively. An extensive rebuilding of some specific sections of FLASH had been done in September 2009 to February 2010 [Sch10]. The linear accelerator (linac) of FLASH is currently capable of accelerating electrons to a maximum energy of 1.2 GeV for achieving short free-electron laser (FEL) pulse wavelengths from extreme ultraviolet (XUV) down to soft x-rays of about 4.5 nm, which is close to the carbon edge and water window [SFF+10a].

Besides being a user facility, FLASH offers the possibility to test future technologies for projects like the European X-Ray Free-Electron Laser (European XFEL) and the International Linear Collider (ILC). In the following section, the accelerator environment in which the development and tests for the bunch arrival time monitor (BAM) has been carried out is shortly described. Other diagnostic tools which are important either for the operation or for performance tests of the BAM are also mentioned.

Injector

FLASH has a laser driven gun which enables a variable spacing between the single bunches inside of a bunch train between 1 µs and 25 µs (1 MHz and 40 kHz bunch repetition rate). The bunching scheme is illustrated in figure 1.1. The macro pulse has a maximum duration of 800 µs, i.e. with a minimum possible bunch spacing of 1 µs, a maximum bunch number of 800 bunches can be achieved.

Although the electron gun is able to deliver long bunch trains with several hundred bunches per macro pulse, the operation mode during user runs typically requires only short macro pulses with maximal 30 bunches. Compared to the user run from November 2007 to August 2009, the fixed

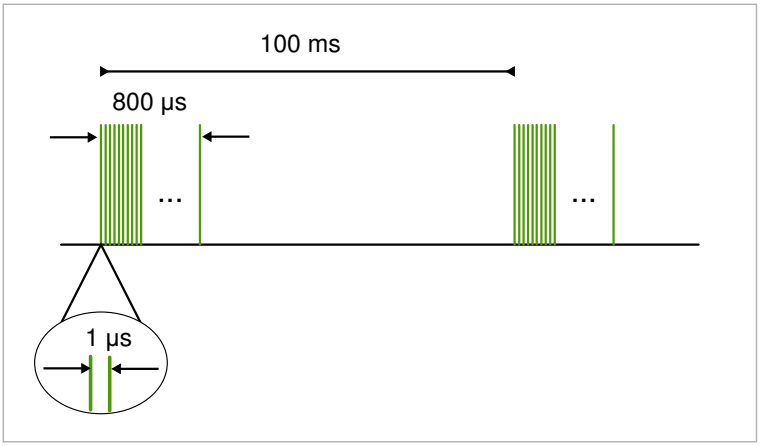

Figure 1.1: Electron buch time pattern at FLASH. With 10 Hz repetition rate and 1 MHz bunch frequency, a maximum number of 800 bunches can be stored in one macro pulse.

value for the bunch train repetition rate was changed in 2010 from 5 Hz to 10 Hz [SFF+10a]. Up to 2009 the requested bunch charge during SASE delivery for user experiments had been typically between 0.5 nC and 1 nC. Since lower bunch charges enable the generation of very short electron bunches and therefore very short FEL pulses, the users indirectly request lower bunch charges to a larger extent lately. FEL pulses with a few 10 fs duration are required for high precision pump-probe experiments with high spatial and temporal resolution, for example the investigation of fast processes on molecular scale. The injector of FLASH is composed of a photo-injector laser, a photo-electric crystal, in this case Caesium Telluride (Cs_2Te) and a radio frequency (RF) gun. The current injector laser system, in the following named IL2, contains a Neodymium-doped Yttrium Lithium Fluoride (Nd:YLF) oscillator, 3 stages of amplifiers and a wavelength conversion stage to produce ultraviolet (UV) laser pulse trains in a 10 Hz burst mode. Details on the operation of this system can be found in [WTSS11].

The electrons are generated through a photo-electric emission process from the Cs_2Te substrate and are immediately accelerated in a 1.6 cell normal conducting cavity to about 5 MeV to overcome space charge effects. The phase of the gun RF field is nominally set to a value which has been experimentally determined to be −38 deg lower than the phase where no charge is accelerated. This zero-crossing phase is measured by use of a charge monitor, i.e. a toroid in case of FLASH, compare section 5.2.1 on page 134. The nominal gun operation point is chosen not to maximise the transmitted charge but to keep a balance between low emittance and preferably high charge. A low emittance is necessary to produce a high charge density for the generation of FEL pulses. To achieve this for non-relativistic bunches the main solenoid is required to focus the bunches in the transverse plane and to largely compensate for space-charge forces.

Acceleration Modules

Figures 1.2 and 1.3 show a detailed schematic of the linac and FEL beam line of FLASH. The acceleration of the electron bunches up to their target energy is done in three stages, using up to eight RF modules. All modules but ACC39 consist of eight nine-cell standing wave Tesla type super-

conducting cavities made from ultra-pure Niobium (Nb). The cavities are operated in the L-band at the fundamental mode of 1.3 GHz with typical gradients of 20 MV/m up to 25 MV/m [SFF+10a]. The RF power is generated in klystrons driven by modulators and is then sent through wave guides to the accelerator modules where the RF energy is coupled into each cavity. Some klystrons drive two modules at once. The vector sums of gradients and phases from the individual cavities are measured and controlled for each module by a sophisticated low-level radio frequency (LLRF) system, compare section A.1 in the appendix on page 167 ff. During the upgrade of FLASH in 2009/2010 an additional superconducting module with a gradient of 15 MV/m, named ACC39, has been added directly behind ACC1. It is operated at the third harmonic of the acceleration frequency, i.e. 3.9 GHz, at nominally up to 19 MV. Since the phase set-point is shifted by −180 deg and is therefore close to the trough phase, ACC39 is operated in deceleration mode [EBH10]. In combination with ACC1 a linear energy chirp is imprinted on the electron bunches. This first acceleration stage boosts the electron bunches to an energy of about 150 MeV in front of the entrance to the first bunch compressor. The electrons reach relativistic energies within the first cavity of ACC1. In this process, the bunch length is decreased further, depending on the phase set-point of cavity 1, due to velocity bunching [BDG+08].

The second acceleration stage consists of two coupled modules, i.e. ACC23, in front of the second bunch compressor, named BC3. At this location of the linac the electron beam energy is further increased to about 470 MeV. The phase set-point of ACC23 is used to control the further compression of the bunch profile in the second magnetic chicane.

The third acceleration stage contains four RF modules, of which two are coupled to a common klystron. The acceleration of the electron bunches to their target energy is controlled by the amplitude and phase vector sums of the two RF module systems ACC45 and ACC67. Using all of the seven modules, the beam energy reaches a maximum of up to 1.2 GeV.

Bunch Compressor

The initially few millimeter long electron bunches with a corresponding beam current of a few tens Ampère have to be compressed longitudinally to reach the high peak currents of up to 2 kA which are required for the SASE process in the undulators. In addition to the peak current, another critical parameter for the generation of high brilliance FEL light pulses is the projected normalised transverse emittance, which in case of FLASH is typically below 2 mm mrad at 1 nC.

By use of bunch compressors the charge density of relativistic electron bunches can be controlled. For the process of longitudinal bunch compression, first an energy chirp has to be imprinted onto the energy distribution of the electrons. The latter enter the RF bucket of the accelerating field at a phase where they effectively gain energy while propagating through the standing wave structure. The phasing of the RF field relative to the electron timing in each cavity is chosen such, that after traversing the acceleration module the electrons at the head of the bunch effectively gained less energy than the trailing electrons. To achieve this, the bunch is on average located at a few degrees off crest on the falling slope of the sinusoidal RF field. Afterwards, the bunch is directed through a dispersive section of the linac, i.e. a trapeze or s-like magnetic chicane, where the energy deviation between different parts of the bunch is translated into a path length difference. Thus, the electrons in the head of the bunch travel on a dispersion orbit of shorter length than the higher energetic

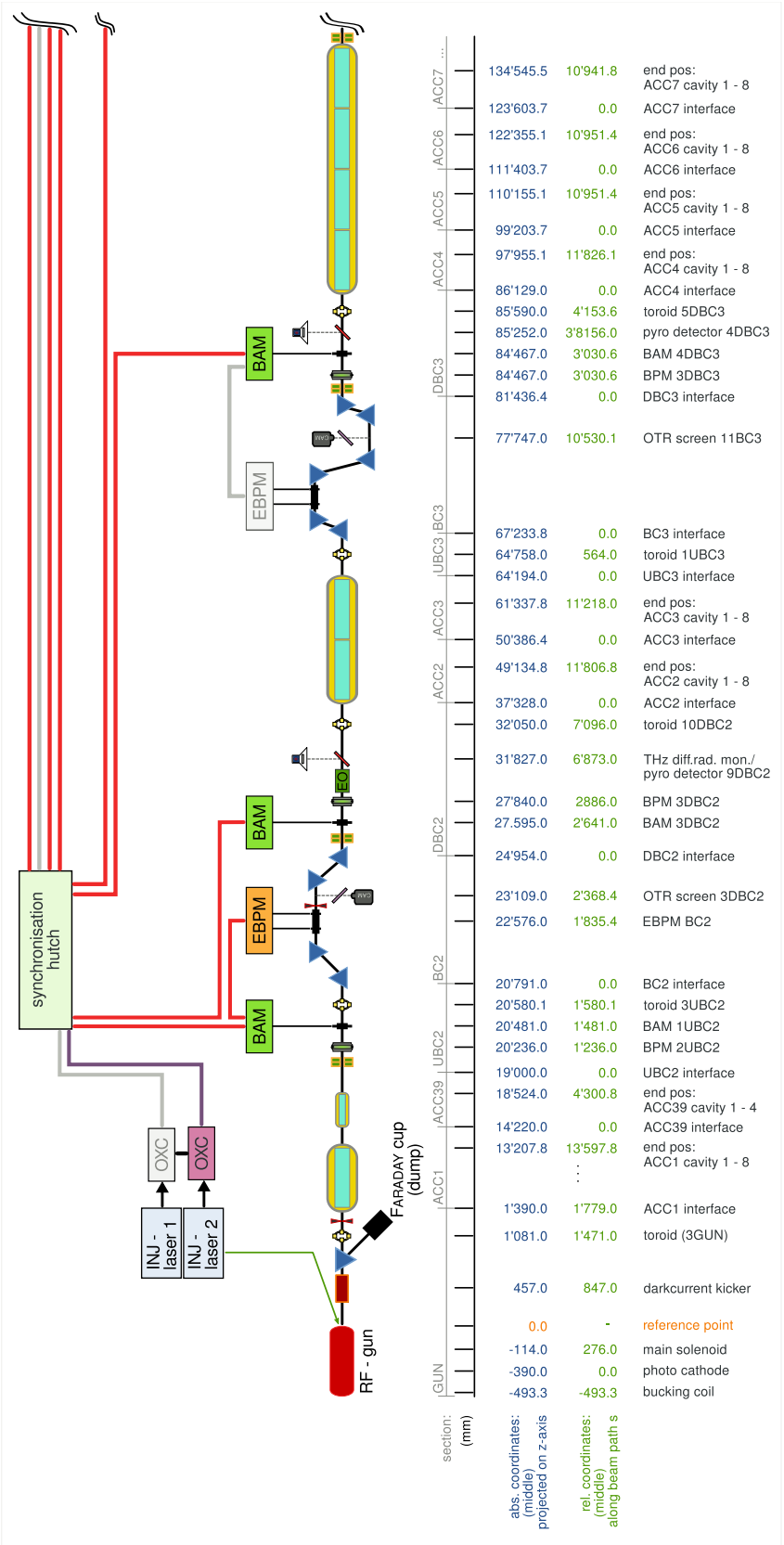

Figure 1.2: LbSyn-infrastructure and FLASH: from GUN to ACC7 section.

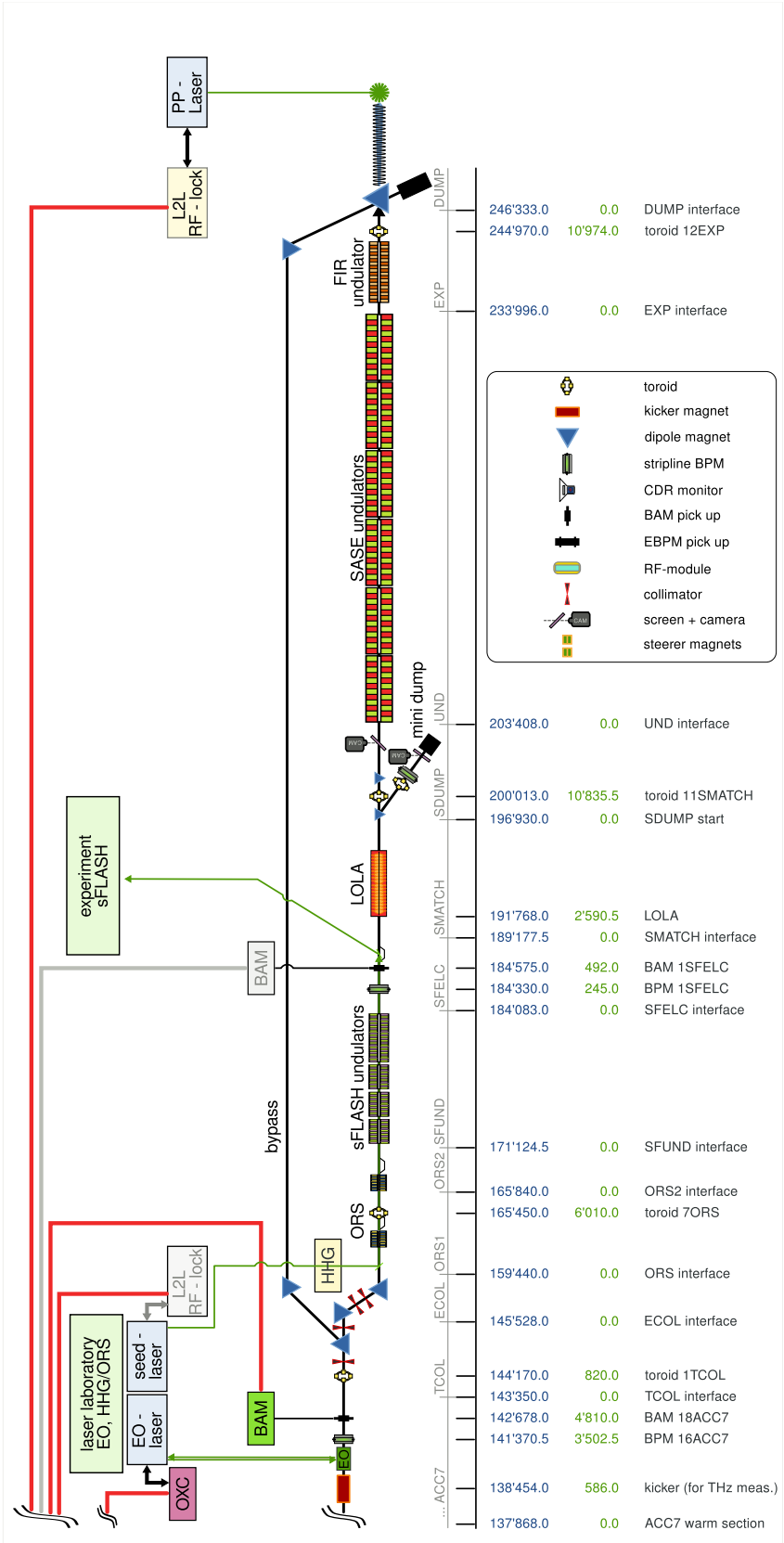

Figure 1.3: LbSyn-infrastructure and FLASH: from ACC7-warm section to DUMP.

electrons in the tail. The result is a shearing of the longitudinal phase space ellipse, so that behind the exit of the magnetic chicane the trailing electrons have caught up with the leading electrons (for details compare [SDR08]). From a simple sinusoidal shape of the RF field, the energy chirp is non-linear which could lead to a roll-over compression resulting in an asymmetric bunch shape where the leading, strongly compressed charge spike with durations less than 10 fs is followed by a long, low current tail [SFF+10a]. To overcome this effect at FLASH the additional module operated at 3.9 GHz had been implemented. With the combined off-crest operation of ACC1 and ACC39 the longitudinal energy profile of the compressed electron bunches can be linearised [EBH10], resulting in a Gaussian shaped current profile. Figure 1.4(a) shows a comparison between the longitudinal phase space of bunches accelerated on-crest and off-crest with linearised energy chirp, as measured with the transverse deflecting structure (TDS) "LOLA" at FLASH [BG10]. The optimisation of bunch compression necessitates a thorough knowledge of the on-crest phases of all RF modules. The usual method where the transverse beam position inside of the bunch compressor is monitored on a screen while adjusting the RF phases of the preceding modules can indeed determine only the phase of smallest energy spread, which is not identical to the real on-crest phase. When operating the RF modules at their nominal vector sum amplitudes, resulting in a beam energy of nominally 150 MeV at BC2 and 450 MeV at BC3, the BAMs at the exits of the two dispersive chicanes can be used for a determination of the on-crest phases. A detailed description is given in chapter 5, section 5.1 about applications of the BAMs on page 119 ff.

Beam Diagnostics

In the following a selection of beam diagnostic tools is shortly described.

Table 1.1: Overview on name, position and design generation of all BAMs currently installed at FLASH. For each BAM possible applications of the arrival time information at the specific location is given.

name	position [m]	generation	application
BAM.1UBC2	20.5	2a	timing of the Gun (laser & RF gun phase)
BAM.3DBC2	27.6	2b	slow or fast feedback on ACC1 & ACC39
BAM.4DBC3	84.5	1	slow or fast feedback on ACC23
BAM.18ACC7	142.7	1	timing at entrance of undulators
			a measure for the FEL pulse timing

BAM: The bunch arrival time monitors (BAMs) as an integral part of the laser-based synchronisation (LbSyn) system are planned to be used as a standard diagnostic tool, not only for FLASH but also for the future European XFEL. The transition from an experimental special diagnostic set-up to a standard device which will be routinely used by the machine operators is almost achieved, which was one of the main objectives of this thesis. This development went in parallel to improvements in the reliable and low-maintenance operation of the LbSyn system. A detailed description of the bunch arrival time monitor system is given in chapter 3 on page 67 ff. An overview of the LbSyn system can

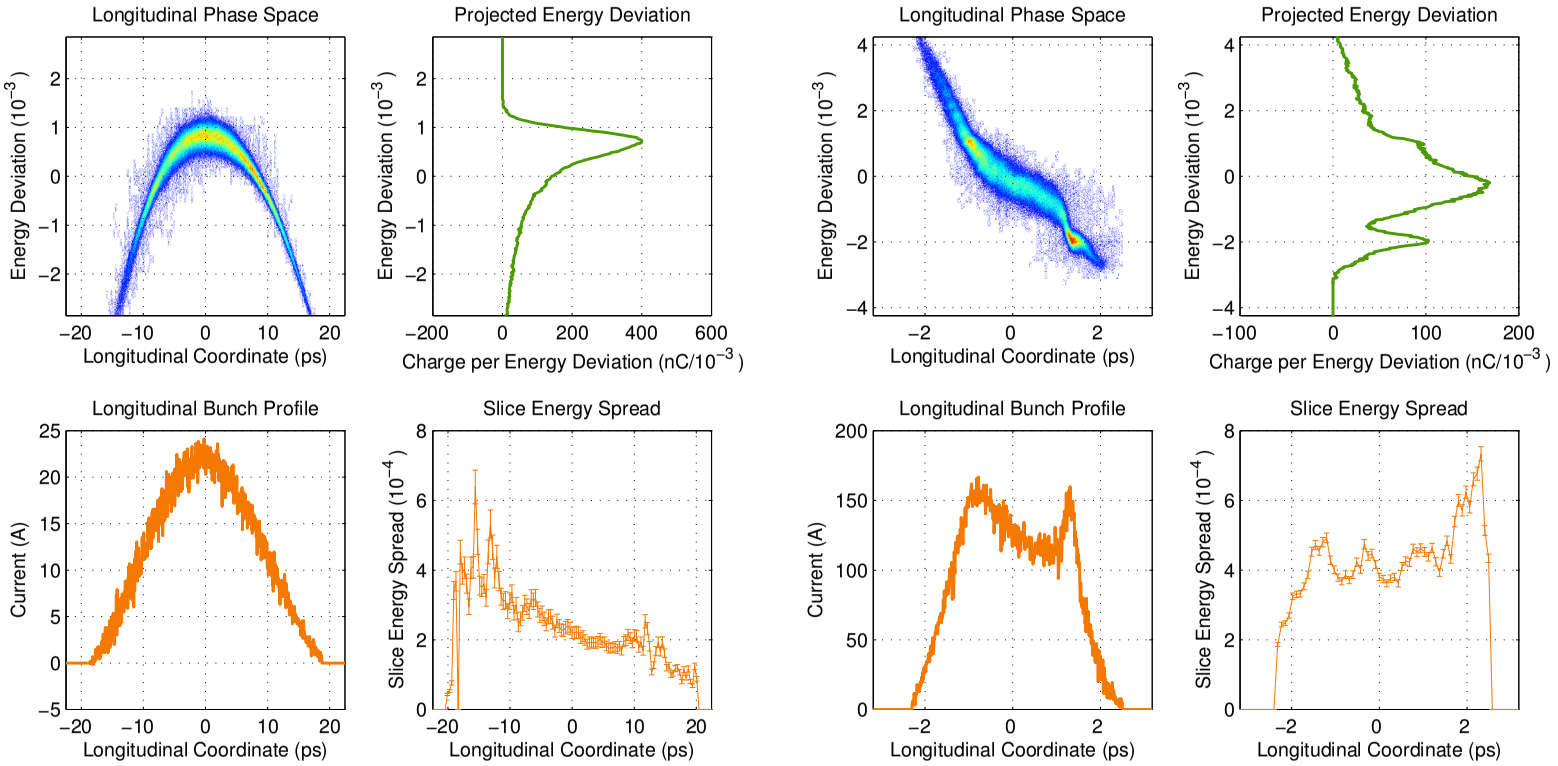

(a) all modules on-crest

(b) *ACC*1 off-crest by −3.5 deg, *ACC*39 off-crest by −13.0 deg and all other modules on-crest

Figure 1.4: LOLA measurement of the longitudinal phase space, duration and slice energy spread of a single bunch at 0.48 nC and 700 MeV, for two different phase settings in ACC1 and ACC39.

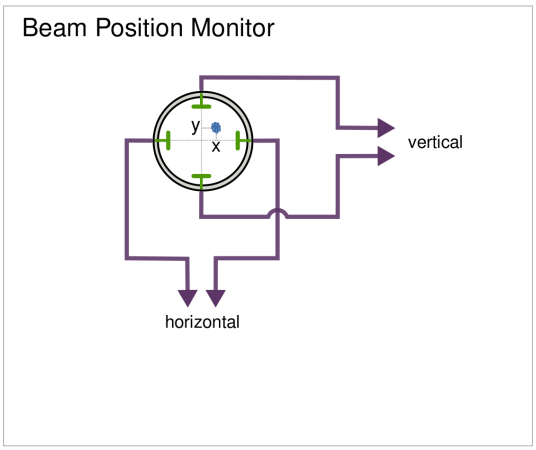

(a) Schematic of an electrode structure and measurement principle of a BPM

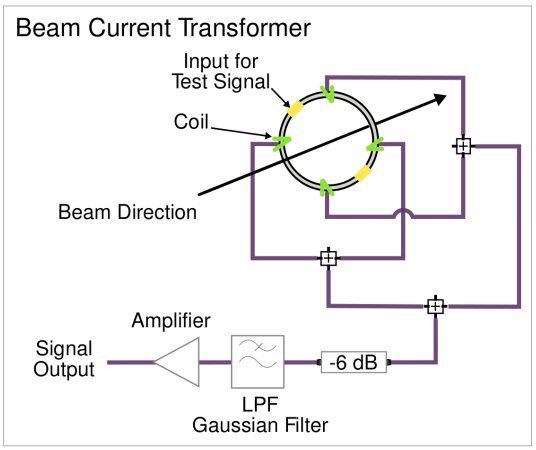

(b) Schematic of a beam current transformer (toroid) with signal processing chain, including an attenuator, a Gaussian filter and an amplifier

Figure 1.5: Schematic of the electrode structures of a toroid and a button-type BPM, as used at FLASH.

be found in the next section 1.2 on page 11 ff. At FLASH four BAMs are currently installed and in permanent operation. A fifth BAM is planned to be installed during 2012. From figure 1.2 and 1.3 the positions of the BAMs can be read. The measurement of the arrival time of each electron bunch delivers valuable information which can be used for different purposes. Table 1.1 gives an overview of the name, the absolute position and the design version of all of the four BAMs at FLASH.

BCM: The bunch compression monitor (BCM) detects the bunch peak current through measuring diffraction radiation by use of pyro-electric detectors. An electron bunch passing a horizontal metallic slit of 5 mm width emits diffraction radiation. Since the slit is tilted by 45° relative to the beam path the radiation is guided to an optics transport system and is focussed onto pyro-detectors [BSWN10]. Such monitors allow for an online, non-invasive measurement of the compression strength and hence the achieved peak current, which is an important parameter for driving the FEL process. BCMs are installed downstream of both bunch compressors at FLASH and are used as a standard diagnostic tool. The output signals are integrated into feedback systems acting on the RF phases of the modules in front of the bunch compressors, compare section 1.3.

BPM: More than 60 beam position monitors (BPMs) are installed along the beam-pipe, while depending on space requirements different electrode types are used in various sections of FLASH [BCH+07]. Those located directly next to BAMs are all strip-line BPMs as used in most warm-sections, providing large signals and good resolution [LNBR07]. Figure 1.5(a) shows the general measurement principle: in both planes, i.e. horizontal and vertical, the amplitude ratio of signals from two electrodes is an intensity-independent function of beam displacement. The signal processing chain uses the AM/PM conversion technique to achieve a single bunch position resolution of less than 10 µm [Wen01] with a linear dynamic range of up to ±5 mm [Bab11].

Toroids: At FLASH the beam current is measured at 12 locations by use of relatively simple devices, so called toroids named after a depiction of their design. They transform the alternating current of a traversing beam into a voltage which is directly proportional to the beam current of the electron bunches and hence to the bunch charge. This measurement set-up is known as an AC current transformer (ACCT) [Fr9]. Figure 1.5(b) shows a schematic of the toroid design as used at FLASH. This design applies to all toroids except for the one in the Gun section, which has a new construction as planned to be used in the European XFEL. The output of 4 single turn Copper (Cu) windings is combined, shaped and sampled. The resolution of the toroid is better than 1 % for bunch charges > 0.5 nC [Neu11]. The toroids are integrated into the machine protection system (MPS) for beam loss detection. Furthermore, bunch charge and transmission are two of those properties from external devices which deliver important information required for the exception handling within the servers of the BAM.

S-FLASH

The seeding experiment at FLASH (sFLASH) is an experiment for generating FEL radiation through direct seeding (for details see [CAB+10]). The sFLASH equipment in the FLASH beam line is located between the collimator section (behind the end of the linac) and the first SASE undulators. The seed source uses the high-harmonic generation (HHG) technology to achieve a seed laser wavelength of 38 nm. This experiment is still in the development phase, but exhibit already a first achievement in 2010 of generating SASE pulses at 38.4 nm [SFF+10b]. A number of challenges has to be overcome to achieve an efficient production of seeded FEL radiation, including the alignment of the seed laser with the electron beam, to find spatial and temporal overlap. The latter is a critical point, so that a precise measure of the electron bunch arrival time becomes a valuable information. The current S-FLASH experiment and comparable projects planned for the near future [WTD+10], will profit from a precise measurement and eventual stabilisation of the electron bunch arrival time at the location of the according undulators.

SASE Undulators

At FLASH the FEL light pulses are generated through the SASE process occurring in the undulators. The latter is a periodic magnetic structure where ultra-relativistic electrons are wiggled on a sinusoidal path around their linear direction of movement. Through a relativistic effect, the electric field lines of the electrons start to separate from their source and radiate as electro-magnetic (EM) waves in forward direction. Under resonant conditions some of the EM waves start to overlap coherently and interact with the electron bunch in such a way, that the energy of electrons within the bunch is modulated, leading to a charge density modulation. This effect in turn increases the extent of coherent interference of the individual EM waves. Thus, the irradiated intensity grows proportional to the square of the number of electrons participating in the radiation process. This self-amplification is started from a spontaneous emission of radiation which is attributed to an initial charge density irregularity caused by shot-noise from the gun. A detailed explanation of the SASE process can be found in [SDR08]. A description of the properties of FEL light pulses, in particular at FLASH, is given in [BBC+10a].

At FLASH six permanent magnet SASE undulators with fixed gaps are installed. The wavelength of the FEL pulses is tuned by adapting the bunch energy. Wavelengths from 40 nm down to 4.5 nm can be achieved. In June 2010 the SASE wavelength reached down to 4.45 nm for the first time, at a beam energy of 1.2 GeV [SFF+10b]. Therefore, FLASH reached the water window between 3.9 and 4.5 nm, allowing pump-probe experiments with biological systems in aqueous solution.

Factors limiting the quality and performance of an FEL are for example

- magnetic field errors in the undulator
- emittance growth of the electron bunch
- increased energy spread of the electron bunches
- fluctuations of the energy chirp imprinted on the electron bunches

The latter beam properties which are influenced by the performance of controllable accelerator components can be stabilised to a certain extent by appropriate feedback systems. Control loops acting on amplitudes and phases of the RF modules are one example for the implementation of those feedback systems which directly use certain beam properties, like arrival time, compression or orbit, as control variables. Section 1.3 on page 15 ff gives a short overview on the longitudinal beam-based feedback system, being currently under development, which incorporates the signals from the two BAMs installed at the exit of the bunch compressors.

Beyond FLASH

As an extension a 2nd FEL beam line of FLASH (FLASH II) is planned to provide additional undulators for seeded FEL operation and an additional experimental hall. The facility will not only offer more beam time for user experiments but also the opportunity to develop new technologies for seeding schemes [Fel10] and approaches for a plasma-based acceleration of electrons [OES+10]. In this context the injector of FLASH will be extended by an additional laser system capable of delivering bunches with very low emittance and low charge [FBA+10]. Further laser systems for seeding and pump-probe experiments will be installed and require a connection to the LbSyn system. At three positions along the beam line the installation of further developed bunch arrival time monitors is foreseen which will be capable of delivering high-resolution arrival time information at low bunch charges. Figure 1.6 on page 12 indicates the planned extensions of the laser-based synchronisation (LbSyn) system in connection with FLASH II.

1.2 Laser-based Synchronisation System at FLASH

The optical synchronisation system at FLASH is based on the distribution of laser pulse trains from the central master laser oscillator (MLO) to various remote stations along the accelerator via actively length-stabilised optical fibres. The timing of the laser pulses at the end-station is stabilised by adjusting the optical path-length of the transmission line, reacting on fast changes (a few kHz bandwidth) of the laser pulse group velocity. Those changes are caused by environmental factors like acoustic vibrations, temperatures drifts and humidity variations which influence the group velocity dispersion (GVD) of the optical fibres.

Based on an early proposal of a pulsed optical system with a desired point-to-point stability of below 10 fs [KCCK08], the laser-based synchronisation (LbSyn) system at FLASH is being developed with continuous improvements regarding robustness and low-maintenance operation. The optical reference clock is realised using a passively mode-locked laser, emitting soliton pulses with about 300 fs full width at half maximum (FWHM). The optical bandwidth of the laser in the telecommunication C-band, with a central wavelength of 1556 nm, offers the advantage that many bulk and fibre optical components are commercially available.

In those respects, the pulsed LbSyn system differs strongly from other synchronisation schemes, which make use of continuous wave (cw) optical laser sources taking the phase velocity instead of the group velocity as a measure of timing reference. In those systems the absolute timing can only be guaranteed within $2\,\pi$ phase advance of the carrier frequency, which might not be sufficient. At FLASH the decision fell on the pulsed optical synchronisation system because it offers a variety of advantages. First of all, the repetition rate of the employed master laser, 216 MHz, allows for setting and recovering an absolute timing range of 4.63 ns. The frequency is the sixth sub-harmonic of the RF used for acceleration in the cavities. The locking of other RF or laser systems to the optical reference is not restricted to the fundamental mode, but it offers the opportunity to convert and filter a wide range of harmonics from the frequency spectrum from the single optical source. Other high-bandwidth applications, which require a pulsed optical reference signal became feasible with the employed LbSyn system.

Figure 1.6 shows a detailed scheme of the LbSyn. All of those components shown in grey are not installed yet but are scheduled for being implemented within the near future. The schematic not only shows FLASH and the synchronisation system in the current configuration but also gives an outlook on the FLASH II [FBA+10]. The additional FEL beam line not only offers room for new experiments and applications but also requires the connection of specific sub-systems to the LbSyn system.

The MLO, free-space distribution unit (FSD) and fibre distribution are located in a temperature stabilised and electro-magnetic interference (EMI)-shielded hutch, next to the laser laboratory of the photo-injector laser. All optical components are installed on a covered optical table. Precautions had been taken to minimise environmental influences like air flow, temperature and humidity fluctuations and vibrations from e.g. klystrons. After a few years of own developments on fibre lasers, in 2010 it was decided to use a commercially available semiconductor saturable absorber mirror (SESAM)-based laser (*Origami-15*) from the company *OneFive*[1]. The MLO is stabilised against long-term drifts by being locked to the RF master oscillator (MO) of the RF timing system. On short-term

[1] Onefive GmbH, In Böden 139, CH-8046 Zurich, Switzerland

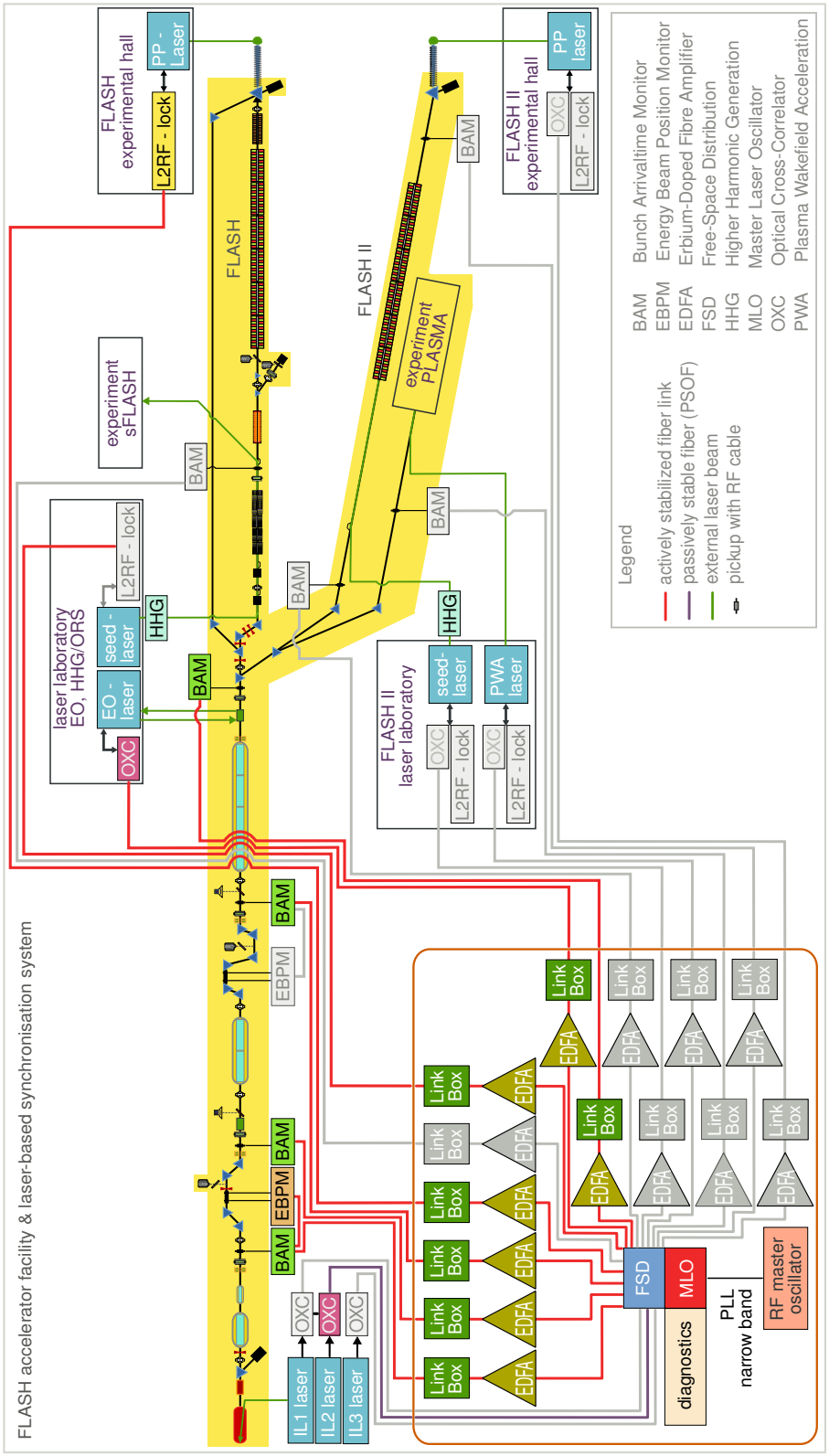

Figure 1.6: Schematic of the LbSyn system at FLASH. In the box on the lower left side, the star topology of the optical timing system is shown. The signals from the MLO are split into several transmission lines, either consisting of a PSO-fibre (violet line) to the injector laser hutch or including an EDFA, link box and SM-fibre (red lines) to various end-stations. Seven actively length-stabilised links are commissioned up to now. Taking the planned extension of the FEL beam line, FLASH II, into account, seven additional links are planned to be installed in the future (grey components).

scale the laser exhibits an excellent noise performance, measured free-running to be less than 5 fs in a frequency range of 1 kHz to 10 MHz. [SWB+10]. Details on developments and performance of the MLO and FSD can be found in [Sch11b].

The distribution of the timing reference is implemented in star topology. The laser pulse energy from the MLO is split in free-space optics (FSD) into several distribution lines, of which eight are currently used. In order to improve the safeguarding to failure, in the near future, a redundant and identical MLO will be installed to allow for fast and automated switching between both master lasers if necessary. For mid-haul links, starting from about 20 m and long-haul links, currently up to 500 m distance, the general layout of the distribution line contains the following elements:

- laser amplification with erbium-doped fibre amplifiers (EDFAs) between MLO and link box
- the link box containing optics and electronics for fibre length stabilisation
- a partially transmissive FARADAY rotating mirror (FRM) at the link ending

Details on the fibre-link design are discussed in chapter 2 on page 21 ff. The large diversity of end-stations taking advantage of a pulsed laser-based synchronisation system, can be divided into three main categories:

1. laser-to-laser synchronisation
2. direct usage of laser pulses
3. laser-to-RF synchronisation

The first category of remote stations comprise different types of laser systems at FLASH:

- photo injector
- pump-probe experiments
- HHG seeding schemes
- laser-based diagnostic systems, e.g. electro-optic (EO) sampling schemes
- experiments for laser plasma acceleration

All of those systems require a low-jitter connection to the synchronisation system. In a first step, this had been realised by RF down-mixing techniques (main category 3) to generate local oscillators (LOs) from the optical laser pulse train [FBG+10]. Nevertheless, the goal is to achieve the synchronisation by a direct laser-to-laser (L2L) connection using two-color optical cross-correlators. Details on achievements and current constraints of this scheme can be found in [Sch11b].

The bunch arrival time monitor (BAM) is the first diagnostic station installed at FLASH of category No. 2. After the first tests of two prototypes in 2006 and 2007, two years later, in 2009 and 2010, the installation and commissioning of two further advanced BAMs has been achieved as an important part of this thesis.

The general principle of the arrival-time measurement relies on detecting the fast RF transient field from the electron bunch by modulating laser pulses making use of the electro-optic effect (for

details see appendix, section B.2). Thus, the information on the arrival time of each electron bunch of a macro pulse is encoded into an amplitude modulation of the reference laser pulses. The accuracy of the arrival-time detection is then, among other constraints, limited by the quality of the amplitude detection in the read-out electronics. A detailed description of the arrival-time monitor system can be found in chapter 3 on 67 ff.

Another example for a direct usage of synchronised laser pulses are the large horizontal aperture beam position monitors (EBPMs). A strip-line antenna is installed inside of the first bunch compressor of FLASH, being mounted transversely to the beam path. The detection principle is the same as used in the BAMs, only that in this case the difference in signal propagation time to both ends of the strip-line provides the information on beam position in the vacuum chamber of the magnetic chicane [Hac10]. Determined by the resolution of a timing detection in the order of 10 fs, the position monitor achieves a resolution of a few micron using the optical sampling scheme.

1.3 Arrival Time Feedback Systems at FLASH

There are various disturbance sources along the linac which influence the slow drift and fast jitter characteristic of the electron bunch timing. Especially the arrival time of the electron bunches at the acceleration modules has large impact on the bunch total energy and energy spread which are two critical parameters for the generation of FEL pulses in the SASE undulators. The main sources of arrival time jitter are found to be

- injector laser arrival time jitter at the photo cathode
- RF gun amplitude and phase jitter
- RF field amplitude and phase errors in superconducting cavities

The arrival time uncertainty in the injector is composed of a combination of laser pulse arrival time on the cathode, contributing with percentage G_{laser}, and a fraction G_{gun} of phase jitter from the RF gun cavity. The ratio of the weights G_{laser} and G_{gun} is depending on the actual operation point of the RF phases. At the normal operation point, the gun contributes with about one third, compare section 5.2.1 on page 134 ff. The arrival time stability behind the bunch compressors is determined by energy fluctuations in the preceding RF modules, because the linear dispersion R_{56} of the magnetic chicane transforms those fluctuations into arrival time jitter. A detailed discussion can be found in appendix A.3 on page 170 ff. Phase fluctuations of the RF modules directly influence the compression factor achieved in the magnetic chicanes, where the phase setting in front of BC2 also directly affects the operation point of BC3. The bunch compression factor is another critical parameter for the FEL light production.

To overcome those performance restrictions, several stand-alone feedback systems based on beam parameters are already employed in the low-level radio frequency (LLRF) system of FLASH and are applied during standard machine operation. Developments and tests are on-going to integrate all of the separate feedback loops into one combined *multiple input multiple output (MIMO)* controller. The operation of separated regulation loops which tend to counteract on each other is impeded through the complicated interplay of different machine parameters acting on the beam dynamics. The regulation bandwidths of the implemented feedback loops are different depending on whether fast changes are corrected within the bunch train or slow drifts are removed. The systems regulate on different beam parameters, such as

- charge (slow)
- bunch compression (slow)
- arrival time (slow and fast)
- energy (slow)
- orbit at different location of linac and FEL section (slow and fast)

where the additions in parenthesis denote the feedback type. In chapter 5, section 5.2.3 on page 145 ff, a small selection of data is presented which has been collected during regular user shifts in 2011, having been dedicated for long-term test runs of slow and fast beam-based feedback systems regulating both, the bunch arrival time and the bunch compression at specific locations of FLASH.

1.3.1 Slow Arrival Time Feedback

Based on the initial idea for a slow feedback stabilisation of the RF phase in the first module, a few years ago, a simple proportional (P) regulator had been implemented into the LLRF system [Kam11]. The feedback takes the information on bunch compression from pyroelectric detector signals of the BCM behind BC2 to adapt the RF phase of the module ACC1. Lately, this simple approach had been embedded into a MATLAB™ environment with a graphical user interface (GUI), which has been successively upgraded to become a versatile structure. Based on this programme, a similar slow feedback systems for phase stabilisation of the module ACC23 has been added. The same programme structure had been adapted to compensate for slow amplitude drifts in both mentioned modules using the arrival time information from BAM.3DBC2 and BAM.4DBC3 as sensor signals for control. Additional to this, the amplitude of selectively ACC45 or ACC67 can be regulated for removing slow beam energy drifts which are measured with a BPM in the *dog-leg* dispersive section following the last module.

It has been proposed to include all of those slow feedback loops into one generic MIMO type system in order to avoid instabilities from individual feedbacks which at some point start working against each other. This happens, because the simple assumption, that the regulation parameters of each slope are independent from each other is not true, especially not for BC2. In the current implementation each slow feedback loop is stand-alone and they are not communicating with each other.

From the FEL studies period in 2012, the generic slow feedback implementation will be tested and further developed to be a valuable complementation of the accelerator operation in the near future. For the MIMO controller, nine input variables from different stations will be taken into account, i.e. BCMs, BAMs and an energy monitor, and ten output parameters acting on the control elements are foreseen to regulate on the amplitude and phase set-points of all five modules.

1.3.2 Fast Intra-Train Longitudinal Feedback

Additional to the compensation of slow drifts, an active stabilisation inside of the macro-pulse is required to compensate for bunch-to-bunch energy fluctuations. Especially during operation with long macro pulses, comprising 30 up to 800 bunches, this becomes important if user experiments are making high demands on the FEL pulse arrival time, width and wavelength stability. Due to a large variety of possible error sources, listed below, a LLRF controller which regulates the RF field based only on cavity probe signals is not sufficient to meet those high demands. The expected energy and energy spread calculated from in-loop RF fields do not necessarily match with the actual beam properties, because of,

- field detection errors
- systematic errors in the calibration of the cavity probes
- common mode drifts and jitter of the MO timing reference
- long-range wake fields
- current fluctuations in the dipole magnets of the chicane

As described in [KBB+10], an additional beam-based feedback control allows for a further improvement of beam properties like compression, energy and arrival time. The bunch pattern of FLASH, with a minimum spacing of 1 µs, is adequate for the purpose of a fast feedback implementation. Nevertheless, such a regulation system requires a well-conceived exception handling and robust structure to remove both fast repetitive errors and slow drifts. First results from a simple version of a beam-based arrival time stabilisation are presented in [LAF+10]. There, the signals from a BCM and one BAM behind BC3 had been used to regulate the phase and amplitude of the first module upstream of BC2.

The present implementation is embedded into the LLRF system, which comprises a variety of process variables and a second-order controller. Thus, it differs significantly from the earlier approaches which used a simple proportional gain regulation [Sch11a]. FLASH is running in pulsed mode, triggered with 10 Hz, but since the RF pulse in the cavity lasts only about 2 ms, there are about 98 ms of time left before the next RF pulse is loaded into the cavity. Figure 1.7 shows a schematic of the pulsed mode time structure. The RF pulse requires up to 500 µs energy loading until the flat top with a duration of 800 µs is reached, followed by a slow field decay.

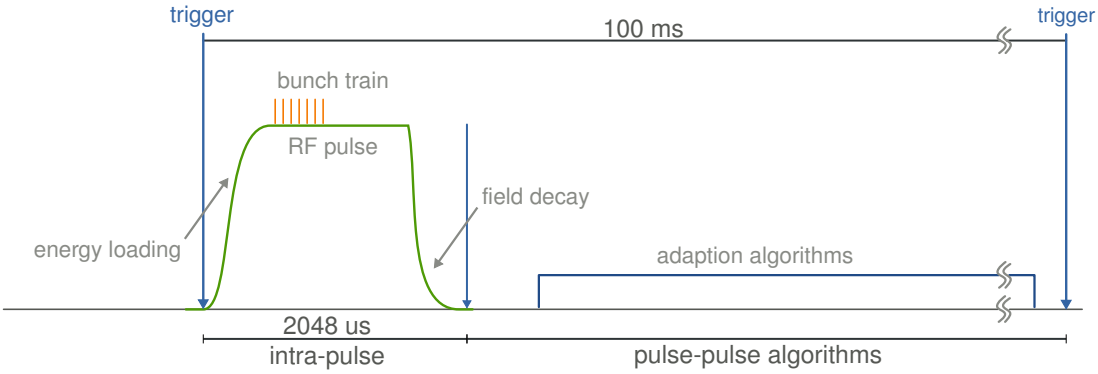

Figure 1.7: Schematic of the RF pulse mode operation scheme at FLASH. (Figure adapted from Waldemar Koprek [KBB+10])

At any time during the operation of the klystrons and modules there are intra-pulse control loops regulating on the signals from field probes inside of the cavity. Those feedback and adaptive feed forward loops, which are applied from pulse-to-pulse for the duration of the RF field period, act on the klystrons to stabilised the RF amplitude and phases in the cavities to compensate for beam loading effects and field errors. The current, sophisticated MIMO controller typically keeps amplitude errors below 0.01 % and phase errors below 0.01 deg.

In contrast to this, the intra-train beam based feedback (BBF) which becomes effective within a latency of 3−4 µs , acts only if bunches are in the machine, since the error signals sent to the controller are calculated from beam properties like arrival time and compression. The latency is caused by the field detection algorithms, the klystron and pre-amplifier delays and a delay from couplers and wave-guides. To avoid conflicts between the fast BBF and other intra-pulse control loops, the system architecture is designed such, that the control factor calculated from beam properties acts on the set-point of the amplitude and phases, so that the existing regulation system adapts subsequently in

real-time the RF fields to the new set-point value. This inter-coordinated implementation simplifies the exception handling, compare [KBB+10]. The regulation range is limited to ±1 % in amplitude and ±1 deg in phase. During the 98 ms before the next trigger signal, additional pulse-to-pulse algorithms are applied. The concept of the longitudinal BBF implementation is illustrated in figure 1.8.

Three main loops are in development, from which two loops are being tested, already. One loop shall be acting on the injector, the other two are acting on the first acceleration stage, i.e. ACC1 and ACC39, as well as on the second acceleration stage, i.e. ACC23. First results have been published in [KBB+10]. Recent achievements are presented in [SBP+11], showing that the out-of-loop arrival time, measured with BAM No. 4 at the end of the linac-section, could be decreased from 60 fs to about 20 fs. Most recently, with a combination of the intra-train BBFs at BC2 and BC3 an arrival time jitter of below 22 fs (rms) was achieved, measured at BAM.18ACC7 for bunch number 5 to 100 during 8 min, as presented in [SBP+11].

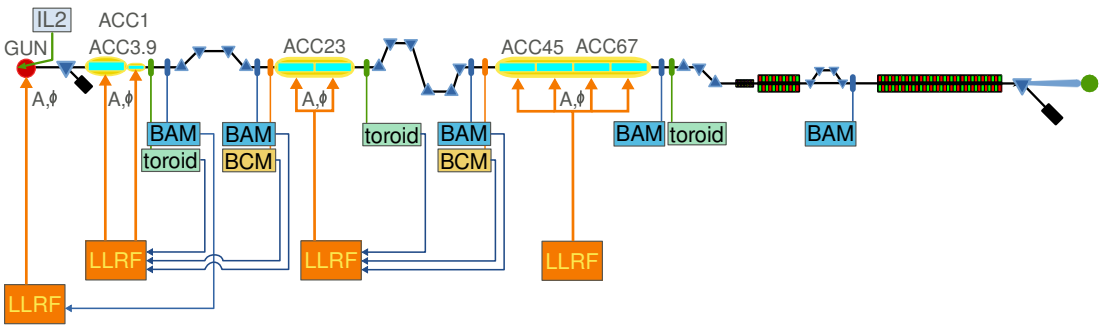

Figure 1.8: Illustration of the concept for a longitudinal beam based feedback at FLASH. (Figure adapted from Waldemar Koprek [KBB+10])

For the intra-train BBF, the digitised information on the arrival time of the bunch train is sent from the electronic BAM front-end, the advanced carrier board (ACB), via an optical link to the LLRF system. The compression monitor installed behind BC2 since lately uses a 140 GHz antenna instead of pyroelectric detectors which significantly improved the signal-to-noise ratio (SNR). The raw values from both monitor systems are used as input error signals for the BBF. Since the bunch arrival time as well as the bunch compression are affected by both the amplitude and phase of the accelerating RF field, the applied regulation factors have to account for the error signals of both monitors simultaneously. In a linear approach, the coupled behaviour of both beam properties is described by a 2 × 4 transfer matrix Λ in form of

$$\Lambda = \begin{pmatrix} \Lambda_{11} & \Lambda_{12} & \Lambda_{13} & \Lambda_{14} \\ \Lambda_{21} & \Lambda_{22} & \Lambda_{23} & \Lambda_{24} \end{pmatrix} \tag{1.1}$$

The relative amplitude and phase errors of ACC1 and ACC39 are then connected to changes in arrival time and compression using the matrix formalism:

$$\begin{pmatrix} \Delta t_{BC2} \\ \Delta C_{BC2} \end{pmatrix} = \Lambda \begin{pmatrix} \delta A_{ACC1} \\ \Delta\Phi_{ACC1} \\ \delta A_{ACc39} \\ \Delta\Phi_{ACC39} \end{pmatrix} \tag{1.2}$$

with amplitude errors abbreviated by

$$\delta A_{ACC1} = \frac{\Delta A_{ACC1}}{A_{ACC1}} \tag{1.3}$$

$$\delta A_{ACC39} = \frac{\Delta A_{ACC39}}{A_{ACC39}} \tag{1.4}$$

The coefficients of Λ are determined empirically by varying the RF amplitude and phase set-points by small amounts while monitoring the signal variation of BAMs and BCMs. The measured transfer matrices are then inverted and applied in the controller. The amplitude variations of the first module, ACC1, dominate the electron bunch arrival time jitter downstream of BC2 with a factor Λ_{11} of typically 7.0 ps/% [SBP+11]. An example for a transfer matrix measurement is described in chapter 5, section 5.1.3 on page 131.

2 Length-Stabilised Fibre Links

Contents

2.1 Opto-Mechanics & Chassis

The optical timing reference of the laser-based synchronisation (LbSyn) system is distributed to the remote stations via individual fibre links in a star topology. Only for very short distances below 25 m, like the connection of the injector laser to the optical reference, passively drift-compensated, phase-stable optical fibres (PSOFs) are used. The layout of the LbSyn system is described in section 1.2 on page 11 ff. The general operation principle of the seven, currently installed mid-haul links is equal to all of them. Nevertheless, they differ in some constructional details, which are shortly discussed in section 2.1.2. The subsequent section, 2.1.3, contains a description of specifications and characteristic improvements of the latest link opto-mechanics version, which is one of the major outcomes of this thesis. But at first, the general principle of operation is described briefly.

2.1.1 Operation Principle & General Layout of the Fibre Links

Laser pulses from the optical reference, i.e. the master laser oscillator (MLO), are amplified in power and then split into a reference and a signal branch, the latter denoted in the following as link pulses, which are directed into the fibre link. The splitting happens in a free-space optics assembly, named link box, which is mounted very close to the MLO, since the first amplification is done in a fibre section which is not length-stabilised and therefore has to be kept as short as possible. The laser pulses are linearly polarised when being launched into the long fibre connecting the link box with the according remote terminal. The distances differ for the various links, ranging between 90 m and 500 m at FLASH. Since the employed single mode fibre (SMF) is not polarisation-maintaining the state of polarisation (SOP) of the link pulses is in general elliptical and varies along the fibre, depending on bending radii and temperature. The link pulses travel the complete path length to the remote terminal where they are partly reflected. The ratio between reflected and transmitted pulses differs, depending on the power requirements of the end-station; typically, partially transmissive mirrors with 50 : 50 up to 95 : 05 transmission-to-reflectance ratio are used. To optimise the power level, an EDFA is interposed in the link fibre to adjust simultaneously the optical power at the link ending and at the origin. On their way back to the link box, the pulses traverse the exactly same fibre path but in reverse order. To avoid interference between forward and backward travelling laser pulses, they are not only reflected at the link ending but also turned in their SOP by 90°. This is accomplished by use of a Faraday rotating mirror (FRM) instead of a simple partially transmissive mirror. Because the returning pulses experience the same birefringence of the fibre as the forward travelling pulses, their polarisations states are always perpendicular to each other, at least in the ideal case when non-linear effects are absent in the optical fibre. It is assumed, that on short time scales the average birefringence of the fibre is not changing within the round-trip time.

The pulses returning from the link ending are spatially and temporally overlaid with new references pulses from the MLO in the optical cross-correlator (OXC) of the link box. In this configuration the perpendicularly polarised pulses are focussed into a non-linear crystal where an interaction between both laser pulses generates a new pulse at their sum frequency. For the 1550 nm laser, the second-harmonic light has a wavelength of 775 nm. The crystal type has been fixed in the very first link prototype. Ever since a periodically poled Potassium Titanyl Phosphate (PPKTP) crystal is used for the cross-correlation. To become insensitive to amplitude variations and common mode drifts, the OXC is constructed such, that the fundamental modes are reflected at the rear-side of the PPKTP crystal generating the sum frequency signal twice.

Two properties of the crystal define the wavelength conversion process: the non-linear properties which are responsible for the frequency mixing and the linear birefringence. The latter is responsible for a difference in the group velocities for both orthogonal polarisation states. The overlaid pulses therefore run through each other once on their way through the crystal, until they are reflected at its rear side. Then the pulses run through each other a second time, but with reversed lateral positions. In this process, the wavelength conversion is most efficient at maximum achievable overlap. This duplication of the cross-correlation process, which is the hardware implementation of a mathematical convolution, guarantees the detection of a balanced signal. This is an important feature, since the intensity of the second-harmonic light is generally not only depending on the spatial and temporal overlap of the two pulses at the fundamental mode, but also on their intensities. Both generated sum-

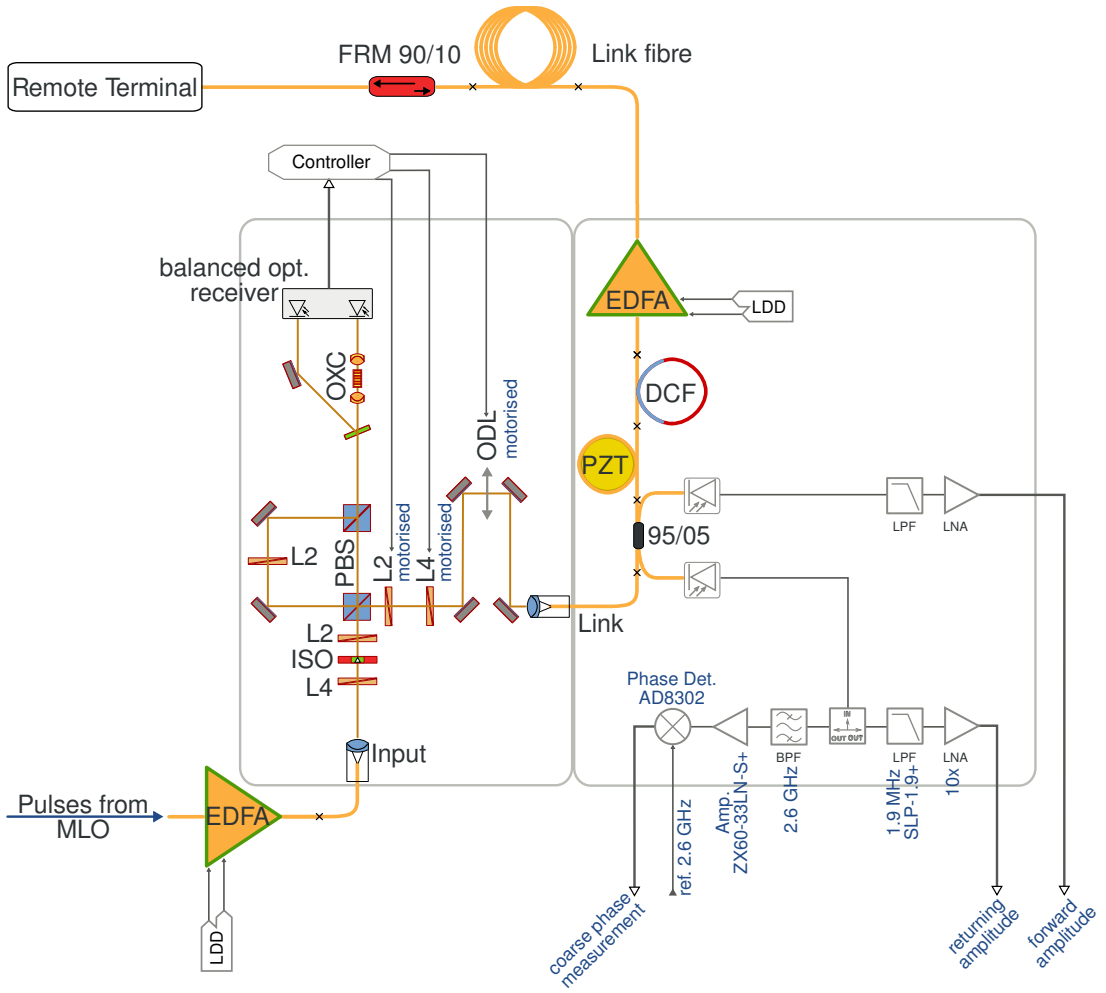

Figure 2.1: Illustration of the latest fibre link layout. The grey-coloured frame on the left hand side encloses the free-space optics of the link box. To the right, a second grey-coloured frame surrounds the analogue electronics which are also mounted in the link chassis. All lines coloured in orange depict SMF.

frequency signals are detected with a commercial, balanced optical receiver. Details on the physical background of the cross-correlation and on the employed non-linear crystal are found in [Sch11b].

Since the wavelength conversion is highly dependent on the temporal overlap of both fundamental mode pulses, the second-harmonic intensity is a measure for the relative timing between the reference pulse and the returning link pulse. The repetition rate of the MLO is stabilised at $R_{\mathrm{rep}} = 216.667\,\mathrm{MHz}$, resulting in a time interval of $T_{\mathrm{rep}} = 4.614\,\mathrm{ns}$ between two adjacent pulses. In free space, two pulses are therefore separated by 1.385 m, corresponding to an in-fibre separation of about 0.93 m. In conclusion, timing variations due to environmental link length changes of $\pm 1/2 T_{\mathrm{rep}}$ can be distinguished unambiguously. When commissioning a new fibre link, the total length is initially adapted such, that the round-trip time of the link pulses is a integer multiple of T_{rep}. During installation of a link, this adaptation is done once by cutting the link fibre to the ideal length, down to $\pm 10 - 15\,\mathrm{mm}$. To compensate for the dispersive pulse broadening introduced in the SMF,

an exactly lengthened piece of dispersion compensating fibre (DCF) is added, having a strong group delay dispersion (GDD) with opposite sign. Although the dispersion compensation is not perfect, the returning link pulses are broadened only by a factor of 1.2 to 3.0, compared to the reference laser pulses with about 300 fs FWHM. Details on the commissioning process and the dispersion compensation of the individual links, can be found in [Sch11b].

The coarse overlap of reference and link pulses in the OXC is found by use of a motorised optical delay line (ODL), which is incorporated in the opto-mechanic chassis (compare figure 2.1). During the closed-loop operation of the links, the ODL is used for compensating slow timing changes within a large dynamic range. For a compensation of fast timing changes within a range of ±3.8 ps, a fibre stretcher is employed. This device consists of a cylinder around which about 40 m of SMF is wound. Its diameter can be controlled by applying a voltage to a piezoelectric transducer (PZT). The latter abbreviation is used in the illustration 2.1 to indicate the position of the fibre stretcher in the layout. Additional to the voltage supply and read-out of the mentioned devices, i.e. ODL, PZT and balanced receiver, the link chassis contains additional analogue electronics for laser amplitude monitoring and an RF-based phase detection.

Calibration curves of both, the OXC signals and the PZT performance can be found in section 2.3.3 and 2.3.2, respectively. The layout and specifications of the ODL are described in section 2.1.4.

2.1.2 Differences between the Various Design Stages

From the very first proof-of-principle experiments performed earlier starting from 2006 [Lö9], the engineered fibre-link design has evolved enormously during the process of setting up a complex synchronisation system, comprising several links of different lengths, connected to various types of remote stations. Especially the opto-mechanics inside of the link box, as well as the chassis itself, has undergone several design iterations to be optimised under different aspects. The growing experience during the assembly and commissioning of the individual fibre links lead to a systematic restructuring of the link-box and its subcomponents, without changing the general operation principle. During this thesis a considerable amount of time and effort has been invested to achieve an engineered link design which meets the demand of a stable and reliable performance. The steps which lead to the configuration of the free-space optics in the latest link (version 3.0), are described in the following on the example of older, existing fibre links. The newest opto-mechanics will not only be used for the installation of the next fibre links, scheduled in the near future, but will also replace the currently employed older versions, to achieve a uniform system.

Version 0.x

The first proof-of-principle experiments had been performed on bread-board set-ups. Measurements of the in-loop timing jitter of two individual links confirmed the feasibility of the general design [Lö9]. However, an important correlation measurement, comparing the out-of-loop timing stabilities of two different links against each other, is still pending. Such a measurement is expected to confirm, that the intended point-to-point stability of below 10 fs can be accomplished.

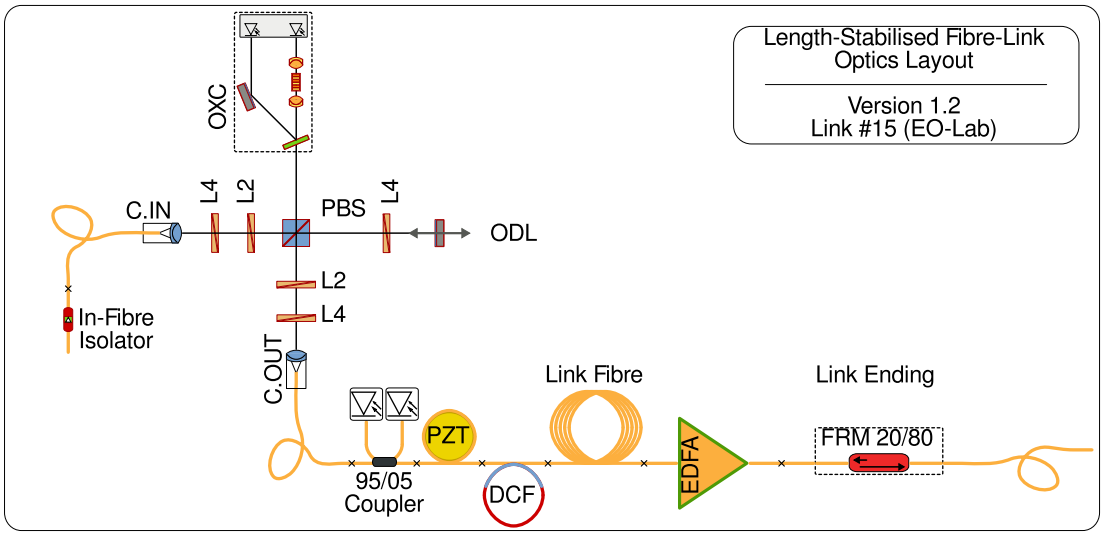

Figure 2.2: Illustration of the optical layout which is applied in link design version 1.2.

Version 1.x

The first engineered design of a link chassis and optics configuration had been planned and constructed in the frame work of Florian Löhl's thesis, compare [Lö9]. By the same time, the laser laboratory in the synchronisation hutch had been assembled [Wino8]. In this regard, especially the size of the optical table had been determined, allocating the space for several main components of the LbSyn system, including the master laser oscillator (MLO), the FSD and the links. Since then, the maximum dimensions of the link boxes have been fixed. All reconstructions therefore are restricted to the tight space limitations. Figure 2.2 illustrates the optical layout which is applied in the design version 1.x. In this scheme, the amplified laser pulses from the MLO enter the link optics from the left hand side. The laser pulses leave the optical fibre at the collimator denoted with C.IN (compare illustration). The pulse power is split by use of a polarising beam splitter (PBS), such that the reference pulses are reflected upwards (according to the illustration) and are vertically polarised (perpendicular to the paper surface). The link pulses, polarised parallel to the optics plane, are transmitted straight on to the ODL, consisting of a motorised linear stage with a plane mirror. Both waveplates left of the PBS are used to adjust the rotation angle of the linear polarisation for controlling the power splitting ratio. Due to the quarter waveplate between the PBS and the mirror of the ODL, the polarisation state of the back reflected link pulses is rotated by 90 deg, such that they are diverted downwards by the PBS. These pulses are coupled into the link fibre by use of a collimator, denoted as C.OUT (compare illustration). The pulses propagate through the fibre section to the link ending, where they are partly reflected by the Faraday rotating mirror (FRM). The latter component also assures, that the state of polarisation is rotated by 90°. When the link pulses are returning again at the PBS, they are polarised parallel to the optics plane and are therefore transmitted upwards, without traversing the ODL a second time. In the OXC, the horizontally polarised link pulses can be correlated with new, vertically polarised reference pulses. The two waveplates between the PBS and C.OUT are used to

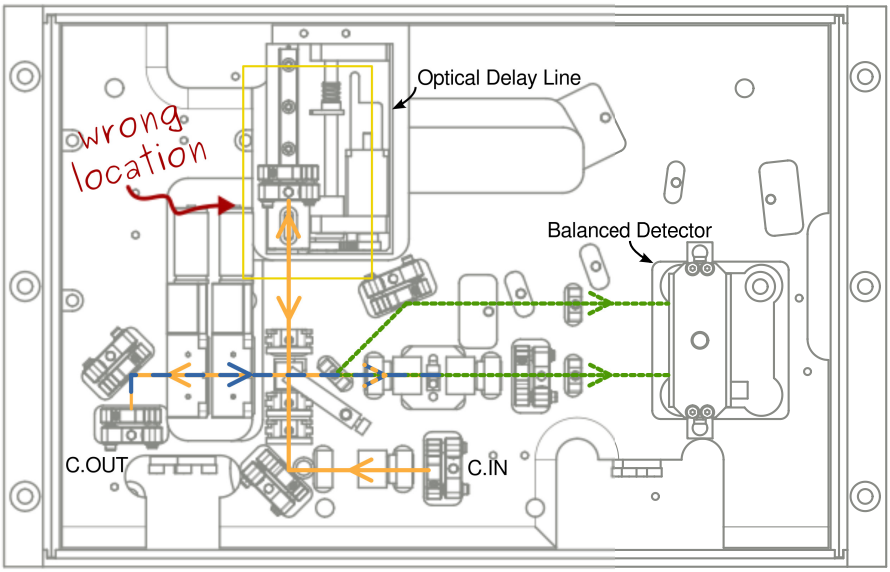

Figure 2.3: Top view on the construction drawing of link version 1.1. The optical path is highlighted to emphasise the incorrectly positioned motor stage.

adjust the rotation angle of the generally elliptical polarisation at the link ending, behind the FRM. This is an important feature for all polarisation-sensitive remote stations, like the bunch arrival time monitors (BAMs).

The main problem, which arose from the featured design scheme, concerns the position of the optical delay line. The ODL is not only used to find the temporal overlap between link and reference pulses, but also to compensate for environmental length changes > 1.2 mm of the optical fibre, in order to keep the optical path length between PBS and FRM constant. But in this old link design the laser pulses pass the ODL only once, namely in forward direction, on their way through the link. This generates the problem, that any position change of the ODL influences only the forward travelling pulses, whereas the path length for the returning pulses remains unchanged. If the motor stage is moved intendedly to compensate for a measured length difference of the total link path, the path length difference is overcompensated in the forward direction by a factor of two, so that the timing at the link ending changes. If the link fibre length changes by a small amount δx, the light pulses will actually experience a path length difference of $2 \cdot \delta x$, because they traverse the fibre twice during a complete round-trip. The motorised ODL has to be moved such, that the path length difference $2 \cdot \delta x$ (in fibre) is exactly compensated by the according free-space distance of $-(2 \cdot \delta x) \cdot {}^{n_{fibre}}/_{n_{air}}$, where the n_i are the refractive indices of glass fibre and air, respectively. Due to this, the timing of the pulses at the link ending is shifted by

$$\delta x|_{\text{forward}} - 2 \cdot \delta x|_{\text{ODL}} = -\delta x$$

Figure 2.3 shows a top view on the construction drawing, in which the optical path is highlighted to emphasise the incorrectly positioned motor stage.

In the first engineered link version, this design fault has been overlooked, until the effect was observed directly with the BAMs. During electron bunch arrival time measurements, a correlation showed up between step-wise arrival time changes and movements of the ODL in the according link. Even though this design error demanded to be removed, it did not prohibit the operation of the deficient links, since the excess timing change of the link pulses behind the FRM can be compensated by the motorised delay stage incorporated in the BAM chassis. This workaround has been included into the control software, in order to always move both delay stages simultaneously by the same amount, such that the timing changes are canceled out.

Version 2.x

The major design flaw, described above, has been removed in the subsequent design iteration, i.e. version 2.x. Figure 2.4 illustrates the adjusted optics configuration, in which the optical delay line (ODL) is integrated at a location where it is passed twice, i.e. in forward and in backward direction. To find a possibility to include the ODL at its new position, a major reorganisation of all other optical components was required due to the limited space on the optics plane. The solution, which in fact also improved the stability of the optical delay line, is describe in detail in the next section (2.1.3). Details on the in-house development of the motorised delay stage, which ran in parallel to the optimisation of the fibre links, are given in section 2.1.4 and 2.3.1. Minor changes had been made to the link chassis in order to achieve a space-saving mounting of components on the underside of the optics plane and on the base plate of the link chassis. Care has been taken, to allow for exchanging critical components in an already assembled link without large effort, concerning for example the motorised delay stage.

Although in earlier link iterations a telescope directly behind the input collimator C.IN has been included, the distribution of the laser beam envelope along the optical path was not ideal. A matched optics is required for achieving a high incoupling efficiency when launching the laser pulses into the

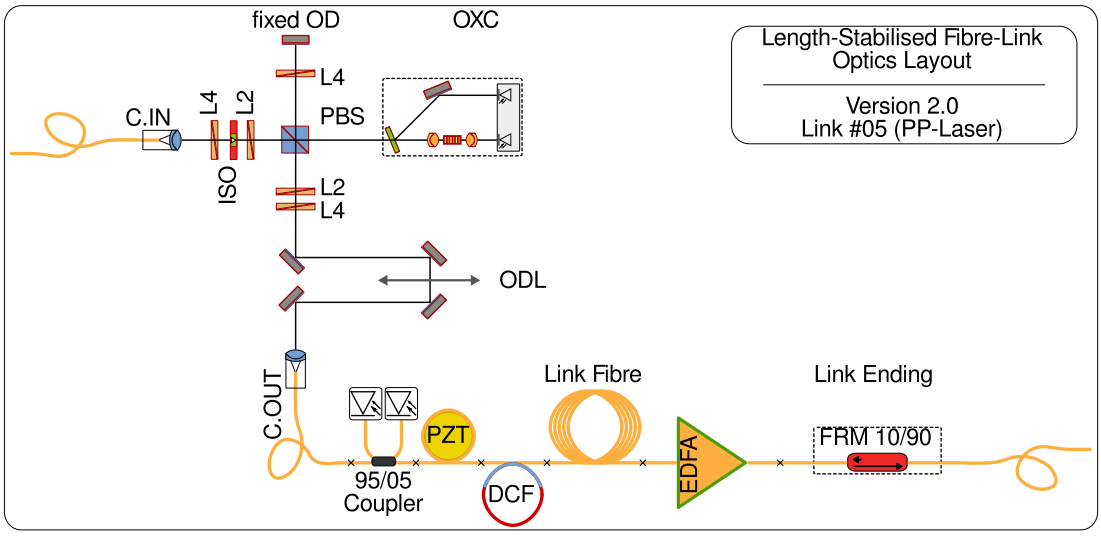

Figure 2.4: Schematic of link optics version 2.0. The motorised optical delay line (ODL) is positioned correctly.

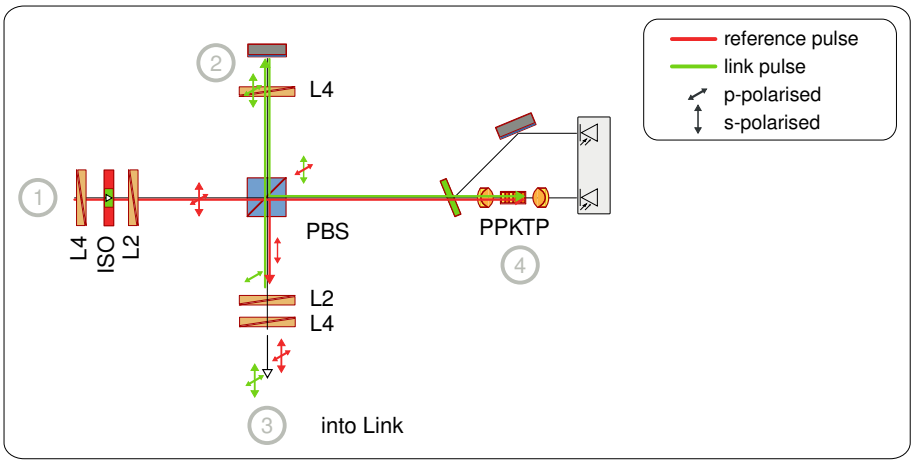

Figure 2.5: Illustration of the problematic optics configuration where an interference occurs between equal polarisation states inside of the PBS.

output collimator C.OUT. But in addition, the focussing of both laser beams, i.e. the reference and the link pulses, into the PPKTP crystal of the cross correlator is a critical factor for the efficiency of the second-harmonic light generation. To achieve a strongly focussed beam spot inside of the crystal, an achromatic lens with a very short effective focal length of +12.6 mm is used since the first link prototype. The optimisation of the optical cross-correlator (OXC) signal is done by adjusting the distance between lens and crystal. The spatial overlap between both beam spots is improved, when the beam sizes and divergence angles of reference and link pulses are similar. From link version 2.0 on, the optics configuration has been optimised by choosing appropriate lens configurations to fulfil both requirements simultaneously.

The calculation of a matched lens combination as well as an estimation of the tolerance against a mismatch in the lens mounting is described in section 2.2 on page 41 ff. All of the optical components, including lenses, beam splitters and prisms, have a narrow-band, anti-reflective coating at wavelengths of 1535 – 1585 nm to reduce optical power losses and back reflections.

Even though the new link design solved several problems and minor flaws, the source for another major problem was identified, which appeared during the link operation but had been undissolved until then. It was observed, that for the case of ideal temporal overlap of reference and link pulses in the OXC a high-frequency amplitude noise appeared at the power monitors inside of the fibre link line and behind the link ending. Even though the integrated relative intensity noise (RIN) amounts to less than 1 % it impedes the operation of remote stations which are sensitive to RF noise contribution below 1 MHz, since the amplitude noise is converted to phase noise in photo detectors. A small selection of single-side band amplitude noise spectra, pointing out the observed effect, are discussed in section 2.3 on page 62 ff.

One contributing error source has been identified to be related to a temporal and spatial overlap of equally polarised parts of the laser pulses inside of the polarising beam splitter. The commercial PBS, having been employed until then, is made of two high-quality prisms, of which one has a dielectric coating for achieving the splitting of light into two orthogonal polarisation states. Both prisms are cemented onto each other to form a cube. The rate of amplitude noise could be decreased a little by

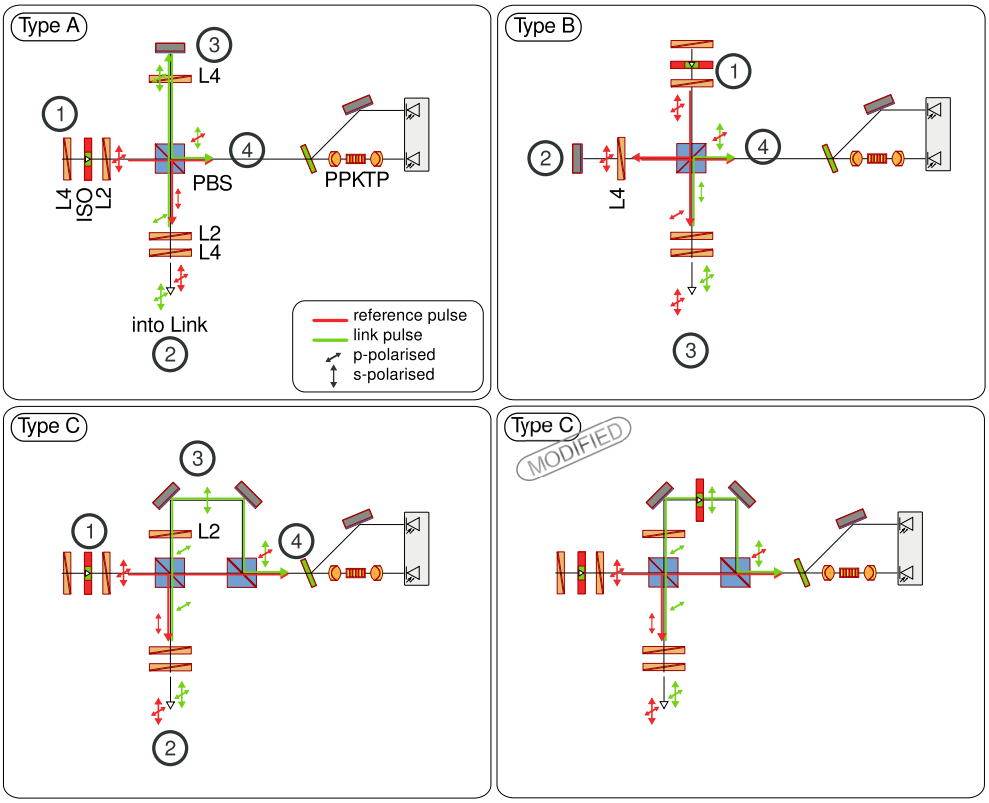

Figure 2.6: Three types of optics configurations, in which a temporal separation of equal polarisation states at the location of the PBS is achieved.

exchanging the cemented beam-cubes with another type of PBC where the two prisms are optically-contacted. The latter means, that the high-grade polished, inner surfaces of the cube are bonded through inter-molecular forces only, like Van Der Waals forces or hydrogen bonds.

Figure 2.5 illustrates the problematic optics configuration which contributes to the observed amplitude noise. The MLO pulses are entering the link optics from the left. The PBC is oriented such, that horizontally polarised (p-polarisation) pulses are transmitted straight on to the OXC and the vertically polarised (s-polarisation) pulses are diverted to the top. They pass a short detour, consisting of a quarter waveplate and a plane mirror, before being transmitted downwards to the link collimator C.OUT with p-polarisation. When thoses pulses return from the link ending they are s-polarised when hitting the PBC again and get reflected to the right hand side in direction of the OXC. In the case, that reference and link pulses have temporal overlap in the PPKTP they inevitably overlap in the beam splitter, too, since the total link length is adjusted such, that the round-trip time for the pulses is an integer multiple of the pulse spacing. Between PBC and PPKTP both orthogonally polarised pulses are co-propagating. But by the time the pulses overlap in the PBC, a third electro-magnetic (EM) field with s-polarisation exists, since a successive reference pulse is split in that moment into two parts. The temporal and spatial overlap of two s-polarised EM fields generates a cross-talk between forward travelling and returning link pulses. It is not exactly clear which physical or chemical reactions are involved in the beam cube, that could lead to an interference effect

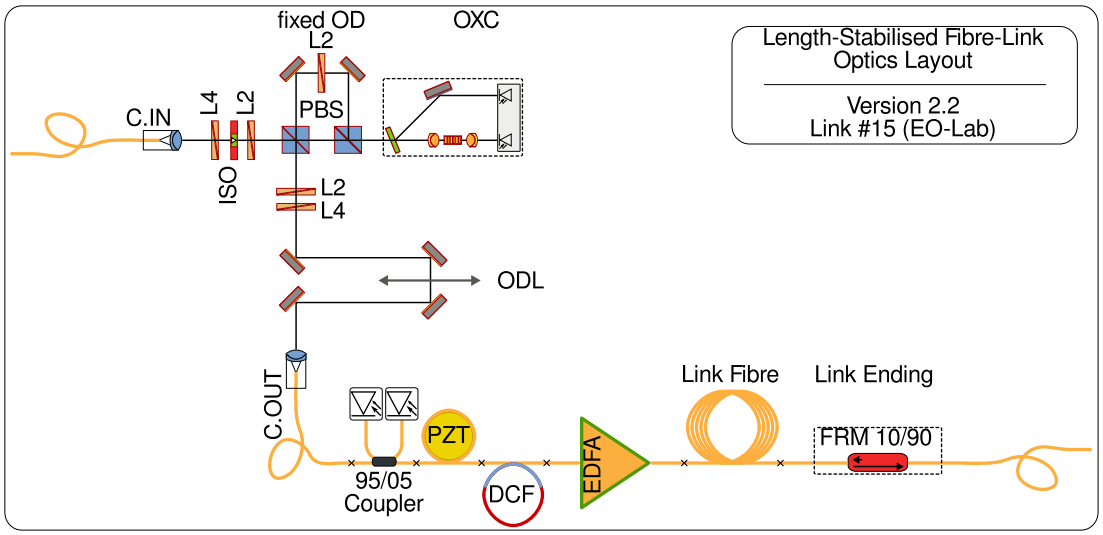

Figure 2.7: Schematic of link optics version 2.2. Besides minor changes in the opto-mechanics, this design is also employed in the latest link (version 3.0).

contributing to the observed amplitude noise. Anyhow, it can be significantly suppressed by avoiding the temporal overlap of equal polarisation states in the beam cube.

Figure 2.6 shows three possible optics configurations which are adequate for this purpose. The optics type A (upper left) resembles nearly the same optical set-up as in figure 2.5 with the difference, that the PBC is turned by 90°. In this case, the detour via quarter waveplate and mirror is taken by the link pulses not until they are returning from the link ending. Thus, the splitting of new MLO pulses in the PBC occurs previously, separated by the time interval that the returning link pulses require for traversing the detour. Type B (upper right) is effectively the same as A, unless in this case the detour is run through by the reference pulses. Compared to both mentioned set-ups, in type C (lower left) the extra time interval between splitting and recombination of reference and link pulses is accomplished by a *two-cube configuration* instead of using a simple plane mirror. The benefit of this solution is the additional degree of freedom which is gained by using two mirrors along the detour for the returning link pulses. Thus, not only angle but also position errors of the laser beam can be compensated for an enhanced alignment in the OXC.

Because of both mentioned advantages, the decision was to use the *two-cube configuration* (type C) in the opto-mechanics of the present link version 3.0. Figure 2.7 illustrates the free-space and fibre optical layout which is used since link version 2.2, employed in spring of 2011. As mentioned above, measurements of the amplitude noise in the old optics configuration and the new one of type C, are presented in section 2.3.4 on page 62 f.

To achieve an optimal performance of the fibre links, any cross-talk between forward an backward travelling pulses has to be avoided. Problems might occur through unwanted reflections on optical components, causing ghost pulses which potentially travel through the fibre links, too. To further decrease the amplitude noise, other disturbance sources have to be identified and surppressed in the planned, future investigations.

Another design change compared to older versions is the fact, that for the two newest fibre links the interconnected EDFA is shifted to the beginning of the link fibre line, directly behind the DCF. In all previously installed links, the amplifier is located at the link ending. This decision was made, because both, the forward travelling as well as the returning link pulses, are dispersively broadened at the location of the amplifier next to the DCF. It is expected, that the broadened pulse suffers less from non-linear effects in the gain fibre of the amplifier which would lead to distortions of the optical spectra. The installation of the EDFA inside or next to the link box has the additional advantage of a simpler maintenance, compared to an installation at the link ending inside of the accelerator tunnel. Influences of fibre properties along the link line on the signal quality are presented in detail in [Sch11b]. Since the main objective of this thesis in conjunction with the links has been the optimisation of the engineered opto-mechanics and chassis, all discussions in this section concentrate on the free-space optics.

Version 3.x

The latest opto-mechanic design has been finished by mid of 2011. It is planned to be used for all mid-haul links. The layout will not only be used for the upcoming installation of additional links with respect to FLASH II, but it is foreseen to exchange the already existing, older links with the new mechanics. To summarise the developments which lead to the latest, engineered link box, the following section (2.1.3) gives an overview on the main characteristics and substantial advantages. For future purposes, especially for long-haul links with length $\gg$ 500 m, additional components might be needed, for example for a higher order dispersion compensation. Since the components density of the present link chassis is considerably high, any additional demands might require a further restructuring of the link mechanics and optics design in the future. But for the LbSyn system at FLASH the mechanical link design is settled, for the time being.

2.1.3 Major Design Changes from the Latest Revision

In the following, the substantial changes compared to all earlier link designs are briefly summarised. All of which have enormously improved the ease of assembly, the alignment of the optics as well as the fibre cabling management, thus fulfilling one of the goals of this thesis. Several aspects have been incorporated in the revision of the link boxes:

- optimised incoupling efficiency of laser pulses to reduce the overall power requirements
- provided an easy assembly of the numerous optical and mechanical parts
- improved the time consumption for the alignment of the whole link optics
- enhanced the degrees of freedom for a collinear alignment of reference and link pulses into the PPKTP crystal of the OXC
- enhanced the directivity of the amplified MLO pulses to isolate the EDFA in front of the link box from back reflected light
- optimised the optical properties of the reference and link laser pulses, like diameter and divergence

- increased the efficiency of the optical delay line to reduce path-length as well as position dependent losses
- allowed for a possible replacement of particular components by hindsight
- improved the management of fibre-connected components which are stored in the link-boxes
- reduced the space requirements of the electronics
- removed constructional errors

Figures 2.8 and 2.9 show technical design drawings of the current link opto-mechanics. The dimensions of the ground plate of the box are about $210 \times 350\,\mathrm{mm}^2$. The chassis is separated into three compartments:

1. free-space optics on the upper layer
2. fibre optics in the middle layer
3. low-voltage components of the read-out electronics in the lower layer

The fibre assembly includes the devices for pulse amplification, power coupling, in-fibre first order dispersion compensation and fibre length control. The individual components are described in a previous section, 2.1.1. All of those fibre-coupled components are well-arranged at the underside of the thick aluminium plate which supports the free-space optics. The electronics, which include fibre-couple photo-diodes, low-noise amplifiers, a band-pass filter, an RF phase detector and a DC voltage divider, are mounted on the base plate of the link box. Currently, developments are on-going to comprise all of the mentioned electrical components into one integrated circuit board for efficient space utilisation and for the favourable price compared to the individual devices.

motorised delay stage

The optical delay line for the coarse tuning of the optical path length along the link transmission line, comprises a free-space configuration with an optical reflective element mounted on a motorised stage. With the first engineered link version, the allocated space for the optics plane as well as the total volume of the link box had been fixed. Nevertheless, the optical delay requires an adjustment range which can cope with the expected timing changes along the fibre link, introduced by environmental changes of the temperature and, less pronounced, by humidity changes. Although the fibres are laid out inside of the the accelerator tunnel for the most part, the temperature fluctuates on average between 27 °C to 34 °C between winter and summer during operation of FLASH, because the tunnel is not actively temperature stabilised. The temperature dependency of the transit time $\delta\tau/\delta T$ along an optical link is a combination of the temperature drift of the glass material and the temperature induced change in refractive index [BEJ83]:

$$\frac{\delta\tau}{\delta T} = \frac{1}{c_0}\left[\frac{\partial n}{\partial T}L + n\frac{\partial L}{\partial T}\right] \tag{2.1}$$

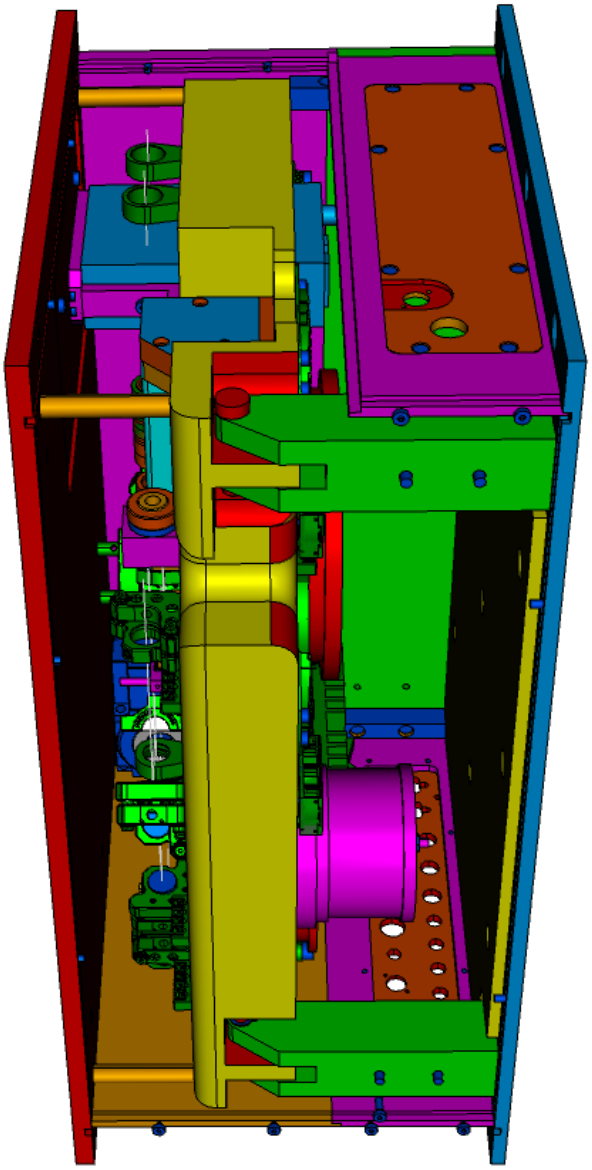

Figure 2.8: Technical design drawing: side view of the latest fibre-link box (version 3.0), with parts of the chassis removed (courtesy of K. Jähnke).

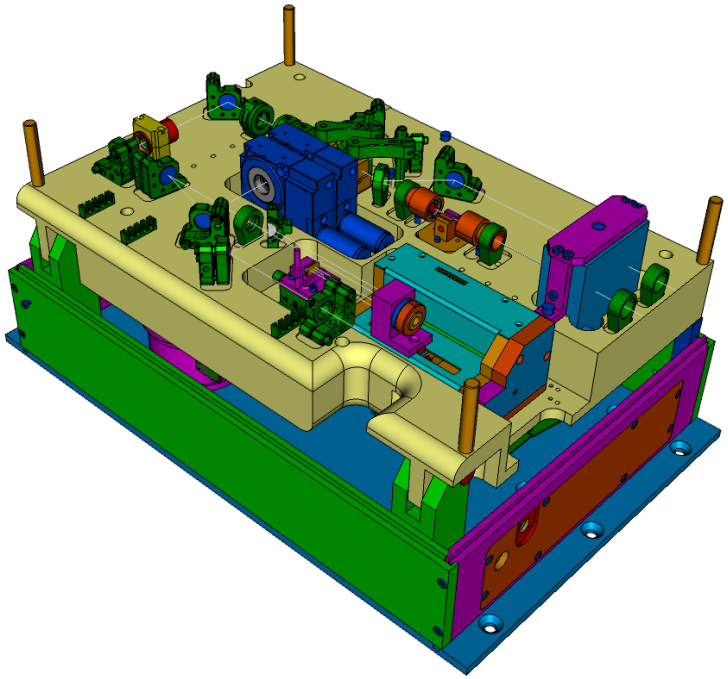

(a) Top-layer of Link Vers. 3.0: The free-space optics with the delay line in the foreground. The two devices mounted in the centre of the base plate are motorised rotation mounts for two waveplates. On the right hand side of the delay line, the commercial balanced optical receiver can be seen.

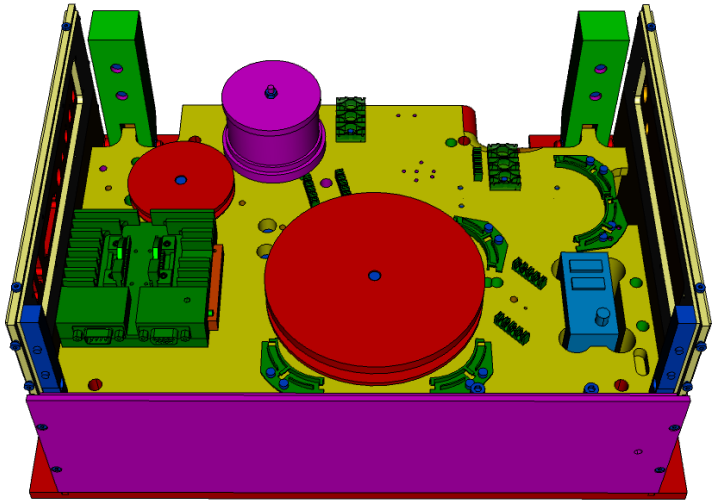

(b) Middle-layer in the opto-mechanics of Link Vers. 3.0: view from bottom. On the left lower side, the commercial laser diode mount can be seen. The large spool in the middle of the base plate is used to wind up the DCF. The small spool next to the laser diode mount is used to wind up the fibre of the pump-diode and the cylindrical device at the rear edge is the fibre stretcher.

Figure 2.9: Technical design drawings of the latest fibre-link box (version 3.0). (courtesy of K. Jähnke)

with c_0 the velocity of light, the fibre length L and the group index of refraction, n, which takes a value of 1.468 in case of SMF28e® Corning fibre at 1550 nm [Web11b]. Typical values for the opto-thermal coefficient $\partial n/\partial T$ and the thermal expansion coefficient $\partial L/\partial T$ in single mode fibre (SMF) are given in table 2.1.

Table 2.1: Typical values for the opto-thermal coefficient $\partial n/\partial T$ and the thermal expansion coefficient $\partial L/\partial T$ of single-mode fibres. The relative coefficients are valid in a temperature range of −65 to +80 °C, according to [BEJ83]

$\frac{1}{n}\partial n/\partial T$	6.1−8.0	$\times 10^{-6}$/K
$\frac{1}{L}\partial L/\partial T$	5.5−7.5	$\times 10^{-7}$/K

Consider an optical link with a total fibre length of $L = 500$ m. Using equation (2.1) with a mean value of the given coefficients, one obtains a transit time delay per unit temperature change for a total fibre length of 500 m of

$$\frac{\delta\tau}{\delta T} = 18.474\,\text{ps/K}$$

Assuming a typical peak-to-peak temperature variation between winter and summer of $\Delta T = 7$ K across the total fibre length (at FLASH), the transit time varies by

$$\Delta\tau = 129.315\,\text{ps}$$

which results in a fibre length change of

$$\Delta s_{\text{fibre}} = 26.430\,\text{mm}$$

This corresponds to a free-space optical path length change of $\Delta s_{\text{air}} = 38.799$ mm. For an optical delay line with a plane mirror mounted on the motorised stage, this would require a travel range of $\Delta s_{\text{air}}/2 = 19.3299$ mm to compensate for the expected timing changes along the fibre link.

In case of the fibre links at FLASH, in which the ODL is still built in at the wrong location, the total path length change for a complete round-trip, $2 \cdot \Delta s_{\text{fibre}}$, has to be compensated completely by a single pass of the delay line. Nevertheless, we observed, that a travel range of about 46 mm (one-way) is sufficient for compensating the deviations during the course of a year, although there is not much safety margin left. Since the laser pulses are reflected once by the plane mirror on the stage, any motor position change δx corresponds to an optical path length change of $2 \cdot \delta x$. In conclusion the fibre length for links shorter than 500 m varies by $\Delta s_{\text{fibre}} < \delta x$, which is less than 45 mm. This shows, that the above calculation with an assumed temperature change of 7 K (peak-to-peak), is a good estimation of the expected, maximum length changes along the total link transmission line. If the ODL was built in at the correct location, one gains a factor of two, since the laser pulses pass the delay on the forward run and a second time on the return path. Thus, the ODL has to compensate the fibre length difference in one way only. Nevertheless, in case of larger temperature drifts and, especially, for links longer than 1000 m, larger adjustment ranges are required while keeping to the strict space

limitations of the link boxes. Therefore, it was decided to change the optical delay line from a simple, moveable plane mirror to a configuration in which any motor position change δx results in an optical path length change of $4 \cdot \delta x$. Additionally, the allocated space for the linear motor stage in the link box, has been enlarged as much as possible to allow for using linear stages with a maximum travel range of up to 85 mm. The technical realisation of this new ODL is described in the next section 2.1.4, but at first, a rough estimation is following to show, that the gain in adjustment range is expected to be sufficient, even in case of long-haul links as planned for the European XFEL. Using equation (2.1) for a 3 km link, the timing change per unit temperature change results in:

$$\frac{\delta \tau}{\delta T} = 110.842\,\text{ps/K} \tag{2.2}$$

For a temperature change of peak-to-peak 7 K along the total fibre path, which is much more than the typically expected temperature variation during operation of the European XFEL, the timing difference amounts to

$$\Delta\tau = 775.892\,\text{ps}$$

which corresponds to a length change in fibre and in air, respectively, of:

$$\Delta s_{\text{fibre}} \approx 158.577\,\text{mm} \rightleftharpoons \Delta s_{air} \approx 232.791\,\text{mm}$$

For a construction of a fourfold pass delay line, in which the laser pulses traverse the travel range of the linear motor stage four times, the actually required adjustment range reduces by a factor of four:

$$\Delta s_{\text{travel}} = \frac{\Delta s_{\text{air}}}{4} \approx 58.198\,\text{mm}$$

From the above estimation it follows, that for the newly developed motor stage, having a total travel range of about 85 mm, this would not only be sufficient but would also leave a reasonable safety margin. From an reversed point of view, the 85 mm travel range correspond to a total optical path length adjustment range in air of:

$$\Delta s_{\text{air}} = 340\,\text{mm}$$

In fibre this is equal to

$$\Delta s_{\text{fibre}} = 231.607\,\text{mm}$$

or in terms of propagation time, regarding the refractive index in fibre, as mentioned above:

$$\Delta\tau = 1.133\,\text{ns}$$

Using the time over temperature coefficient of 110.842 ps/K (eq. 2.2), the calculated worst-case timing deviation of $\Delta\tau$ would be induced by an average temperature difference of 10.22 K along the total fibre length of 3 km.

polarisation dependent separation of reference and link pulses

Another major change in the optics of link version 3.0 is the use of a free-space FARADAY isolator. With a specified isolation of ≥ 28 dB at 1550 ± 25 nm it should avoid signals travelling the wrong way back to the EDFA between MLO and link box. The functional principle of such an polarisation dependent isolator is shown in figure 2.10. The wanted signals, travelling from left to right (in this illustration) become linearly polarised. The FARADAY crystal rotates their state of polarisation (SOP) under the influence of the static magnetic field by 45° before the pulses are transmitted through a second polariser which is also rotated by 45°. If any unwanted signals are travelling in reverse direction their SOP becomes rotated by 90° against the plane of polarisation of the left polariser so that no signal is transmitted. The maximum isolation of this device is determined by the deviations from the ideal 45° rotation angle induced by the crystal. There are various sources for unwanted

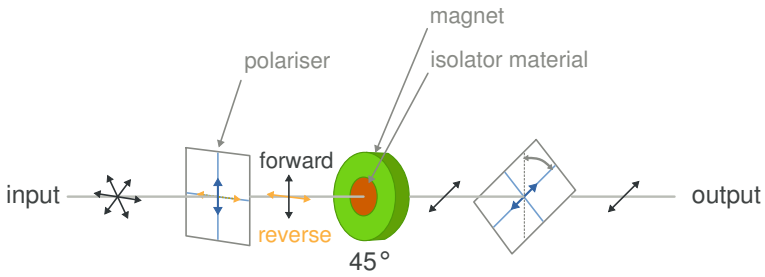

Figure 2.10: Illustration of a FARADAY isolator. In dark grey the forward directed signal and in orange the parasitic, backward travelling signal is shown. Both are rotated by 45° in the FARADAY crystal, so that the forward light is transmitted at the second polariser on the right hand side. Any backward travelling light is stopped at the polariser on the left hand side, because its SOP and the polariser enclose an angle of 90°.

signals in the free-space optics between the collimator C.IN and the first polarising beam cube (PBC):

- reflections on optical components of less than 0.5 % despite narrow band anti-reflective coating
- return loss of the fibre coupled collimators C.IN and C.OUT
- residual reflections of the p-polarised, returning link pulses at the first PBC
- reflections on the first PBC due to a non-ideal state of polarisation, deviating from a p-polarisation, of the returning link pulses

Most of them can be suppressed by use of the free-space isolator. If parasitic signals at 1550 nm propagate back in direction of the MLO, they are also amplified in the EDFA of the free-space distribution unit (FSD), lowering the gain for the wanted, forward travelling signals. This effect has been observed earlier, leading to the decision of using an isolator. Furthermore, those signals can lead to a cross-talk between different links, compare [Sch11b].

2.1.4 Design of the Motorised Delay Stage

In older link versions the optical delay line (ODL) comprised a motorised linear stage and a plane mirror. This configuration is very sensitive to angular errors introduced by the stage movement.

When the first engineered link opto-mechanics had been designed, there has not been paid much attention to the quality of the in-house constructed motorised stage. Due to the fact, that by that time no linear stage had been commercially available, which could comply with the strict space limitations in the link chassis, one had been dependent on a self-made construction.

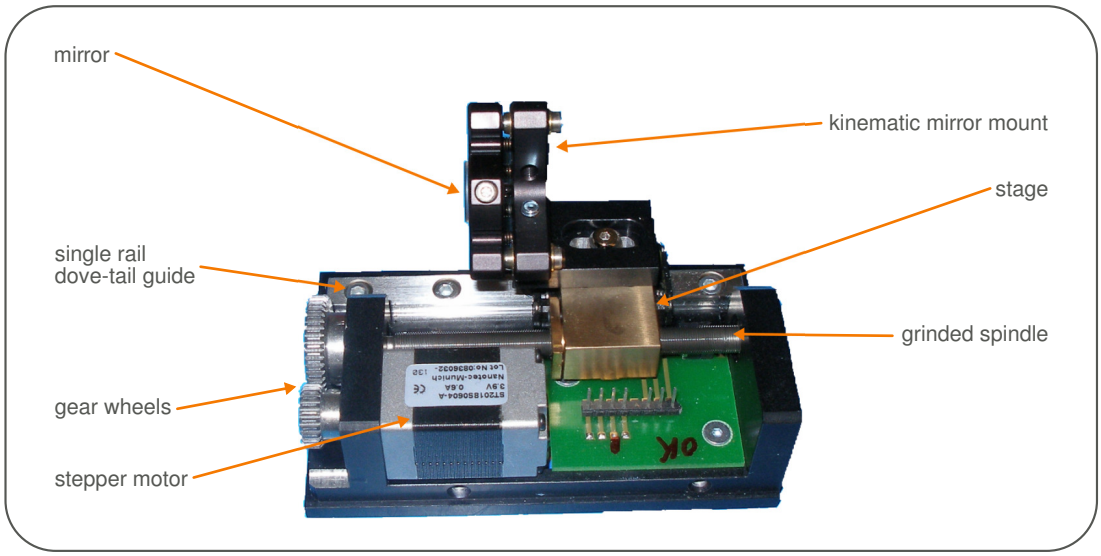

Figure 2.11: Photograph showing one of the first versions of an in-house developed linear motor stage. Design iteration: LMS-Vers. 2.0 - Type 1

Figure 2.11 shows a photograph of one of the first motor stage iterations. It consists of a ground spindle which is driven by a stepping motor. The torque is transferred via two gear wheels which are directly toothed with a gear ratio of 1 : 2. The stage holding the mirror mount is carried by only one dove-tail rail. The spindle in this construction is clamped on both sides, so that the positioning of the stage is done by the spindle only. If the spindle shows deviations from a circular cross-section or if the rail is not plane enough due to the five locking screws, there will appear transverse forces due to tension and increased friction during the movement of the stage. Those forces are position dependent and lead to sudden transverse and angular errors of the stage. The angular deviations in the transverse plane, i.e. pitch and yaw, are estimated with $\gg 5\,\mathrm{mrad}$, but had not been measured directly. The argument for the disqualification of this stage design was found by measurements of the incoupling efficiency of the laser pulses into the collimator C.OUT within the link optics. The collimators used in the first links have a clear aperture (CA) of 4.3 mm and a full divergence angle (θ_{DA}) of about 2 mrad at a beam diameter (BD) of 0.7 mm. The distance from the input collimator C.IN to the plane mirror on the stage is about 0.5 m and another 0.25 m from the mirror to the output collimator C.OUT. The beam diameter is enlarged from the initial 0.7 mm by a factor of three at the location of C.OUT, being about half the size of the clear aperture. For angular deviations of the plane mirror on the stage of 5 mrad the position error of the beam centre in 0.25 m distance amounts to $\delta r = 1.25\,\mathrm{mm}$. Compared to the radius of the clear aperture, this amounts to

$$\frac{\delta r}{\frac{1}{2}\mathrm{CA}} \cdot 100\,\% \approx 60\,\%$$

For this large deviations the laser beam diameter slips out of the CA, by at least 20 %. Since in reality very large and sudden jumps of the incoupling efficiency of 60 % and more had been observed, the pitch and yaw must have been worse than 5 mrad which is a very poor performance. Even for normal precision linear stages the typically specified pitch and yaw is well below ±750 µrad.

Because of these findings, in parallel to the link chassis improvements, the further development of the in-house constructed linear motor stage (LMS) has been started in 2009. The new LMS was planned directly for the use inside of the link optics (with the 0.7 mm BD collimators) with a total travel range of at least 45 mm in an ODL with a plane mirror. The targeted specifications have been:

- a variation of incoupling efficiency of less than 10 % peak-to-peak across the total travel range
- a variation of incoupling efficiency of less than 5 % on short distances in the order of a few millimeter travel
- low slippage (about 1000 steps compared to $> 2 \times 10^6$ steps over the total range)
- smooth movement of the stage
- pitch and yaw of less than ±500 µrad (estimated)

It took about $1^1/_2$ years of development time during the course of this thesis to achieve an LMS design which could fulfil all of the above requirements. The costs for this stage of about 2000 € are comparable to a similar stage which has become commercially available only recently. Nevertheless, the advantage of an in-house development is the large flexibility. The latest design of the LMS is shown in figure 2.12. The ground, recirculating ball spindle is still clamped on both sides being used for the positioning. But now, the stage is guided by two high-quality rods with ball-bearing cages. The complete frame of the stage is cut from one piece of chipping-free aluminium except for the piece which holds the spindle and rods on the left hand side (opposite of the stepper motor). This allows for a very precise assembly. The toothed gear wheels are exchanged by two cogwheels and one toothed belt, which has trapeze-shape instead of V-shaped cogs to reduce the slippage. This design shows very good transverse positioning stability due to the parallel guiding rods. The friction is strongly suppressed through the ball-bearing cages. Any pitch and yaw is mainly due to imperfections of the spindle and secondary due to residual vibrations which are transferred from the motor to the spindle in spite of the damping by the tooth belt. In addition, the end switches have been changed from mechanical to Hall sensors to gain a few millimeters in travel range.

When changing the layout of the ODL from a simple plane mirror configuration to a set-up with two deflecting prisms, the measured performance of the new LMS exceeded all expectations, since the prisms are nearly insensitive to angular errors. Measurements showing a comparison of both configurations with the newest motor stage design are presented in section 2.3.1 on page 54 f.

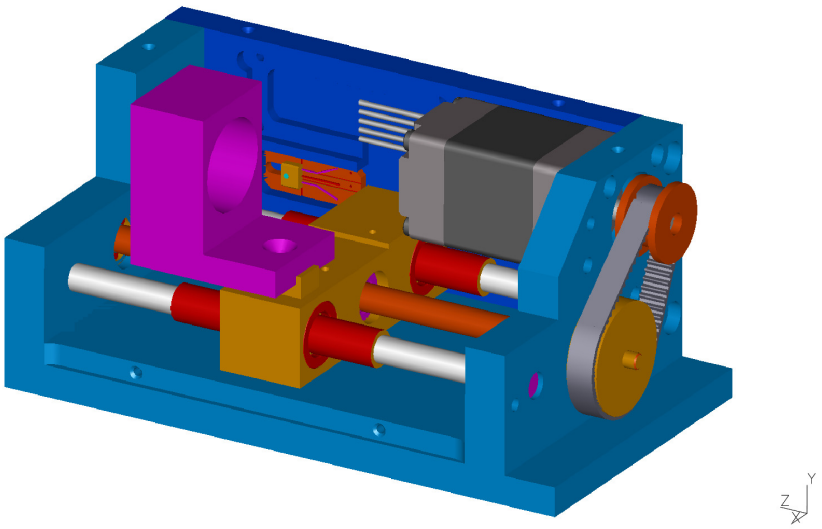

(a) LMS-Type 3-Vers.10.2

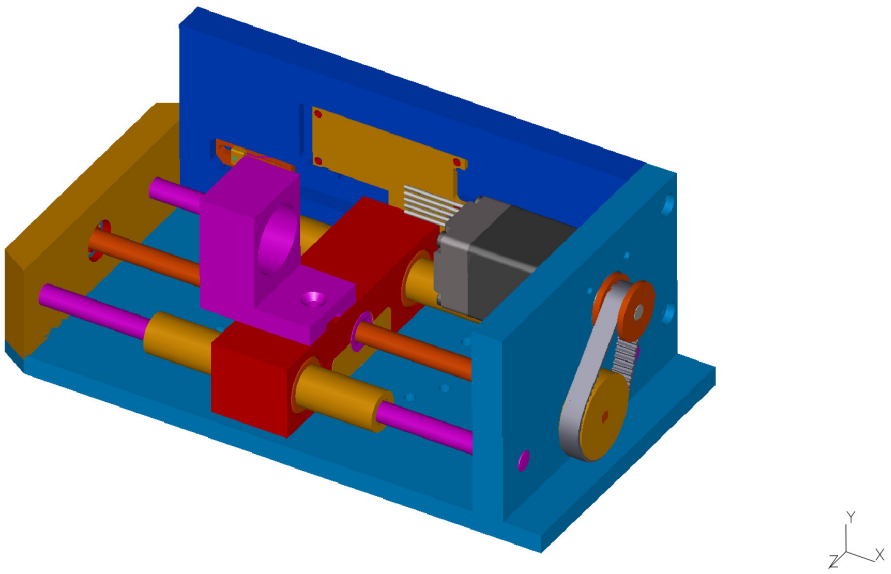

(b) LMS-Type 4-Vers.1.0

Figure 2.12: Technical design drawings of two in-house developed motorised linear stages, with a travel range of (a) 45 mm and (b) 85 mm. (courtesy of K. Ludwig)

2.2 Optimisation of the Link Optics

With an imaging system of up to three lenses, the diameter and divergence of the Gaussian beam envelope can be controlled. One part of this thesis is concerned with the optimisation of the free-space optics for the link. During the planning of the latest link design (version 3.0, see figure 2.13) three additional lens mounts have been foreseen. In the strict space limitations of the optical plane there are only two reasonable locations available for lens mounts: one directly behind the input collimator C.IN, where a fixed lens mount (LM.1) with an adjustable lens tube (LM.2) is provided and another fixed lens mount (LM.3) closest possible to the front of the optical delay line (ODL), compare figure 2.13 After having decided the lens positions, the development of the beam envelope along the link optics has been calculated for three possible cases:

1. 0-lens configuration: no lenses between C.IN and C.OUT
2. 1-lens configuration: only one convex lens at location LM.3
3. 3-lens configuration: a Galilean telescope at location LM.1 & LM.2, using a bi-concave and a plano-convex lens, and a third lens (plano-convex) at location LM.3

The effective focal lengths of the involved lenses have been optimised with regard to a minimum mismatch of the laser beams at the location of the output collimator C.OUT. The simulation results are given in section 2.2.1.

Kinematic mirror mounts, which are adjustable in two planes, are used in the link optics to simplify the alignment procedure. Using the adjustable mounts of C.IN and the first mirror (M.1) the alignment of the laser beam along the OXC branch can be optimised with the help of iris diaphragms, which can be inserted temporarily into the lens mounts LM.OXC1 and LM.OXC2, respectively, as well as into one mount behind the removable balanced detector (not shown in fig. 2.13).

The illustration shows the latest design of the ODL, in which two deflecting prisms are used to achieve a fourfold pass adjustment range. The laser beam passes the lens mount at LM.3 and propagates in a straight line to the retroreflecting prism (RR). There, the beam is deflected by 180° with a diagonal offset (a quasi point reflection at the centre of RR) in direction of the right-angle prism (RP), which is mounted below the centre of RR. The prism RP also deflects the laser pulses by 180°, but with a horizontal offset only. When returning to the retroreflector, the laser pulses are, again, deflected by 180° with a diagonal offset to the centre of RR. Thus, the laser beam exits the RR at the same height as the entering beam, but with a horizontal offset. Using this spatial separation, the laser beam is reflected at a D-shaped mirror (M.DS) in direction of the mirror M.4, from where it is directed to the output collimator C.OUT and coupled into the link fibre. When returning from the link ending, the laser pulses traverse the ODL again, in reverse manner. Using this configuration, any position change of the motor stage generates a four times larger optical path length change.

To avoid a migration of the laser beam spot on the collimator C.OUT when the motor stage moves, the optical axis has to be aligned parallel to the motor axis, determined by the arrangement of the spindle. For this purpose, a two mirror combination (M.2 and M.3) is used, where the second mirror has an acute angle of 15° relative to the extension of the motor's symmetry axis. The adjustable mounts of mirror M.4 and C.OUT are then used to optimise the laser beam incoupling.

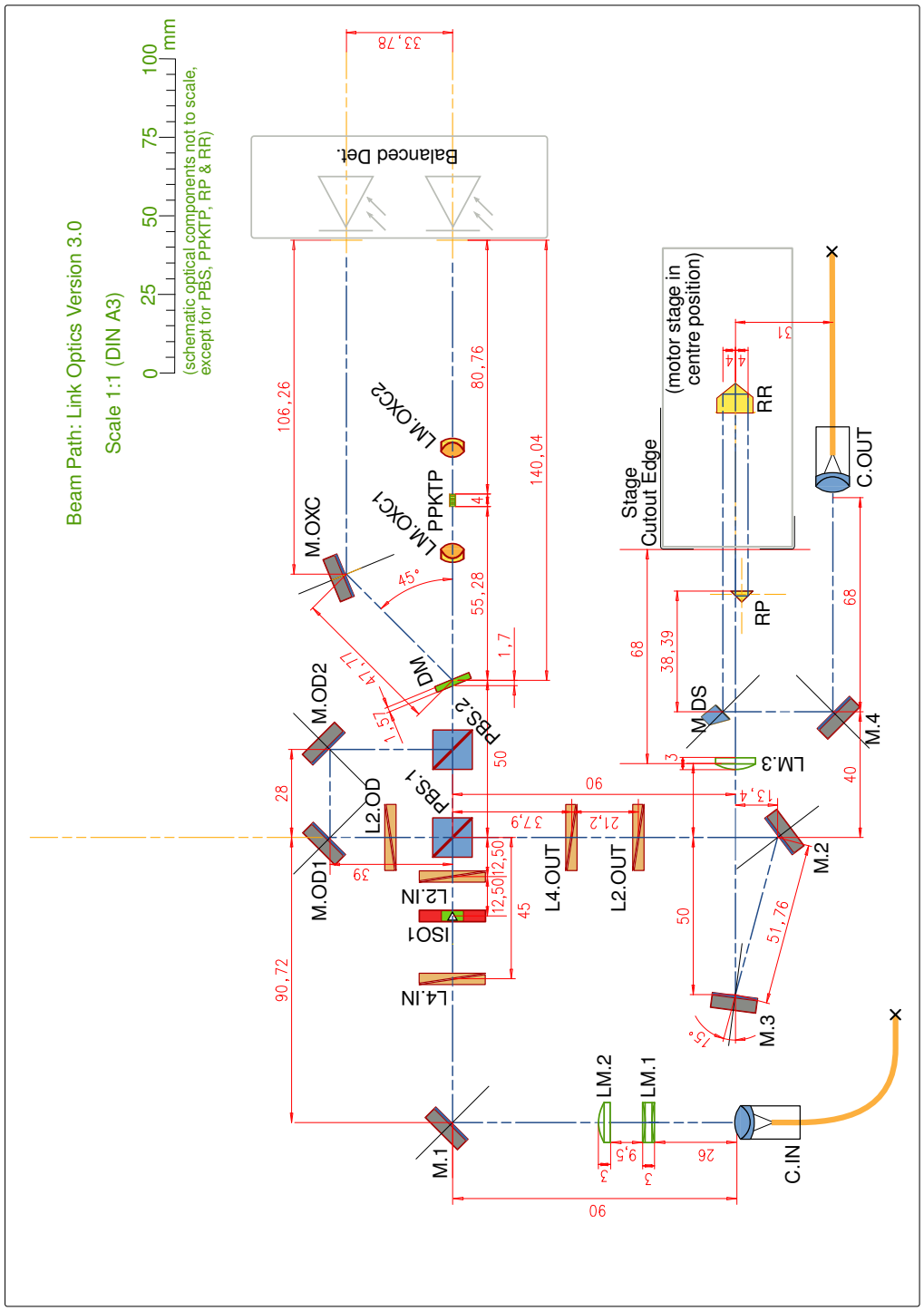

Figure 2.13: Scaled layout of the free-space optics plane in link version 3.0.

2.2.1 Design Study

The simulation and optimisation of the GAUSSian beam envelope of laser beams propagating through the link optics have been calculated in MATLAB™ using a matrix formalism. The mathematical relations and algorithms which were used, are described briefly in the appendix, section B.1 on page 175 ff. The dimensions and distances are taken from the scaled schematic of the link optics, as shown in figure 2.13.

The total optical path length from C.IN via the first polarising beam splitter PBS.1 to the output collimator C.OUT amounts to 842 mm, with the motor stage at its centre position. The optical path length difference introduced by the ODL reaches up to ±140 mm in case of the present links. The incoupling efficiency will be less influenced by stage movements, if the beam divergence along the optical path of the ODL is smallest possible. To minimise the divergence, the beam diameter has to be enlarged, limited by the transverse dimensions of critical optical components. In case of the ODL the limiting factors for the beam diameter are the lateral dimensions of the right-angle prism (RP) and the retroreflecting (RR) prism. The latter had to be chosen with an outer diameter of 15 mm to fit with its aluminium mount onto the stage and to be suited for the height of the optical axis. The right-angle prism requires a length of the hypothenuse which is half of the RR diameter. A much broader prism works also, but has no additional advantage. The height of the prism is limited by the height of the optical axis. The laser beam which enters the ODL passes over the top of the RP.

Regarding those requirements, the right-angle prism was chosen with an area over the cathetus of 7×7 mm and thus has a hypothenuse of $\sqrt{2 \cdot 7^2} \approx 10$ mm length. The specification for the beam diameter at the right-angle prism and in case of the largest optical path length along the ODL was decided such, that the beam cross-sectional area should be smaller than one ninth of half the hypothenuse area, i.e. 3.90 mm^2. With regard to the commercially available components, a collimator has been chosen with an output diameter, measured at $1/e^2$ of the GAUSSian intensity profile, of

$$\mathrm{BD} = 1.2\,\mathrm{mm}$$

The full divergence angle θ_{DA} is calculated approximately from the formula [Web11c]:

$$\theta_{\mathrm{DA}}[\mathrm{mrad}] = \frac{a[\mu\mathrm{m}]}{f[\mathrm{mm}]} \tag{2.3}$$

with the fibre core diameter a and the effective focal length f of the collimator's lens. In this case, SMF with a core diameter of 9 µm is used. The lens of the commercial collimator has a focal length of 6.2 mm with a clear aperture of

$$\mathrm{CA} = 5.0\,\mathrm{mm}$$

According to the formula above (eq. 2.3), the full divergence angle is specified with

$$\theta_{\mathrm{DA}} \approx 1.45\,\mathrm{mrad}$$

With these collimators used at C.IN and C.OUT, the GAUSSian beam diameter stays well below

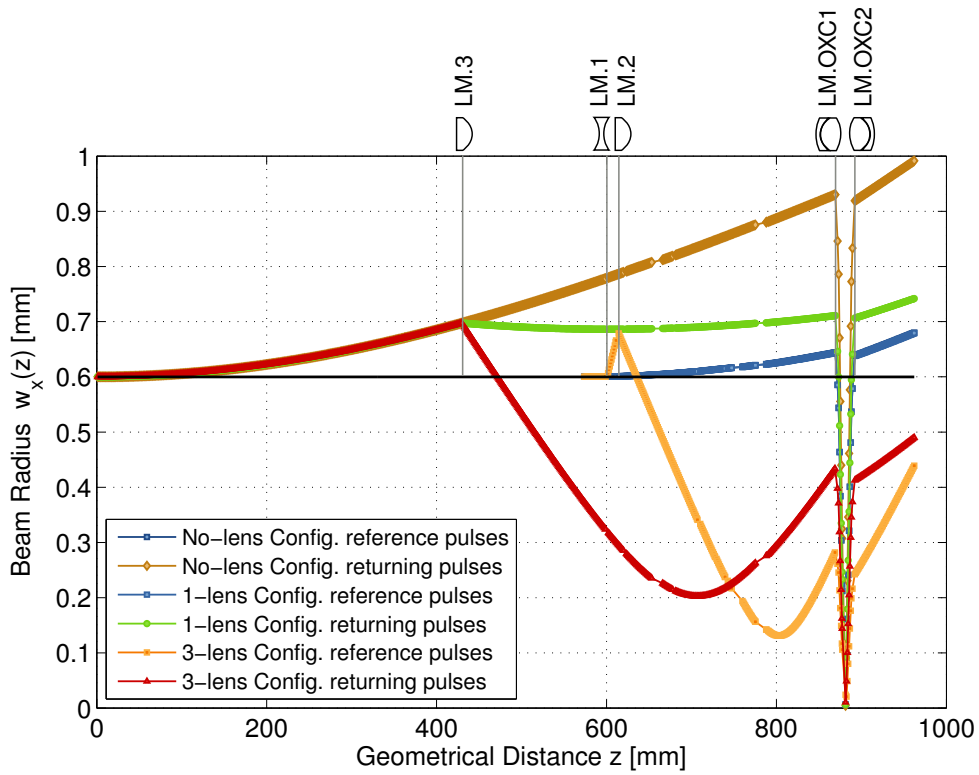

Figure 2.14: Behaviour of the beam diameter along the free-space optics of the link design version 3.0. Three different lens configurations are shown for locations LM.1, LM.2 and LM.3. In the OXC, two lenses with an effective focal length of 12.6 mm are used, reducing the laser beam diameter at the location of the PPKTP crystal to below 0.02 mm.

1.4 mm across the total range of the ODL for both, the returning link pulses and the forward travelling pulses, if at least one appropriate lens is used (at position LM.3). If no lenses are used to focus the laser beam propagating from C.IN to C.OUT, the beam diameter reaches a maximum value of about 1.8 mm at the location of RP. The calculated beam diameters at RP correspond to the following beam cross-sectional areas:

$$\mathrm{BD}_1 = 1.4\,\mathrm{mm} \rightsquigarrow \text{ø} \approx 3.08\mathrm{mm}^2$$
$$\mathrm{BD}_2 = 1.8\,\mathrm{mm} \rightsquigarrow \text{ø} \approx 5.09\mathrm{mm}^2$$

In the first case, the beam diameter stays well within the specified limits of a ninth of half the hypothenuse area. In the second case, the beam diameter is larger than this limit, but still smaller than one seventh of half the hypothenuse area. Thus, even if the beam alignment is not ideally set to the centre of the prism, there is enough clearance left on the entrance surface of the RP.

Figure 2.14 shows the calculated behaviour of the beam diameter along the link optics. The curves for all of the three lens configurations, as mentioned in the section before, are shown. The curves starting at $z = 0\,\mathrm{mm}$ correspond to the returning link pulses, exiting the collimator C.OUT. Their

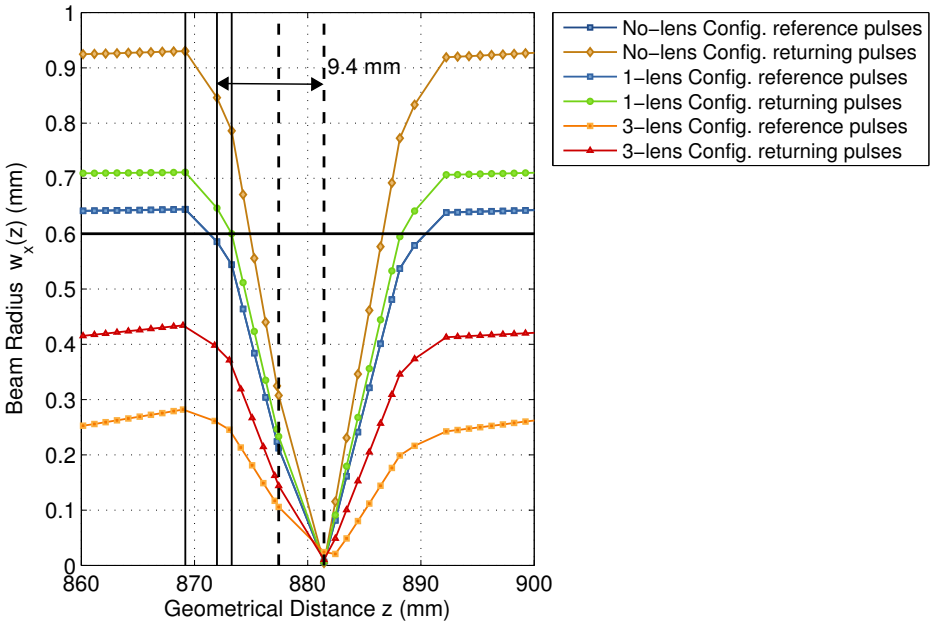

Figure 2.15: Behaviour of the beam diameter along the free-space optics of the link design of version 3.0, showing a zoomed view on the vicinity of the PPKTP crystal inside of the OXC. Both lenses L.OXC1 and L.OXC2 are positioned at their calculated ideal positions, providing a beam waist in the rear part of the crystal and focussing the exiting beam such, that its diameter and divergence is comparable to the values in front of L.OXC1.

beam path is traced from C.OUT, via the ODL, along the detour between PBS.1 and PBS.2 to the OXC, ending at the surface of the balanced detector. The reference laser pulses, exiting the collimator C.IN, are starting in this plot at $z = 570\,\text{mm}$. Their path is traced from C.IN to M.1 and in a straight line through PBS.1 and PBS.2 to the OXC at around $z = 890\,\text{mm}$, also ending on the surface of the balanced detector ($z = 970\,\text{mm}$). This representation was chosen to show the laser beam overlap at the location of the OXC. The geometrical path length for the reference pulses amounts to about 389.5 mm, while the path length for the returning link pulses is, with 962.2 mm, a factor of about 2.5 longer. A detailed view of the beam diameter in the OXC is given in figure 2.15. The plot shows the beam diameter of reference pulses and returning link pulses for all three optics configurations. Both lenses L.OXC1 and L.OXC2 (compare fig. 2.13), which are located around the PPKTP crystal, are set to their calculated ideal positions. Both achromatic lenses are indeed a composition of two individual lenses of different glass types, glued together. The three vertical lines around $z = 870\,\text{mm}$ indicate the positions of the three curved surfaces of L.OXC1. Its distance is chosen such that the beam waists become minimal at the rear side of the PPKTP crystal. The second achromat (L.OXC2), identical to the first one, is positioned such, that the laser beam exiting the crystal is focussed to a beam diameter and divergence similar to the values left of L.OXC1. This is achieved for a distance of 8.75 mm between the crystal's surface and the surface of L.OXC2. The second achromat is necessary to achieve a small beam spot of the generated second harmonic light signal on the active detector

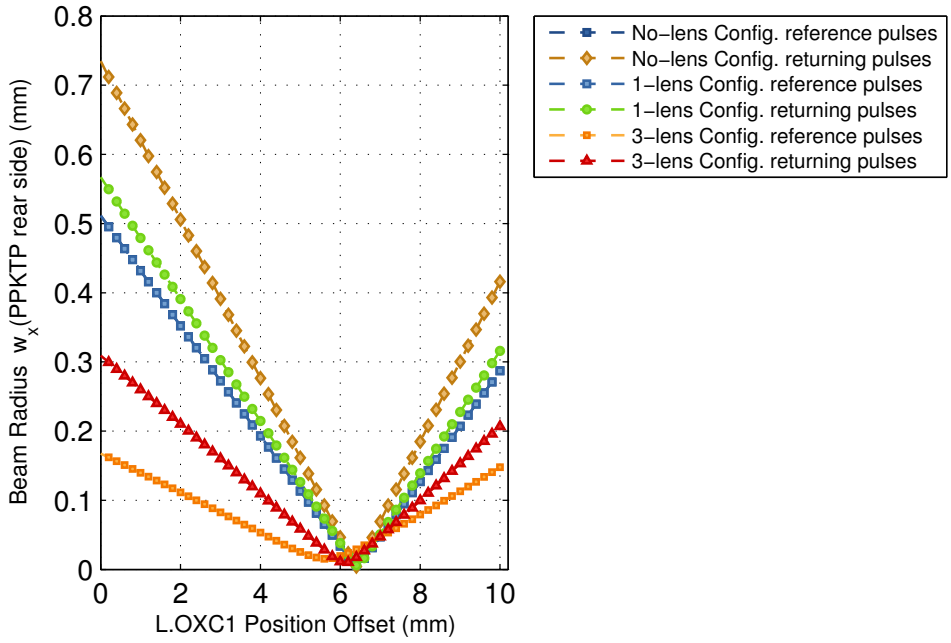

Figure 2.16: Behaviour of the beam diameter at the rear edge of the PPKTP crystal depending on the longitudinal displacement of lens L.OXC1.

surface.

Figure 2.16 shows the dependency of beam diameter at the rear edge of the PPKTP crystal on the offset position of L.OXC1. The offset is calculated relative to the location of the mount LM.OXC1, which is positioned such, that the distance between the rear surface of L.OXC1 and the front surface of the PPKTP crystal is 12.6 mm. The positive offset values reduce the distance between lens and crystal. To compare all three optics configurations, involving either no, one or three lenses, the following conclusions can be made. The beam diameter in front of L.OXC1 is smallest for the 3-lens configuration, but the beam envelopes of reference and link pulses differ in size by about 25 %. In the 0-lens case, the beam diameters take the largest values of all configurations and they differ by about 30 %. Only in the 1-lens case both beam envelopes are nearly of the same size, differing by less than 7 %.

An experimental investigation of the influence of those beam properties on the OXC signal quality is pending. Although, two assumptions are made: first, a smaller beam diameter and hence a larger beam intensity at same optical power, is preferred over a large diameter. Second, beam cross-sectional areas of similar size are preferred over beams differing strongly in size, since the second-harmonic generation depends on the overlap of both laser beams. Regarding the simulation results, the 1-lens configuration seems to be favourable, having the additional advantage, that the single lens is mounted in a fixed holder without the need for position adjustment. In the 3-lens configuration, the distance between both lenses in the Galilean telescope has to be chosen carefully, complicating the assembly and alignment of the lens system.

For the optimisation of the link optics using either a single lens or a combination of three lenses, the radii of curvature as well as the thickness of the lenses have been varied to obtain the smallest possible mismatch of the forward travelling link pulses and the returning link pulses at the location of the output collimator C.OUT. For the calculation of the mismatch factor MF both, the diameter and the divergence of the GAUSSIAN beam have to be regarded. For details see section B.1 in the appendix.

The mismatch factor MF is a property defined in the transverse phase space, which describes the evolution of beam divergence relative to the beam radius. The size of MF is determined by the overlap of two elliptical beams within the transverse phase space. For the calculation concerning the optimisation of the link optics, the input beam from the first collimator, i.e. the forward directed link pulses, are compared to the returning link pulses at the position of the output collimator, which is of the same type as the input collimator. Therefore, the initial beam parameters of the input beam are compared to the final parameters after propagating through the free-space link optics. The factor MF takes values of $\geqq 1$.

The relationship between the calculated MF and the measured incoupling efficiency is estimated from the practical experience gained during the alignment of different link optics configurations. Depending on the clear aperture of the employed collimator lens, the incoupling efficiency can be estimated from the calculated mismatch. For example, an *OZ Optics* SMF-collimator with BD = 0.7 mm has a specified clear aperture of CA $\leqq$ 4.3 mm. Using two of those collimators in the link optics, only 50 % of the optical power could be coupled in if the beams have a mismatch of MF = 3.0. On the other hand, the mismatch factor MF had to be smaller than 1.7 to achieve an incoupling efficiency of more than 80 %. The now employed SMF-collimators with a beam diameter of BD = 1.2 mm and with a larger focal length, the clear aperture is specified to be CA = 5.0 mm. Therefore, the restrictions on the incoupling efficiency are more relaxed. Measurements showed, that an incoupling of > 70 % could be achieved with a calculated mismatch factor of MF = 2.96 between forward and returning laser beams at the location of the output collimator. In this case, no lenses had been added to the current link optics. With a matched optics configuration the incoupling efficiency can be increased to even > 95 %.

Table 2.2 gives an overview on initial and optimised beam parameters (diameter and divergence) at the locations of C.IN and C.OUT, for both, the 1-lens and 3-lens configurations. In any case, a minimum MF of less than 1.1 is achieved, corresponding to an incoupling efficiency of larger than 95 %, when using the collimators with a beam diameter of BD = 1.2 mm and an clear aperture of CA = 5.0 mm. For this general optimisation of the link optics, the motor stage of the ODL has been positioned at the middle of the travel range. In the following section, 2.2.2, the effect on motor stage movement on the MF is discussed. The effective focal lengths of the lenses can be calculated from the ROC values using the thin-lens approximation:

$$\frac{1}{f} \approx \frac{n_2 - n_1}{n_1} \left(\frac{1}{\mathrm{roc}_{x1}} - \frac{1}{\mathrm{roc}_{x2}} \right) \tag{2.4}$$

with n_1 and n_2, respectively, being the refractive indices of air and lens material. roc_{xi} are the radii of curvature of lens x. For the 3-lens configuration the optimum distance between both lenses of the GALILEAN telescope at position LM.1 has been calculated to be 9.5 mm. In this case, a bi-concave lens with a relatively short effective focal length of $f \approx -95$ mm is used, therefore the restrictions on

the distance between bi-concave (L.1) and planoconvex (L.2) lens are relaxed. From the simulation it seems advantageous to first strongly widen the initial laser beam behind C.IN, and then focus it such, that the beam waist is located symmetrically between the first planoconvex lens (inside of the telescope) and the second one at position LM.3. The latter lens creates a stretched beam waist, exactly matching the slightly divergent envelope of the beam, exiting the collimator C.OUT and propagating through the link optics in reverse direction.

2.2.2 Tolerance Study

In this section, the influence and restrictions of the distance between lenses L.1 and L.2 are described shortly.

3-lens configuration

Figure 2.17(a) shows the influence of a distance change between lenses L.1 and L.2 of the Galilean telescope. For this calculation the position of L.1 has been fixed, only the position of L.2 has been varied around the ideal distance of $\mathrm{d}sL1 = 9.5\,\mathrm{mm}$. The left plot shows the ratio between the beam cross-sectional areas of forward travelling and returning laser pulses at the location of C.OUT. The plot on the right hand side depicts the same effect of lens distance variation, but in terms of change in mismatch factor (MF). The influence is negligible for an offset of $\Delta\mathrm{d}sL1 < \pm 1.5\,\mathrm{mm}$, since the MF stays below 1.1, which has been set to the acceptable value and corresponds to an incoupling efficiency of better than 95 %.

Figure 2.17(b) shows the influence of a motor position change, while all three lenses are set to their ideal positions. For a travel range of ±35 mm around the centre position of the stage, the MF deteriorates by maximum +0.2 which is expected to be less than 5 % loss in incoupling efficiency. Note, that there is no linear behaviour between MF and incoupling efficiency. The latter is not only depending on the diameter and divergence of the laser beam, but also on the clear aperture of the collimator.

In figure 2.18(a) the change in mismatch between forward travelling and returning link pulses at the location of C.OUT is illustrated for the case, that the third lens, L.3, is mounted by an offset $\delta\mathrm{z}(L.3)$ away from its ideal position. Each curve of the set corresponds to one position offset of L.3, at which the variation of MF has been calculated for an adaptation of $\mathrm{d}sL1$, i.e. the distance between both lenses, L.1 and L.2, inside of the telescope. A position error of L.3 within $\delta\mathrm{z}(L.3) < \pm 4\,\mathrm{mm}$ can be compensated by a change of $\mathrm{d}sL1$ of ±1.5 mm. Within these limits, the mismatch factor MF stays below 1.1.

Figure 2.18(b) shows a similar behaviour, but in this case the first lens, L.1, is mounted at a wrong position. Here, each curve corresponds to one position offset of L.1, while the curves themselves show the variation of the mismatch when, again, adapting the distance $\mathrm{d}sL1$ between both lenses, L.1 and L.2. Similar to the above mentioned case, a position error of L.1 within $\delta\mathrm{z}(L.1) < \mp 4\,\mathrm{mm}$ can also be compensated by a change of $\mathrm{d}sL1$ within the limits of ±1.5 mm, keeping the MF below 1.1. Note, that a positive position offset $\delta\mathrm{z}(L.1) > 0$ has to be compensated by a decreasing distance between both lens of the telescope, i.e. $\Delta\mathrm{d}sL1 < 0$.

Table 2.2: Lens parameters for minimum MF at C.OUT. In case of the 3-lens configuration, the bi-concave and the plano-convex lens of the GALILEAN telescope at LM.1 have an optimum distance of dsL1 = 9.5 mm. In both cases, 1- and 3-lens configuration, the motor stage of the ODL was set to its initial position at the middle of the travel range. The motor-stage position offset has been set to ds = 0 mm

geometrical pathlength [mm]		842.47				
	initial parameters at C.IN				initial parameters at C.OUT	
theta [mrad]	θ(C.IN)	0.828			θ(C.OUT)	0.828
alpha [mrad]	α(C.IN)	0.00			α(C.OUT)	0.00
z position of beam waist [mm]	z(C.IN)	0.00			z(C.OUT)	0.00
beam waist [mm]	w(C.IN)	0.60			w(C.OUT)	0.60
3-lens configuration:						
minimum mismatch factor MF at C.OUT						1.022
	lenses at LM.1 & LM.2				lens at LM.3	
lens distance [mm]	dsL1	9.5				
ROC [mm]	rs11	95.00	rs21	0.00	rs31	−86.00
ROC [mm]	rs12	−95.00	rs22	34.00	rs32	0.00
lens thickness [mm]	dlLM1	3.00	dlLM2	3.00	dlLM3	3.00
refractive index	dn1	1.50	dn2	1.50	dn3	1.50
1-lens configuration:						
minimum mismatch factor MF at C.OUT						1.042
					lens at LM.3	
lens distance [mm]	dsL1	−−				
ROC [mm]	rs11	−−	rs21	−−	rs31	−421.6
ROC [mm]	rs12	−−	rs22	−−	rs32	0.00
lens thickness [mm]	dlLM1	−−	dlLM2	−−	dlLM3	3.00
refractive index	dn1	−−	dn2	−−	dn3	1.50

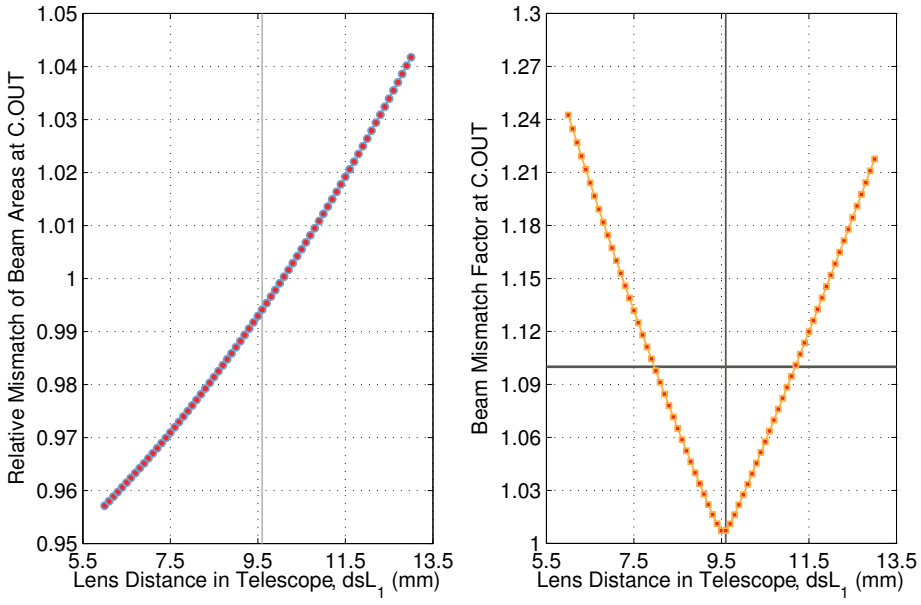

(a) Influence of distance d$sL1$ between lenses L.1 and L.2 inside of telescope.

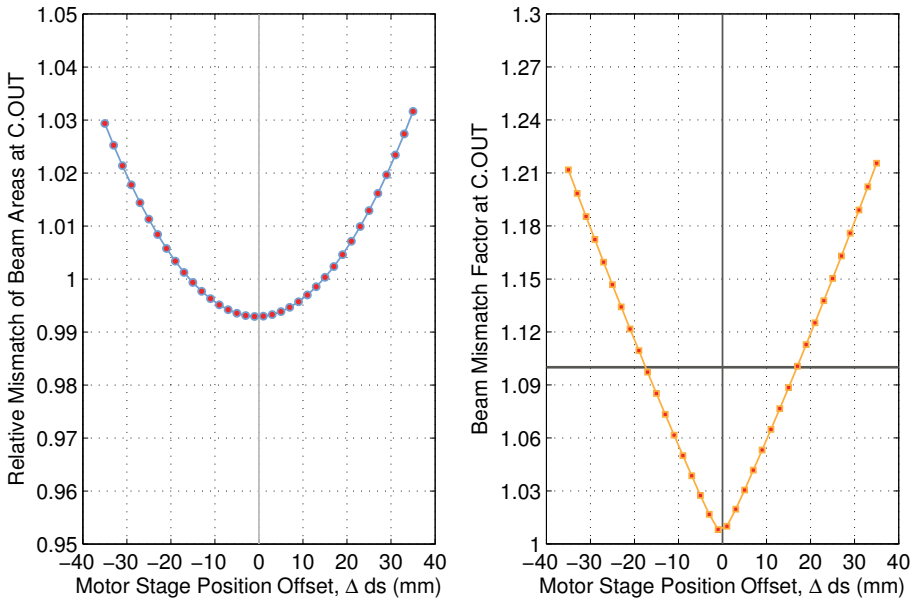

(b) Influence of the motor stage position offset ds (from its centre position).

Figure 2.17: 3-lens configuration: Variation of the calculated mismatch between forward travelling and returning link pulses at the location of C.OUT as a function of (a) lens distance d$sL1$ and (b) motor stage position offset ds. The plots on the left show the change in the ratio of beam cross-sectional areas at C.OUT, while the plots on the right hand side show the corresponding change in mismatch factor at C.OUT.

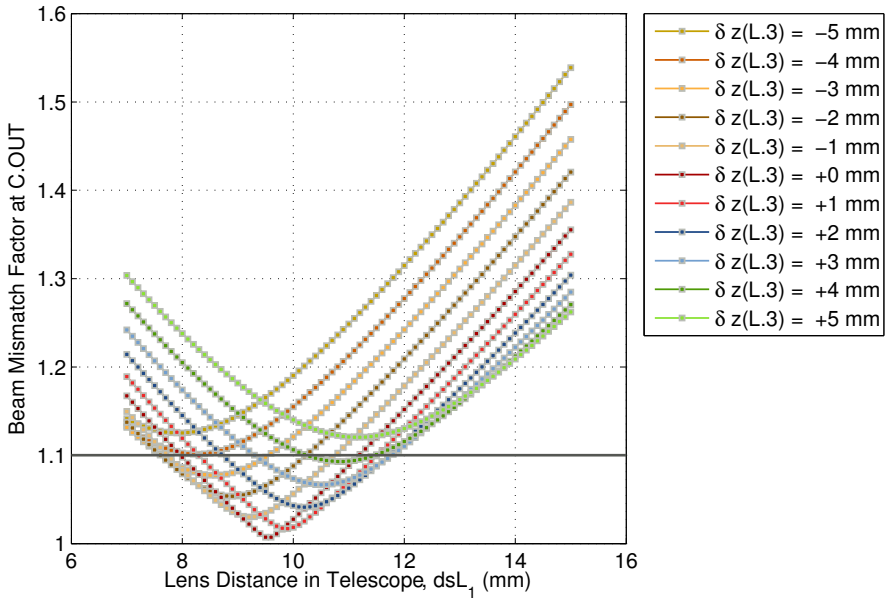

(a) Influence of a position offset of lens L.3.

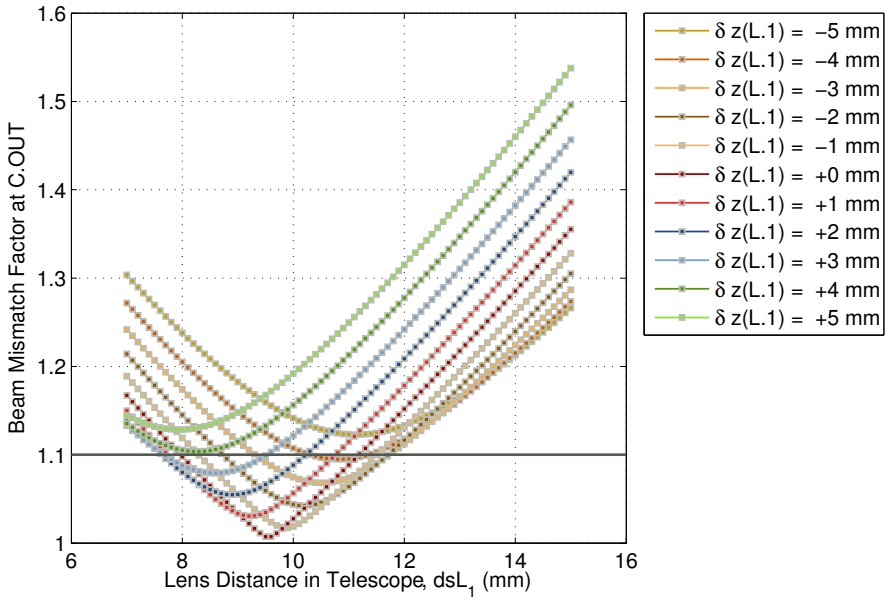

(b) Influence of a position offset of the very first lens, L.1.

Figure 2.18: 3-lens configuration: Variation of the calculated mismatch between forward travelling and returning link pulses at the location of C.OUT as function of position errors of lens (a) L.3 and (b) L.1. The set of curves show the compensation of the deteriorated mismatch by adapting the distance d$sL1$ between both lenses of the telescope, within certain limits. The plots on the left hand side show the calculated effect on the ratio of beam cross-sectional areas, while the plots on the right hand side show the dependency of MF on the position offsets

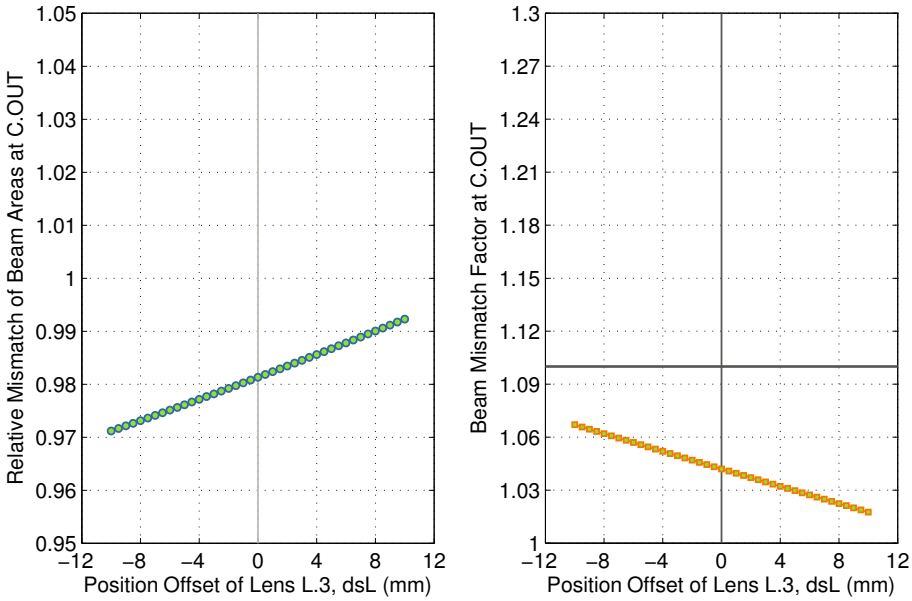

(a) Influence of lens positioning error $\delta z(L.3)$.

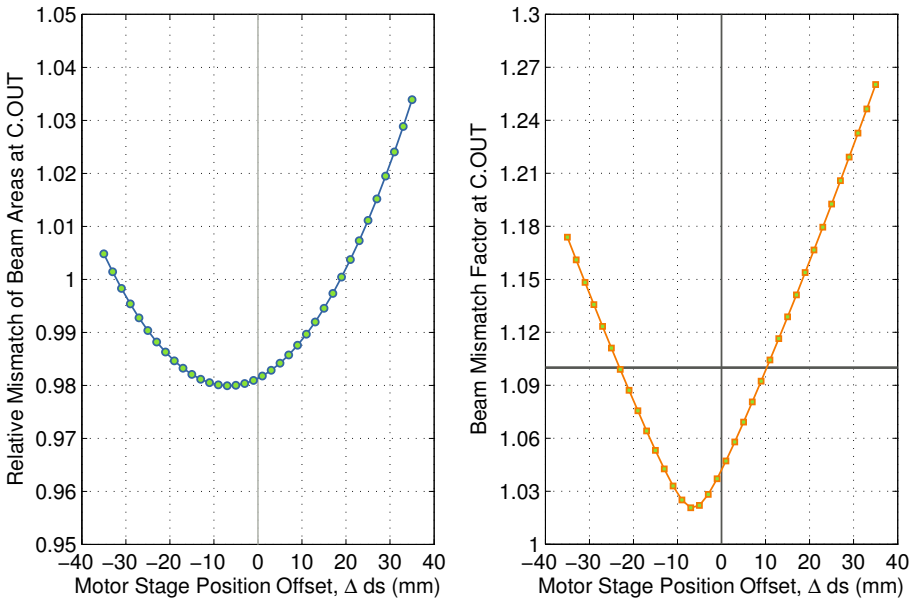

(b) Influence of the motor stage position offset ds (from its middle position).

Figure 2.19: 1-lens configuration: Variation of the calculated mismatch between forward travelling and returning link pulses at the location of C.OUT as a function of (a) a lens positioning error $\delta z(L.3)$ at location LM.3 and (b) a motor stage position offset ds. The plots on the left show the change in the ratio of beam cross-sectional areas at C.OUT, while the plots on the right hand side show the corresponding change in mismatch factor at C.OUT.

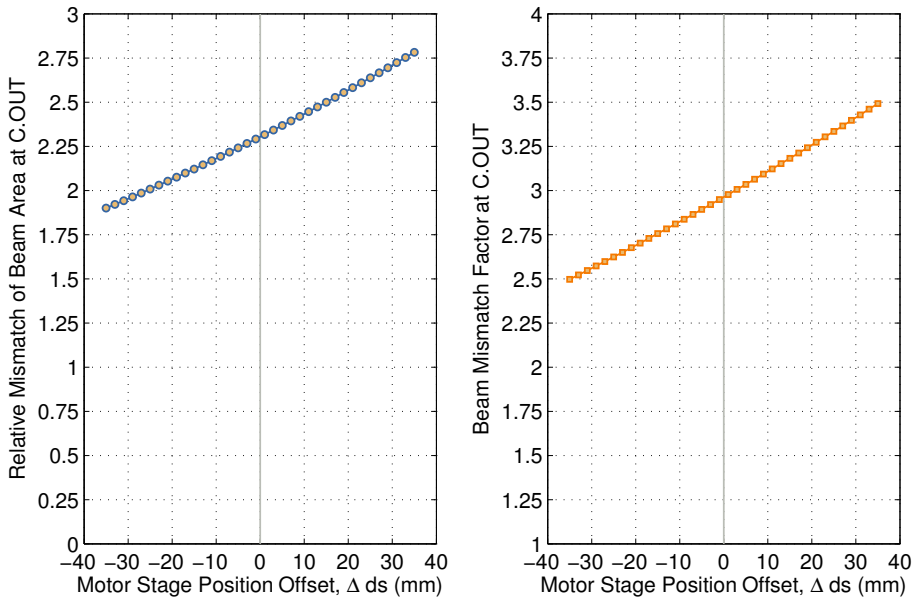

Figure 2.20: o-lens configuration: Variation of the calculated mismatch between forward travelling and returning link pulses at the location of C.OUT during the motor-stage movement by ds. The plot on the left shows the change in the ratio of beam cross-sectional areas at C.OUT, while the plot on the right hand side shows the corresponding change in mismatch factor at C.OUT.

1-lens configuration

When using only a single lens at location LM.3, any positioning error in z which influences the beam mismatch at C.OUT cannot be compensated by other optical components. However, expected position offsets of $\delta z(L.3) < \pm 5$ mm have only little effect on the calculated MF, as shown in figure 2.19(a). A positive offset $\delta z(L.3)$, i.e. a shorter distance between L.3 and C.OUT, rather improves the calculated mismatch, following a linear slope.

Figure 2.19(b) illustrates the variation of beam mismatch at the location of C.OUT during a movement of the motor stage, between ds < ±35 mm. In the worst case, for positive offsets ds, the calculated MF deteriorates by only +0.25, which is expected to generate a decrease in incoupling efficiency of well below 5 %. With regard to the conclusion of the preceding section (2.2.1) concerning the optics of the OXC inside of the link, again, the usage of a single lens at location LM.3 seems to be advantageous over a 3-lens configuration.

0-lens configuration

If one foregoes the usage of any lenses, the beam mismatch at C.OUT becomes $MF \approx 3$, due to the large distance between C.IN and C.OUT of about 1 m. Depending on the involved collimators, especially regarding their clear aperture, this value limits the maximum reachable incoupling efficiency considerably below 95 %, which has been used as quality criterion in the process of selecting matching lenses. If the narrow beam-diameter collimators with BD = 0.7 mm are used, like in the earliest

link versions, a mismatch of $MF = 3$ corresponds to a typical incoupling efficiency of only 50 %. To the contrary, with the currently used collimators with BD = 1.2 mm, even at $MF = 3$, nearly 70 % of the optical power can be coupled into the fibre at C.OUT. In this case, the motor stage movement across a total range of $ds = \pm 35$ mm has a slightly larger influence, leading to a linear change in MF of about ±0.5, see figure 2.20. In this region, the incoupling efficiency is expected to change within approximately ±5 % to ±10 %.

All of the above considerations assume ideal properties of the laser beam and of the involved optical components. When measuring effects in the real optics assembly, deviations from the theoretical case have to be expected. In fact, in the real link optics without any focussing elements between C.IN and C.OUT, the variation of the incoupling efficiency with motor stage movement is less pronounced than expected; the measurement is described in section 2.3.1.

2.3 Commissioning & Performance Test

2.3.1 Performance of the Optical Delay Line

In this section, two measurements are presented, showing the incoupling efficiency of laser pulses being launched into a single mode fibre as used in the opto-mechanics of the links. In both set-ups, which are shown and described in figure 2.21, the latest type of an in-house constructed motorised delay stage is used. Its current design as well as the improvements compared to earlier versions, are briefly described in section 2.1.4 on page 37 ff.

The measurements compare two fundamentally different layouts of an optical delay line (ODL). The old configuration uses a twofold optical path along the motorised stage with a plane mirror mounted on it. The new configuration comprises two solid glass prisms. The retroreflector resembles the vertically cut corner of a cube, so that three orthogonal faces are oriented around their longitudinal symmetry axis, mounted parallel to the optical axis. An incident laser beam is reflected on all three internal faces of the corner cube through total reflection. If the beam enters the vertical front surface of the retroreflector at a point above the symmetry centre, the deflected beam exits the retroreflector such, that it is quasi point-reflected at the centre of the front surface. The second prism is right-angled with symmetrical sides (roof prism) and is used for a 180° deflection of the laser beam at a small horizontal offset.

The measurements have been performed within the real link optics of two different design iterations. The simple delay line using a plane mirror belongs to the link of version 2.0, whereas the more complex delay line involving the two prisms and a fourfold optical path, is used in the latest link design, i.e. version 3.0. A description of the general differences between both link layouts are given in section 2.1.2 on page 24 ff.

The incoupling efficiency is measured as percentage of optical laser power at the end of the SMF compared to the value measured in free space directly in front of the collimator. For the operation of the fibre links it is crucial, that the coupled optical power varies only weakly when moving the motorised stage of the ODL.

In figures 2.22 the measurement results are presented. Both plots comprise identical data, but in the upper figure 2.22(a) the change in incoupling efficiency is shown as function of the motor stage position in millimeter, whereas in figure 2.22(b) the same data is shown as function of the actual

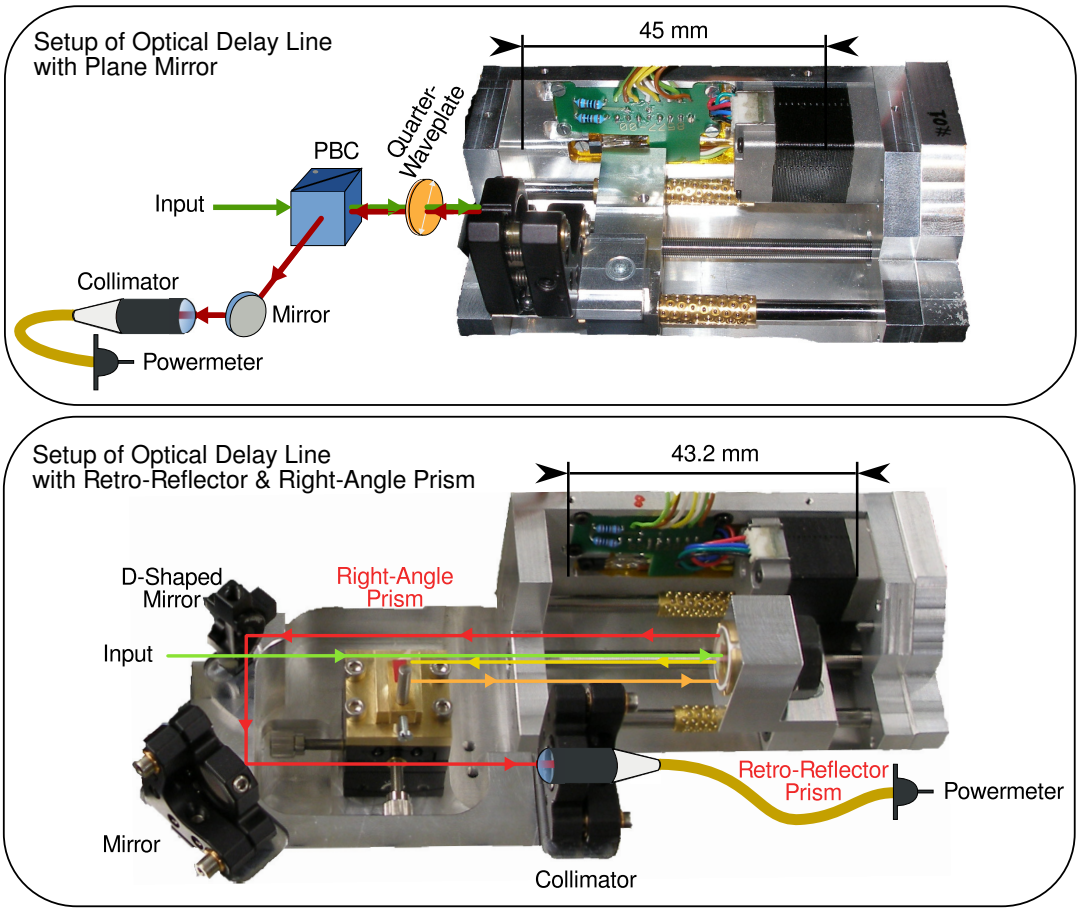

Figure 2.21: Set-up of the optical delay line within the fibre-link free-space optics. In the upper illustration the free-space laser beam enters from the left, traversing the PBC in a straight line into the direction of the plane mirror, which is mounted on the motorised delay stage. On its way to the mirror and back, the laser beam passes twice a quarter-waveplate, which effectively rotates the linear state of polarisation of the laser beam by 90°, so that the beam gets deflected downwards by the PBC onto the mirror and into the direction of the collimator, where it is coupled into the fibre.
In the lower set-up, the plane mirror on the motorised stage is exchanged by a fourfold optics path using a retroreflecting prism (RR) and an right-angle prism (RP). The laser beam coming from the left (green), propagates in a straight line to the RR, entering it at its right upper corner. The laser beam gets deflected by 180° in a point reflection at the centre of RR, becoming diagonally separated (yellow). At RP the laser beam is also deflected by 180° but with an horizontal offset only (orange). The laser beam then enters the RR at its lower right corner and exits at its upper left corner (red). Thus, both laser beams, the one propagating towards the retroreflector and the one returning from it, are horizontally offset. The spatially separated returning laser beam is reflected by a D-shaped mirror towards another mirror and further to the collimator, to be coupled into the fibre.

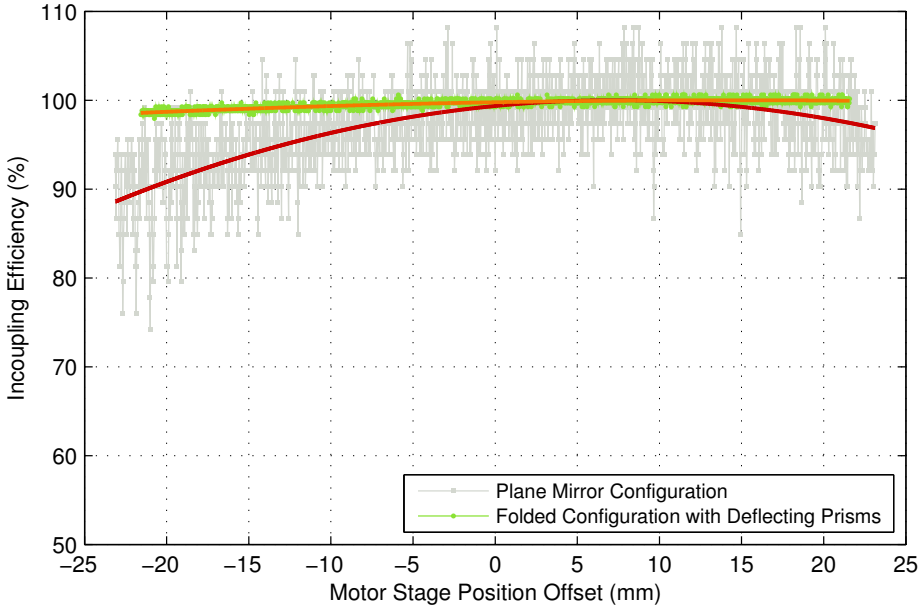

(a) Incoupling efficiency as function of motor stage position

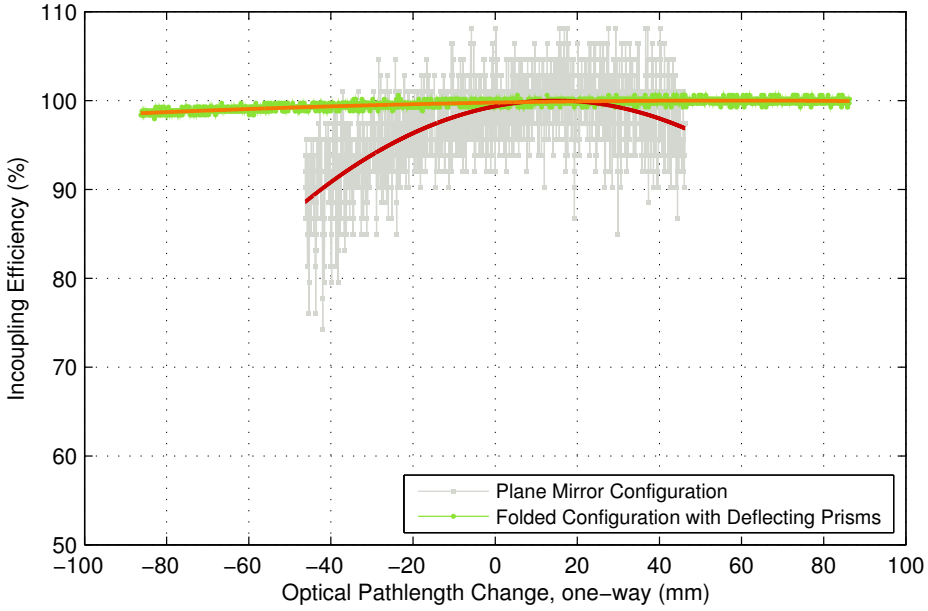

(b) Incoupling efficiency as function of the actual optical path length variation

Figure 2.22: Measurement of the incoupling efficiency using two different ODL set-ups. Both plots comprise identical data, but in (a) the change in incoupling efficiency is shown as function of the motor stage position in millimeter, whereas in (b) the same data is shown as function of the actual variation in optical path length. This redundant illustration shall point out, that the change in optical path Δs_{opt} depending on the change of the motor position $\Delta s_{\mathrm{stage}}$ differs between both ODL set-ups by a factor of two.

variation in optical path length. Note, that for a better qualitatively comparison both curves have been normalised to their maximum mean values. In reality the absolute efficiency is less than 100 % in both configurations. The redundant illustration points out, that the change in optical path Δs_{opt} depending on the change of the motor position Δs_{stage} differs between both ODL set-ups by a factor of two:

- twofold, mirror configuration: $\Delta s_{\text{opt}} = 2 \cdot \Delta s_{\text{stage}}$
- fourfold, prism configuration: $\Delta s_{\text{opt}} = 4 \cdot \Delta s_{\text{stage}}$

Besides the gain in delay-length adjustment range, the fourfold optical path of the latest ODL design shows an enormously improved stability during a movement of the motor stage. Compared to this, the incoupling efficiency in the plane-mirror configuration not only shows large peak-to-peak variation across the total motor stage range, but also follows a parabolic curve, which is bent much stronger than for the alternative ODL design. This effect can be traced back to the used collimator, which has a clear aperture of CA $\geq$ 4.3 mm in the old configuration. During a movement of the stage both, the beam position and beam diameter, vary such, that the laser beam partly slips out of the aperture of the collimator's lens. In the new ODL design, collimators with CA $\approx$ 5.0 mm are used. Additionally, the divergence of the laser beam is decreased to about 60 %, resulting in a much weaker change of beam diameter along the length of the delay line. Both factors lead to a nearly flat curve of incoupling efficiency along the total motor stage range in the new ODL set-up.

The fact, that the peak-to-peak variations differ strongly between the twofold and the fourfold optical path, are related to the mechanical stability of the motor stage. Due to its design, using the two guiding rods, the transverse position stability is achieved with high precision. Any instabilities are mainly angular errors, especially in the vertical plane. The old ODL set-up using a plane-mirror is much more sensitive to transverse angular rotations, i.e. pitch and yaw, than to transverse movements of the mirror.

For the fourfold prism configuration, the dependency is nearly reversed. In fact, previous MATLAB™-based 3-D simulations of the fourfold optical path through the prisms [Lam10], have shown that the new configuration is mainly sensitive to angular errors in one plane. If the right-angle prism is rotated in the vertical plane such, that both laser beams, the incident and the reflected one, are not parallel to each other, then a motor stage movement generates a transverse walk-off of the laser beam on the surface of the retro-reflector and,hence at the collimator. This can be avoided by a thorough alignment of the ODL. The retroreflector itself is, in certain limits, nearly insensitive to angular errors, i.e. pitch and yaw, of the motorised stage. Only the residual, transverse positioning errors during the movement lead to a beam position jitter on the collimator, affecting the incoupling efficiency. But this performance deficit is minimised for the currently used motorised linear stage.

In summary, the latest in-house developed ODL design using a fourfold optical path in combination with the latest in-house produced motor stage shows an excellent performance, indeed, much better than the initially projected specifications, compare page 37 f. The peak-to-peak variation of the measured incoupling efficiency stays well below 2.5 % across the total motor-stage travel range of 45 mm. Over short distances, the variation is even below 1.5 % (peak-to-peak).

In order to compensate even bigger delays, an experimental, longer stage (LMS-Vers.1.0-Type 4, compare page 40) has been assembled, using a similar design as the current version, but with a travel

range of 85 mm. For practical reasons, like short delivery times, this stage design is partly modified. It uses a commercial spindle instead of an individually grinded one. Also the guiding rods are of a simpler type. Because of this, the transverse positioning errors during a stage movement are expected to be worse, so that this design is planned to be used exclusively for ODLs using the fourfold prism-configuration. In a first measurement, it was shown, that even with the travel range increased by a factor of 1.9, the incoupling efficiency of such an ODL used in the link optics varies by only 2.5 % (peak-to-peak) over the whole travel range.

2.3.2 Calibration of the Piezo-Stretchers

The fibre-stretchers with piezoelectric transducers (PZTs) are used as actuators of a fast and highly resolved control of the fibre length and hence of the optical path length of the laser pulses travelling from the link-box to the remote station. Since there are some manufacturing tolerances, the time delay generated by the applied voltage differs for each PZT by a small amount. Furthermore it is of great importance, that the fibre stretcher reacts linearly in the adjusting range of about 200 V. Both properties can be checked with a calibration of the PZT during the closed-loop operation of the link. For this purpose the optical delay of the link line is changed on purpose by use of the motorised delay stage while monitoring the change in voltage driving the piezo element to compensate for the enforced timing change. Because of the fact, that in all links in which the PZT had been calibrated the linear motor-stage is built in the wrong position (compare section 2.1), the following considerations had to be made for calculating the timing change per unit voltage for a single pass through the fibre stretcher. The optical configuration of all calibrated links resembles the design version 1.1 and 1.2 (see fig. 2.2), respectively. In this configuration the laser pulses being sent in forward direction into the link line first pass the free-space optical delay line (ODL), are then coupled into the fibre and pass the PZT once on the forward run. On the return path the pulses once more pass the PZT but not the ODL before being overlaid with reference pulses in the OXC. The time delay introduced by the stage is:

$$\Delta t_{\text{motor}}\,[\text{fs}] = 2 \cdot \Delta x_{\text{motor}}\,[\text{mm}] \cdot 3.333\,[\text{ps/mm}] \tag{2.5}$$

This Δt_{motor} is compensated by twice Δt_{PZT}. Therefore, the calibration constant is given by

$$\text{cc}\,[\text{fs/V}] = \frac{\Delta t_{\text{motor}}}{2\,\Delta V_{\text{PZT}}} \tag{2.6}$$

It is derived from the inverse slope of voltage V_{PZT} versus stage position x_{motor}. As shown in figure 2.23 the calibration curves of four different links result in constants between 18 fs/V and 24.1 fs/V.

The optical time delay as specified by the manufacturer [Web11g] should be 19 fs/V for a fibre stretcher with a double layer of 40 m SMF wound around the piezo-electric element. The measured deviations from the specification are a combination of small tolerances in the diameter of the cylindrical fibre-stretcher and errors in the position read-out of the motor stage. For a position information the travel range of the stage has to be calibrated first in terms of [mm/step]. Although the range is determined with micro-meter precision, the stage has a uni-directional positioning inaccuracy of a

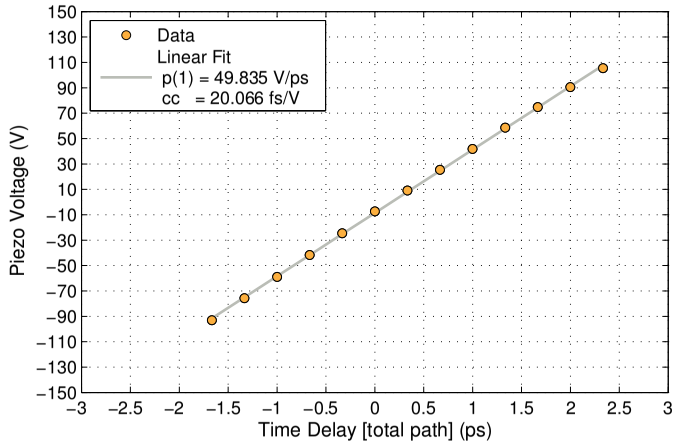

(a) Link.01: Design Version 1.1

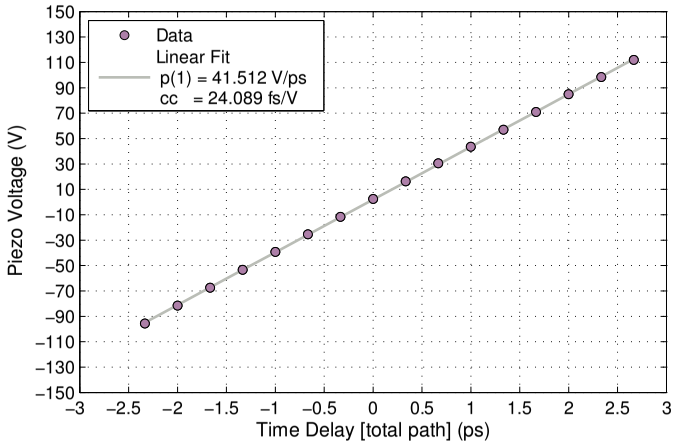

(b) Link.03: Design Version 1.1

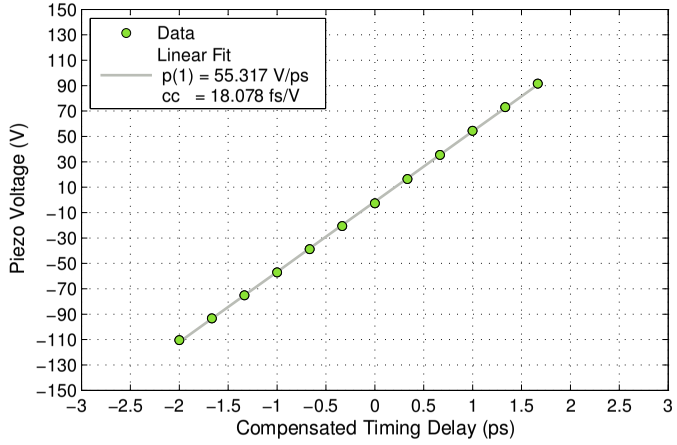

(c) Link.09: Design Version 2.0

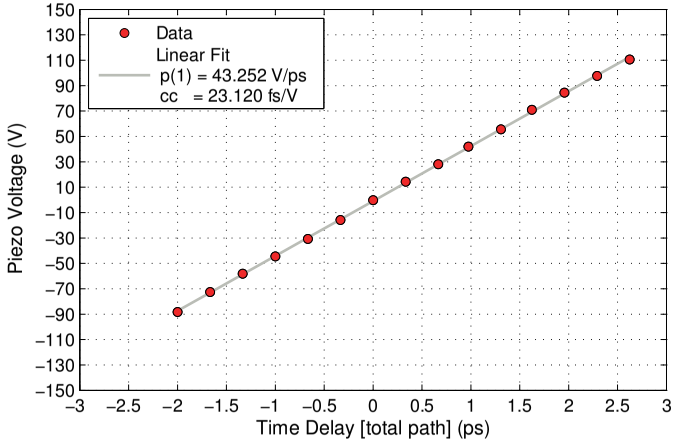

(d) Link.15: Design Version 1.2

Figure 2.23: Measured calibration curves of four different links. The inverse slope of voltage V_{PZT} versus stage position x_{motor} results in calibration constants between 18 fs/V and 24.1 fs/V

few hundred steps. For a total travel range of typically 40 mm corresponding to roughly $2 \cdot 10^6$ steps, the smallest distance resolved is 0.02 µm. In case of an inaccuracy of better than 1000 steps over the total travel range, this amounts to an error of 0.02 mm. For the calibration the position increment Δx_{motor} was set to 0.333 mm, corresponding to about 16650 motor steps. Since on short distances, the slippage amounts to typically 100 steps, the position can be set with a precision of about 2 µm, which results in a relative position error of 0.6 %. Therefore the motor position error cannot explain the maximum deviation of roughly 25 % of the calibration constant from the specified value. Instead, it can be attributed to production-related deviations. Apart from this, all curves show a nearly perfectly linear behaviour, which applies to a linearity error of less than 1 % for drive voltages below 100 V peak-to-peak and less than 3 % across the total range, as specified by the manufacturer.

2.3.3 Calibration of the OXC Signal

In section 2.1.1 on page 22, the generation as well as the meaning of the optical cross-correlator (OXC) signal for the fibre links has been described in detail. In the following, examples for measured OXC signals are presented for each of the seven, presently commissioned fibre links, see figure 2.24. The s-shaped curves result from the balanced detection of the second-harmonic signals. A steeper and less noisy slope is favourable for a higher sensitivity of the measurement. The digitised information is used as an error signal for the digital signal processor (DSP) regulation which calculates correction signals. The latter are sent via an digital-to-analogue converter (DAC) to a piezo driver, which adjusts the voltage of the PZT, and to the stepper motor controller. In order to sample the total signal, the time delay between reference and link pulse has to be varied stepwise in a range of at least ±5 ps, which is done by use of the motorised optical delay line (ODL). At each scan step, the signal from the balanced detector is sampled by an ADC. The mean values of the ADC traces are plotted against the timing delay introduced by the motor stage. An alternative, fast calibration using the piezo-electric fibre stretcher is presented in [Sch11b].

To measure and calibrate the OXC signals in the first place, one has to determine the conversion factor between motor steps and timing change. Therefore, every motor stage is calibrated before commissioning a link. Besides small construction-conditioned deviations, the conversion factor is typically 0.0647 ± 0.0039 fs/step. This value is determined by simply monitoring the required motor steps for passing through the total adjustment range, measured in millimeter. Using the value of velocity of light in air, the latter is converted to femtoseconds.

For the measurement, one has to account for the fact, that different layouts are applied in different links. By the time of the measurement, Link.05 and 07 (labelled after their position on the optical table) already comprised the new opto-mechanics, in contrary to the older links, which still contain the wrongly located ODL (compare section 2.1.2 on page 2.1.2 f. for explanation). The important difference between those links is, that any one-way counted motor position change generates a change in laser round-trip time, which is either a factor of 2 or 8 larger.

A comparison of the presented OXC curves shows, that they resemble similar shapes, but differ strongly in height and width. This is related to the fact, that the signal quality depends on many parameters:

- power ratio between reference and returning link pulses

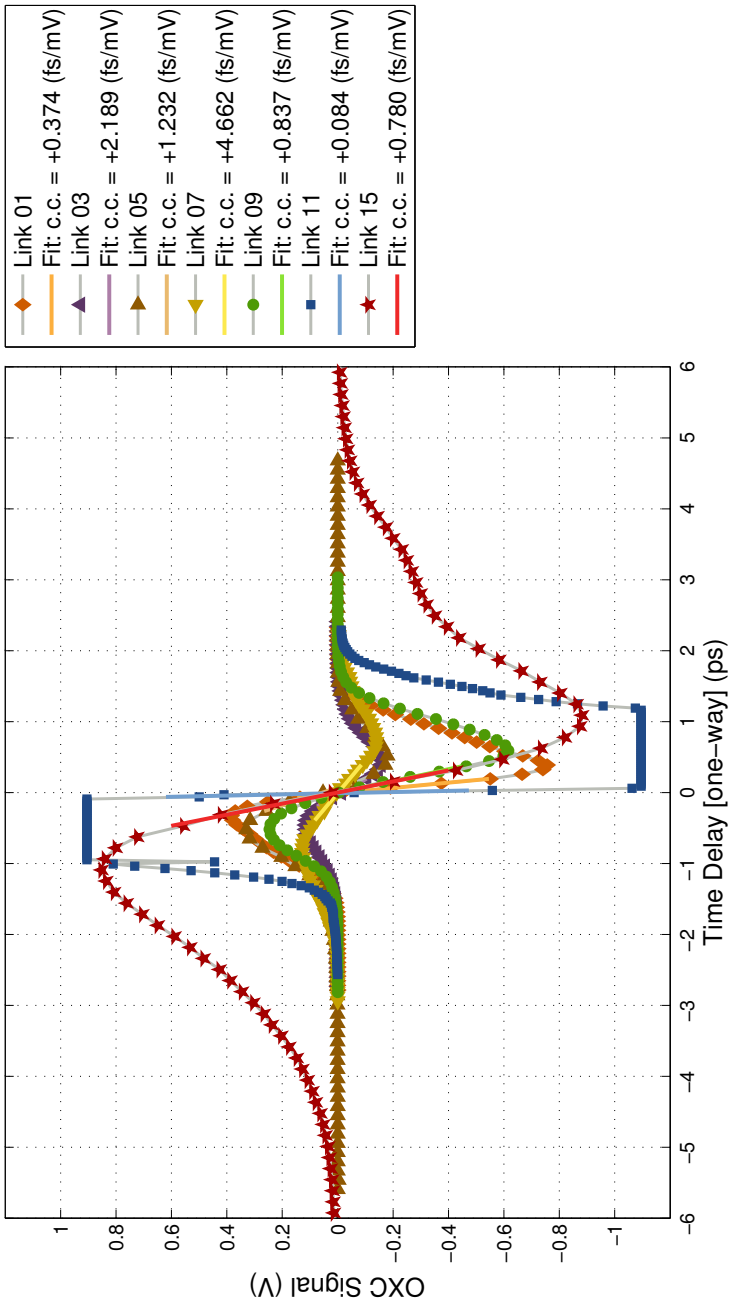

Figure 2.24: OXC calibration signals for all links, which had been installed and commissioned until July 2011. The individual links resemble different design versions of the opto-mechanic: Link.01 & 03 are version 1.1, Link.09, 11 & 15 are version 1.2, Link.07 is version 2.0 and Link.05 comprises the newest version 3.0. The latter two are the only ones with a correctly positioned ODL

- ratio between their pulse widths (i.e. rate of dispersion compensation)
- spatial pulse overlap in the PPKTP crystal
- focussing strength and position of the beam waists of both signals inside of the crystal

This underlines an important difficulty in commissioning of the featured fibre links. Even if the same design layout will be used for each of the links, they are still individuals, because of, for example, their different total fibre lengths, which require an individual adjustment of dispersion compensation. Furthermore, the intra-link optical power levels have to be balanced to optimised simultaneously the power splitting ratio between reference and link pulses and to adjust the out-coupled power at the link ending.

2.3.4 Base-Band Noise Measurements

Figure 2.25 shows a measurement of the single side band (SSB) amplitude-noise spectra for two different fibre links, during their close-loop operation. The latter means, that in both links the laser pulse round-trip time has been controlled to be exactly an integer multiple of the inverse repetition rate, so that the reference and link pulses have temporal and spatial overlap inside of the PPKTP crystal in the OXC.

For this measurements, small parts of the forward travelling and returning link pulses have been coupled out at a location between link box and PZT element, using an in-fibre directional coupler (compare schematic on page 23). The forward and returning amplitude signals are converted into electrical signals by use of photodiodes (PDs)[1]. After a low pass filter with 1.9 MHz bandwidth, the signal is amplified in voltage by a factor of 10 in a low-noise amplifier (LNA). Using a commercial signal-source analyser (SSA)[2], the baseband noise spectra of the amplified signals can be determined. The curves presented here, show the voltage spectral densities $\sqrt{\mathcal{S}_\mathcal{V}}$, given in $\left[{}^{\mathrm{nV}}/_{\sqrt{\mathrm{Hz}}}\right]$. With the knowledge of the direct current (DC) voltage levels $\mathrm{V_{DC}}$, the relative intensity noise (RIN) can be calculated.

If the analyser stores the baseband signals $\mathcal{L}_\mathcal{V}$ in logarithmic units of $\left[{}^{\mathrm{dB}}/_{\mathrm{Hz}}\right]$, the following conversion to a voltage spectrum in $\left[{}^{\mathrm{V}^2}/_{\mathrm{Hz}}\right]$ is used:

$$\mathcal{S}_\mathcal{V} = {\mathrm{V_{DC}}}^2 \cdot 10^{\frac{\mathcal{L}_\mathcal{V}}{10}} \tag{2.7}$$

The relative intensity noise per frequency interval $[\nu_1, \nu_2]$ is calculated, according to

$$\delta_{\mathrm{RIN}} = \frac{1}{\mathrm{V_{DC}}} \sqrt{\int_{\nu_1}^{\nu_2} \mathcal{S}_\mathcal{V}\, d\nu} \tag{2.8}$$

In each of the four plots both, the voltage spectral densities from 100 Hz to 10 MHz and the RIN in the first four decades are shown. In the left column, (a) and (c), the SSB noise of the forward travelling pulse amplitudes are shown, whereas the right column, (b) and (d), contains the amplitude noise spectra of pulses returning from the link ending. The plots in the top row belong to Link.11, which

[1] EOTect ET3010, 3 dB bandwidth at 1.5 GHz
[2] Agilent E5052B

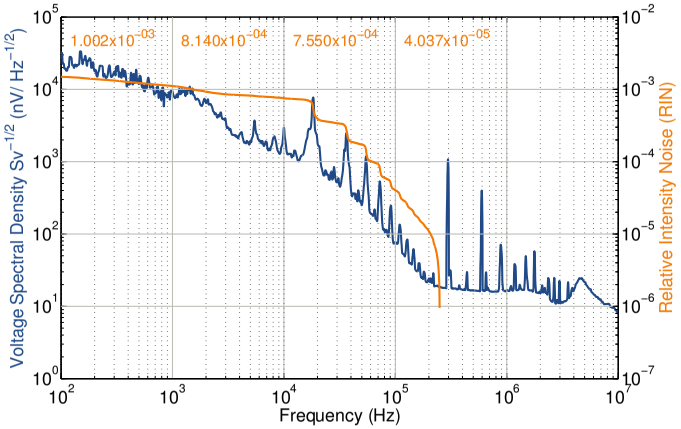

(a) Link 11, amplitude noise in forward travelling pulses

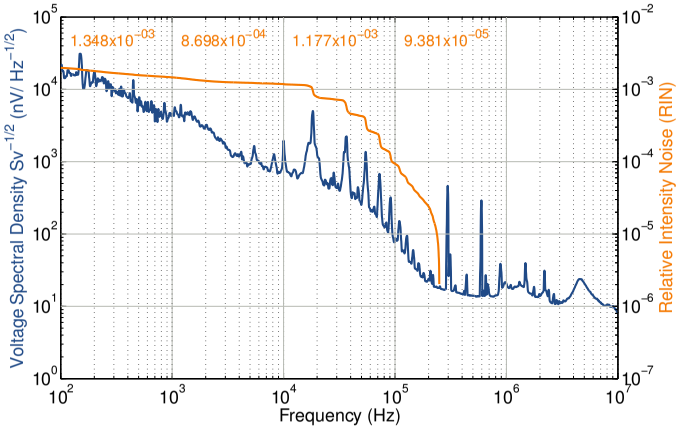

(b) Link 11, amplitude noise in reflected laser pulses

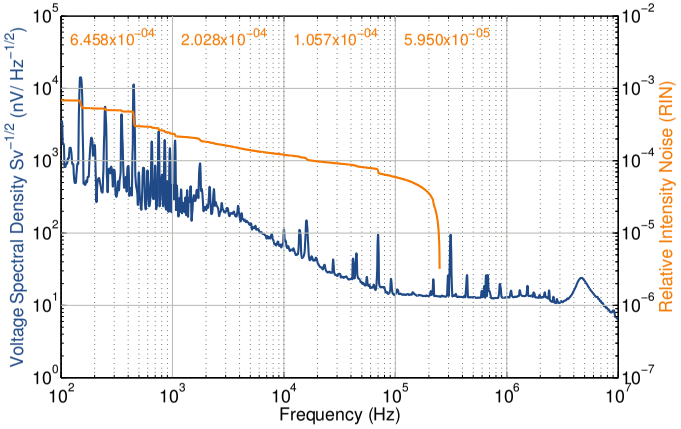

(c) Link 05, amplitude noise in forward travelling laser pulses

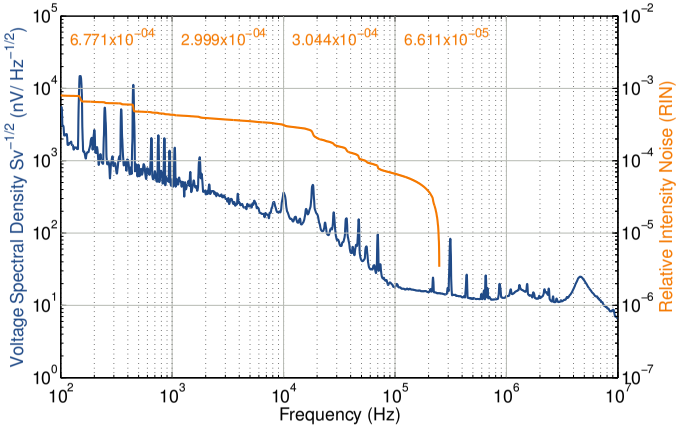

(d) Link 05, amplitude noise in reflected laser pulses

Figure 2.25: Baseband noise measurements with two different links for both forward and reflected laser pulses. The signals are taken from the internal amplitude monitor chain, composed of a photo-diode, a low-pass filter, a low-noise amplifier and roughly 5 m RF cable. The RIN between 100 Hz and 250 kHz amounts to (a) 0.150 %, (b) 0.199 %,(c) 0.069 % and(d) 0.080 %.

comprises the opto-mechanic design version 1.2, while the lower row shows the measurement in Link.05 with the latest design version 3.0. The major difference between those links, is the orientation of the PBC. In a closed-loop operation of Link.11 the reference and link pulses not only have temporal and spatial overlap in the PPKTP, but also in the PBC. Furthermore, at this incident also a third EM field is present in the beam-cube with the same state of polarisation (SOP) as the returning link pulses. The special feature in Link.05 is the avoidance of a simultaneous, spatial overlap of parallel polarised laser pulses in the beam-cube, to prevent a cross-talk between returning and forward travelling link pulses. Compare section 2.1.2 on page 28 for a detailed description.

The most noticeable difference between the SSB amplitude noise of Link.05 and Link.11 concerns its behaviour up to a frequency of 250 kHz. The RIN, integrated from 100 Hz up to this frequency, are given in table 2.3. In the latest design (Link.05), the amplitude noise of the forward travelling

Table 2.3: RIN for Link 05 & and 11 integrated from 100 Hz up to 250 kHz.

	Relative Intensity Noise [%]	
amplitude monitor	Link 05	Link 11
forward	0.069	0.150
returning	0.080	0.199

link pulses is reduced by a factor of ~ 2.2, compared to the old configuration. For the returning link pulses, the difference is even larger, with a reduction by a factor of ~ 2.5. Both noise spectra shown here for Link 11 are similar to each other, whereas in Link.05 a clear difference between forward and backward travelling pulses is visible.

The noise source at lower frequencies, i.e. below 1 kHz, is predominantly electronic, instead of optical. It is related to the measurement process, in which the low voltage signal from the LNA (located in the link box) is guided through roughly 5 m of RF cable to the electronic racks, where it is sampled by an ADC, or in this case, connected to the SSA. Both, the PD and LNA are connected to a self-constructed voltage source, which adds electronic noise. The spikes which appear at a frequency of about 18 kHz are most probably a resonance of the interconnected piezoelectric fibre stretcher. In Link 11, higher harmonics of this frequency are visible.

The main reduction of the amplitude noise in Link.05 compared to the old design version appears within the decade of 10 kHz to 100 kHz. Here the reduction factor of the RIN for the forward travelling pulses is about ~ 7.1, while in the returning pulse amplitude the factor is only about half of this (~ 3.9). At this high frequencies, the noise is assumed to be generated in an optical process. Since it is larger for the returning pulses, amplitude noise is added on the round-trip of the pulses from the link box to the FRM at the link ending and back.

It was observed, that the high RIN contribution in Link.11 can be reduced when in the opened link-lock loop, a timing delay between reference and link pulses is introduced by use of the motor stage. In this case, the simultaneous overlap of equally polarised pulses in the PBC is prevented. On the other hand, if in Link.05 the additional detour for the returning link pulses between the two PBCs is avoided by adjusting the ODL, an increase in amplitude noise is observed in both, forward

and returning link pulses. By this adjustment, the simultaneous overlap of reference and link pulses in the first PBC is restored.

These reproducible effects underline the achievement of the redesigned opto-mechanics. A large contribution to the amplitude noise was suppressed by the new link optics, using the *two-cube* configuration. Nevertheless, additional, minor contributions to the amplitude noises still exist, especially observed at the link ending. Through AM-to-PM conversion, the latter impedes the generation of a low-timing jitter (below 30 fs) reference at the remote stations. Therefore, potential candidates for residual, electronic and optical noise sources are presently under investigation.

2.4 Summary & Outlook

In the following the contributions to the length-stabilised fibre links in conjunction with this thesis are shortly summarised. During three years in which a vast amount of experience in assembly and installation of the links has been gathered, the opto-mechanics have evolved from the very first version to an engineered design which comprises a large number of improvements. Part of these enhancements are related to constructional and technical issues, like a simpler assembly, better fibre and cable management and faster alignment. Other design changes directly improved the operation of the links enormously. This concerns, for example, the matching of the free-space optics to reduce the overall required power levels. Even though additional noise contributions still exist, a major contribution to the observed amplitude noise has been identified and suppressed; by this, the redesigned opto-mechanics paved the way for future improvements.

In parallel to the developments of the link box, the performance of the in-house constructed motorised delay stage, being an essential link component, has been significantly improved in the frame of this thesis. Its performance regarding stability and adjustment range now fulfils the initial requirements, making it suitable for the links at FLASH and also at the future European XFEL.

Photographs of the latest link design, taken during the assembly and commissioning phase of Link 15, are shown in section C.3.1 of the appendix, on page 202 f. A detailed list of components and prices for one complete fibre link can be found in the appendix section C.3 on page 198 ff.

To give a short outlook on upcoming activities related to the links some important open points are mentioned here. With regard to the design of link version 3.0, the low-voltage electronics inside of the link box will be comprised onto a printed circuit board (PCB). It requires less space and reduces the total costs, while promising a better performance due to short and impedance-matched signal paths. Furthermore, the older links presently installed at FLASH will be exchanged by the revised design, to achieve a uniform system.

Concerning the operational performance of the links, further investigations will follow in the near future. Especially an out-of-loop measurement is scheduled, to determine the presently achievable point-to-point stability between two individual remote stations. With regard to long-haul links of more than 500 m length, as they are necessary for the European XFEL, the suitability of the present design will be determined in test set-ups which are presently constructed. The planned measurements should reveal, if further adjustments of the free-space and fibre-optical link design are required. For example, concerning a higher order dispersion compensation.

3 Bunch Arrival Time Monitors ▸ Functionality & Design

Contents

3.1 Layout & Operation Principle

The bunch arrival time monitor (BAM) detects the arrival time of electron bunches relative to the optical timing reference, which is provided by the laser-based synchronisation (LbSyn) system. The latter is described in section 1.2 on page 11 ff. All of the BAMs are connected to the optical timing master through individual length-stabilised fibre links. The current design and performance of the links is described in chapter 2 on page 21 ff. Additional information on the timing master and the link performance can be found in [Sch11b].

Currently, four BAMs are installed at FLASH. Two monitors, which comprise the latest opto-mechanical design, are installed around the first bunch compressor (BC2). Two older versions of the BAM (first prototypes with engineered chassis) are installed further downstream of FLASH. One of those monitors is located at the exit of the second bunch compressor (BC3) and the other one is installed in the warm section behind ACC7, but in front of the dog-leg. For a description of the accelerator facility of FLASH comprising explanations on specific subsections, compare section 1.1 on page 1 ff.

The two prototypes, having been installed in the course of Florian Löhl's doctoral thesis, already allowed for arrival time measurements with sub-10 fs resolution [Lö9]. The next BAM with a revised design, has been installed during this thesis in 2009, directly in front of the entrance of BC2. The experience gained during assembly, installation and commissioning of this third BAM necessitated a further design revision before installing the fourth BAM in May of 2010, behind the exit

of BC2. The optimisation of the opto-mechanical BAM front-end has been one of the key topics of this thesis. Before installing the fifth monitor, scheduled for 2012, in the section SFELC behind the sFLASH radiators, another design revision is required, to cope with the increased demands for operational stability and resolution. A brief description of important differences between the various BAM generations is given in section 3.2 on page 80 ff.

In the next section, the general operation principle of the BAM is explained briefly. Subsequent to this, a general overview on the three main subsystems of the bunch arrival time monitor is provided.

3.1.1 Operation Principle

For detecting the arrival time of an electron bunch at specific locations of the accelerator, an RF antenna picks up the electric field of a traversing bunch and generates a broad-band, bipolar voltage transient, with a steep slope in the order of 100 mV/ps. The signal shape is determined by the charge distribution of the electron bunch folded with the beam pick-up response function. The zero crossing of the linear voltage slope can be used as reference for precisely measuring the time of arrival. More specific, the arrival time of the centre of bunch charge can thus be determined. For RF signal bandwidths of a few 10 GHz, this measurement is not sensitive to any structural details of the longitudinal bunch shape. The time duration of the transient slope between the two peaks is typically in the order of a few ten picoseconds, followed by up to several hundred nanoseconds of ringing, depending on the construction of the RF pick-up. For an online measurement of a bunch-resolved arrival time, the timing change of the voltage zero crossing is monitored relative to an optical reference, i.e. the short laser pulses of the LbSyn system.

Figure 3.1(a) shows a schematic of the general operation principle of the optical sampling scheme. The key component is an optical integrated circuit (OIC) device, which is a commercial electro-optic modulator (EOM). The latter is an intensity modulator, constructed as a Mach-Zehnder-type interferometer. Optical signals, which are launched into the device are split into the two branches of the interferometer. In the simplest version, the signal in only one branch experiences a phase shift depending on the strength of an applied, external electric field. When the two optical signals are recombined, the relative phase shift leads to an interference, thus changing the initial amplitude. The transmitted optical intensity I_{out} depends on the applied voltage signal V according to:

$$I_{\text{out}} = I_{\text{in}} \cos^2\left(\frac{\Gamma_0}{2} + \frac{\Gamma_{\text{mod}}}{2}\right) \quad \text{with} \quad \Gamma_{\text{mod}} = \pi \frac{V}{V_\pi} \tag{3.1}$$

with the input intensity I_{in}. The phase of the cosine function consists of two terms: the first is a constant phase offset, which can be controlled by an applied DC bias voltage V_{bias}. The value of Γ_0 at zero V_{bias} is device-specific. V_π, which is device-specific as well, is the half-wave voltage. It is the required voltage difference for switching between total transmission ($I_{\text{out}} = I_{\text{in}}$) and nearly total extinction ($I_{\text{out}} \approx 0$). Details on the operation principle and on the technical layout the employed intensity modulator can be found in section B.2 of the appendix, on page 179 ff.

The optical reference signals are given by laser pulses with durations in the order of 1.0 ps FWHM at the location of the EOM, slightly varying between the different set-ups. The laser pulse repetition rate is 216.667 MHz, resulting in a temporal separation between two pulses of 4.614 ns. According to figure 3.1(a), the laser pulses propagate inside of an optical fibre and enter the EOM from the left,

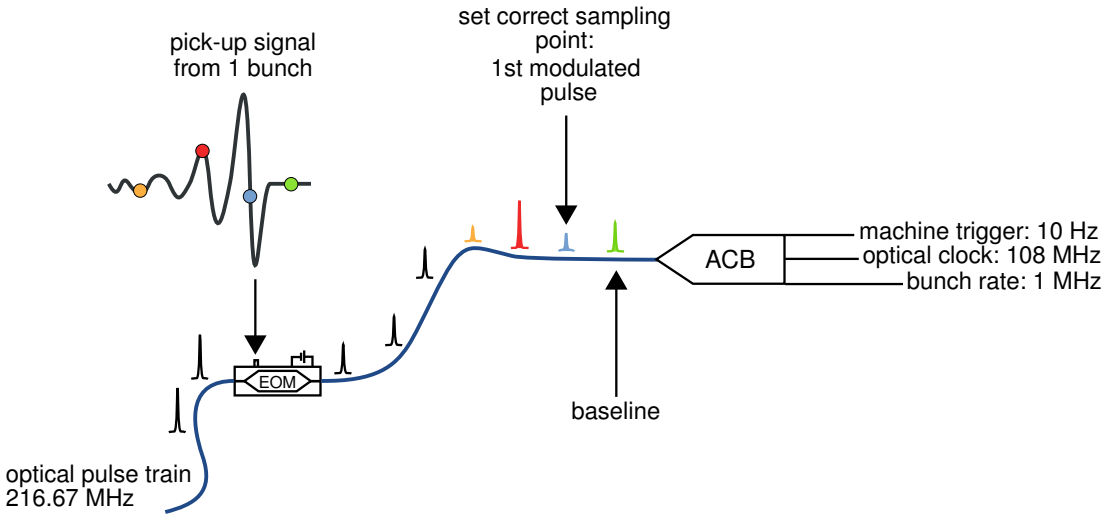

(a) Principle of transferring the arrival time information from an electron bunch at the RF pick-up to an amplitude modulation of the optical reference laser pulses

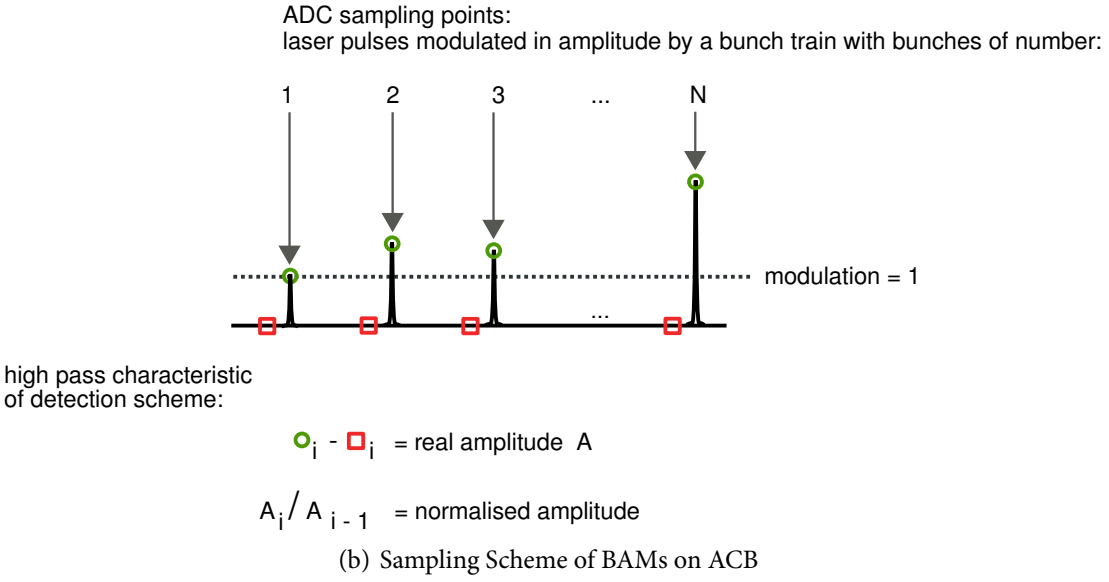

(b) Sampling Scheme of BAMs on ACB

Figure 3.1: Illustrations depicting the operation principle of the BAM system. (a) The voltage transient from an RF pick-up is fed into an EOM to modulate the amplitude of the reference laser pulses proportional to the electric field strength. The operation point of the BAM is chosen such, that the RF signal is sampled around its zero crossing. (b) The signal sampling and processing procedure detects the modulated and unmodulated laser pulses (temporally before the RF transient) and calculates the normalised relative amplitude variations. With a suitable calibration in terms of percentage of modulation per femtosecond, the measured amplitude variation is converted into a timing change.

while the bipolar voltage signal from the pick-up antenna is fed into the device. If the timing between both, the optical and the RF signal, is set correctly, exactly one of the laser pulses experiences the electrical field on the linear slope of the pick-up signal. The preceding laser pulse passes the EOM temporally before the voltage transient arrives. Thus, this pulse traverses the modulator undisturbed. The subsequent pulses indeed are modulated in their intensity, but except for the one on the linear slope, all following pulses sample only the ringing of the pick-up signal. When exiting the EOM (on the right), the laser pulses are transported via an optical fibre to the specialised read-out electronics, the so-called advanced carrier board (ACB). There, the optical signals are converted to electrical pulses by use of photodiodes (PDs) and a pulse shaping electronics before being further processed. For determining the actual rate of laser amplitude modulation, not only the pulse, which samples the pick-up signal on its linear slope, but also the preceding, unmodulated laser pulse has to be taken into account. By subtracting the baseline amplitude (i.e. the unmodulated pulse) from the signal amplitude (i.e. the modulated pulse), one can calculate the real amplitude modulation, A_i:

$$A_i = I_{\text{signal}} - I_{\text{baseline}} \tag{3.2}$$

Figure 3.1(b) shows a schematic of the signal processing scheme. When knowing the A_i for each of the N bunches of a macro pulse, the values are normalised to each preceding bunch, such that the normalised amplitudes become:

$$A_{\text{norm},i} = \frac{A_i}{A_{i-1}} \qquad \text{for} \qquad i > 2 \tag{3.3}$$

With this high-pass processing scheme, slow amplitude drifts and amplitude jitter of a few MHz frequency from the optical reference can be filtered out. Since the currently employed ADCs have a sampling rate of 108 MHz, one requires two separate ADC channels for sampling the signal and baseline intensities. This has a few technical disadvantages, which will be discussed in the following sections. The accuracy of an amplitude detection is limited by several factors throughout the total signal processing chain, related to especially electronic noise, resolution and SNR of the ADCs and EMI. The cumulative effect can be monitored by calculating the mean amplitude noise in the baseline, by averaging over 100 successive unmodulated laser pulses. Since the ADC samples only with half of the repetition rate of the laser pulse train, the averaging time amounts to:

$$2 \cdot 4.614 \times 10^3\ \mu\text{s} \cdot 100 = 0.923\ \mu\text{s} \tag{3.4}$$

Figure 3.2 shows the principle of detecting an arrival time jitter of subsequent electron bunches. For any case, in which the relative timing between the RF signal and the optical reference is set correctly, the laser pulse samples the voltage signal at its zero crossing. All electron bunches, for which this is true, arrive at the reference time. For every bunch, which arrives earlier than the reference bunch, the voltage signal is shifted to the right relative to the laser pulse (dotted, green line). In this case the laser pulse experiences a voltage $V < 0$, thus gets modulated when traversing the EOM. In the opposite case, the voltage signal from electron bunches, which arrive late at the pick-up, is shifted to the left (broken-dotted, red line). The laser pulses get modulated by a voltage $V > 0$. Thus, the sign of the RF voltage on the linear slope of the pick-up signal contains the information on the direction of timing

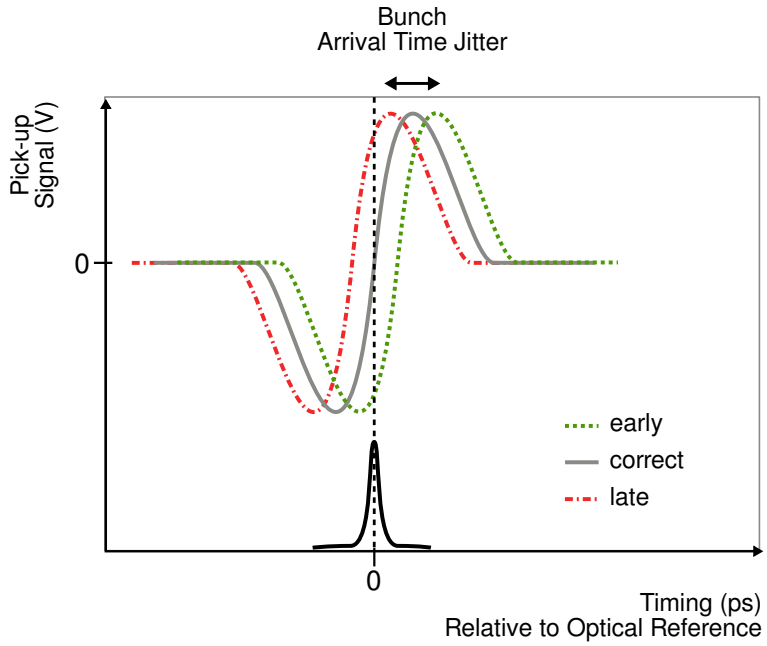

Figure 3.2: Illustration of the principle for detecting an arrival time jitter of subsequent electron bunches. The arrival time of any electron bunch is stated as correct, i.e. it complies with the reference, if the laser pulse samples the RF voltage at its zero crossing. For any bunch, which arrives earlier than the reference, the laser pulse is modulated by a voltage $V < 0$. In the opposite case, the modulation voltage gets larger than zero, $V > 0$, for all bunches, which arrive late at the pick-up.

shift. To translate this information into an amplitude $A_{\mathrm{norm},i}$, which changes linearly with applied RF voltage, one has to adjust the operation point of the EOM by carefully choosing the bias voltage V_{bias}. As given by equation 3.1, the transmission of the EOM follows a squared cosine function. Figure 3.3 shows a measurement of the transmission curve in dependence of the DC bias voltage. If for this particular EOM a bias voltage of $V_{\mathrm{bias}} = -1.1\,\mathrm{V}$ is applied, the operation point of the modulator is set to about 50 % (depicted by the position of the orange-coloured dot) For any applied modulation voltage of $V_{\mathrm{bias}} \pm 1.0\,\mathrm{V}$ the transmission varies linearly between 20 % and 80 %. This region determines the dynamic range in conjunction with the steepness of the RF-voltage slope. If the additional modulation voltage exceeds $|1.0|\,\mathrm{V}$, the transmission slides into the non-linear region. At very large modulation voltages, the transmission even rolls over the crest or through the trough onto the neighbouring slope of the $\cos^2$-curve. The limit for this *over-rotation* is defined by the half-wave voltage V_π, i.e. the required voltage to switch between maximum and minimum transmission, in this case $V_\pi \approx 4.5\,\mathrm{V}$. Depending on the actual set-up, it can be advantageous choosing an operation point of less than 50 % transmission. This is optimised for each of the BAMs individually in connection to other settings in the electronics. Measurements of the corresponding transmission curves are shortly described in section 4.1 on page 97 ff.

Despite the linear behaviour of the RF pick-up signal around its zero crossing voltage, this reference point offers another advantage. At this point, the inherent dependence of the arrival time detection on the bunch charge is reduced. The bunch charge influences the amplitude of the signal. When measuring the arrival time in a small region around the zero crossing, only charge dependent

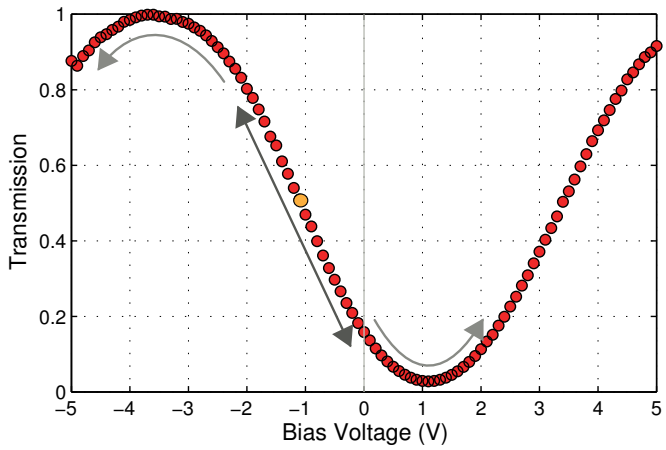

Figure 3.3: Measured transmission curve of one EOM (as used in BAM.1UBC2) in dependence of the bias voltage V_{bias}.

slope variations have to be taken into account, but not the absolute amplitude of the RF signal. In fact, a significant dependency is only observed below a certain threshold of the bunch charge, which leads to a deterioration of the resolution. Apart from that, any residual dependence of the slope gradient on the bunch charge can be eliminated from the calculated arrival time by including an appropriate calibration constant. A description of the calibration procedure and the charge dependency of the calibration constant is given in section 4.2.1, on page 104 ff.

Not only during the initial commissioning of a new BAM, but also in between for maintenance reasons, one eventually needs to determine or affirm the operation point of the BAM. For this purpose, one has to measure the temporal location of the reference sampling point, i.e. the relative timing between the RF-voltage zero crossing and the laser pulses. In assumption, that during this determination the electron arrival time is stable within ±100 fs, one can sample the RF voltage curve for subsequent bunches at different temporal location by introducing a timing delay for the laser pulses. There are two possible methods for sweeping the laser pulse timing, which are explained in the following section, in connection with a detailed description of the optical design of the BAMs. One of those methods makes use of a motorised optical delay line which is incorporated in the BAM opto-mechanics.

An exemplary timing scan for BAM.3DBC2 is shown in figure 3.4. Here, the laser pulse time delay has been scanned in small steps of 3.33 ps (≡ 1mm). The delay has been changed from −115 ps, i.e. before the arrival of the RF signal at the EOMs, up to about +81 ps, relative to the reference point (at 0 ps). The illustration shows two different curves, according to the two detection channels of the BAM. They differ in the size of the dynamic range. One *fine* channel offers a high precision arrival time detection, with a resolutions of less than 10 fs, but for the restriction of the dynamic range to typically 3 to 7 ps. In this detection channel the RF signal is only sent through a power limiter without additional attenuation before being fed into the EOM. The limiter is required to avoid a damage of the modulator, which can occur for voltages beyond ±8 V. The second, or *coarse*, channel offers a large dynamic range of typically 20 to 70 ps, but with a resolution which is worse by a factor of ten compared

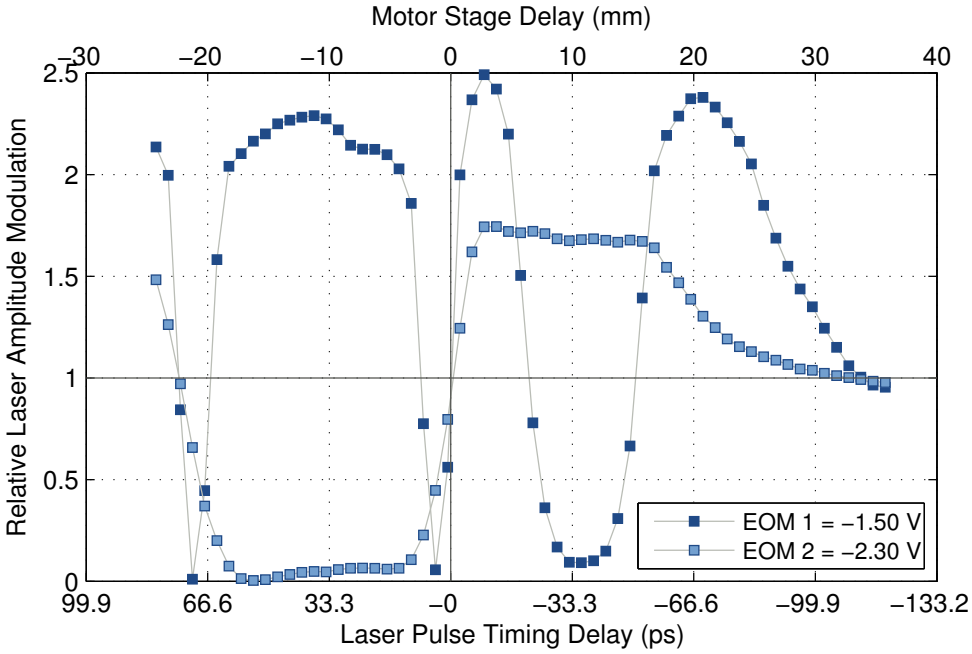

Figure 3.4: Measurement of the amplitude modulation in the two channels of BAM.3DBC2. The laser pulse timing delay has been swept from a point of time before the arrival of the RF signal at the EOMs, i.e. −115 ps, to a point of about +81 ps after the reference point (at 0 ps).

to the high resolution of the *fine* channel. To achieve a broadened dynamic range, the RF signal is sent through an attenuator of typically −20 dB. By lowering the RF amplitude, the steepness of the voltage slope is decreased, such that the *over-rotation* inside of the EOM can be avoided (compare the light-blue curve of EOM No. 2 in figure 3.4).

In contrast to this, the amplitude transmitted from EOM No. 1 in the *fine* channel (dark blue curve) ran out of the linear dynamic range at about −4 ps and +8.5 ps. Beyond those points, the transmission shows a strong *over-rotation*, resulting in the pronounced over- and undershoots when veering away from the reference point at 0 ps. One can picture the resemblance of an s-shape curve if folding the right overshoot upwards and the left one downwards. In operation, the *fine* channel is used to measure the actual electron bunch arrival time and timing jitter, while the *coarse* channel is used to recover the operation point for large arrival time variations. Each time the electron bunch timing deviates by an amount which is large enough to shift the *fine* signal out of its dynamic range, the information from the *coarse* channel is used to adjust the internal optical delay line to shift the laser pulses back to the reference point at the zero crossing of the RF signal. For an automated optical arrival time measurement, a complex infrastructure is required. The bunch arrival time monitor, which is an integral part of the laser-based synchronisation system, actually consists of three subsections. A schematic overview is shown in figure 3.5 In the upper left corner, the layout of the laser-based synchronisation system is depicted. An individual length-stabilised fibre link distributes the timing-stabilised laser pulses to the opto-mechanical BAM front-end (middle part), which is located in close vicinity to the RF pick-up system (lower right corner). The third subsys-

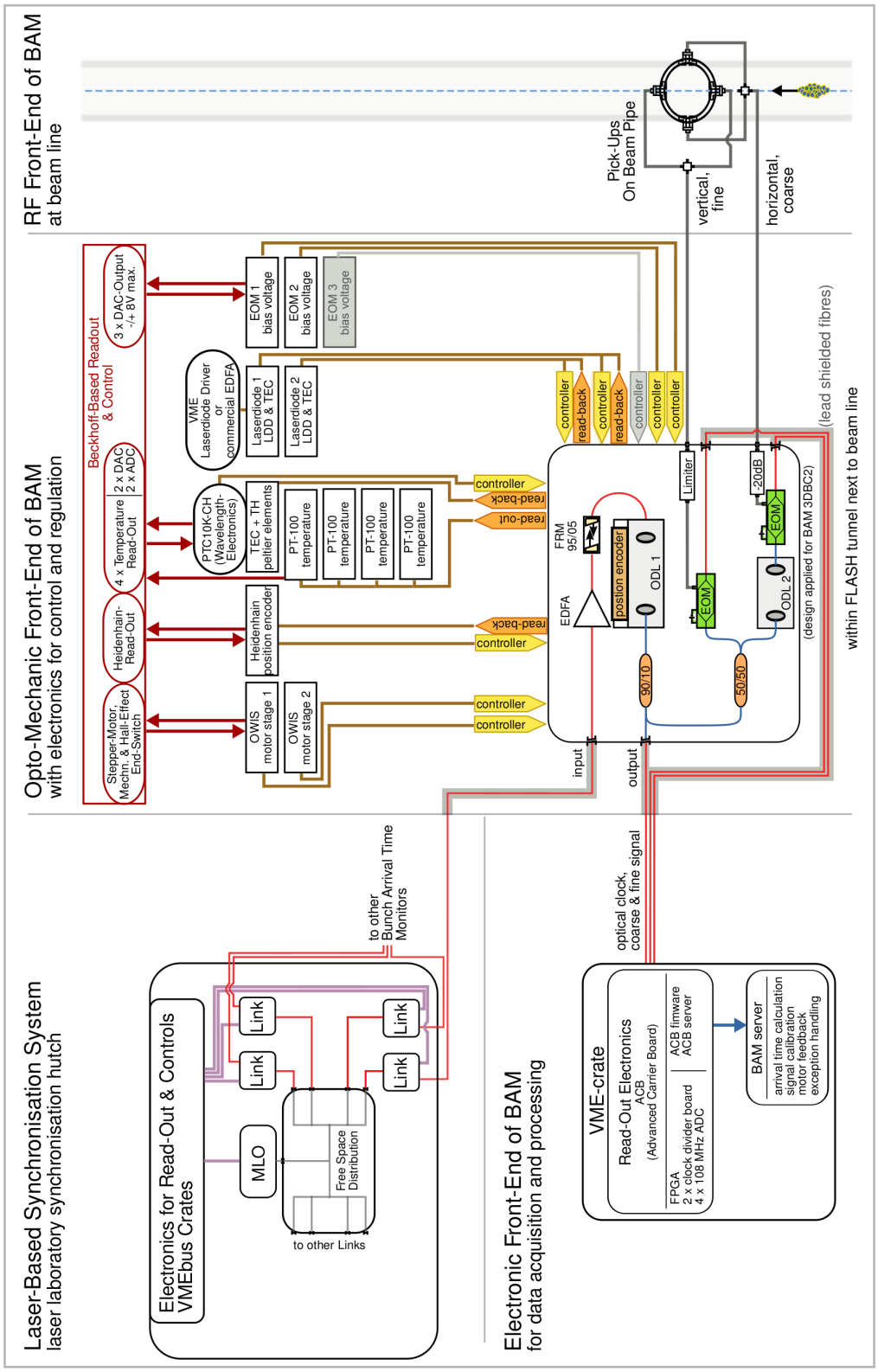

Figure 3.5: Schematic illustrating the infrastructure of the BAM as part of the laser-based synchronisation system. The BAM-system comprises three comprehensive sub-systems, i.e. the RF-front end, the opto-mechanical front-end and the electronics for data read-out and processing.

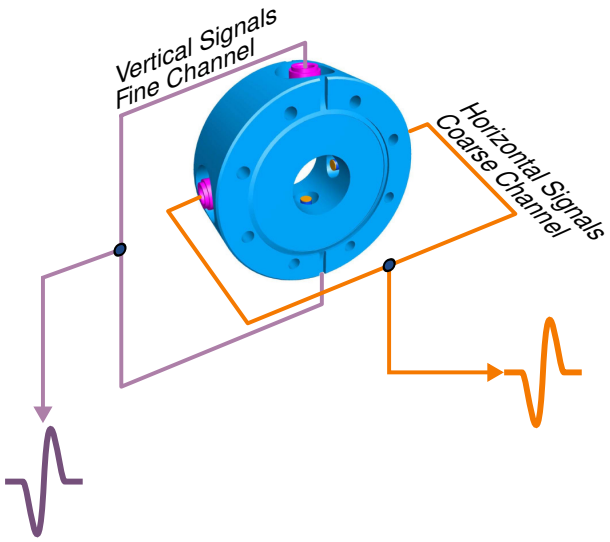

Figure 3.6: Design drawing of the RF pick-up system, including an illustration of the signal combination. The vertical signals are used for a high-resolution measurement in the *fine* channel, while the horizontal signals are used for the low-resolution measurement of the *coarse* channel.

tem (lower left corner) contains all read-out electronics as well as low- and mid-level software, i.e. firmware and server, for data processing.

In the following, all of the three subsystems are briefly introduced and described.

3.1.2 RF Front-End

The RF front-end comprises button-type pick-up antennas, which have been developed and tested before 2008, compare [Hac10] and [Lö9]. Four of those pick-ups are mounted symmetrically onto a metal ring. Vacuum feed-throughs are used to couple the voltage signal from the antennas, which are located inside of the ultra-high vacuum of the beam pipe, into the RF cables. The signals of two opposing pick-ups, i.e. two in the vertical and two in the horizontal plane, are combined, by use of exactly lengthened cables and commercial power combiners. Figure 3.6 shows a schematic, including the technical design drawing of the pick-up system and an illustration of the signal combination. Until 2010, in-house constructed cold combiners had been used, before they were exchanged by commercial 3-dB combiners [1]. The latter show less internal reflections and have a lower insertion loss (~ 1 dB) at a bandwidth from 1 to 18 GHz . The RF pick-up itself has been design to deliver a signal bandwidth from DC up to about 12 GHz, appropriate to the 3-dB bandwidth of the EOMs.

By combining the signals from two opposing pick-ups, the orbit dependency of the arrival time measurement is reduced [Lö9]. The signals from the vertical plane are used in the *fine* channel, since orbit fluctuations of the electron beam are less pronounced in this direction. The combined pick-up signal from the horizontal plane is used in the *coarse* channel. For small transverse displacements of the electron bunches of ±1 mm from the design orbit, the detected arrival time change is typically less than ±50 fs and a second order effect. But for much larger bunch orbit changes, especially in the

[1] Advanced Technical Materials, Inc. power combiner P213H 1-18GHz

vertical plane, the influence on the RF pick-up signal becomes linear and cannot be neglected any more. Measurements of the residual orbit dependence of the arrival time detection are presented and discussed in chapter 4, section 4.2.2 on page 110 ff.

3.1.3 Electro-Optical Front-End

The general operation principle and therefore the main features of the opto-mechanical design have been the same for all BAMs, beginning with the first prototypes. Nevertheless, a large constructional effort has to be made to ensure a stable, high-resolution measurement of the electron bunch arrival time. This has impact on both, the opto-mechanical design and the read-out electronics. As explained in the preceding section, the basic functionality of the BAM is the electro-optical detection of the RF-voltage transient outside of the vacuum chamber, by use of an OIC, in this case an EOM[2], one for each of the two detection channels.

Details on the commercial EOMs can be found in the appendix, section B.2.4 on page 183 ff. (general principle), as well as on page 191 f. (specifications).

Figure 3.5 shows a schematic of the complete monitor system, as applied for BAM.3DBC2. In the middle part, the opto-mechanical subsystem is shown in detail with a framed box containing the actual opto-mechanics chassis at the lower part of the illustration. This box contains the complete fibre-optical set-up of the BAM. On the left upper corner of the box, the fibre from the length-stabilised link is connected to the chassis, while the actual link ending is located inside the BAM box. The link end consists of an erbium-doped fibre amplifier (EDFA) and one partly transmissive Faraday rotating mirror (FRM). Details on the link design can be found in chapter 2 on page 21 ff. The fibre-optical part of the BAM starts with the output of the FRM. From this point on, the laser pulse propagation time through the fibre is not actively stabilised, but drifts, influenced by environmental factors, especially by temperature. Therefore an active temperature stabilisation of the complete fibre section is mandatory. Following the FRM, the laser pulses traverse the first optical delay line (ODL), named ODL1. It consists of two opposing fibre-coupled collimators, of which one is mounted on a motorised linear stage. Its position is measured on-line by use of an absolute position encoder[3], which has a resolution of 5 nm at an accuracy of ±3µm across the total range of 120 mm. The ODL1 is used to simultaneously shift the timing of the laser pulses at both EOMs by the same amount, i.e. to introduce the same timing shift of the optical reference in fine and coarse channel. As explained in section 3.1.1, this is required for two purposes:

- the adjustment of the laser pulse timing to cope with arrival time changes of the generated RF signal, and hence of the electron bunches; this is required to keep the temporal overlap of laser pulses and RF signal at the correct operation point in both EOMs. Large arrival time variations, i.e. in the order of a few picoseconds, are caused by changed machine settings.
- for scanning the shape of the modulated amplitude signal in a short temporal range around the zero crossing of the RF signal.

Behind the ODL one part of the laser pulse power, in this case 10%, is split off by use of an in-fibre directional coupler. The separated signal is sent via an optical fibre to the read-out electronics for gen-

[2] Zero-Chirp Intensity Modulator Mach-10™056 from Covega
[3] *Heidenhain* LC 483 [Web12]

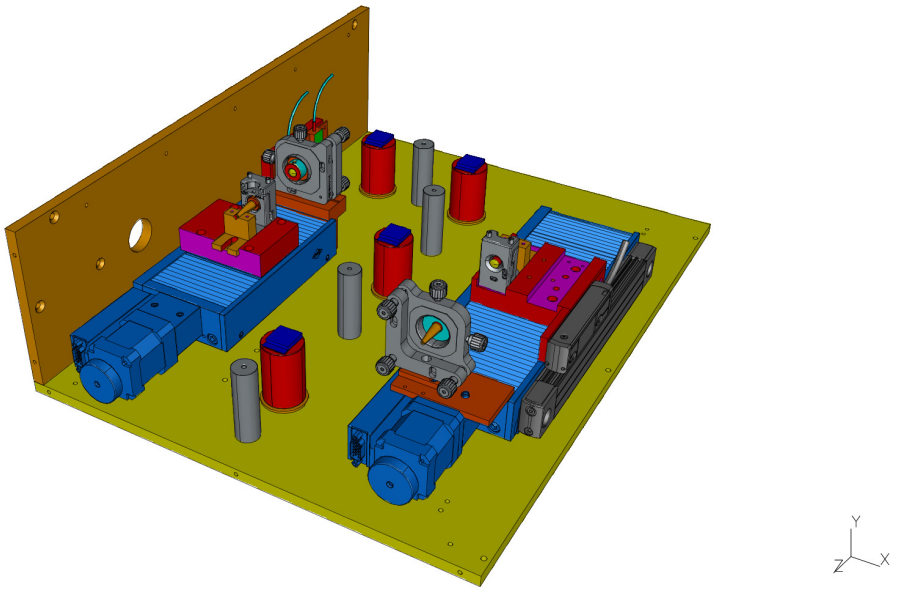

Figure 3.7: Technical drawing of the opto-mechanical design, applied for BAM generation 2. The illustration shows the ground plate with the two motorised stages used in the optical delay lines. An absolute position encoder is attached to the stage on the right hand side. The thinner posts are used for mounting an aluminium plate in the middle layer (compare figure 3.8(a)), whereas the other posts are holding PELTIER elements.(courtesy of K. Ludwig)

erating a clock signal from the optical pulse train. The remaining optical pulse power is then divided in equal parts into the two detection channels, by use of a second directional coupler. According to the illustration, the upper optical path is the fine channel, where the EOM1 is connected. The lower path comprises a second, shorter ODL, namely ODL2, which is constructed similarly to ODL1, but without the position encoder. This delay line serves the purpose of setting the correct, relative timing between fine and coarse channel. Behind ODL2, the second EOM is connected. Thus, the BAM delivers three optical output signals, i.e. the clock signal as well as the two amplitude modulated signals from the *fine* and *coarse* channel. All of them are transported through individual optical fibres to the read-out electronics. Additional, electronic devices are connected to the BAM chassis, as can be seen in figure 3.5:

- two stepper-motor controller and one position encoder read-out for the ODLs
- a laser diode driver (LDD) for the EDFA
- a commercial temperature controller, which connects to four PELTIER elements and a thermistor, all of which installed within the BAM chassis
- read-out of four temperature sensors, installed inside of the BAM chassis
- a DAC with two channels for controlling the DC bias voltage of both EOMs

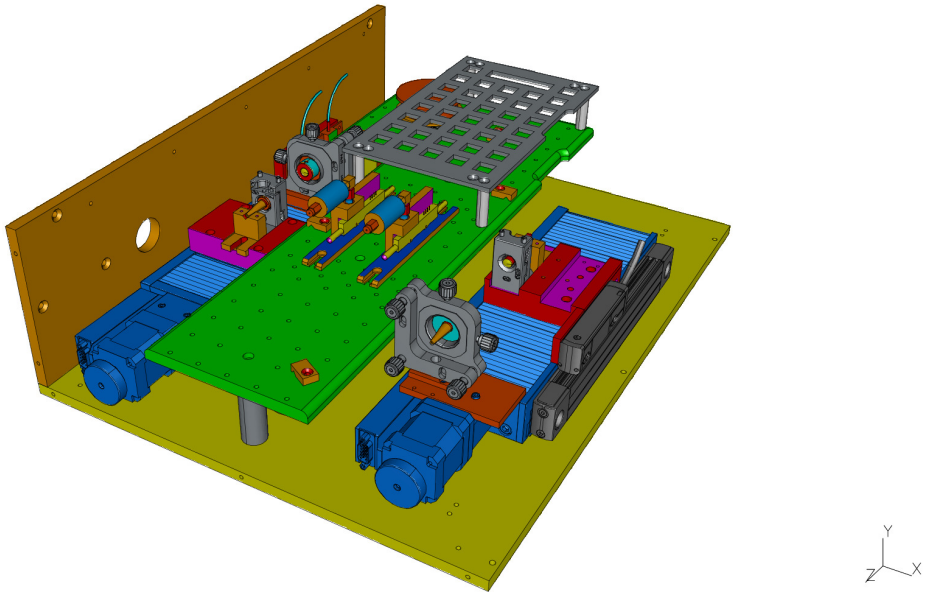

(a) The illustration shows the middle layer, which comprises a temperature stabilised aluminium plate. On the latter, most of the fibre-optical components are attached, including the two EOMs. Both are mounted on individual holders in the middle of the plate. The third layer, composed of an aluminium mesh is used for fastening cables.

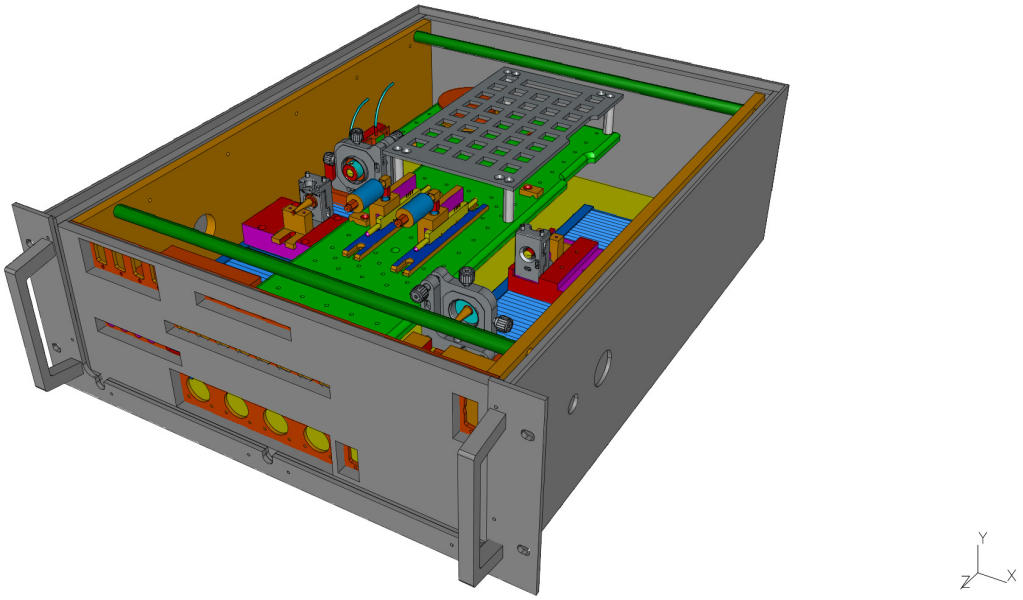

(b) The illustration shows the most important parts mounted inside of the aluminium chassis. The box is designed to fit into a 19 inch rack, consuming 4 height units.

Figure 3.8: Technical design drawings of the opto-mechanics, as applied for BAM generation 2. The mid and top layers are shown.(courtesy of K. Ludwig)

Except for the commercial temperature controller, all other electronics are based on components from the company *Beckhoff*. Details on the performance and further improvements of the temperature stabilisation are discussed in section 3.2.2 on page 88 ff.

Three technical design drawings of the described BAM chassis are shown in figures 3.7 and 3.8. In figure 3.7, the inner, bottom layer with both motorised delay stages is shown. The absolute position encoder is attached to the side of the foremost motor stage. The thinner posts along the centre line of base plate are used for attaching an aluminium plate, on which all fibre-optical components, including the EOMs, are mounted, compare figure 3.8(a). The thicker posts are holding the PELTIER elements. Figure 3.8(b) shows a view onto the assembled opto-mechanics chassis, with the cover removed (also visible are the slots for connectors on the front panel).

A major part of this thesis comprises extensive design improvements having been applied to the opto-mechanics of the currently installed BAMs. Furthermore, the critical and weak points of the latest design, BAM generation 2, have been identified. The gained experience is introduced into a concept for the following BAM generation, which will be implemented and tested starting in 2012. The on-going revision of the opto-mechanics runs in parallel to a redesign of the RF pick-up, which has been started in 2011 in cooperation with a group of the *University of Darmstadt*.

The different generations of the opto-mechanical BAM front-ends are described briefly in section 3.2 on page 80 ff.

3.1.4 Electronic Front-End

The third subsystem comprises all read-out electronics as well as a comprehensive server architecture, which is required to detect and further process the amplitude modulated output signals from the *fine* and *coarse* channels of the BAM. Although the taken area of this subsystem in illustration 3.5 is relatively small, the actual participation of the electronics in the arrival time detection process amounts to roughly 50%.

The large amount and widespread variety of high demands on the read-out electronics necessitated the in-house development of a sophisticated, analogue and digital hardware. Besides the high-signal quality of the arrival time detection, the electronics have to fulfil a digitising and signal processing in real-time. The latter, in conjunction with the signal distribution via high-speed links to specialised hardware of accelerator subsystems, enables the application of feedbacks for an active arrival time stabilisation. Since no off-the-shelf hardware had been available, which could have performed all of the demanded tasks, in 2006, the development of a specialised hardware has been started at DESY in cooperation with a group at the *University of Warsaw*. A detailed description of the present ACB electronics can be found in [GBF+10a] and [GBF+10b].

3.2 Design Changes & Improvements of the BAM

3.2.1 Improvements in Generation 2

A considerable amount of time during this thesis has been spent on improving the opto-mechanical and electro-optical set-up, especially concerning the fibre-optics. Figure 3.9 gives a detailed overview on the fibre-optical layout, which is used for BAM No. 1, i.e. BAM.1UBC2. It comprises the opto-mechanical design of generation 2a. For an explanation of the numbering and naming of all BAMs, compare section 1.1 on page 6. The schematic shows all of those components which are mounted inside of the BAM box, i.e. the opto-mechanics chassis, which had been described in the previous section. In this illustration, the single mode fibre (SMF) from the fibre link is attached to a feed-through at the upper right corner. The fibre-link ending, i.e. the Faraday rotating mirror (FRM), is also safely stored within the box. Between the fibre feed-through and the FRM an erbium-doped fibre amplifier (EDFA) is inserted. As described in chapter 2 on page 21 ff., the interconnected fibre-coupled amplifier is used to adjust simultaneously the optical power levels inside of the link fibre and at the remote station, i.e. in this case the BAM. Depending on the ratio between transmission and reflection of the FRM, a second EDFA is required behind the link ending, i.e. within the fibre-optical set-up of the BAM.

Both, the first prototype as well as the second generation design, comprise such an additional fibre-coupled amplifier. The disadvantage is an increased length of the total optical path, in this example about 950 mm of additional fibre. The in-fibre distance between the FRM and the electro-optic modulator (EOM) is a critical factor, since this part is not actively length-stabilised. Any timing drifts of the laser pulses in this section deteriorate the accuracy of an electron-bunch arrival time measurement. The temperature dependent timing drifts of signals within optical fibres, necessitate an adequate temperature stabilisation of the total fibre-coupled path within the BAM box. This feature has been neglected for the first two prototypes, which degrades especially their long-term performance. From opto-mechanics generation 2 on, a simple temperature regulation has been included. Due to its layout and the environmental conditions, the first, simple realisation of a stabilisation did not achieve the demanded stability of less than a few ten mK (RMS) for a long-term operation. A detailed discussion of this issue is given in section 3.2.2 on page 88 ff.

As can be seen in figure 3.9, the fibre-optical layout inside of the BAM comprises SMF components up to and including the second amplifier, which is followed by the first and longest optical delay line (ODL). In the BAM of generation 1, the transition between normal optical fibre and polarisation maintaining fibre (PMF) is located in front of this ODL. The transition is accomplished by a simple fusion splice of both fibres. The use of PMF is required, because the EOMs are sensitive to the state of polarisation (SOP) of the laser pulses. Since the total preceding fibre section from link box to BAM box is made from SMF, the SOP of the laser pulses is not stable but changes with environmental factors, like temperature and fibre bending radii. Because of this, an active adjustment of the linear SOP of the laser pulses at the location of the EOM is required. The polarisation control is achieved by an automated adjustment of two waveplates (quarter-wave and half-wave) inside of the link box. In order to achieve a simultaneous optimisation of the SOP for both EOMs, the laser pulses have to be inserted into a polarisation maintaining (PM) fibre at a location in front of the point, where the pulses are split into the two different detection channels.

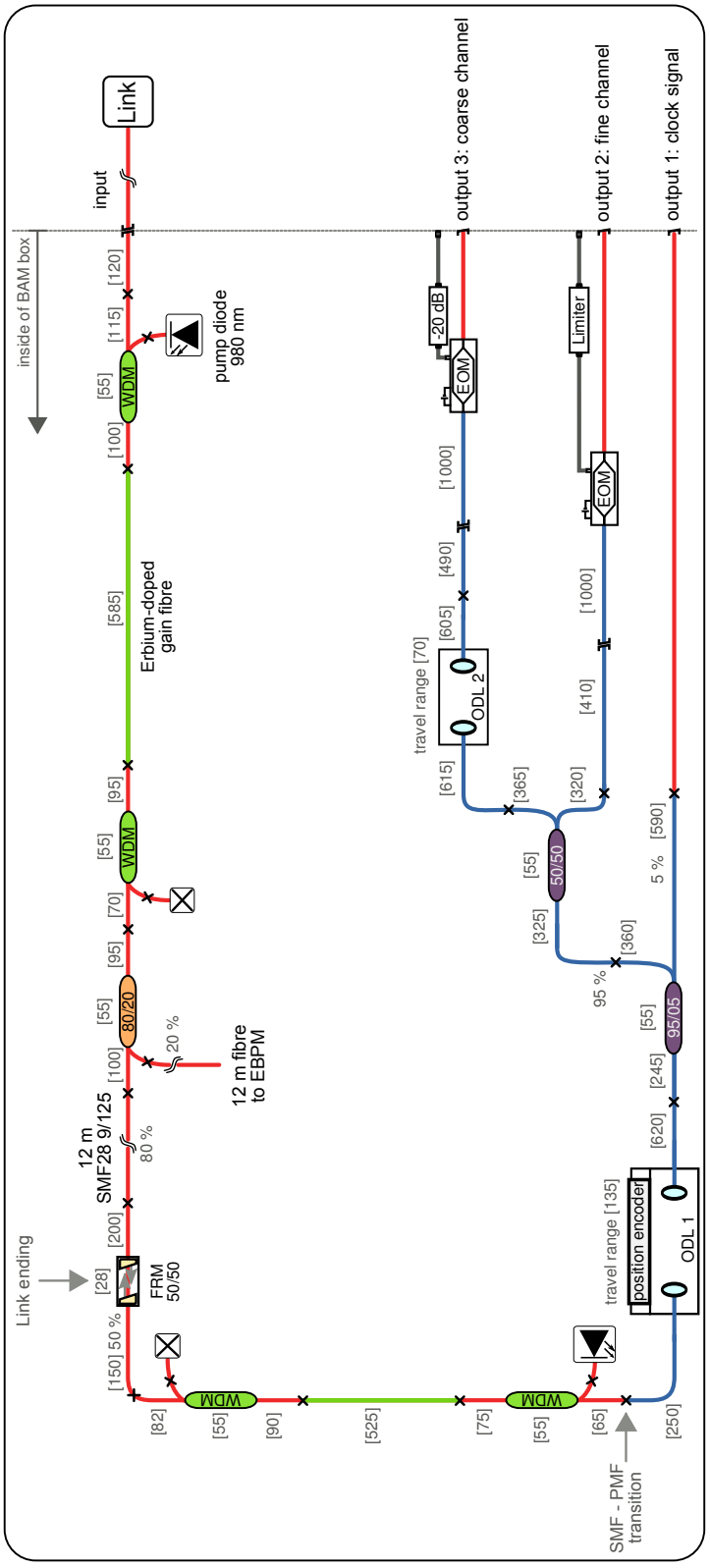

Figure 3.9: Schematic of the fibre-optic layout as used for BAM.1UBC2 (generation 2a). The values in parentheses are actual lengths of the fibres and components given in millimeter. Input laser pulses from the length-stabilised fibre link enter the BAM optic at the upper right corner. The three optical output signals of the BAM are shown on the lower right hand-side. The first half of the fibre section is built in standard SMF while the second half consists of PM fibre. The red lines indicate the SMF, green lines are the Er-doped gain fibres of the two EDFAs and the PMF is shown in blue. Dark grey lines indicate RF cables.

A noteworthy complication results from the usage of PMF components. The self-made fusion splices are a time-consuming and difficult task, even by usage of the best commercially available devices. In an automated procedure, the two orthogonal, optical axes – slow and fast axis – of two PM-fibres are aligned to each other, which requires a process-related excess fibre length of up to 250 mm. In contrast to this, fusion splices between SMF-components can be made much shorter. Furthermore, the alignment of both PM-fibres is not perfect, i.e. a typical polarisation extinction ratio (PER) of only 20 to 25 dB is achievable. Consider a linearly polarised laser pulse which is launched completely into the slow axis. When propagating through the fibre and passing a low PER splice, part of the laser pulse power couples into the orthogonal optical axis. This part will be lost, since the electro-optic modulator only utilises light from the slow axis. If many subsequent PM-fusion splices are required inside of the fibre-optical set-up, the overall optical power requirements will increase to compensate for those losses. Subsequent to this section, a measurement is shortly discussed, which shows the problems arising from omitting the essential polarisation regulation.

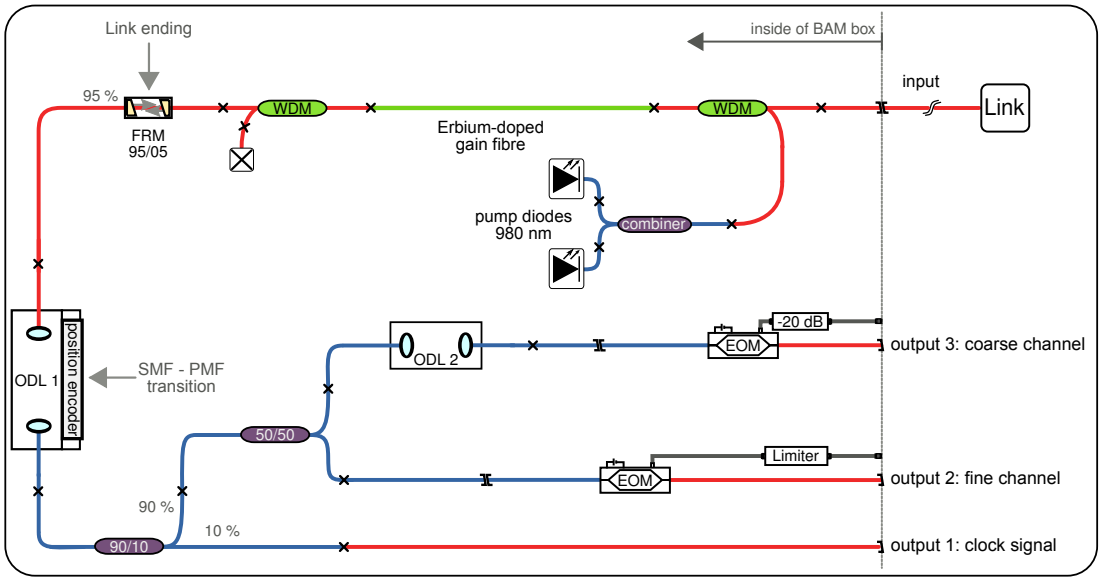

Figure 3.10: Schematic of the fibre-optic layout as used for BAM.3DBC2 (Generation 2b). Input laser pulses from the length-stabilised fibre link enter the BAM optic at the upper right corner. The three optical output signals of the BAM are shown on the lower right hand-side. The first third of the fibre section is built in standard SMF while the rest consists of PM fibre. The red lines indicate the SMF, the green line is the Er-doped gain fibre of the EDFA and the PMF is shown in blue. Dark grey lines indicate RF cables.

Figure 3.10 shows the fibre-optic set-up as used for BAM generation 2b, i.e. BAM.3DBC2. Compared to the earlier versions, the overall fibre length within the BAM box and behind the FRM has been reduced enormously, by about 2.0 m. This has been accomplished by using an FRM with 95 % instead of 50 % transmission. To achieve a balanced optical power ratio between the fibre link and its end-station, the intra-link EDFA has been extended, with the option of using two pump-diodes simultaneously. With this, typically 40 to 60 mW of optical power are achieved for the BAM optics and 15 to 25 mW for the reflected link pulses. Even when pumping the EDFA with only one laser diode (LD), the optical power is still sufficient to operate this particular BAM. This has been a useful

feature by the time when one of the LDDs failed. Furthermore, in this BAM generation, the transition between PMF and SMF has been shifted to the point between the two collimators, which are mounted on the first ODL.

Finally, one of the main improvements made in the BAMs of generation 2a and 2b compared to the earlier versions is the use of long-living and high precision motorised delay stages. Especially the linear motor stage of the first (long-range) ODL is suited for a high-duty cycle usage while maintaining a very high mechanical stability. Both slightly different motor stages comprise a high-precision spindle, directly driven by a stepper motor.

In section C.2 of the appendix, a detailed listing of all components used for the latest BAM is given. In section C.2.1, a small selection of photographs are shown, which were taken during the assembly of BAM.1UBC2.

Consequences from a misaligned state of polarisation

In this section a measurement is briefly discussed, which shows the problems arising from a misaligned polarisation of the laser pulses inside of the BAM optics. The measurement had been performed with BAM No. 1, which had been operational and showed a mean resolution of 19.25 fs. The initial value of the average amplitude noise from the unmodulated signals amounted to about 0.57 %.

During the normal operation of the BAM with both motor feedbacks switched on, the half-waveplate in the corresponding link has been rotated in small steps by 90 °, thus rotating the orientation of the linear polarisation. What can be observed are two effects: As shown in figure 3.11, by

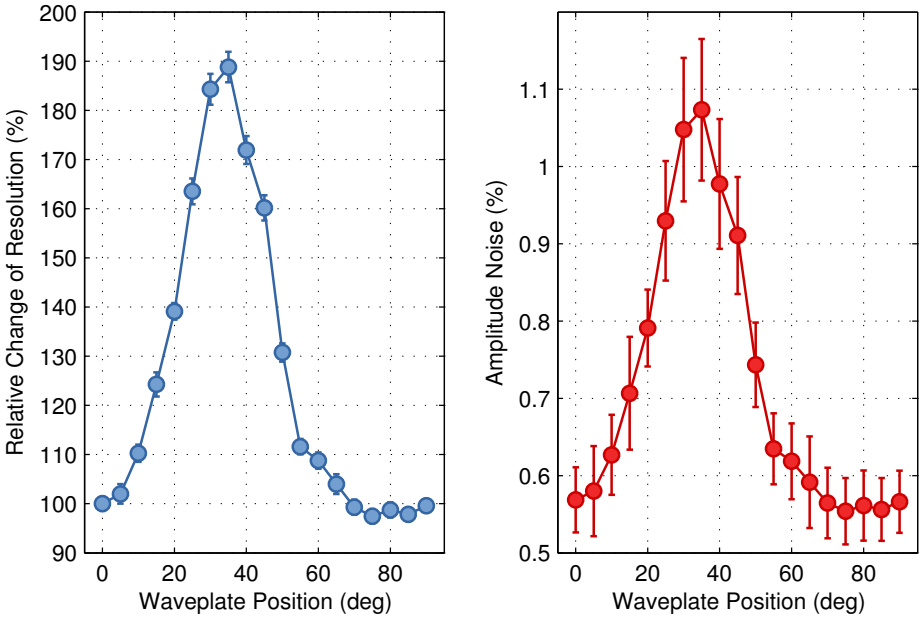

Figure 3.11: Measurement of the polarisation dependent deterioration of mean amplitude noise and resolution of the BAM.

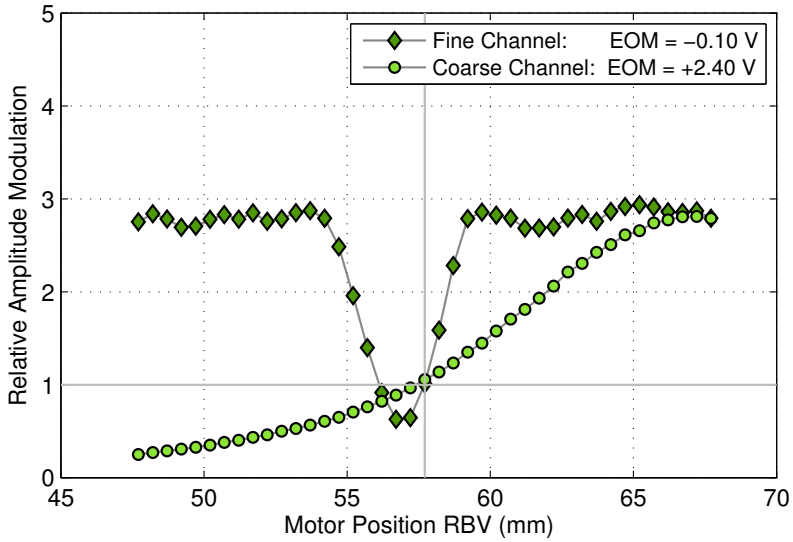

(a) BAM signal scan around normal operation point.

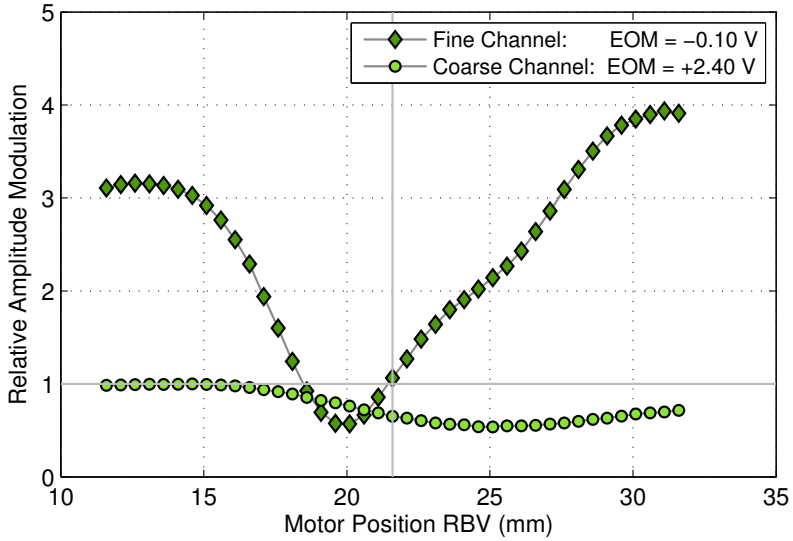

(b) BAM signal scan around erroneous operation point.

Figure 3.12: Two signal scans performed with the motorised ODL inside of BAM No. 1. Shown are both, fine and coarse signals of the calculated amplitude modulation. The motor position had been varied by ±10 mm around the (a) normal operation point and (b) the falsely determined new operation point at a waveplate rotation angle of 25 °.

rotation of the SOP the mean amplitude noise increases dramatically, which in turn deteriorates the calculated resolution of the arrival time measurement, by up to 190 %. The amplitude noise resets to its initial value, when the half-waveplate reaches an angle offset of 90 °, which is equivalent to the state at 0 °.

One explanation for this behaviour is that the power levels at the EOMs decrease when misaligning the state of polarisation of the laser pulses. Thus a smaller intensity is transmitted through the EOM to the ADCs, which deteriorates the signal-to-noise ratio. This not only increases the amplitude noise, but also changes the transmission curve of the EOM. The latter is shown in figure 3.12. When initially commissioning a BAM, the bias voltage of the EOM has to be optimised, as explained in section 3.1.1. It is not only used to set a certain transmission of the EOM, to e.g. 30 % at zero RF voltage, but it also has impact on the saturation degree of the ADCs, when not adjusting any internal clock delays. An imbalance between signal and baseline ADCs, leads to a deformation of the calculated curve of amplitude modulation, as determined in a BAM signal scan. The latter method is also briefly explained in section 3.1.1.

A second explanation of this is related to the fact, that the splitting ratio in the PMF directional coupler changes with the SOP. The specified coupling ratio is only valid for one optical axis (in this case, the slow axis) of the device. As a result, the optical power level, which is tapped off for the clock output, changes. When the power level falls below a certain threshold, typically 0.2 to 0.4 mW at the PD of the ACB, no stable clock signal can be generated. Thus, the resynchronisation to the external trigger fails, and the actual signals on the ADCs are not sampled at the correct point any more. The resynchronisation is essential, since the laser pulse with a repetition rate of 216 MHz have to be sample by the fast ADCs in the correct 108 MHz bucket, because only there the arrival time information is encoded. If the sampling jumps to the wrong bucket, the modulation of those laser pulses will be measured, which actually traverses the EOM at a time after the zero crossing of the RF signal from the electron bunch. Thus, only the ringing of the RF signal will be determined.

Figure 3.12(a) shows the BAM signal scan of fine and coarse channel before the polarisation misalignment. The signal scan has been performed with the motorised ODL, thus on the x-axis the motor position is shown instead of the relative timing, which are complementary parameters. The operation points of both detection channels are aligned to each other, i.e. the points of amplitude modulation 1 on the correct, linear signal slope overlap at the same motor position. During the measurement of the polarisation dependency, the internal BAM motor feedback had been switched on, which tries to keep the operation point of the fine channel around the point of an amplitude modulation of 1. In contrast to the first signal scan, figure 3.12(b) shows two amplitude modulation curves which have been measured around the momentarily operation point at a waveplate setting of 25 °. The shape of the signal curve had changed such dramatically, that the feedback adjusted the motor position to 21.5 mm, to find a location along the fine signal, which has both the correct sign of slope and an intersection at 1. Anyhow, since the electron bunch timing had not changed during the measurement, a false deviation in arrival time is detected. A maximum position change of −35.5 mm corresponds to a timing change of 118.3 ps. Although, this is an extreme example, even small deviations from the optimum state of polarisation can lead to erroneously detected electron arrival time changes. Because those can be as small as a few hundred femtoseconds, which is in the range of typical values during machine operation, the polarisation-related malfunction of a BAM might not attract attention immediately.

To avoid these effects, an automated polarisation adjustment had been implemented. Firstly, it was only based on a MATLAB™ programme, but soon it will be implemented in the BAM server. The tool for a polarisation adjustment uses a *timer* object, as implemented in the MATLAB™ syntax. The source code is printed in section E of the appendix on page 209 ff. In the main file of this tool, one can define different parameters:

- time to wait until calling the sub-routine the first time
- time delay between two calls of the sub-function which actually executes the adjustment
- number of repetitive calls
- selection of those BAMs, which should be included in the procedure
- decision, if the polarisation should be optimised to achieve the maximum value in the ADC signal of each BAM or if the ADC value should be optimised to a predefined value, which can be set in the main file

The general procedure, every time the *timer* calls the subroutine, is the following: At first, the motorised rotation mount of the waveplates is moved in a large step of 4 ° in positive direction. By comparing the sign of the mean change in the ADC signal, the algorithm decides whether to proceed with a rotation of the mount into the same or in the opposite direction. The rotation mount is turned in large steps forward, until the maximum or the predefined ADC value is passed through by the last step. The large step size is chosen to exclude the possibility, that the procedure stops at a local maximum. Afterwards, the waveplate angle is adjusted in small steps of 2 ° in the reverse direction to slowly approach the target value.

Another important decision resulted from those findings, which are explained above. That is the exchange of the PMF directional coupler by an SMF component. The latter design change is also mentioned in the next section 3.2.2, in connection to the planned layout for the next generation of BAMs.

3.2.2 On-Going Developments for Generation 3

A major topic of this thesis has been the optimisation of the opto-mechanical set-up of the bunch arrival time monitors. From the vast amount of experience, which has been gathered during the assembly and commissioning of BAM.1UBC2 and BAM.3DBC2, several decisions have been made how to improve the opto-mechanics of the following BAM generation. The planned changes and further suggested improvements are briefly discussed below:

Fibre-optical set-up

Figure 3.13 shows a proposal for the fibre-optics of the 3rd generation BAM, based on the experience gained during this thesis from the operation of the existing BAMs. The layout of the link-ending is adopted from BAM No. 2, using an intra-link, double-pumped EDFA. Since this is a feature related to the link design, the EDFA will possibly be moved from the link ending to the link box, compare chapter 2. This would have the positive side effect of reducing the component density in the BAM box.

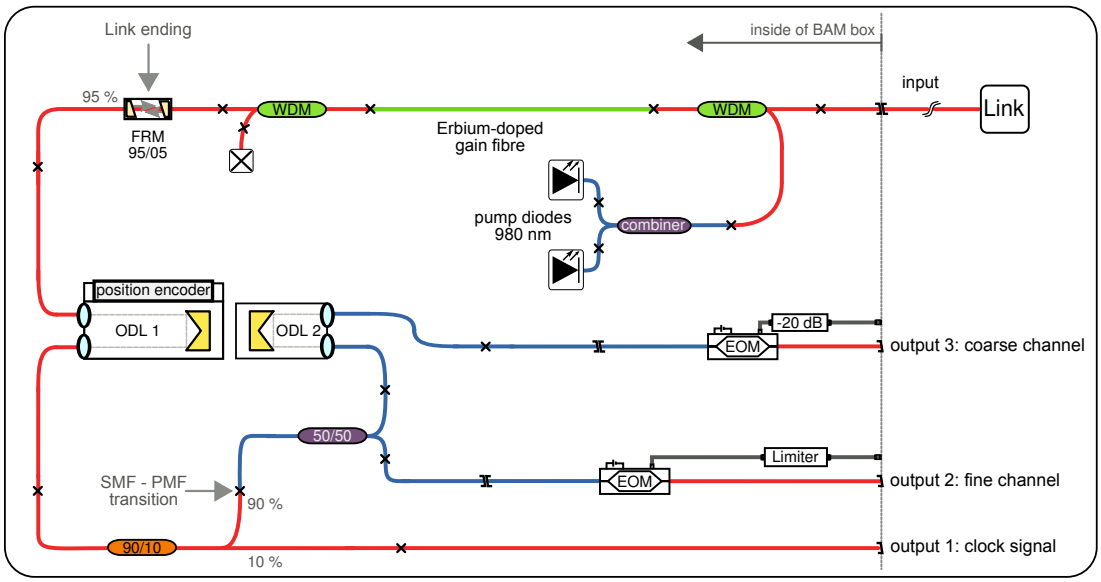

Figure 3.13: Schematic of a fibre-optic assembly as a possible design for the next generation of BAMs (generation 4). Input laser pulses from the length-stabilised fibre link enter the BAM optic at the upper right corner. The three optical output signals of the BAM are shown on the lower right hand-side. Two thirds of the fibre section is built in standard SMF while the rest contains PM fibre components. The red lines indicate the SMF, the green line is the Er-doped gain fibre of the EDFA and the PMF is shown in blue. Dark grey lines indicate RF cables. The optical delay lines consist of fixed fibre collimators in combination with retro-reflectors.

Anyhow, it will be advantageous to resign the usage of a second EDFA behind the FRM. One of the major design changes concerns the layout of both ODLs. Instead of two opposing collimators, as used in all previously installed BAMs, the new design foresees an optical delay line with fixed collimators and a retroreflecting element, mounted on the stage. The main advantage is, that any movement of the fibres is avoided and the fibre length of the collimators can be reduced. In the old design, the collimator, which has been mounted on the stage, required a specific excess fibre length to be moved along the total travel range. Since this leads to a change in fibre bending radius, even in PMF, this might lead to an unwanted change in polarisation rotation. Furthermore, the mechanical stress on the collimator could disturb the light incoupling such, that the incoupling efficiency is deteriorated, depending on the motor position. The new design not only avoids those mentioned disadvantages, but also doubles the adjustment range of the optical path length between the two collimators.

A detailed view on the realisation of such an ODL with the usual, commercial components is given in figure 3.14. For a simplified alignment, the usage of two additional mirrors is suggested to optimise the angle and position of the laser beam at the incoupling collimator. Furthermore, in this scheme, the fibres of the collimators directly lead into the temperature stabilised box (thermo box). Thus, the fraction of the fibre-length in the BAM chassis, which is not temperature stabilised, can be reduced enormously.

Another important design change concerns the directional coupler, at which the optical power for the clock signal is tapped off. Due to the problems which arise from the usage of a PMF coupler, in future, a SMF component will be used instead. This issue is explained in detail in the previous

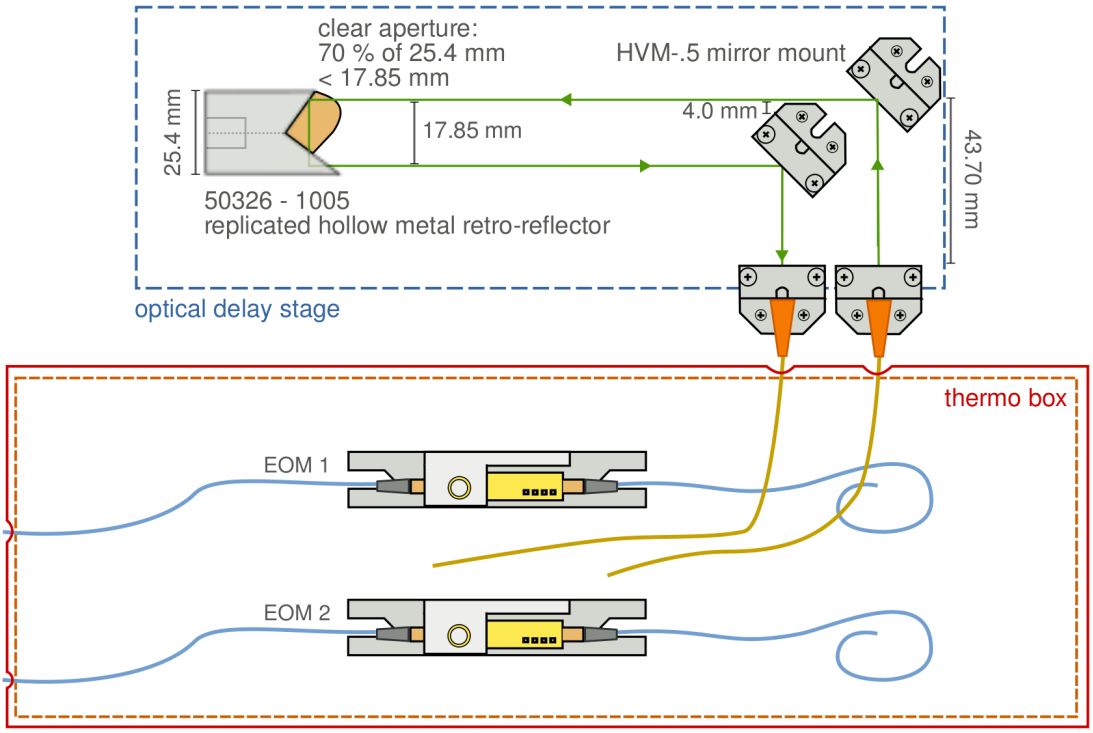

Figure 3.14: The layout of the ODLs in the 3rd generation of BAMs foresees the usage of two fixed collimators and a retroreflector. The latter is a gold-coated, replicated hollow metal retroreflector from the company *Newport*®. The fibres of the collimators directly end in the temperature stabilised volume of the thermo box.

section. The transition between standard and polarisation maintaining-fibre will be located at the last possible location, i.e. directly in front of the 50 : 50 PMF coupler, which divides the optical power into the fine and coarse channel.

Temperature regulation

The current temperature regulation scheme, which is used in BAM No. 1 and 2, foresees the stabilisation of the complete thick Aluminium (Al) plate of the middle layer, which supports the fibre-optical components (compare fig. 3.8(a) in section 3.1.3, pg. 76).

This is done by use of only four, small Peltier elements, which are connected in series. The fibres and the Aluminium plate itself are not shielded. Thus, not only the metal, but also the surrounding, inert air has to be stabilised in temperature. Although air is a relatively good thermal isolator its temperature varies slowly, due to the lost heat from the aluminium plate through convection and radiation as well as from a conduction of ambient heat from outside of the BAM box. Furthermore, the thermal bridge, which connects the Peltier elements with the ambient air, is connected to the outer metallic housing of the BAM box. Even though there is an isolation layer between the outer and inner chassis, the Al ground plate of the inner BAM box heats up to a temperature which is higher than the stable temperature of the middle layer, showing that the Peltier elements are mainly cool-

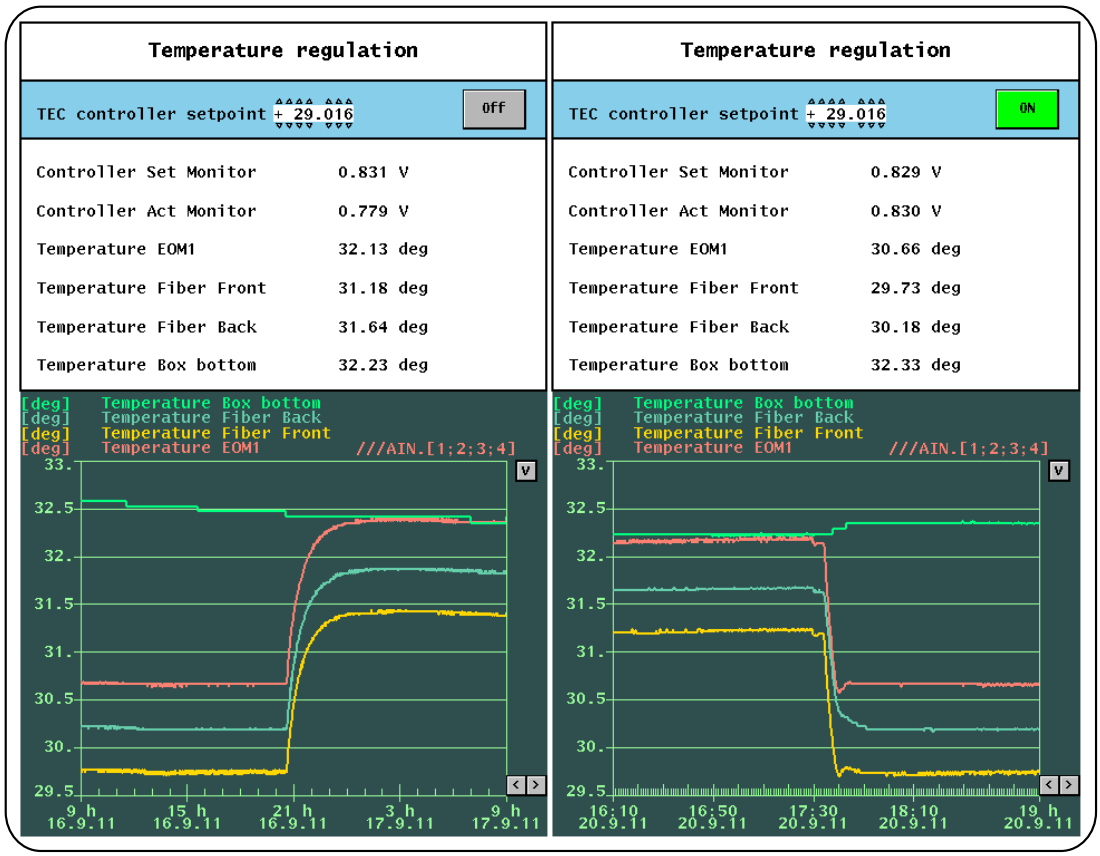

Figure 3.15: Illustration showing two snapshots of the DOOCS control panel for the temperature regulation. It comprises a button for switching the controller on and off, one input field for the temperature set-point and six read-back values, whereas four of those belong to temperature sensors inside of the BAM box. Below the listing, a history plot shows the temperature curves. Two different occasions are shown: on the left hand side, the controller has been switched off in between, and on the right hand side, the controller has been switched on again

ing the Aluminium plate and thus are transferring heat to the bottom of the box. If the temperature set-point deviates from the tunnel temperature by more than 2 to 3 K the regulation gets unstable and starts to oscillate severely with a very short period between a few minutes and up to 30 min. This behaviour cannot be suppressed by an adjustment of the P-gain of the controller, only by changing the temperature set-point. This can be done remotely, since the controller is implemented in the distributed object-oriented control system (DOOCS) of FLASH. Figure 3.15 shows a snapshot of the corresponding panel. It comprises a button for switching the controller on and off, one input field for the temperature set-point and six read-back values (RBVs), four of those from temperature sensors inside of the BAM box. Below the listing of the momentarily RBVs, the history of the temperature curve is plotted. The illustration shows the panel for two different occasions: on the left hand side, the controller has been switched off in between, and on the right hand side, the controller has been switched on again. In this particular example, the regulation operates very stable, but the pronounced though stable temperature gradient between the different locations in the BAM box are clearly visible.

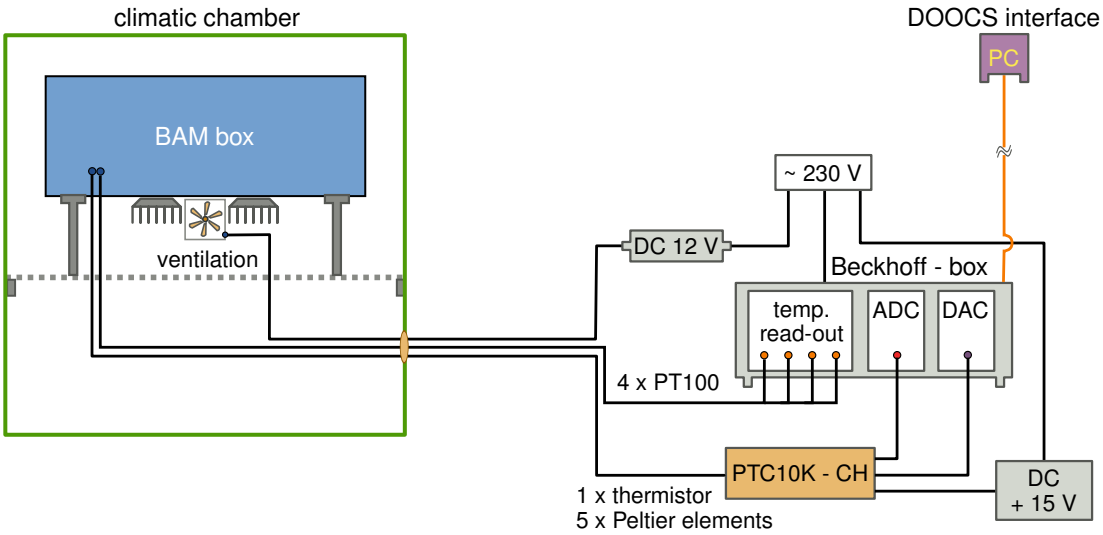

Figure 3.16: Schematic of the set-up for testing the new temperature stabilisation scheme, as planned for BAM generation 3. To simulate a realistic environment, the whole BAM box has been mounted in a climatic chamber. On the outside, the commercial temperature regulator board, voltage supply and electronics for monitoring of the temperature sensors are placed.

In order to improve the long-term stability of the temperature regulation and to remove large temperature gradients, a new configuration has been tested in preparation of the next generation of BAMs. The adapted set-up has been measured under laboratory conditions as well as in a climatic

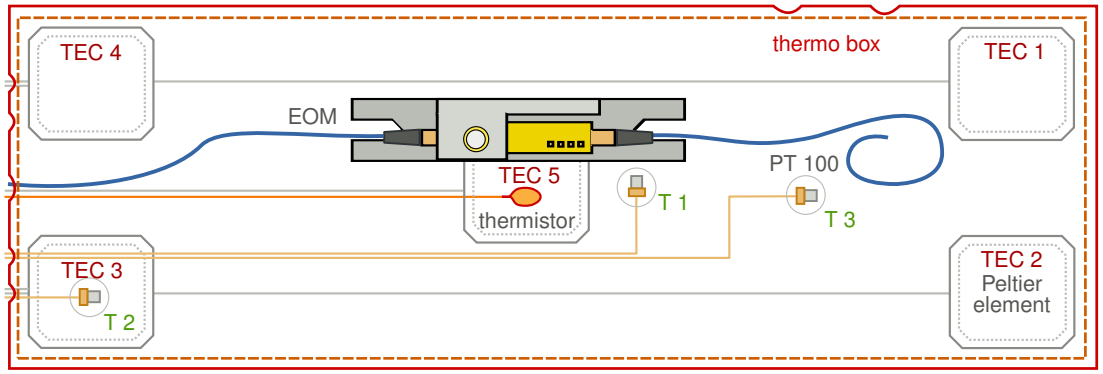

Figure 3.17: Setup used for tests of the temperature regulation. An isolating plastic housing with an Aluminium plate as under floor. Underneath five Peltier elements (TEC 1 to 5) are mounted symmetrically, driven by a commercial temperature-regulator (not shown here). The control variable is the temperature measured by a thermistor (directly above TEC 5, middle). Three temperature sensors (PT100) named with T1 to T3, inside of the thermo box are used for a long-term monitoring. One additional PT100 sensor (T4 - not shown here) is mounted outside of the thermo box but still within the BAM box volume. It measures the air temperature in 10 mm height above the base plate. The sensors T2 and T3 are mounted directly to the Aluminium plate, while the sensor T1 is arranged 30 mm above the ground plate in air, next to the EOM mount. For simplicity only one of the two EOMs are shown here. It is fastened upright to an Aluminium holder.

Table 3.1: Proportional gain settings of thermal regulator board: PTC10K-CH.

resistance [kΩ]	P_{GAIN}
58	10.0
84	14.6
113	19.8
144	25.0
169	29.4
196	34.3
219	38.2

chamber to simulate the conditions inside of the FLASH tunnel. A schematic of the test set-up is shown in figure 3.16. Underneath the base plate of the BAM box, which is made from hard plastics, several heat sinks are mounted in line with a ventilator. In the illustration, the heat sinks are shown on both sides of the ventilator for better visibility. The area inside of the BAM chassis, which should be stabilised in temperature, is enclosed within an extra box to delimit this region from the rest of the inner air volume. The thermo box is located directly on the base plate, such that the length of the heat bridges for the currently five PELTIER elements is as short as possible. A heating of the base plate is suppressed by use of hard plastic instead of metal. The housing of the thermo box is made from a the same type of hard plastic as used for the ground plate of the BAM chassis. Additionally, a soft, foamed plastic with a low heat conductance is wrapped around the sides and on top of the thermo box. The efficiency of the PELTIER elements will be increased distinctly through the constant air flow underneath the box. The commercial temperature controller "PTC10K-CH" (see fig. 3.16) from *Wavelength Electronics Inc.* has three inputs and two outputs. The inputs are:

1. controlling element, in this case a 10 kΩ thermistor
2. external on/off control by applying a DC-voltage, done with a DAC
3. external setting of the temperature set-point, done with a DAC
4. power supply with up to +15 V at maximum 10 A

The outputs connect to:

1. actuators, in this case five PELTIER elements (also named thermo-electric cooler (TEC)) connected in series
2. external read-out of the actual value of temperature set-point, read out by an ADC

To monitor the performance of the temperature regulation, four temperature sensors (PT100) are installed inside of the BAM box. They are read out remotely by use of commercial electronic boards from the company *Beckhoff*.

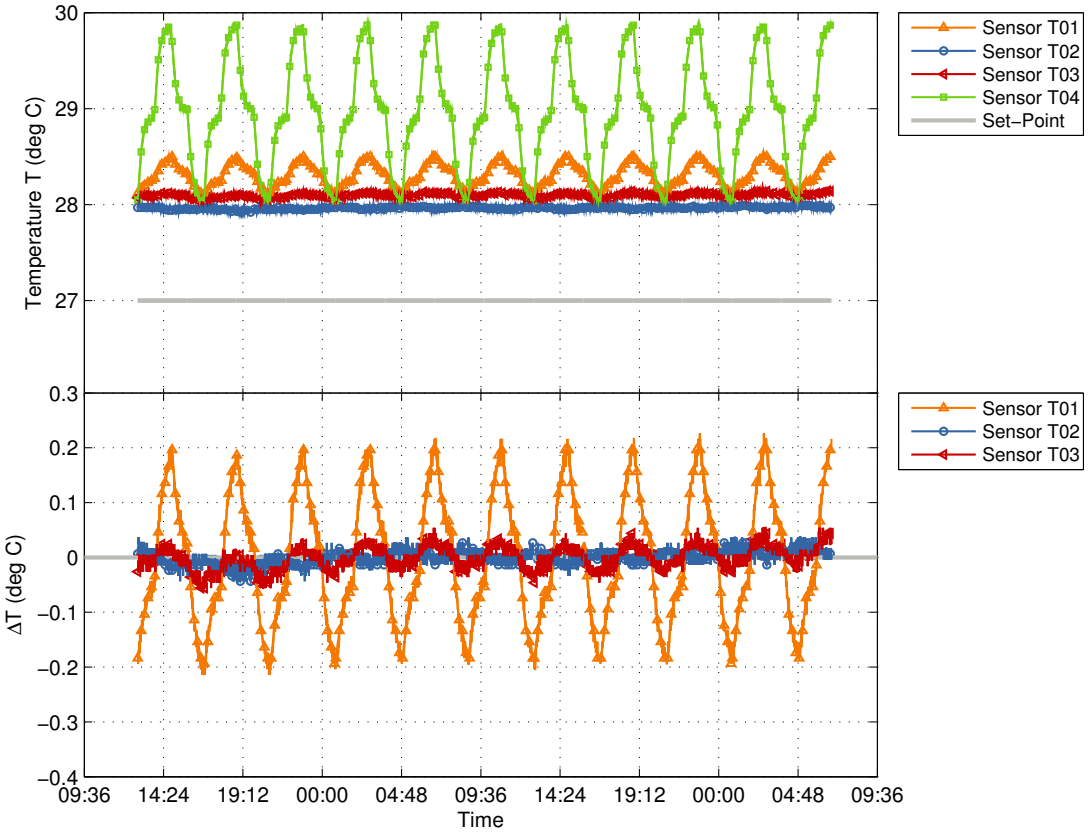

Figure 3.18: Test No. 1: A temperature change of 2 K (peak-to-peak) with a period of 200 min, during 35 hours.

Figure 3.17 shows a detailed schematic of the thermo box, illustrating the configuration of all required components. The thermo box comprises a thin Aluminium base plate, underneath which the five Peltier elements are mounted symmetrically (denoted by dashed lines). On the top of the base plate, the thermistor is mounted directly above the central TEC. One of the two EOMs is shown, mounted on a special metallic holder. Three of the four temperature sensors are mounted inside of the thermo box:

- T1: next to the EOM in air, approximately 30 mm above the base plate
- T2: in the lower left corner, directly above TEC 3 with contact to the metal
- T3: centred between the three Peltier elements on the right hand side with contact to the metallic plate
- T4: outside of the thermo box, but within the BAM box in air, approximately 10 mm above the ground plate (not shown in the illustration)

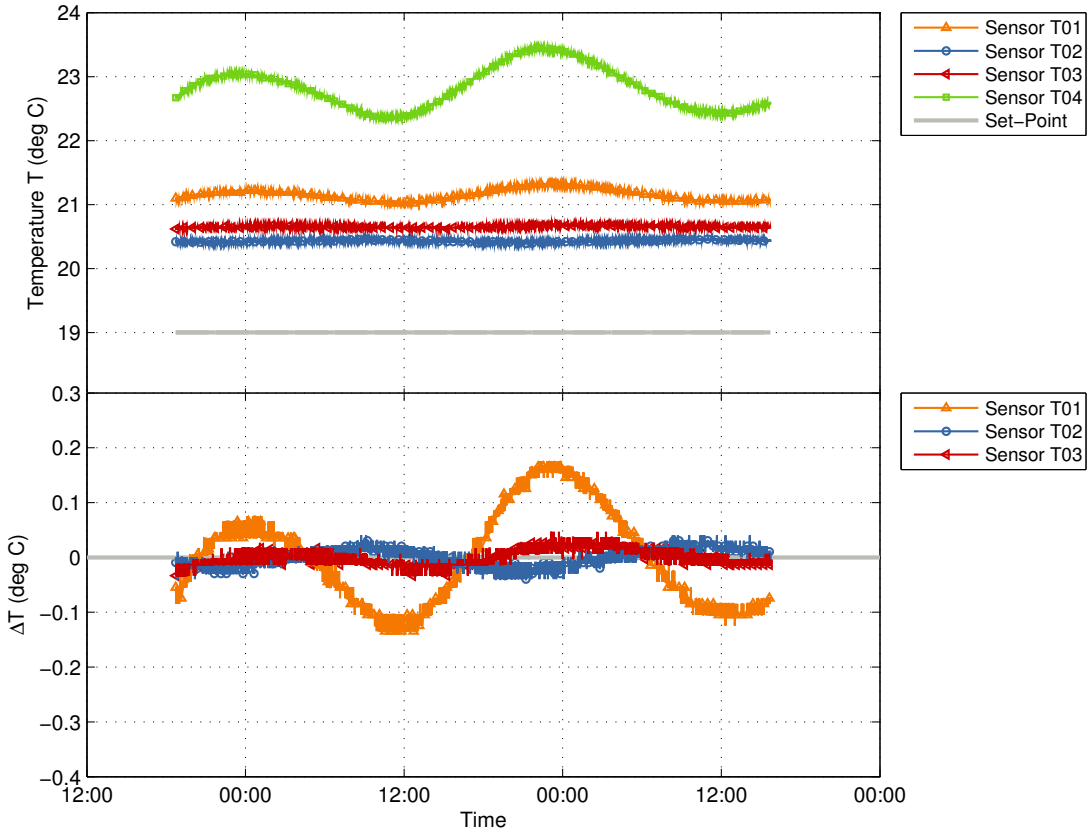

Figure 3.19: Test No. 2: A temperature change of 1 K (peak-to-peak) with a period of 24 h, during 2 days.

The P-gain of the commercial controller cannot be set remotely, but can only be adjusted with a set-screw of a potentiometer on the electronics board. When measuring the resistance R_{TP} between two test points TP1 and TP2 the actual P-gain value can be calculated by use of a formula as given in the data-sheet [Web11f]:

$$P_{\mathrm{GAIN}} = \frac{R_{\mathrm{TP}}}{R} \cdot G \tag{3.5}$$

with an internal resistance of $R = 7\,\mathrm{k\Omega}$ and a model-dependent parameter $G = 1$. The integrator gain has a fixed value of 1.8 A/Vs. The default setting of the P_{GAIN} is 12, which is designed to optimise 90 % of the load. Several tests have been made, to find the ideal setting for the described thermo-box design. Table 3.1 gives an overview on the different P-gain values. In the following two of the measurements performed are shortly described. In both cases, P_{GAIN} had been set to 30. In the first example the temperature inside of the climatic chamber has been varied periodically ranging from 28 and 30 °C, in steps of 1 K and with a very short period of 3.33 h. The temperature of the thermo box was regulated to a set-point of 27 °C, i.e. 2 K below the average ambient temperature. This scenario is extremely exaggerated, although the temperature gradient fits to the situation of a maintenance day

at FLASH. The fast variation of the ambient temperature was meant to benchmark the stability of the regulation, and to try if the controller starts to oscillate.

Figure 3.18 shows the measured temperature during 35 hours of operation. The temperature sensor T4, outside of the thermo box, resembles the set-point curve of the climatic chamber. Thus, the inner air volume of the BAM box follows the ambient temperature nearly without time lag. The most important value as a measure of the temperature stability is sensor No. T2, since it directly measures the behaviour of one of the Peltier elements. Temperature sensor T3 shows the stability of the Aluminium base plate, on which the fibre-optical components will be mounted. Despite the rapid and strong variation of the outer temperature, the controller maintains a stable operation. The achieved mean and RMS temperatures inside of the thermo box are listed in table 3.2. The RMS variations have also been calculated in a moving window of 1 h, the corresponding maximum and minimum values are given here.

Table 3.2: Overview of the achieved mean and RMS temperatures inside of the thermo box.
Test No. 1: A temperature change of 2 K (peak-to-peak) with a period of 200 min, during 35 hours.
Test No. 2: A temperature change of 1 K (peak-to-peak) with a period of 24 h, during 2 days.

sensor No.	Pk-Pk [K]	Mean [°C]	max. RMS [K]	min. RMS [K]
Test No. 1:				
T1	0.440	28.304	0.118	0.108
T2	0.080	27.963	0.014	0.008
T3	0.110	28.096	0.020	0.013
Test No. 2:				
T1	0.310	21.155	0.030	0.008
T2	0.080	20.429	0.010	0.006
T3	0.080	20.653	0.010	0.005

In the second example, the long-term stability of the temperature regulation has been tested for the case of only small and slow variations. The set-point of the climatic chamber has been varied by 1 K (peak-to-peak), between 22 and 23 °C, with a period of 24 h during two days. The set-point of the temperature stabilisation has been chosen to be 3.5 K below the average temperature of the climatic chamber. Figure 3.19 shows the measured temperature during 48 hours of operation. The controller reacted relative weakly at the set P-gain of 30, thus all temperature sensors inside of the thermo box slightly followed the ambient temperature. Nevertheless, very good RMS stabilities of below 10 mK have been reached for the temperature sensors T2 and T3, compare table 3.2.

Electro-optics

Another consideration concerns the electro-optic modulators. The currently used, commercial devices deliver only one output signal. In principle, it is possible to order EOMs which have an additional output, thus providing two, complementary signals. Though, only one of those is required for a determination of the amplitude modulation rate, the second signal could be used for an on-line

monitoring of the momentary modulation depth η, influenced by the transmission at zero RF voltage. The latter set-point is controlled by a DC bias voltage, which might drift over time. An adjustment of the DC voltage might also be required if the optical power level at the input of the modulator is changed. Thus, the signal from a second output of the modulator can be implemented in a feedback loop, which controls the bias voltage. The comparison between both complementary signals would also allow for a direct measurement of the maximum modulation depth $\eta_{\max}$ of the EOM, compare section B.2.4 in the appendix for details.

Electronics

The read-out electronics, especially the advanced carrier board (ACB), have been subject to a continuous development over the last few years. Changes have been applied, in order reduce the electronic noise and to achieve an enhanced shaping of the pulses from the photodiodes (PDs). Nevertheless, there are some critical points, which deteriorate the determination of the amplitude modulation of laser pulses coming from the EOMs. In fact, permanent and temporary deficiencies of the electronics are a main contribution to an impaired performance of the BAMs.

A major complication results from the fact, that the ADCs have a maximum sampling rate of 130 MHz, while the optical laser pulse train has a repetition rate of 216 MHz. Thus, only every second laser pulse can be sampled. To achieve an inherent synchronisation between both, the fine and coarse channel signals, a local clock for the ADCs is generated from an optical signal. For this purpose, a fraction of the optical power is split off in the fibre-optics of the BAM before the laser pulses are divided into fine and coarse channel, where they are used for sampling the RF signal within the EOMs.

But the advantage of generating an inherently synchronised, local clock signal is constrained by an essential requirement in the current electronics: It is demanded to provide the correct bucket of the clock signal at a frequency of 108 MHz. For this purpose, the initial signal of 216 MHz, which is generated from the optical pulse train by use of a commercial clock buffer chip, has to be divided by two. The divider chip delivers a signal at 108 MHz, whose phase relation to the input frequency can take two values, i.e. it can be synchronous to either of both buckets. This phase relation is not fixed in the hardware, but depends on the initial state of the chip when the electronics are (re)started. This generates an uncertainty, which demands the resynchronisation of the clock signal to the external machine trigger. Only then, it can be guaranteed, that the ADCs sample the correct modulated laser pulses, which contain the arrival time information of the electron bunches. Unfortunately, the resynchronisation process is very sensitive to external influences on the current electronics, like variations in the optical power of the clock signal, EMI from surrounding electronics, electronic noise added from the internal electronics and too large timing jitter of the trigger signal. All of those factors lead to irregular, but partly often jumps in either the trigger signal or the clock signal or both. Those jumps can be detected and removed easily for the moment, but require the experience and attendance of an expert. The frequency, with which those electronic failures occur has been reduced enormously during the last year of BAM operation. The down-time of the monitors amounts to roughly 30 %, for a nearly permanent operation in 2010 and 2011. Nevertheless, most of the problems have been related to the mentioned electronic constraints. A detailed description of the present ACB electronics can be found in [GBF+10b, GBF+10a].

In the near future, an essential and promising improvement will be the use of faster ADCs. This is connected to the on-going developments for a transition from the currently employed Versa Module Eurocard (VME) systems to a Micro Telecommunications Computing Architecture (uTCA) system. Besides the avoidance of a clock resynchronisation, the implementation of faster ADCs which can sample the laser pulse train with 216 MHz, offers the possibility of detecting both, the modulated and unmodulated laser pulse amplitudes, with only a single ADC. Both signals are required for the calculation of amplitude modulation, which provides a high-pass characteristic in the sampling scheme. This is explained in detail at the beginning of this chapter, in section 3.1.1, on page 3.1.1 ff.

4 Bunch Arrival Time Monitors ▸ Performance

Contents

4.1 Commissioning

BAM signal scan

An important feature required for the long-term operation of the BAMs is the possibility to inspect the shape of the BAM signal, i.e. the curve of laser amplitude modulation A_{norm} in dependence of the relative timing between the optical and the RF signal.

There are two strategies, to perform such a timing scan:

- locally, for each BAM individually, by use of the internal, motorised optical delay line
- globally, by shifting the timing of the optical reference for all links at once

The latter method is applied by use of a vector modulator (VM), which is interconnected in the RF-lock loop of the master laser oscillator (MLO). It is used to rotate the phase of the 1.3 GHz line from the RF frequency comb, which is generated out of the laser pulse train. To recall, the fundamental repetition rate of the master laser oscillator is 216.67 MHz, thus the sixth harmonic has a frequency of 1.3 GHz. By rotating the phase of this harmonic six times by 360 deg, shifts the phase of the 216.67 MHz line simultaneously by one bucket. Therefore, when scanning the VM settings and monitoring the BAM signals, one can easily check, if the 108 MHz ADCs of all BAMs are clocked in the correct 216 MHz bucket. The technical background of this is explained in section 3.1.1, page 68 f., and more detailed in section 3.2.1 on page 83 f.

The laser phase-shift supported BAM-signal scan has a big advantage, but there is also one critical restriction. Due to the fact that when rotating the phase of the MLO the laser pulse timing at each link ending will change, not only at the BAMs, this method can only be chosen at dedicated maintenance times of the LbSyn-system. The advantage and indispensable prerequisite, on the other hand, is to make sure, that all BAM signals from every monitor in both channels, *fine* and *coarse*, are aligned at

the same reference timing (reference RF phase) of the master laser oscillator. This is necessary, since any timing offsets of the laser pulses at the position of the EOMs in each BAM can be corrected locally, i.e. by use of the motorised ODLs, only in the range of a few ten picoseconds. Any larger offsets can be compensated by adjusting the RF cable lengths between pick-up and the according EOM. This strategy, however, is not advisable for high-bandwidth RF signals, to avoid signal distortions and attenuation. The alternative, is to adjust the absolute timing of the link pulses by introducing additional optical delays in front of the individual boxes, hence changing the path length of the laser pulses between the MLO and BAM-box.

Figure 4.1 shows an example of a VM-supported BAM-signal scan. All *fine* and *coarse* channel signals from all of the four BAMs are plotted. The correct and expected signal shape is explained in section 3.1.1, pg. 68 f. In this illustration however, it can be seen, that the signals from BAM No.1, 2 and 4 are all visible and aligned at the same reference phase of 150 deg. At this phase setting, the operation points of all three BAMs are overlapping. The correct operation point is the intersection of the modulated amplitude with 1 on the first steep slope, when following the signal shape beginning at the right hand side. Only BAM No. 3, i.e. BAM.4DBC3, is not operated correctly. Its *coarse* signal is constant and $A_{\mathrm{norm}} = 1$, while the *fine* signal is shifted by +30 deg. The fact, that the *coarse* channel signal is not visible in this scan, was caused by a wrong sampling point in the ADC. It was shifted such, that only the baseline signal has been measured. The latter has to be equal to 1, since the baseline is given by the unmodulated laser pulses. The timing shift, which has been measured in terms of degrees at a phase of 1.3 GHz, can be converted to units of time, by use of the relation

$$\frac{1}{360\,[\mathrm{deg}]\cdot 1.3\,[\mathrm{GHz}]} \equiv \frac{2.1368\,[\mathrm{ps}]}{\delta\Phi\,[\mathrm{deg}]} \tag{4.1}$$

Thus, the timing difference has been

$$\Delta t_{\mathrm{BAM3}} \approx 64.2\,\mathrm{ps} \tag{4.2}$$

This corresponds to a required adjustment of the motorised optical delay line ODL1 of:

$$\Delta z_{\mathrm{BAM3}} = -19.3\,\mathrm{mm} \tag{4.3}$$

Figure 4.2 shows a repetition of the BAM-signal scan, with the adjusted timing for BAM No. 3 applied. Both presented signal scans have been performed at a relatively large bunch charge of 0.78 nC.

For comparison, in figure 4.3, a BAM-signal scan at a much lower bunch charge of 0.25 nC is shown. Here, the peak-to-peak signal height of the RF signal is strongly reduced, i.e. the magnitude of the modulation voltage is decreased. When comparing the *fine* signals, the difference is clearly visible, since the *overrotation* in the EOM is significantly reduced, see figure 4.1 and 4.3. Nevertheless, the steepness of the slope around the operation points is nearly unchanged. This already allows to assume, that the resolution of the BAM changes only slightly with a reduction of the bunch charge in a region between the two mentioned charge settings.

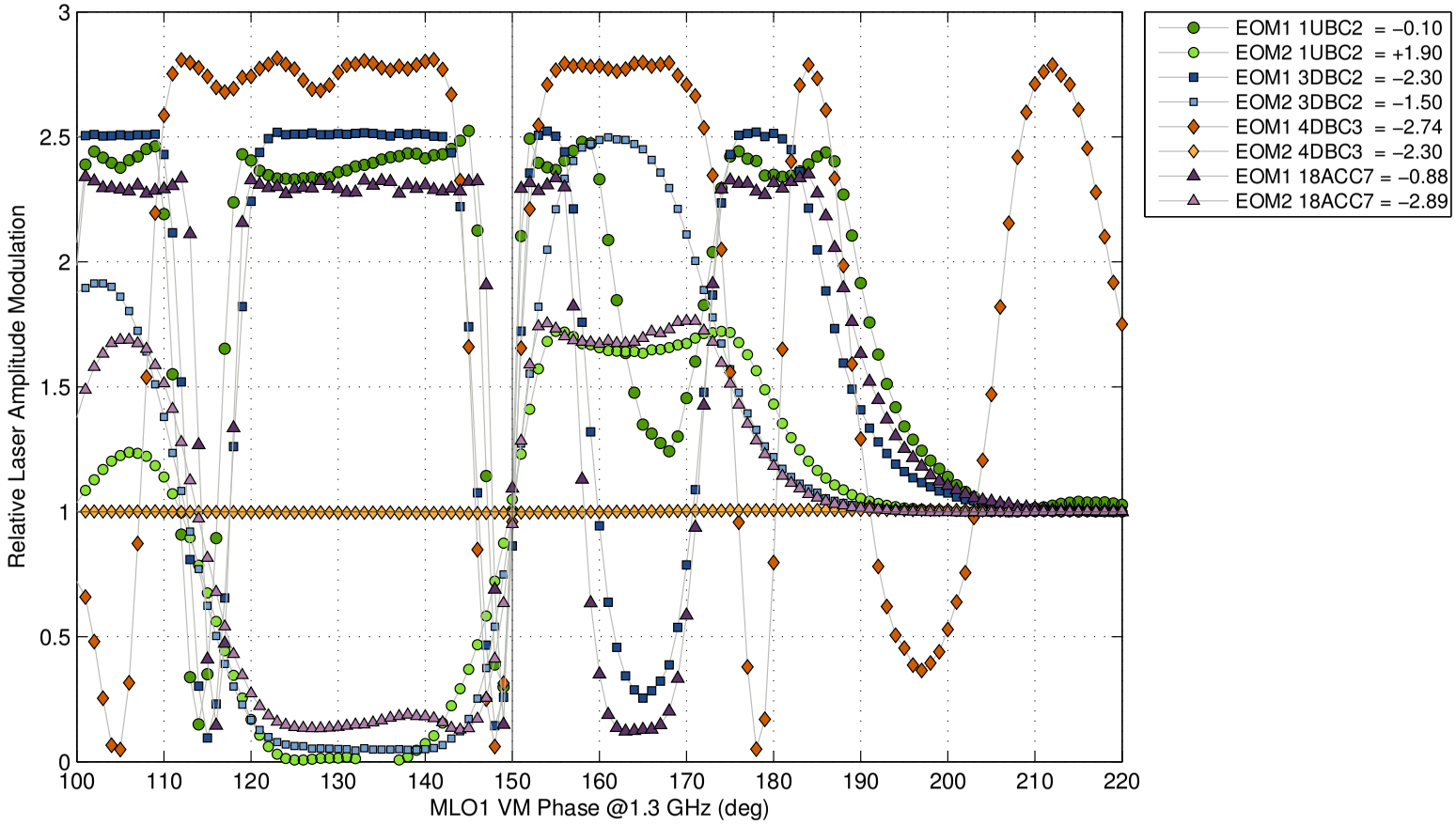

Figure 4.1: Signal scan of all BAMs at a bunch charge of 0.78 nC. The timing of the laser pulses has been changed globally, by shifting the phase of the MLO at 1.3 GHz (RF). In this case, all BAMs have been operational, except for BAM.4DBC3. The operation point of the latter monitor has an offset of +30 deg (at 1.3 GHz), according to −62 ps. By adjusting the optical delay line of this BAM, the signal can be optimised to be aligned with the signals from the other monitors. The *coarse* signal of BAM.4DBC3 is constant in this scan, due to a wrong sampling point in the ADC.

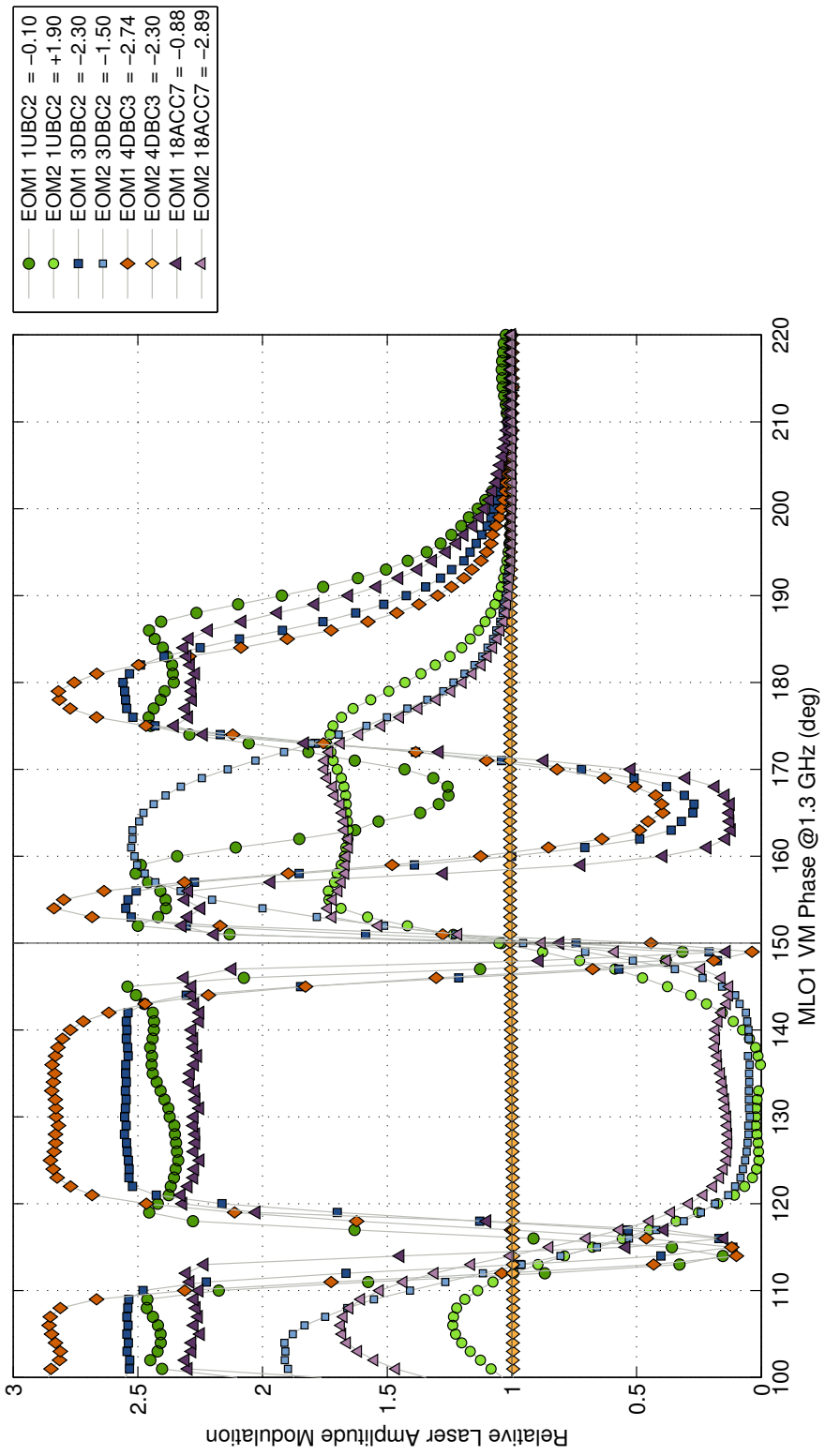

Figure 4.2: Repeated signal scan of all BAMs at a bunch charge of 0.78 nC, after the timing adjustment of the ODL in BAM.4DBC3; the according *coarse* channel is still at a wrong sampling point.

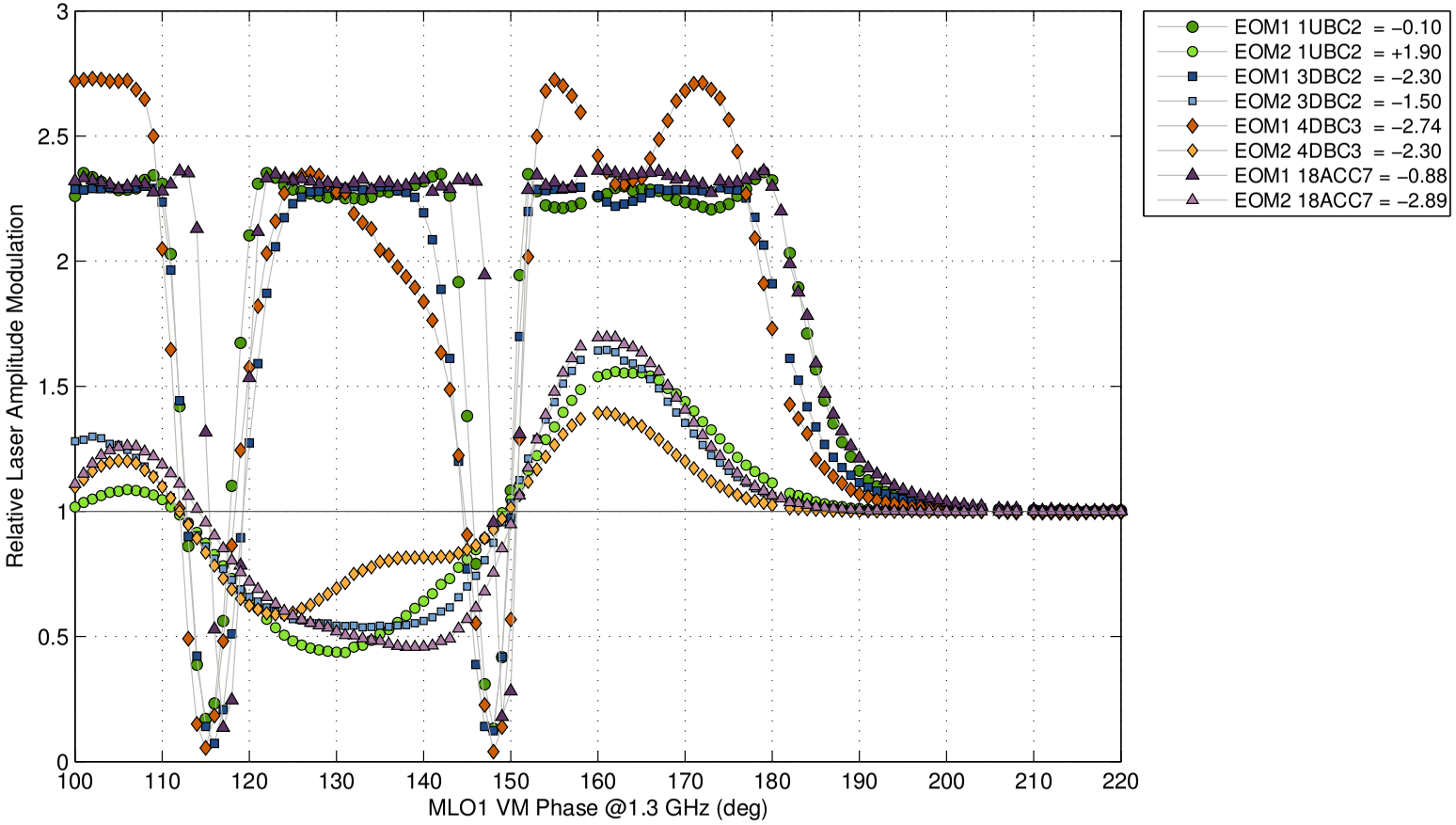

Figure 4.3: Signal scan of all BAMs at a bunch charge of 0.25 nC. Here the operation points of all BAMs are aligned at the same reference phase. Compared to the signal scan at a higher bunch charge (fig. 4.2), the *over-rotation* in the EOMs is reduced (*fine* channel) or even avoided (*coarse* channel), due to the lower RF modulation voltage.

EOM voltage scan

One critical parameter for an optimisation of the BAM signal shape is the applied EOM bias voltage V_{bias}. By choosing a specific DC voltage set-point, the transmission of the EOM at zero modulation voltage can be adjusted. This in turn influences the achieved modulation range of the calculated, normalised amplitudes A_{norm}. For example: the measured modulation of the *fine* channel in BAM.4DBC3, as shown in figure 4.3, ranges between 0.05 and 2.7, which is nearly optimal. The linear range from the reference point at $A_{\text{norm}} = 1$ upwards is more than twice as large as the linear range downwards in direction of decreasing modulation. The normalised amplitude can of course vary only between 0 and 1, due to the cosine-shaped transmission curve, as described in section 3.1.1.

In terms of arrival time changes, this means: electron bunches, which arrive early at the pick-up, i.e. for modulation voltages $V_{\text{mod}} < 0$, the linear measurement range can be enlarged by carefully choosing the zero-signal transmission set-point of the EOM; it is recommendable to not choose 50 % , but rather 30 % zero-signal transmission.

As explained earlier, the BAM is kept automatically at its operation point around $V_{\text{mod}} = 0$ by applying a feedback on the position of the motorised delay stage ODL1. The preceding discussion shows, that this feedback needs to react already at small deviations from the reference arrival time for those electron bunches which arrive late at the pick-up, i.e. for $|A_{\text{norm}} < 1|$. Otherwise, the arrival time measurement would slip directly into the non-linear region of the transmission curve. In fact, this can happen, if the internal settings for the feedback are not set correctly, or if the proportional gain of the feedback is too low.

The optimum DC bias voltage is not the same for all EOMs, because the transmission at zero bias voltage and zero modulation voltage is device-specific and related to the production process. On the other hand, the criterion for optimising V_{bias} is actually independent of the optical power levels. As explained above V_{bias} has to be chosen such, that the modulation range of the normalised signal A_{norm} meets two conditions simultaneously:

- the modulation for $V_{\text{mod}} > 0$ has to reach down closest possible to 0
- the modulation for $V_{\text{mod}} < 0$ has to reach up to at least 2.0

In conjunction with the adjustment of V_{bias}, the internal clock settings of the ACB optionally have to be adjusted to assure that all four ADCs sample the laser pulses at their peaks for optimum signal quality. Figure 4.4 shows the results from bias voltage scans in both channels of all BAMs. In this case, not the normalised but the real amplitudes A are plotted, which are calculated by subtracting the baseline from the (modulated) signal, according to equation 3.2 on page 70. The real amplitudes are given in units of ADC bits, and their values depend on the actual optical power levels of the EOM inputs. This illustration has been chosen, to show, that the available power levels differ strongly for the various BAMs. BAM.4DBC3 has the lowest ADC level, whereas the input signal in the *fine* channel of BAM.1UBC2 is large enough to saturate the ADC, which has a range of ±1 V corresponding to roughly 0 to 1 mW optical power on the photodiodes (PDs). A decreased optical power level leads to a decreased level of saturation in the ADCs, which in turn deteriorates the SNR. On the other hand, the total saturation of the ADC could lead to a limitation of the maximum normalised amplitude to a value lower than 2, which is not favourable. The yellow dots indicate the momentary operation points of the according EOMs.

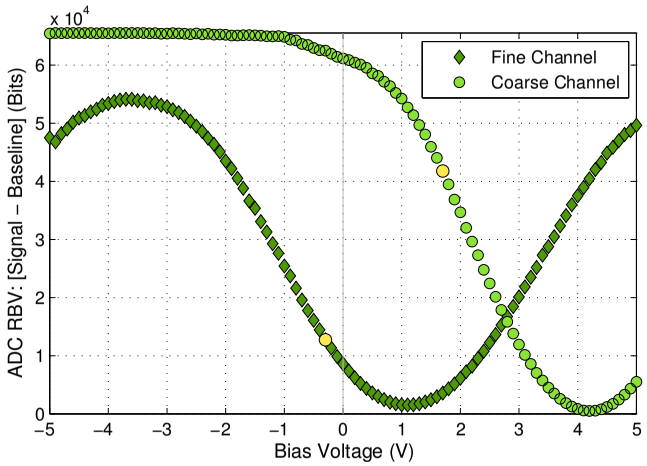

(a) BAM.1UBC2

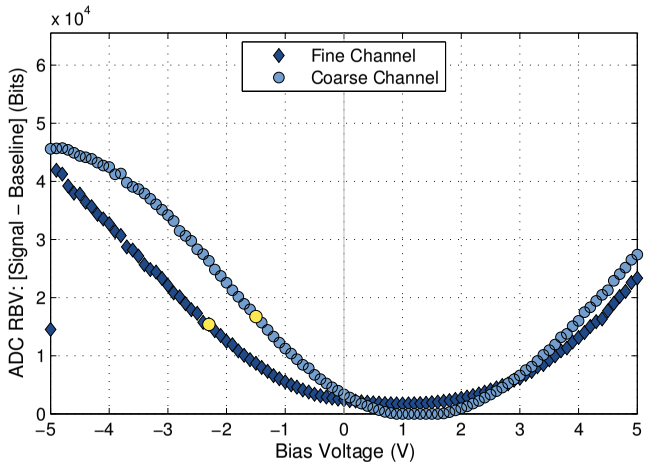

(b) BAM.3DBC2

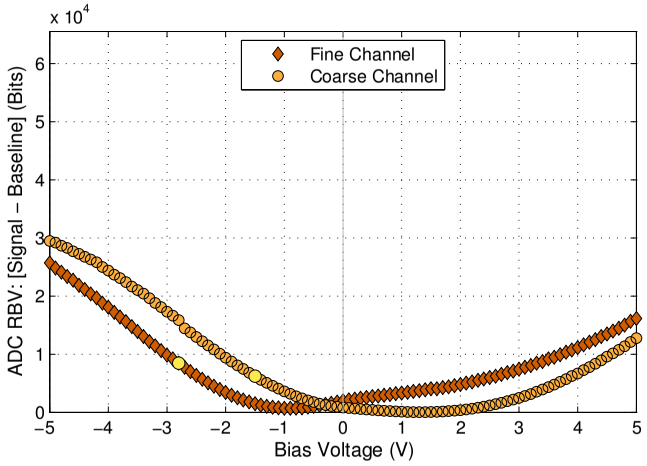

(c) BAM.4DBC3

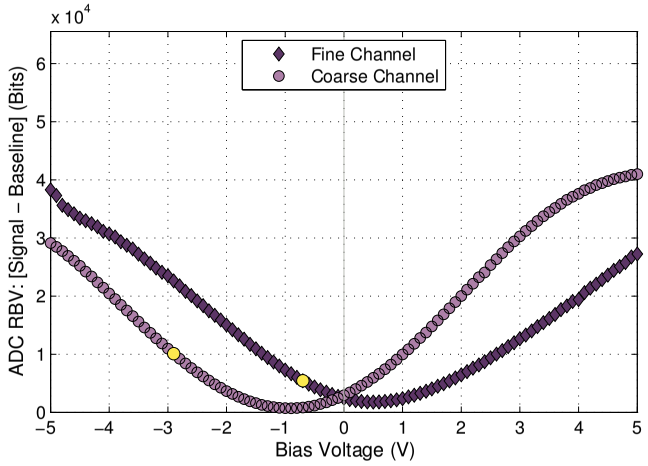

(d) BAM.18ACC7

Figure 4.4: Bias voltage scans for both channels, i.e. *fine* and *coarse*, in all BAMs. The yellow dots indicate the actual bias voltage settings at the time of the measurement. The scans show the fact, that the optical power levels are very different for the various BAMs.

4.2 Performance Studies

In this section the results of two relevant performance studies are shortly discussed. In one of those studies, the charge dependency of the calibration constant, i.e. the sensitivity, of the arrival time measurement has been investigated systematically. In this connection, first the calibration process is briefly described, followed by a discussion of the results. Those measurements delivered valuable information for an on-going redesign of the RF front-end of the BAM system.

The second performance study concentrates on deviations in the determined arrival time due to orbit changes of the electron bunches at the locations of the bunch arrival time monitors. The orbit dependency a quadratic effect for small deviations through combination of the signals from opposing pick-up antennas. This second order effect is expected and can be partly explained from actual path length changes due to deviations from the design orbit. Nevertheless, for large orbit deviations the observed orbit dependence is actually much larger than expected; it seems to be a residual error caused by components in the RF front-end. Subsequent to the discussion of the measurement results, the possible compensation of any orbit-dependent errors through an appropriate algorithm in the BAM server is presented.

4.2.1 Charge Dependency

Before discussing the results from the performance study, the calibration routine, as implemented in the BAM server, is briefly described. The goal of the calibration is to calculate the relation between the normalised amplitude modulation and small arrival time changes within the linear region around the normal operation point at $A_{\mathrm{norm},i} = 1$, using the definition from equation 3.3, pg. 70. In other words, the calibration detects the linear response, i.e. sensitivity, of the monitor to small changes in the electron bunch arrival time, which shift the RF voltage signal back and forth in a narrow temporal region around the reference arrival time.

During the calibration procedure, one assumes in first approximation, that the electron bunch timing is stable. The required timing shift between the RF signal and the laser pulses is accomplished by shifting the laser pulse timing in small steps within a narrow range in the order of ±500 fs, by use of the optical delay line (ODL), i.e. ODL1 according to figure 3.5, pg. 74. The position change of the motorised stage is tracked with high-resolution by use of an absolute position encoder. This value can then be converted into the corresponding change in timing delay, by

$$\Delta t_{\mathrm{delay}} = \frac{c_0}{n_{\mathrm{air}}} \cdot \Delta z \tag{4.4}$$

When approximating the refractive index of air, n_{air} with 1.0, it follows:

$$\Delta t_{\mathrm{delay}}\,[\mathrm{fs}] \approx 3.33\,[\mathrm{fs}/\mu\mathrm{m}] \cdot \Delta z\,[\mu\mathrm{m}] \tag{4.5}$$

Since the electron bunch arrival time jitters by typically several tens of femtoseconds, the measured amplitudes $A_{\mathrm{norm},i}$ at each scan step are averaged over 20 successive pulses. The calibration constant, in terms of [fs/%(modulation)], is then given by the slope of a linear fit of the measured data. Since the calibration procedure is automated, it required a thorough exception handling. Especially, the setting of a false calibration constant in the BAM server has to be circumvented. The linear data

fitting has to take into account, that the variances in both measured signals contribute to the estimated error. The signal variances result not only from arrival time jitter of the electron bunches, which is the largest contribution, but also from detection errors in the $A_{\mathrm{norm},i}$ values due to amplitude noise in the ADCs. Because of those restrictions, Patrick Gessler has implemented an upgraded calibration algorithm in the BAM server, which calculates the confidence level for the actual calibration constant and compares the latter to previously determined values. This is described in detail, in [GBF+10a] The knowledge of both, the calibration constant C_{calib} and the amplitude noise $A_{\mathrm{noise},j}$ as detected from the ADC read-out values, allows for calculating the momentary resolution $\mathcal{T}_{\mathrm{Res}}$ of the arrival time measurement:

$$\mathcal{T}_{\mathrm{Res},j}[\mathrm{fs}] = -C_{\mathrm{calib}}[\mathrm{fs}/\%\,\mathrm{mod.}] \cdot A_{\mathrm{noise},j}[\%] \tag{4.6}$$

for each macro pulses j.

The systematic study of the charge dependence has been performed during a single bunch operation. The bunch charge has been changed from 1 nC to 0.05 nC in small steps of 0.05 nC. Any phases or gradients in the RF modules have been adjusted a little for the different bunch charges, to guarantee a good transmission through the linac. Therefore, the electron bunch arrival times varied with the bunch charge, but those timing changes were slow enough for the internal *fine* channel motor-feedback to follow. Thus, all of the BAMs have been kept automatically at their correct operation point, i.e. at the zero crossing of the RF voltage signal.

Figure 4.5 shows the measured $C_{\mathrm{calib},n}$ values averaged over ten successive calibrations at each charge set-point. As can be seen from this, C_{calib} depends only weakly linearly on the bunch charge above 0.2 nC. In contrast to this, from a specific bunch charge downwards the calibration shows a strong linear decrease. BAM No.1 to No.3 behave similarly, as expected. The deviations between those curves do not necessarily indicate a difference in the RF pick-up performance. Since the signal optimisation in the BAM electronics depends on many properties. The small deviations in the measured calibration constants are likely to be related to the individual settings, like the EOM bias voltages. In contrast to this, the determined, absolute values of C_{calib} for BAM.18ACC7 are systematically and significantly smaller compared to the other three BAMs. This behaviour is most probably caused by an utterly better performance and signal quality from the according RF pick-up and the RF cables.

To summarise, the currently installed bunch arrival time monitors are capable of measuring the arrival time at bunch charges as low as 50 pC, but with limited performance. On the other hand, a resolution of less than 10fs is achieved for bunch charges higher than 200pC. The deterioration of the measured resolution $\mathcal{T}_{\mathrm{Res}}$ at small bunch charges is a combination of several effects. For decreasing bunch charges the peak-to-peak height of the RF signal decreases. In parallel, the longitudinal dimension of the bunches shortens. Thus, it is required to pick-up a larger bandwidth of RF frequencies in the antenna, to generate a bipolar voltage signal with a reasonably steep slope. The latter limits the maximum achievable resolution in the detection process.

The electrical field strength of a bunch scales linear with the bunch charge, hence, with the number of electrons. Therefore, one expects the strength of the induced pick-up signal to scale linearly with the bunch charge. The peak-to-peak height as well as the slope steepness of the bipolar voltage signal would increase proportional to the charge. The same behaviour would be expected for the

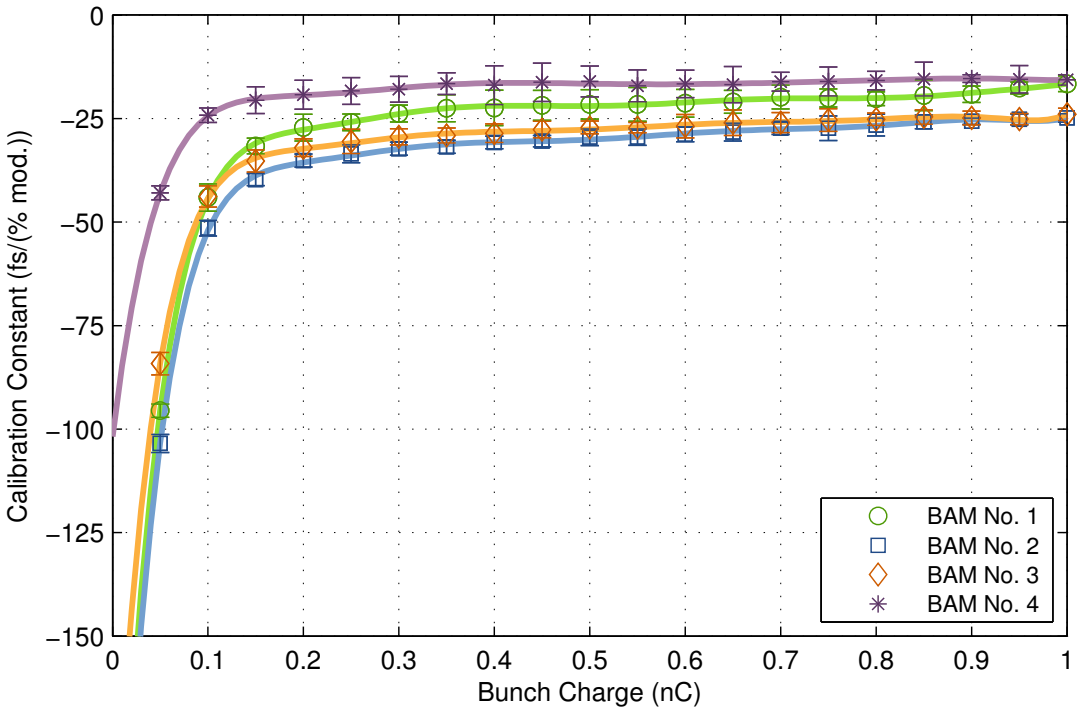

Figure 4.5: Calibration constants C_{calib} as function of the bunch charge, measured for all of the four bunch arrival time monitors: BAM.1UBC2 (green circles), BAM.3DBC2 (blue squares), BAM.4DBC3 (orange diamonds) and BAM.18ACC7 (violet asteriks)

resolution of the *fine* channel signal.

As the measurement showed, this is only true for low bunch charges, where indeed a proportional behaviour is indicated for bunch charges lower than 100 pC, compare fig. 4.5. But beyond the transition region between 0.1 nC and 0.25 nC, the linear dependence is nearly completely suppressed, showing only a slight correlation between bunch charge and slope steepness, the latter being represented by the calibration constants. Most probably, this behaviour is caused by the finite bandwidth of the RF power limiter[1]. This device is interconnected between the RF combiner and the *fine* channel EOM. Its purpose is to limit the RF power with a 1 dB compression point of 27 dBm; thus, the RF peak voltages are limited to about ±5 V, to avoid a damage of the EO-modulator. The power limiting is achieved by simply clipping the bipolar voltage signal, producing sharp edges and a rectangular signal. The high-frequency parts of the clipped signal are not transmitted through the limiter, since its bandwidth has been measured to be smaller than 26 GHz [Pen11]. The bandwidth limitation scales the slope steepness of the RF signal down. Thus, for different bunch charges above a certain threshold, the transmitted bipolar signal has a comparable, slightly varying slope steepness. Therefore, the correlation between bunch charge and calibration constant is nearly compensated.

This might appear as disadvantage, since a higher bunch charge does not result in a higher resolution. Although, the described bandwidth limitation of the RF signal, can also be used to the advantage

[1] Agilent N9356C

Table 4.1: Charge dependency of calibration constant as measured for BAM 3DBC2. Exemplarily, the intrinsic resolution of this BAMs is calculated for three different and typical values of RMS amplitude noise of the unmodulated laser pulses.

		amp.noise = 0.45 %	amp.noise = 0.3%	amp.noise = 0.2%
charge	calib. const.	resolution	resolution	resolution
[nC]	[fs/%]	[fs]	[fs]	[fs]
0.05	−103.46	46.56	31.04	20.69
0.10	−51.47	23.16	15.44	10.29
0.15	−39.76	17.89	11.93	7.95
0.20	−35.16	15.82	10.55	7.03
0.25	−33.52	15.08	10.06	6.70
0.30	−32.29	14.53	9.69	6.46
0.35	−31.81	14.31	9.54	6.36
0.40	−30.76	13.84	9.23	6.15
0.45	−30.45	13.70	9.14	6.09
0.50	−29.51	13.28	8.85	5.90
0.55	−29.49	13.27	8.85	5.90
0.60	−28.80	12.96	8.64	5.76
0.65	−28.28	12.73	8.48	5.66
0.70	−27.36	12.31	8.21	5.47
0.75	−27.32	12.29	8.20	5.46
0.80	−26.59	11.96	7.98	5.32
0.85	−25.78	11.60	7.73	5.16
0.90	−25.66	11.55	7.70	5.13
0.95	−25.20	11.34	7.56	5.04
1.00	−24.85	11.18	7.46	4.97

Table 4.2: Charge dependency of calibration constant as measured for BAM 18ACC7. Exemplarily, the intrinsic resolution of this BAMs is calculated for three different and typical values of RMS amplitude noise of the unmodulated laser pulses.

		amp.noise = 0.45 %	amp.noise = 0.3%	amp.noise = 0.2%
charge	calib. const.	resolution	resolution	resolution
[nC]	[fs/%]	[fs]	[fs]	[fs]
0.05	−42.94	19.32	12.88	8.59
0.10	−24.21	10.90	7.26	4.84
0.15	−20.56	9.25	6.17	4.11
0.20	−19.24	8.66	5.77	3.85
0.25	−18.34	8.25	5.50	3.67
0.30	−17.93	8.07	5.38	3.59
0.35	−16.58	7.46	4.97	3.32
0.40	−16.94	7.62	5.08	3.39
0.45	−16.24	7.31	4.87	3.25
0.50	−16.05	7.22	4.82	3.21
0.55	−17.10	7.70	5.13	3.42
0.60	−16.62	7.48	4.99	3.32
0.65	−16.79	7.56	5.04	3.36
0.70	−16.11	7.25	4.83	3.22
0.75	−16.03	7.21	4.80	3.20
0.80	−15.82	7.12	4.75	3.16
0.85	−15.45	6.95	4.64	3.09
0.90	−15.35	6.91	4.60	3.07
0.95	−15.50	6.98	4.65	3.10
1.00	−15.64	7.04	4.69	3.13

of a monitor, which is operational at a wide range of different charge settings with the same performance. For this purpose, the bandwidth of all employed RF components has to be broadened. In the current BAM design, the RF bandwidth of the EOM is limited to about 10 to 12 GHz[2]. The EOM transmission for higher RF frequency components does not decrease abruptly, but leads to a progressive degradation in the velocity matching between the RF and optical signals, compare section B.2.4 in the appendix, page 183 ff. The commercial power combiner[3], which is interconnected between the two outputs of the vertical RF antennas, indeed shows a low-pass filter characteristic for frequencies larger than 18 GHz [Pen11].

The resolution of the arrival time monitor depends largely on the cumulative amplitude noise A_{noise}, as detected in the baseline of the ADC spectra. Typical values for A_{noise} range between 0.2 % and 0.45 %. There is a variety of possible sources for the observed noise. Partly, it can be connected to high-frequency phase jitter from the optical signal, which is converted to amplitude noise in the photodiodes. But, to a large extent, it originates from electronic noise in the ACB. Table 4.1 shows the calculated resolution values $\mathcal{T}_{\mathrm{Res}}$ for BAM.3DBC2, which showed the lowest performance during the calibration study. For each determined calibration constant C_{calib} the resolution has been calculated according to equation 4.6, for three different values of amplitude noise. In table 4.2 the same calculation is listed, but for BAM.18ACC7, which showed the best performance throughout the investigation. According to those values, the best achieved intrinsic resolution of a single BAM at high bunch charges has been about 3 fs, whereas the worst resolution is about 46 fs at the lowest measured bunch charge of 50 pC.

[2] Specification of the commercial EOM from the company *Covega* [Web11d]. Compare section C.1.1 in the appendix.
[3] Advanced Technical Materials, Inc. power combiner P213H 1-18GHz

4.2.2 Orbit Dependency

The behaviour of the RF pick-up signal on orbit changes of the electron bunches has been simulated and measured in earlier studies, as presented in [Hac10] and [Lö9]. An orbit variation has impact on two properties of the RF signal, i.e. its slope around the zero-crossing and the detected arrival time of the zero-crossing. According to the simulations, the influence on the slope steepness can nearly be extinguished by combining the signals from two opposing pick-ups, leaving only a small, second order effect. In [Lö9], a measurement of the orbit dependence in BAM.18ACC7 is shown. There, the timing of the zero crossing from the combined horizontal RF signals has been monitored during horizontal and vertical orbit scans. The horizontal orbit has been varied in a range between −5 mm +5 mm, whereas the vertical orbit has been varied between −2.5 mm and +7.5 mm. Despite a very large spread of the measured arrival time, the results had suggested, that there is no orbit dependence in the vertical plane (that is perpendicular to the orientation of the used pick-up antennas). In the horizontal plane, however, a residual orbit dependence has indeed been detected, which showed a linear slope for positions smaller than $x = 3\,\mathrm{mm}$.

In order to compare the behaviour of the individual, currently installed RF pick-ups, thorough investigations have been performed during this thesis. The orbit dependence of the zero crossing arrival time from the *fine* channel signals has been measured for all of the four BAMs.

The measurement itself was performed by sweeping the electron bunch orbit with steerer magnets a few meters in front of the according BAM while monitoring the detected arrival times as well as the beam positions. The latter have been measured with strip-line BPMs in direct vicinity of the particular BAM. The bunch orbit was changed by several millimeters in both planes relative to the actual momentarily orbit through the machine. The scans were performed for each BAM individually. As far as the detected arrival time variations were correlated to the orbit changes, a quadratic polynomial fit of the data has been calculated.

The distance between the steerer magnets and the monitors has been chosen as large as possible, in order to avoid an arrival time change due to an actual, significant path length changes, if the orbit kick would have been too large.

The following, rough estimation shows that the effective change in electron bunch path length for the largest orbit offset of +5 mm can in principle generate observed arrival time changes in the order of a few ten femtoseconds. Larger deviations are most likely generated in the RF signalling chain between the pick-up and the EOM. If the steerer magnet was located maximal $z = 10\,\mathrm{m}$ in front of the BAM, and if assuming a linear orbit between steerer and monitor, then the induced angle for a transverse offset $\delta x = 5\,\mathrm{mm}$ amounts to:

$$\alpha = \arctan\left(\frac{\delta x}{z}\right) \approx \frac{\delta x}{z} = 0.5\,\mathrm{mrad} \tag{4.7}$$

The length of the diverted orbit becomes:

$$l = \frac{z}{\cos(\alpha)} \tag{4.8}$$

Therefore, the resulting longitudinal distance change amounts to

$$\Delta z = l - z \approx 1.25\,\mu\text{m} \tag{4.9}$$

Which generates a timing difference of $3.33\,\text{fs}/\mu\text{m} \cdot \Delta z \approx 4.16\,\text{fs}$. Due to the small angle deviations, this factor scales linearly with the distance between steerer magnet and BAM. At a minimum separation of 2 m, this would lead to an actual arrival time change of about 20.6 fs. Even when regarding the actual beam orbit through the magnetic quadrupole lenses, any timing changes due to path length deviations stay below a few ten femtoseconds.

In the following the observed arrival time dependence on orbit variations is shortly presented and discussed.

Measurement Results

Any observed orbit dependent arrival time change could presume, that there is an asymmetry in either the RF pick-up itself, in the RF cabling between pick-up and power combiner or in the pick-up position within the vacuum chamber.

Figure 4.6 shows the measurement results for BAM.1UBC2. There is no orbit dependency observed in the horizontal plane. In contrast to this, in the vertical direction, a pronounced, linear orbit dependent arrival time change has been measured. The same behaviour is expected for an arrival time measurement which makes use of only one RF pick-up, instead of a combined signal from two opposing antennas. Therefore, most likely, one of the vertical RF pick-ups is damaged at this location. The result from the calculated fit function is given in table 4.3.

Figure 4.7 shows the measurement results for BAM.3DBC2. In this case, there is only a small, residual correlation observed between the measured arrival time and orbit variations in the vertical plane. The horizontal orbit variations result in a small, second order effect of a detected arrival time change. This complies with the expectations. The result from the polynomial fit to the data is given in table 4.4.

Figure 4.8 and 4.9, respectively, show the measurement results for the two monitors BAM.4DBC3 and BAM.18ACC7. The according results from the calculated polynomial fit functions are given in table 4.5 and 4.6. In both monitors, the orbit dependence is only a second order effect. The quadratic relation between the detected arrival time changes and the orbit variations have opposite signs in the two orthogonal directions. One would expect, that the nominal beam position is located around $(x, y) = (0, 0)\,\text{mm}$ and that any orbit change around the centre of the beam pipe should have an symmetric effect on a detected arrival time change. This has been observed for BAM No. 3 and 4, except for the fact, that the horizontal beam position is displaced by +3.0 mm at the location of BAM.18ACC7. Since this complies with the usual read-back values of the according BPM, and as it also had been observed in an earlier studies presented in [Lö9], this effect seems to be related to a real, horizontal displacement of the beam position monitor.

Table 4.3: Calculated parameters for a second order polynomial fit of the measured orbit dependency in the arrival time at BAM.1UBC2

	quadratic fit: $f(x) = a_2 \cdot x^2 + a_1 \cdot x$	
	a_2[fs/mm^2]	a_1[fs/mm]
horizontal	−−	−−
vertical	4.6	−148.0

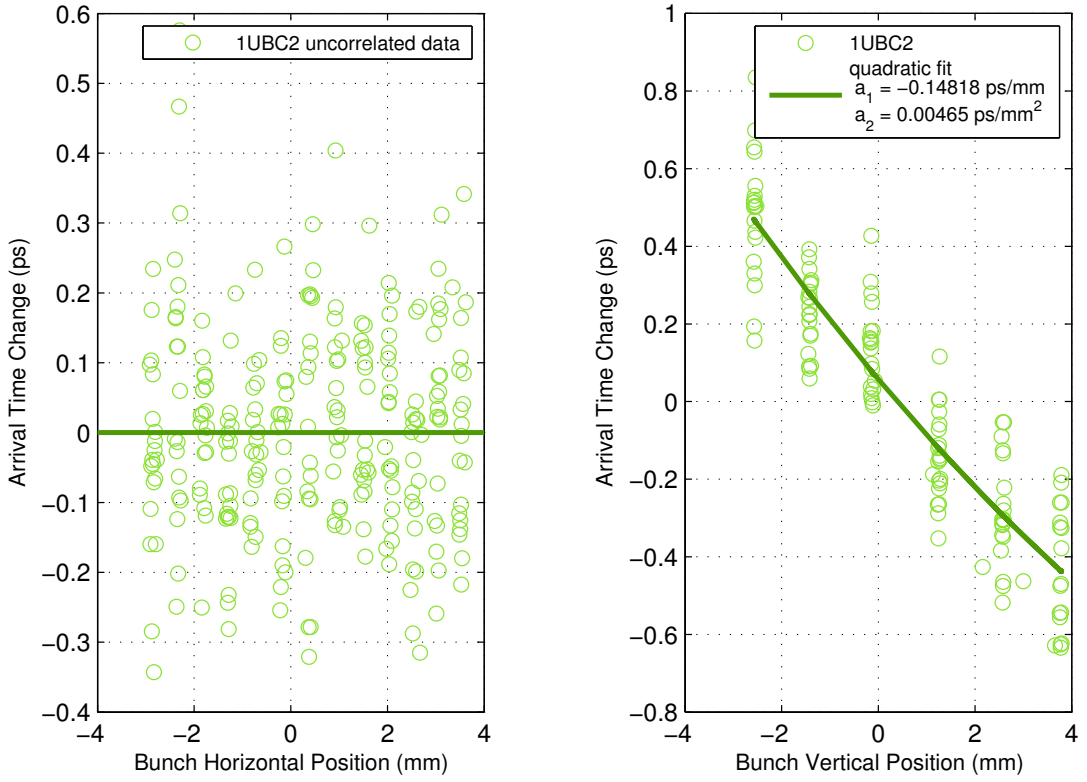

(a) BAM.1UBC2 - horizontal scan - x orbit variation

(b) BAM.1UBC2 - vertical scan - y orbit variation

Figure 4.6: Orbit dependency of the arrival time measurement with BAM.1UBC2 for electron bunch orbit variation in the (a) horizontal and in the 4.6(b) vertical plane.

Table 4.4: Calculated parameters for a second order polynomial fit of the measured orbit dependency in the arrival time at BAM.3DBC2

	quadratic fit: $f(x) = a_2 \cdot x^2 + a_1 \cdot x$	
	a_2[fs/mm^2]	a_1[fs/mm]
horizontal	13.3	−19.5
vertical	−15.8	90.0

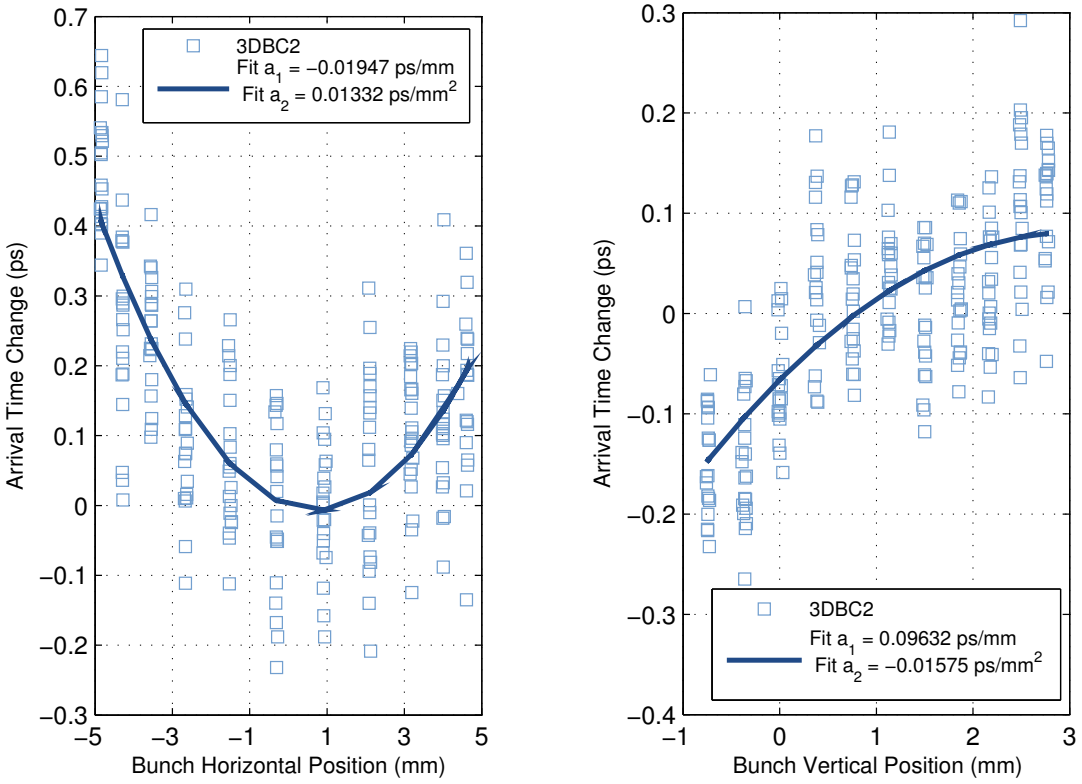

(a) BAM.3DBC2 - horizontal scan - x orbit variation

(b) BAM.3DBC2 - vertical scan - y orbit variation

Figure 4.7: Orbit dependency of the arrival time measurement with BAM.3DBC2 for electron bunch orbit variation in the (a) horizontal and in the 4.7(b) vertical plane.

Table 4.5: Calculated parameters for a second order polynomial fit of the measured orbit dependency in the arrival time at BAM.4DBC3

	quadratic fit: $f(x) = a_2 \cdot x^2 + a_1 \cdot x$	
	a_2[fs/mm^2]	a_1[fs/mm]
horizontal	−28.36	11.74
vertical	22.54	11.96

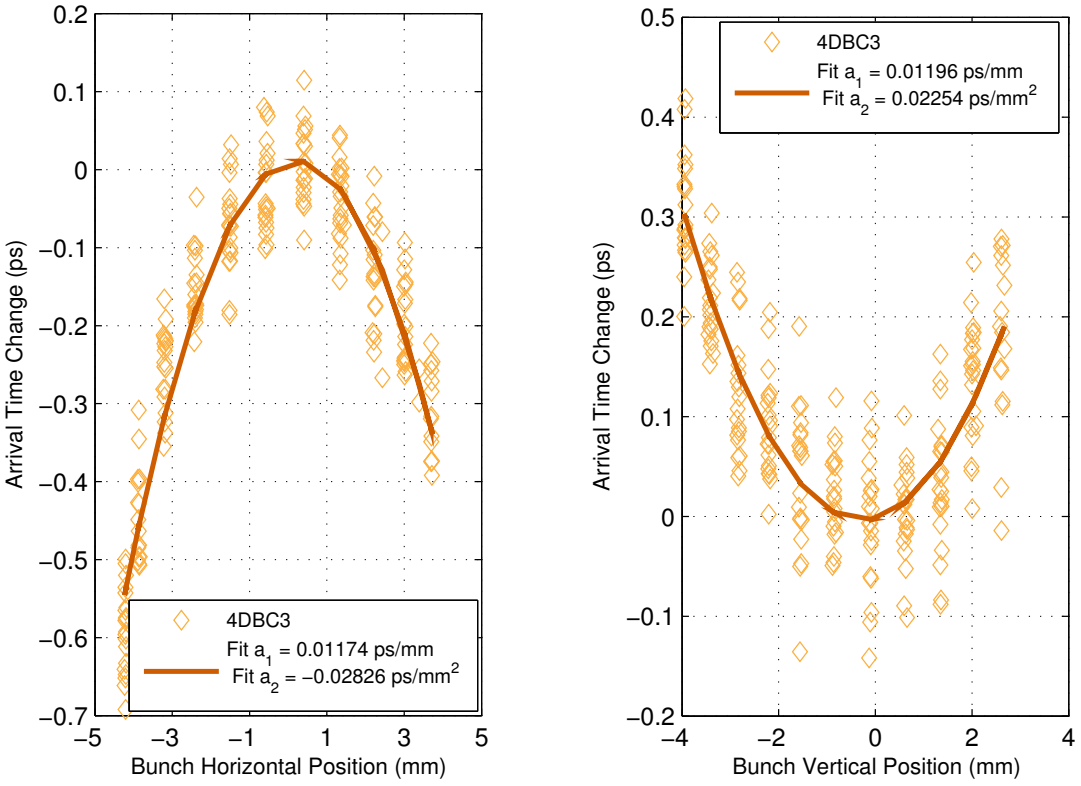

(a) BAM.4DBC3 - horizontal scan - x orbit variation

(b) BAM.4DBC3 - vertical scan - y orbit variation

Figure 4.8: Orbit dependency of the arrival time measurement with BAM.4DBC3 for electron bunch orbit variation in the (a) horizontal and in the 4.8(b) vertical plane.

Table 4.6: Calculated parameters for a second order polynomial fit of the measured orbit dependency in the arrival time at BAM.18ACC7

	quadratic fit: $f(x) = a_2 \cdot x^2 + a_1 \cdot x$	
	a_2[fs/mm^2]	a_1[fs/mm]
horizontal	−18.23	−44.59
vertical	−21.30	135.46

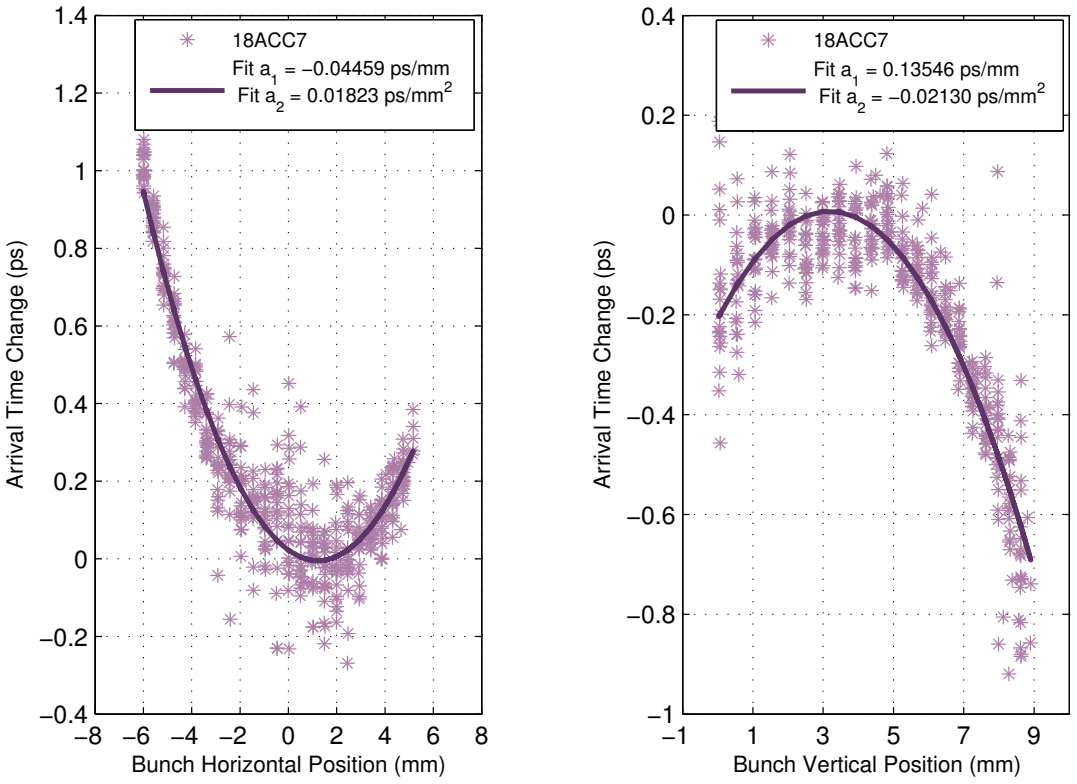

(a) BAM.18ACC7 - horizontal scan - x orbit variation

(b) BAM.18ACC7 - vertical scan - y orbit variation

Figure 4.9: Orbit dependency of the arrival time measurement with BAM.18ACC7 for electron bunch orbit variation in the (a) horizontal and in the 4.9(b) vertical plane.

Correction within BAM-Server

The source code of the BAM server already foresees an automated correction of orbit-dependent errors in the arrival time detection. This has been implemented earlier [Lö9], but has not been tested until lately. The correction requires the on-line read-out of a least one BPM in direct vicinity to the BAM, or a combination of two BPMs, located in front and behind of the BAM, respectively. In the latter case, the beam position at the location of the BAM pick-up can be calculated from the measured beam positions up- and downstream.

The according polynomial fit-parameters from the measurements presented above, can be used in the correction algorithm:

$$t_{\mathrm{corr}}^{(x)} = t_{\mathrm{meas}} - \left(a_1^{(x)} \cdot x + a_2^{(x)} \cdot x^2\right) \tag{4.10}$$

$$t_{\mathrm{corr}}^{(y)} = t_{\mathrm{meas}} - \left(a_1^{(y)} \cdot x + a_2^{(y)} \cdot x^2\right) \tag{4.11}$$

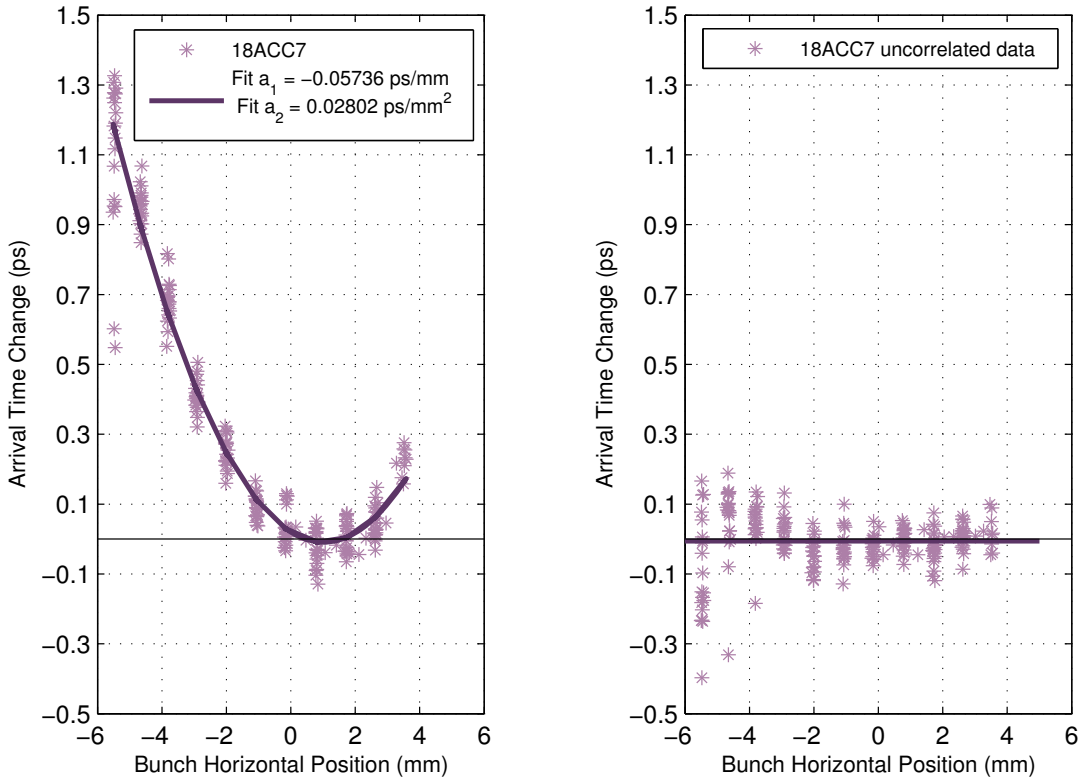

(a) BAM.18ACC7 - horizontal scan - without orbit correction

(b) BAM.18ACC7 - horizontal scan - with orbit correction

Figure 4.10: Repeated Orbit Scans for BAM.18ACC7, in the horizontal plane, before and after switching on the orbit feedback, implemented in the BAM server.

For testing the automated orbit correction in BAM.18ACC7, first the orbit scan in both transverse directions has been performed, in order to determine the actual polynomial parameters. Afterwards, the orbit scans have been repeated with the orbit correction in the BAM server having been enabled. Figures 4.10 and 4.11, respectively, compare the results for beam position offsets in the horizontal and vertical direction. Except for a slight over- or under-compensation for large beam orbit offsets, the calculated corrections remove the orbit dependence from the measured arrival time data.

This result underlines the usefulness of a real time read-out of beam position monitors in order to enable an online-correction of the measured arrival times. Especially for those BAMs which are or will be incorporated in longitudinal beam-based feedback systems for stabilising the arrival time at certain positions along the linac.

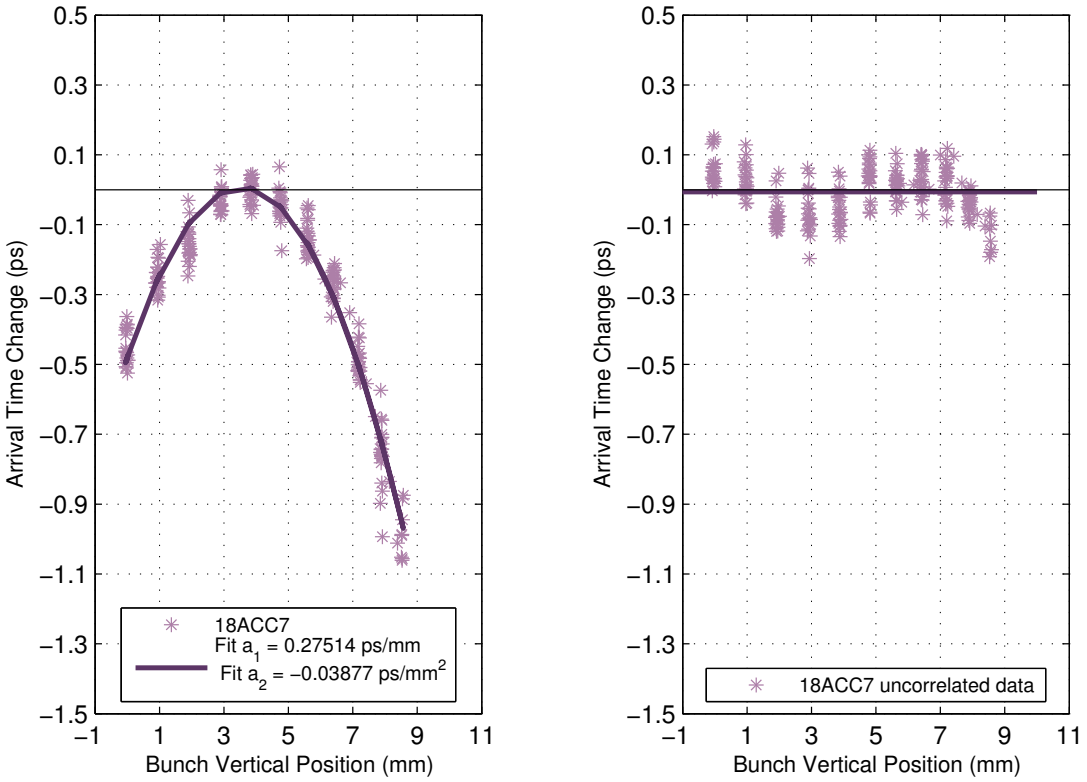

(a) BAM.18ACC7 - vertical scan - without orbit correction

(b) BAM.18ACC7 - vertical scan - with orbit correction

Figure 4.11: Repeated Orbit Scans for BAM.18ACC7, in the vertical plane, before and after switching on the orbit feedback, implemented in the BAM server.

5 Bunch Arrival Time Monitors ▸ Applications & Machine Studies

Contents

5.1 Applications

5.1.1 On-Crest Phase Measurements for ACC1, ACC39 & ACC23

The usual determination of the so-called on-crest phase is performed by using optical transition radiation (OTR) screens in the straight section of the bunch compressing chicanes, BC2 and BC3.

Electron bunches with a higher energy are deflected less in the dipole magnets of the chicane, thus passing the screen off-centre, i.e. outside of the region of interest (ROI) of the OTR screen. There are two possibilities in order to adjust the actual beam orbit through the chicane such that the beam position on the screen is optimised. One can either modify the magnet current in the dipoles of the chicane or decrease the energy gain in the preceding acceleration module through decreasing the RF amplitude. Both strategies, move the beam spot on the OTR screen to the centre. When shifting the RF phase of ACC1 into direction of the on-crest phase, the beam spot moves to the one side, i.e. in this case the right handside, until it moves backwards after the phase has passed the crest of the cosine shaped curve of the RF wave. The on-crest phase can in principle be determined through maximising the energy gain, thus approaching the on-crest phase. The latter would be determined from the farthest position shift of the beam spot on the screen. Anyhow, this would be too inaccurate, since $\cos(\Delta\Phi) \approx 1$, for only small deviations $\Delta\Phi$ around the actual on-crest phase.

Another approach is to minimise the energy spread, i.e. to obtain symmetric tails of the bunch. At phases far off-crest, the electron bunches experience a large energy chirp. Parts of the electron bunch

with a lower energy will take a distinctly different and longer path through the chicane than those parts with a higher energy. The spot on the OTR screen gets smeared out. With changing the phase of the accelerating module towards the on-crest phase the smaller the energy chirp gets, thus the more compact the spot on the OTR screen looks. This circumstance is then used as indication, whether the on-crest phase is reached. There are two problems arising from this method: firstly, the phase of the least energy correlation deviates from the real on-crest phase (the maximum point of accelerating RF wave) by 1 to 2 deg. Secondly, in case of the modules ACC1 and ACC39, the determination of the on-crest phase for the latter module depends on the energy being set in ACC1.

Thus, there are three practical disadvantages which arise from the OTR-screen method:

1. The view regions of the OTR cameras are quite small, requiring an adjustment of the RF gradient to set the beam on the screen.

2. The movment of the screen is not only time-consuming but implies a major intrusion into the normal operation of the accelerator, since e.g. the macro pulse length has to be reduced to one bunch.

3. In case of BC3, the determination of the phase of least energy spread depends on the energy gain from modules upstream of ACC23.

A less invasive technique for the determination of the on-crest phase is offered by the bunch arrival time monitors. With a BAM in the straight section behind a magnetic chicane, the on-crest phase can be determined to be the point of minimum (or maximum) time of flight. The measurement does not depend on the energy chirp, but on is a function of bunch energy, or more precisely of the energy gain. When sweeping the phase of ACC1 from far off-crest towards the on-crest phase, the bunches experience a larger field amplitude, i.e. a stronger acceleration, thus the time-of-flight through the chicane gets smaller. The minimum time-of-flight and thus the earliest arrival time at the exit of the chicane is reached at on-crest phase. When further changing the phase in the same direction, the bunches roll over the crest and thus experience lower field strengths resulting in a longer flight time and later arrival times 5.1(a). In case of ACC39, this works as well with the difference that this module is operated at 180 deg, i.e. it acts decelerating. Thus the on-crest phase is reached, when the arrival time of the bunches at the exit of BC2 is maximal 5.1(b). In the same way, the on-crest phase of ACC23 5.1(c) is measured, using BAM.4DBC3, downstream of BC3.

The measurement principle relies on the fact that the path length through the chicane changes for small energy deviations. Connected to the R_{56} values of the bunch compressors, this translates into energy-dependent arrival time changes. In case of BC2, this adds up to typically 5 – 7 ps/%, whereas the relation is about half as large, 2.5 ps/%, for BC3.

The BAM-based measurement is not applicable for modules ACC45 and ACC67 in front of the Dogleg, even when the fifth BAM will be installed further downstream (at position 1SFELC), because of a too low R_{56} value of this magnetic chicane. In this case, the on-crest phase can be determined directly by using the energy server, measuring the point of maximum bunch energy in the Dogleg chicane by varying the phases of ACC45 (5.1(d)) and ACC67 (5.1(e)).

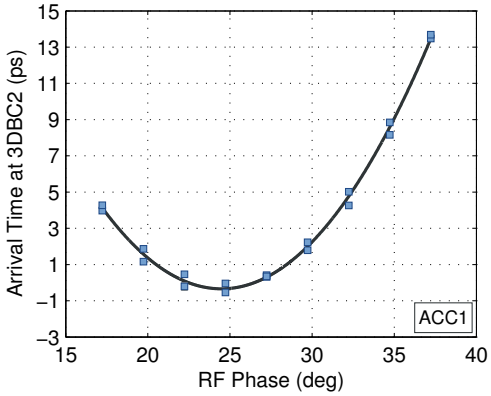

(a) ACC1: estimated on-crest phase = 24.48 deg

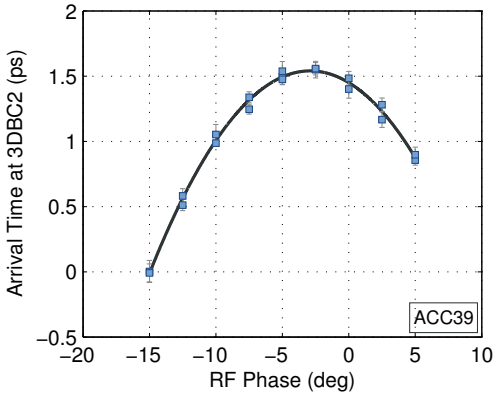

(b) ACC39: estimated on-crest phase = −2.91 deg

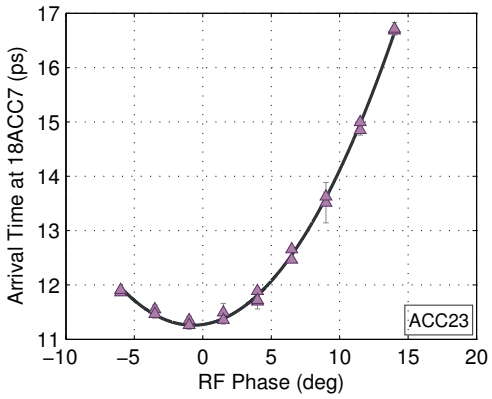

(c) ACC23: estimated on-crest phase = −0.71 deg

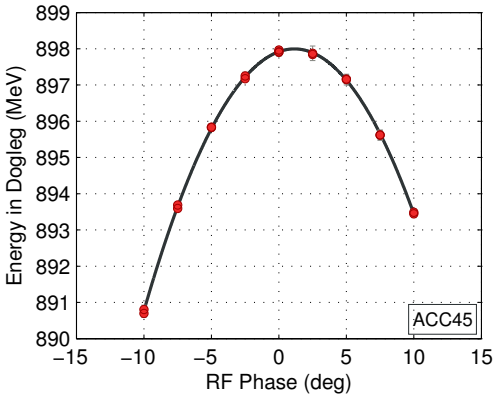

(d) ACC45: estimated on-crest phase = 1.15 deg

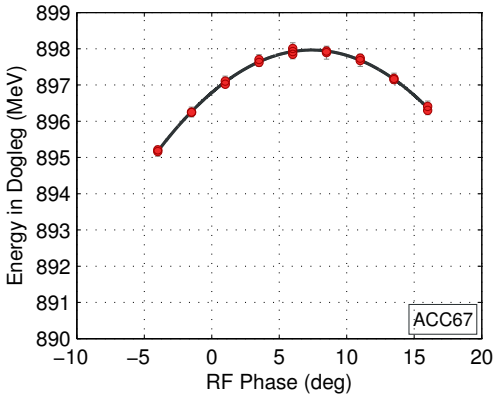

(e) ACC67: estimated on-crest phase = 7.39 deg

Figure 5.1: Measurement of the on-crest phases of all acceleration modules using BAMs and the energy server.

5.1.2 Relative Energy Measurement in BC2

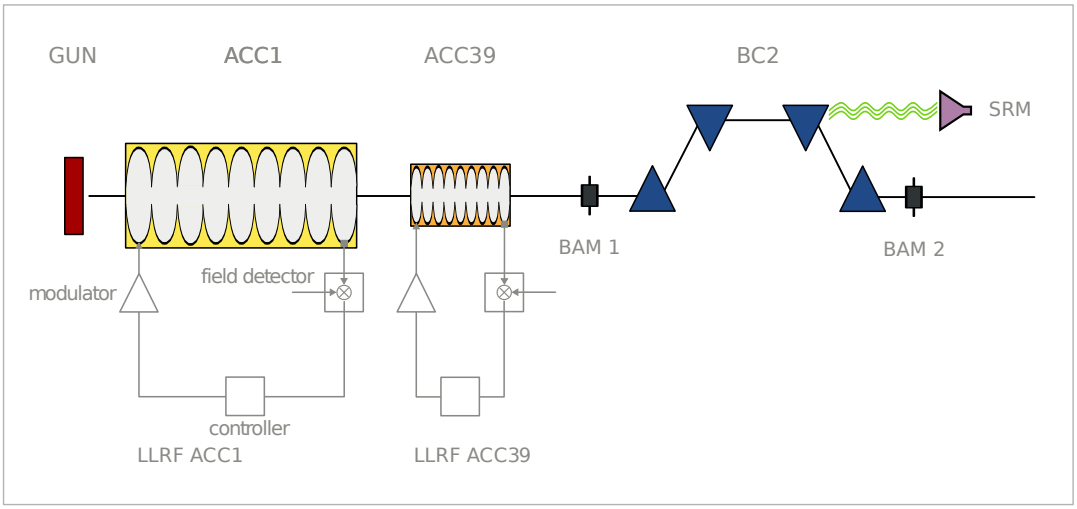

Figure 5.2: Illustration depicting the injector of FLASH. The RF gun is followed by two superconducting accelerations modules, for each only one nine-cell cavity is shown. Downstream of the modules, a 4-dipole magnetic chicane is used for bunch compression. In front of the entrance and at the exit of the bunch compressor BAMs are installed. Opposite of the third dipole a SRM is mounted.

The relative energy variation $\Delta E/E$ from the injector of FLASH has been measured in a comparative study of two monitor systems, i.e. one synchrotron radiation monitor (SRM) and two BAMs, see figure 5.2 for a schematic of the set-up. The timing of the electron bunches in the bunch compressor BC2 is measured with the two BAMs up- and downstream of the chicane. The change in arrival time difference between both monitors, i.e. the deviation of the time of flight through the magnetic chicane, is a measure for the energy deviation ΔE from the nominal value for each bunch. The value is dependent on the actual longitudinal dispersion R_{56} of the chicane. Comparing the energy deviations between two adjacent bunches within one macro pulse delivers a measure for the bunch-to-bunch energy fluctuation δE.

Any deviation ΔE from the nominal beam energy E transforms into a horizontal beam displacement Δx in the straight section of BC2 due to the horizontal dispersion R_{16} of the chicane. Therefore, bunches with different average energies $\langle E \rangle$ will traverse the bunch compressor with a significantly different path length which is transformed into an arrival time difference Δt behind BC2, compared to the arrival time at nominal energy. This effect is governed by the longitudinal dispersion R_{56} of the magnetic chicane. In first order, i.e. neglecting T_{566} and T_{166}, the energy dependent position and timing deviations are given by

$$\Delta x = R_{16}\frac{\Delta E}{E} \qquad \text{and} \qquad \Delta t = R_{56}\frac{1}{c}\cdot\frac{\Delta E}{E} \tag{5.1}$$

where the horizontal dispersion R_{16} for BC2 typically takes values of $300 - 400\,\text{mm}$ and the longitudinal disperison R_{56} is $\approx 140 - 230\,\text{mm}$. By determining the bunch arrival times at both BAMs up- and downstream of BC2, the time of flight $t = t_2 - t_1$ is calculated. Details can be found in the

appendix sections A.2 and A.3.

Before presenting the measurement results, the operation principle of the SRM is shortly described. Within the dipole magnets of the chicane, both incoherent synchrotron radiation (ISR) and coherent synchrotron radiation (CSR) are generated due to the curved trajectory of the relativistic electron bunches. The radiation becomes coherent for wavelengths longer than the bunch length and the intensity grows inversely proportional to the third power of the bunch length. The ISR light which propagates in a straight line from the bending magnet in forward direction is split and focussed onto a multi-anode photomultiplier tube (PMT) and a charge-coupled device (CCD) camera. The radiation is imaged onto two adjacent anodes of the PMT for using both signals to calculated the centre of gravity beam position s:

$$s = \frac{I_1 - I_2}{I_1 + I_2} \tag{5.2}$$

where I_i are the signal intensities of the two anodes. Due to the normalisation, the influence of a bunch charge jitter on the signal is eliminated. For details, see [Gero7].

comparison of BAM with SRM

For a calibration of both monitor systems, an intended change in both, beam position and path length, had to be generated. This was done by changing the magnetic field strengths of the dipoles in BC2, thus changing the bending angles in the chicane, which is comparable to a relative energy change $\Delta E/E$. For a detailed derivation, see section A.2 in the appendix. The calibration was then performed by varying the magnet current of the dipoles while recording the SRM signals and the time of flight Δt. This was done at two different machine settings:

1. with ACC1 and ACC39 on-crest
2. with ACC1 and ACC39 off-crest under self-amplified spontaneous emission (SASE) conditions

The calibration constants of both monitors and for both machine settings are listed in table 5.1. Figure 5.3 shows the corresponding calibration curves for the SRM signal and the time-of-flight (ToF) measurement, respectively. The calibration constants have been determined by a linear fit. For the time-of-flight measurement the calibration is nearly independent of the operation mode. But the linear range of the SRM depends significantly on the rate of bunch compression, i.e. on the phase

Table 5.1: Calibration constants for the relative energy determination using SRM and two BAMs.

mode of operation	SRM [units/%]	BAMs [ps/%]
on-crest	3.09	5.56
off-crest	0.61	5.54

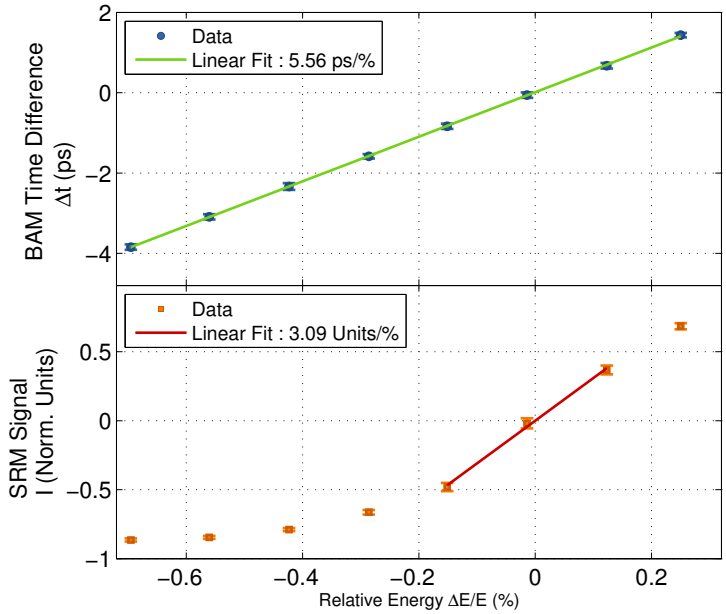

(a) ACC1 and ACC39 on-crest

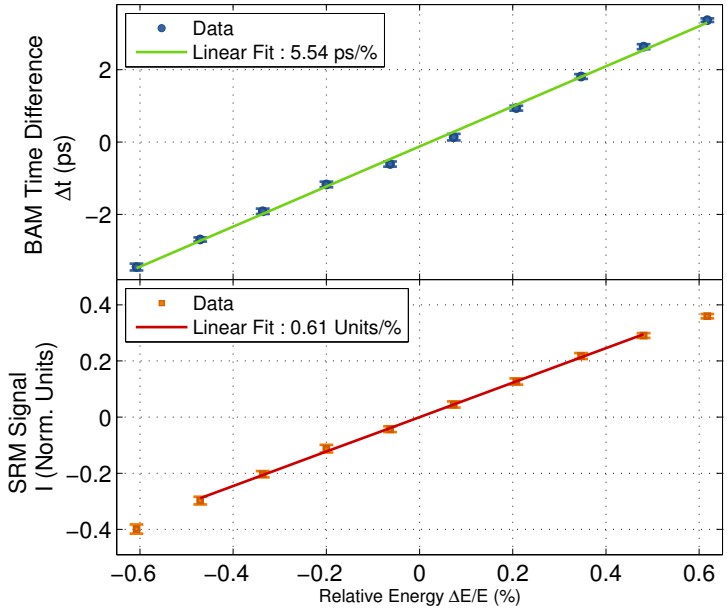

(b) ACC1 and ACC39 off-crest under SASE conditions

Figure 5.3: Calibration curves for SRM and the difference signal of the two BAMs around BC2 for two machine settings. The relative energy deviation has been generated through a magnet current scan in the dipoles of the chicane.

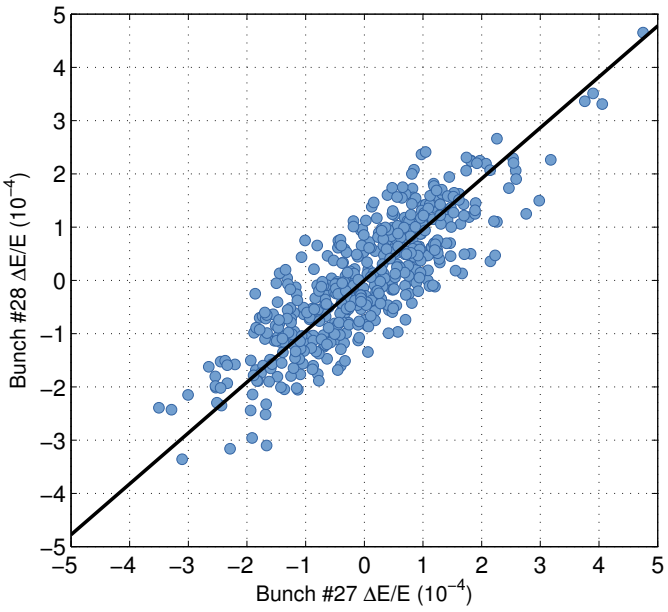

Figure 5.4: Determination of the bunch-to-bunch relative energy resolution, here for one example of the ToF-measurement.

settings in both modules. At on-crest operation the linear range is relatively small, due to the narrow horizontal beam size. For stronger compressed bunches the dynamic range of the SRM is wider but with reduced sensitivity.

The bunch-to-bunch energy resolution of both monitors had been determined by correlating the calculated energy deviation of each two adjacent bunches within one bunch train. When assuming that the resolution is identical for each bunch, the single bunch energy resolution reduces by a factor of $1/\sqrt{2}$. An example is shown in figure 5.4, where the relative energy deviation $\Delta E/E$ for 100 macro pulses is calculated from the time-of-flight for bunch 28 in comparison to bunch 27. The statistical evaluation was done by use of the principal component analysis (PCA), compare section D, page 205 ff. In this example the correlation between both bunches, measured under SASE conditions, yields:

- $\sigma_{\text{signal}} = 16.3238 \times 10^{-5}$
- $\sigma_{\text{noise}} = 4.46443 \times 10^{-5}$
- SNR = 12.35

Since both signals vary around the value $\Delta E/E = 0$, the SNR has been calculated from the ratio of signal variance σ^2_{signal} to noise variance σ^2_{noise}. This yields a significance test of the measurement and should take values of SNR $\gg 1$.

When applying this analysis pairwise to all 30 bunches to the determined calibration curves, the bunch-to-bunch energy resolution values for the SRM and ToF measurement at on-crest operation result in $4.2 \pm 0.2 \times 10^{-5}$ and $4.4 \pm 0.1 \times 10^{-5}$, respectively. Under SASE conditions, the value for the ToF-signal, i.e. $4.8 \pm 0.1 \times 10^{-5}$, is only slightly decreased whereas the bunch-to-bunch resolution for

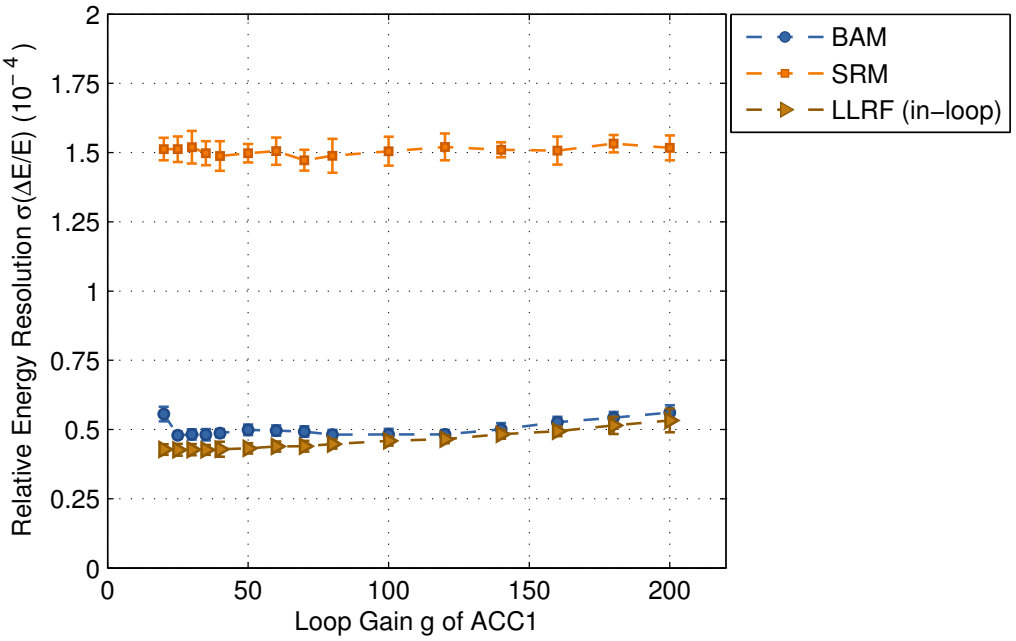

Figure 5.5: Resolution of the relative energy jitter measurement during the proportional gain scan at off-crest operation. Comparison between the values from three different monitor systems: i.e. BAMs, SRM and in-loop LLRF monitor.

the SRM is significantly decreased to nearly one third, i.e. $1.6 \pm 0.1 \times 10^{-4}$. The measured value for the time-of-flight signal corresponds to a resolution of about 35 fs (RMS) using the up- and downstream BAMs.

Influence of proportional loop gain in ACC1

The digital control loop of the low-level radio frequency (LLRF) system has been set up with a simple proportional feedback gain $\mathcal{G}$ for regulating the RF field inside of the superconducting cavities of ACC1, compare figure 5.2. In the course of the measurement, both the mean energy deviation $\Delta E/E$ and the relative energy jitter $\delta E/E$ caused by ACC1 has been determined in dependence on $\mathcal{G}$, for values between 0 and 200. At each gain setting 500 subsequent macro pulses with 30 bunches have been recorded. For data analysis, the values from each bunch within the macro pulse have been averaged over 500 pulses.

Resolution of all monitors: Figure 5.5 shows the characteristic resolution of an energy jitter measurement during the gain scan at off-crest operation, using three different monitor systems: the LLRF in-loop signal, the ToF measurement and the SRM signal.

The resolution of the BAM-based detection is comparable to the calculated resolution of the in-loop signal. As mentioned before, the energy-resolution of the SRM is significantly decreased for a machine setting with larger compression in BC2. It depends only weakly on the loop gain setting and thus on the actual energy jitter.

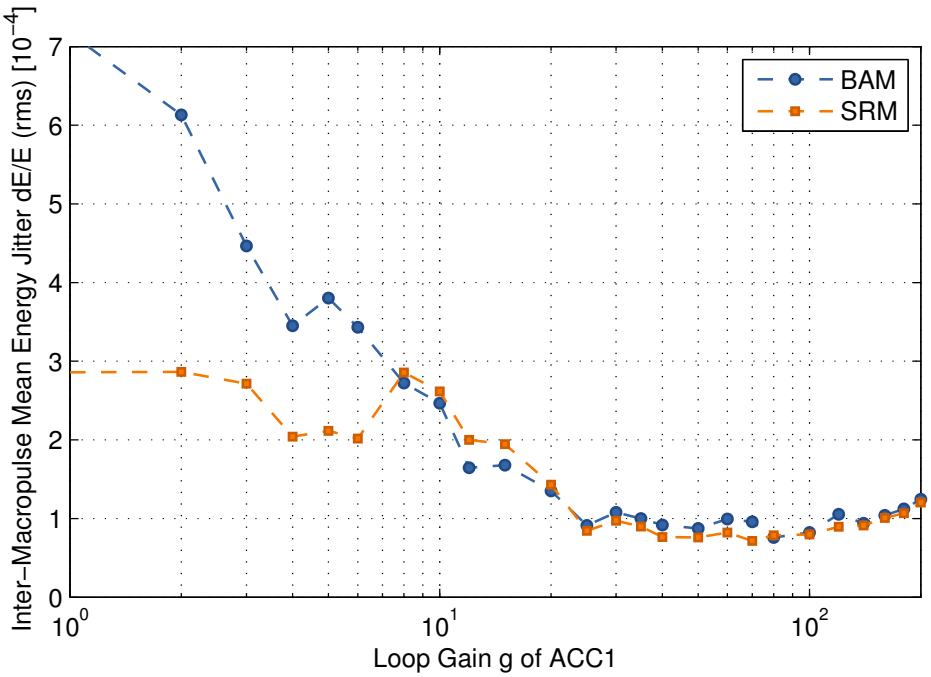

(a) ACC1 on-crest. Measured inter-macro pulse energy jitter, averaged over 30 bunches.

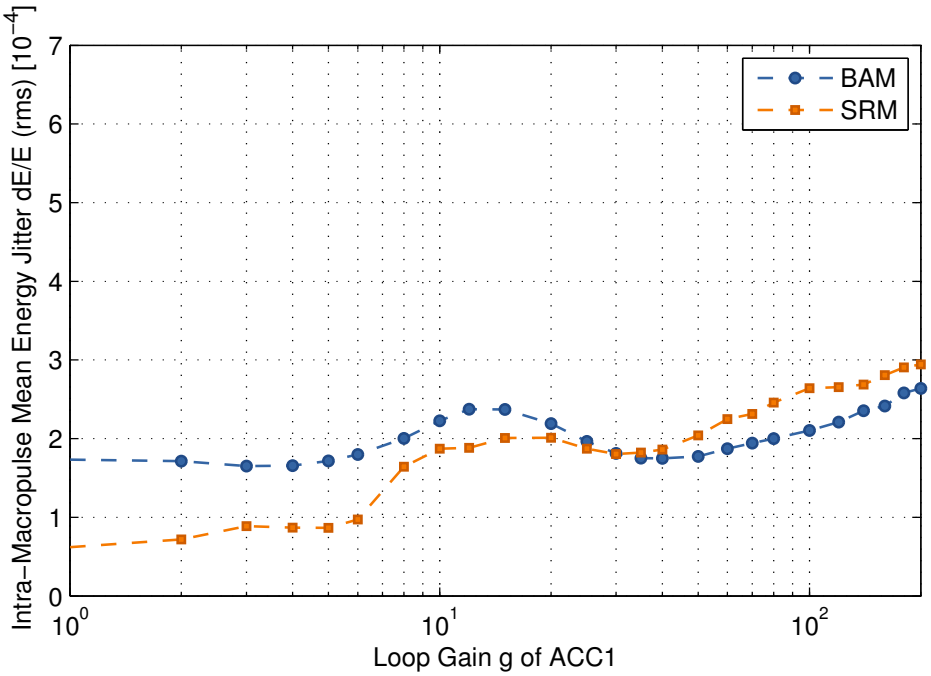

(b) ACC1 on-crest. Measured intra-macro pulse energy jitter, averaged over 500 pulses.

Figure 5.6: Relative energy fluctuation $\Delta E/E$ as function of the gain setting $\mathcal{G}$ measured with both out-of-loop monitor systems, i.e. SRM and BAMs, at on-crest operation. Shown here, are the (a) energy jitter from macro pulse to macro pulse and the (b) intra-macro pulse energy jitter, for 30 bunches.

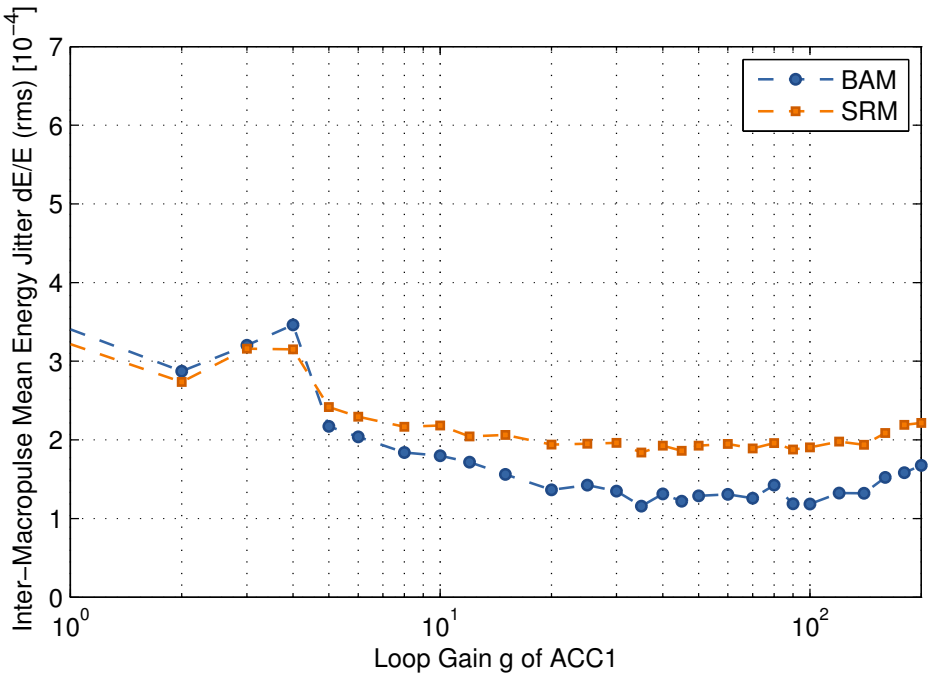

(a) ACC1 off-crest. Measured inter-macro pulse energy jitter, averaged over 30 bunches.

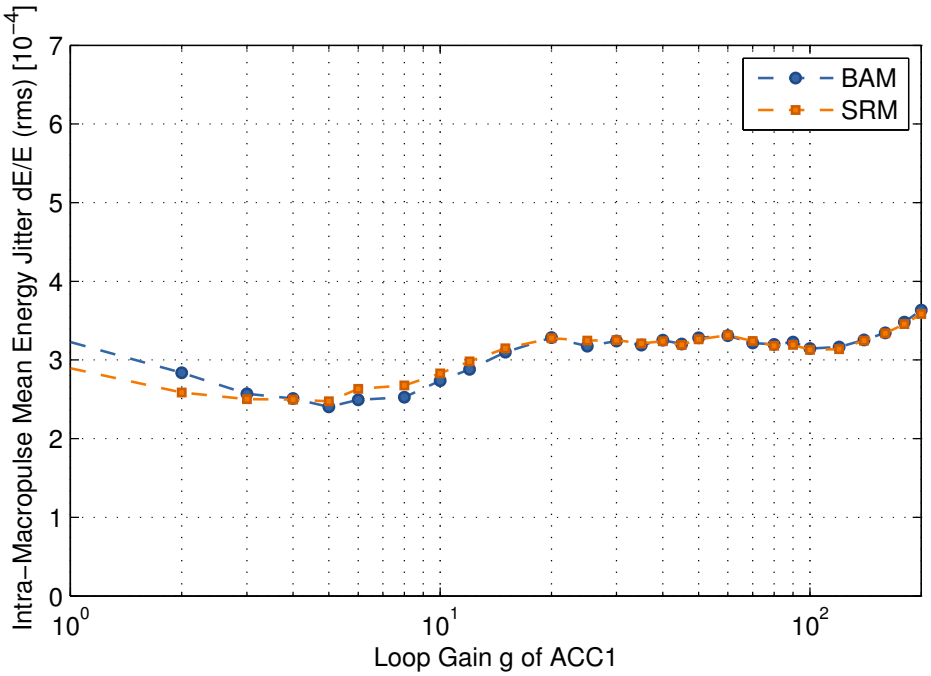

(b) ACC1 off-crest. Measured intra-macro pulse energy jitter, averaged over 500 pulses.

Figure 5.7: Relative energy fluctuation $\Delta E/E$ as function of the gain setting $\mathcal{G}$ measured with both out-of-loop monitor systems, i.e. SRM and BAMs, at off-crest operation, under SASE conditions: (a) energy jitter from macro pulse to macro pulse and (b) intra-macro pulse energy jitter, for 30 bunches.

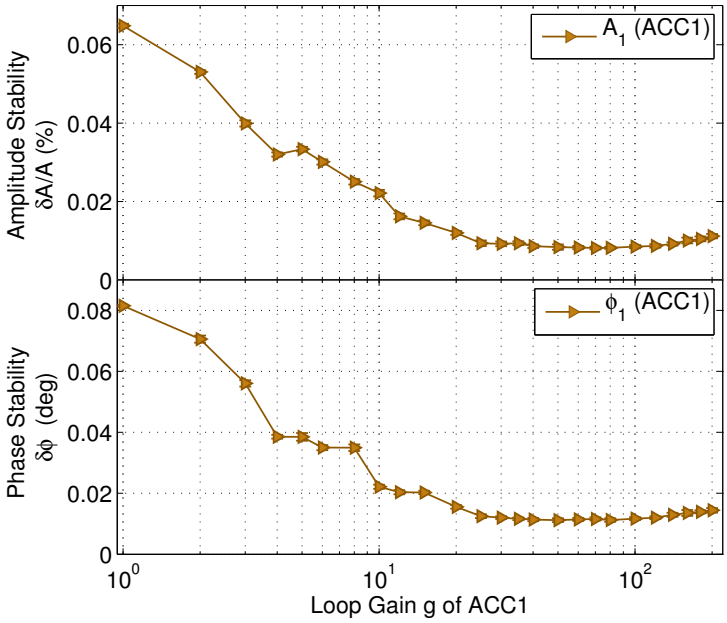

(a) ACC1 on-crest

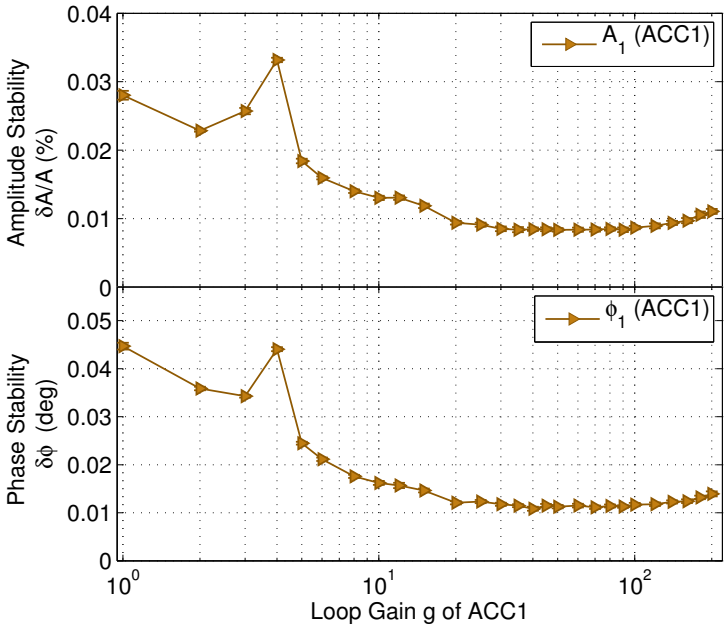

(b) ACC1 off-crest under SASE conditions

Figure 5.8: Measurement of the in-loop amplitude and phase variations for ACC1 during the proportional gain scan.

Relative energy jitter - bunch to bunch: The bunch-to-bunch relative energy jitter $^{\Delta E}/_{E}$ as function of the gain $\mathcal{G}$ has been measured with both out-of-loop monitor systems, i.e. SRM and BAMs. Figure 5.6(b) shows the energy jitter for on-crest operation and figure 5.7(b) for SASE operation. The RMS jitter values have been calculated for each of the 30 bunches, estimating the energy jitter for 500 successive macro pulses. For the plot, the individual errors have been averaged of the bunch train. At on-crest operation the SRM deviates significantly from the BAM measurement. At low gain settings, the jitter is underestimated whereas at gains $\mathcal{G} > 30$ the SRM overestimates the bunch-to-bunch energy jitter. Under SASE conditions, i.e. for stronger compressed bunches, both monitors measure a nearly identical behaviour. In summary, the bunch-to-bunch energy jitter shows only a weak dependency on the gain setting, but tends to be lower at lower $\mathcal{G}$.

Relative energy jitter - pulse-to-pulse: In comparison to the bunch resolved energy deviation, the energy jitter values $^{\Delta E}/_{E}$ between different macro pulses are shown in figure 5.6(a) at on-crest operation and in figure 5.7(a) for SASE operation. For the statistical evaluation, first, the energy deviation of each macro pulse has been calculated as mean value over 30 bunches. Afterwards, the jitter of the mean macro pulse energy has been calculated for 500 successive pulses. The energy jitter has not only been measured by use of both out-of-loop monitor systems, i.e. SRM and BAMs, but has also been calculated from the vector sums of the LLRF field detector, which is shown in figure 5.8(a) (on-crest) and figure 5.8(b) (SASE conditions). At low gain settings the large difference in nominal and actual energy is underestimated in the SRM due to the limited dynamic range in on-crest operation. The SRM-data starts to deviate for $^{\Delta E}/_{E} \geq 0.2\,\%$.

At SASE conditions, the relative energy deviation measured with both BAMs and SRM shows a similar behaviour, where the SRM is in in better agreement with ToF-data at small gains due to the larger dynamic range for large bunch compression factors. However, the SRM data deviates at larger gain settings. The energy jitter as calculated from the ToF data is in good agreement with the in-loop measured LLRF signals, compare figure 5.1.2. The mean energy has been calculated from those in-loop amplitude and phase values using

$$\langle E \rangle = A_{\mathrm{ACC1}} \cos\left(\Phi_{\mathrm{ACC1}}\right) + A_{\mathrm{ACC39}} \cos\left(\Phi_{\mathrm{ACC39}}\right) + E_{\mathrm{GUN}} \tag{5.3}$$

The loop gain $\mathcal{G}$ acts only on ACC1. Here, the amplitude and phase stability increases linear with $\log(\mathcal{G})$ until it reaches a minimum at a loop gain of about 80. For higher gains the stability decreases again by a small amount, because the noise generated internally by the feedback loops starts to contribute significantly.

Conclusion: In contrast to the SRM, the resolution of a relative energy measurement using two BAMs is only weakly depending on the actual amplitude and phase settings in ACC1 and ACC39. This is related to the fact, that the arrival time measurement does not depend on the longitudinal bunch shape but rather reflects the arrival time of the centre of charge for each bunch. During the loop gain scan, the lowest relative energy jitter of about $7.6 \pm 0.3 \times 10^{-5}$ (value from ToF measurement; compare figure 5.6(a) and 5.7(a)) was found to be at $\mathcal{G} \approx 80$. This value agrees with the prediction based on the noise characterisation of sub-components, as published in [LHSS06]. The difference sig-

nals of both BAMs installed around BC2 deliver a bunch-to-bunch relative energy resolution which is high enough to be used for comparative measurements with the large horizontal aperture beam position monitor (EBPM). The opto-mechanical design of this monitor is basically a combination of two BAMs into one device, but incorporating another type of RF pick-up and specialised electronics. For details on the optical EBPM compare [Hac10]. Presently, developments are on-going to enhance the resolution and reliability of an RF-based EBPM. First results are expected in the course of 2012.

5.1.3 Transfer-Function of RF Accelerator Modules

As mentioned in section 1.3.2 the two BAMs and BCMs installed at the exits of the two bunch compressors are implemented in a beam based feedback (BBF) system to compensate for fast amplitude and phase fluctuations of the RF field in the acceleration modules upstream of the chicanes. Fluctuations in the RF field generate a jitter of the mean energy and energy chirp of the electron bunches. Due to the horizontal and longitudinal dispersion, R_{16} and R_{56} respectively, those fluctuations lead to simultaneous variations of the bunch arrival time and bunch compression. The energy fluctuations are a combination of amplitude and phase variations in both modules ACC1 and ACC39:

$$\Delta E_{\mathrm{BC2}} = A_{\mathrm{ACC1}} \cos(k_{\mathrm{RF}}\, z + \Phi_{\mathrm{ACC1}}) + A_{\mathrm{ACC39}} \cos(3k_{\mathrm{RF}}\, z + \Phi_{\mathrm{ACC39}}) \tag{5.4}$$

In first approximation the combined effect is described by a 2×4 transfer matrix Λ with coefficients Λ_{ij}. Since the interplay of small amplitude and phase variations is depending on the actual operation point, presently, the transfer matrix has to be determined every time the BBF is set up for a dedicated user shift or for system tests. In future, this will not be necessary any more, when the RF phase deviations are significantly decreased, so that phase drifts contribute less to the energy deviations.

In the following, a transfer matrix is described, measured at the initial machine settings as given in table 5.2.The on-crest phases of the modules ACC1, ACC39 and ACC23 had been determined beforehand by use of the BAMs. The latter procedure is described in section 5.1.1 on page 119 f. For

Table 5.2: Initial settings of the accelerator modules before measuring the transfer matrix of BC2 (compare figure 5.9).

	Gun	ACC1	ACC39	ACC23	ACC45	ACC67
gradient [MV]	3.748	164.6	18.3	316.3	233.0	0.0
phase [deg]	0.0	+2.97	−16.70	+16.30	0.0	–
on-crest phase [deg]	–	0.0	0.0	0.0	0.0	–

an identification of the coefficients Λ_{ij} it is sufficient to vary the amplitude and phases in a narrow region around their nominal set-points, typically $< \pm 0.5\,\%$ and $< \pm 0.5$ deg respectively, to induce a linear change in the BAM and BCM signals. The amplitudes and phases of both modules are scanned successively and the monitored signals are averaged over 20 subsequent pulses. The variations are small enough to perform the scan during normal machine operation while only slightly disturbing the SASE process. The slope of each curve determines the according coefficients Λ_{ij}.

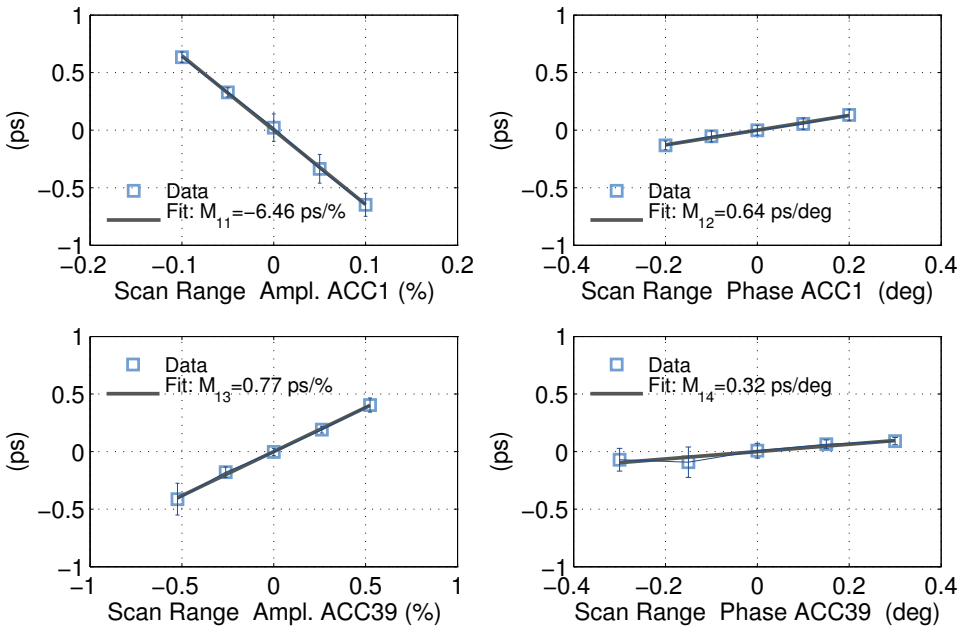

(a) Arrival time change measured at BAM.3DBC2

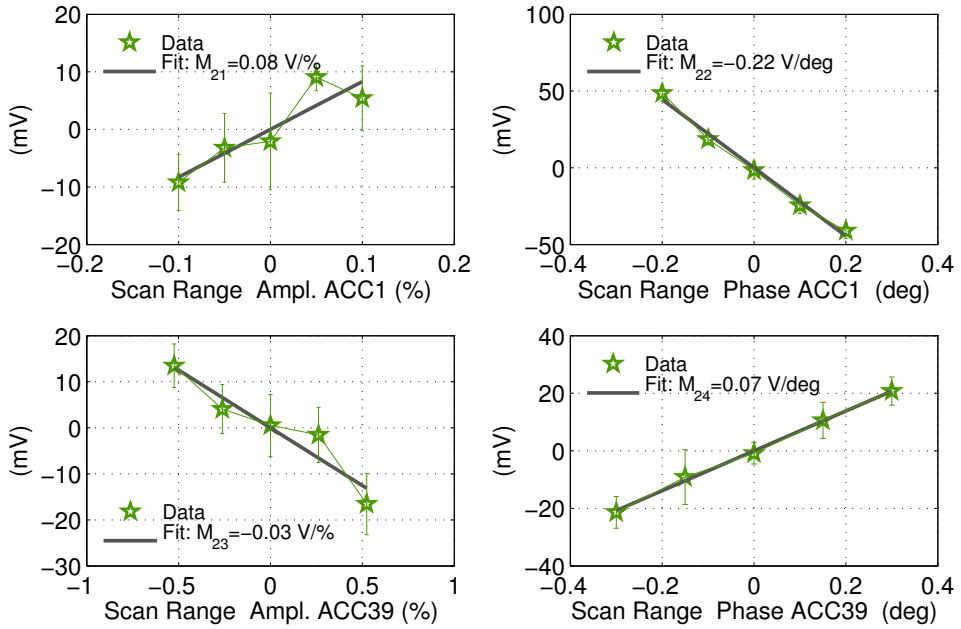

(b) Signal variation measured with BCM.9DBC2

Figure 5.9: Determination of the transfer matrix Λ (in the plots denoted with M) for BC2. The gathered data for BAM.3DBC2 (a) and BCM.9DBC2 (b) are shown with the applied linear fits.

Figure 5.9 shows the gathered data during a transfer matrix measurement for BAM.3DBC2 (a) and BCM.9DBC2 (b). The Λ coefficients could be identified to

$$\begin{pmatrix} \Delta t_{BC2} \\ \Delta C_{BC2} \end{pmatrix} = \begin{pmatrix} -6.46\,\mathrm{ps/\%} & -0.64\,\mathrm{ps/deg} & -0.77\,\mathrm{ps/\%} & -0.32\,\mathrm{ps/deg} \\ -0.08\,\mathrm{V/\%} & -0.22\,\mathrm{V/deg} & -0.03\,\mathrm{V/\%} & -0.07\,\mathrm{V/deg} \end{pmatrix} \begin{pmatrix} \delta A_{ACC1} \\ \Delta\Phi_{ACC1} \\ \delta A_{ACC39} \\ \Delta\Phi_{ACC39} \end{pmatrix} \tag{5.5}$$

As expected, the amplitude variations in ACC1 are the dominant contribution to arrival time deviations behind BC2. For many BBF applications and machine set-points, the contribution of energy deviations on the bunch compression is negligible.

5.1.4 Delivery of Timing Information for Experiments

All of the above mentioned applications of the bunch arrival time monitors (BAMs) concern mainly the machine operation, with regard to a monitoring and regulation of the bunch arrival time at different locations of the linac. But the monitors also deliver useful information for experiments, for instance sFLASH, and for user applications. Especially the rearmost installed BAM serves as a diagnostic tool to determine the actual timing jitter between the optical lasers, as used in pump-probe (PP) experiments, and the electron beam. In this case, BAM.18ACC7 is by default included in the data stream of the data acquisition (DAQ) system for the user experiments.

The general idea behind this is to post-sort the experimental data in time with the timing and jitter information. The time resolution of the experiments will then be limited by the resolution of the timing measurement instead of the jitter characteristic of either the laser system or the FEL pulses.

Besides the BAM, two further bunch resolved diagnostics had been implemented or tested for this purpose, which both compare the timing of the FEL pulses to the PP laser pulses. Those tools comprise a streak camera and the set-up for measuring timing by electro-optical sampling (TEO). Details can be found in [RASA+11]. TEO reaches a timing resolution of currently better than 100 fs (RMS).

A shot-to-shot, high precision arrival time measurement is expected to deliver the possibility to gain a timing resolution of the experimental set-ups in the range of a few 10 fs and less. The actual improvement of the temporal resolution has not been demonstrated yet, which is due to a vast variety of reasons. Although the PP-laser system is already connected to the laser-based synchronisation (LbSyn) system, further developments are needed to increase the phase-locked loop (PLL) performance and decrease the resulting out-of-loop timing jitter. In the next section it will be become clear, that also on the side of the BAM there are still developments of especially the electronics required to improve the long-term performance. The high demands on the point-to-point stability of the LbSyn system became attainable during the last few years of development time. Though, the desired point-to-point stability of below 10 fs had not been demonstrated yet, the required measurements are planned for the near future in futher thorough investigations. Nevertheless, the extensive improvements of all key components of the LbSyn system, partly achieved in the frame of this thesis, promote the enhancement of timing stability and resolution of timing measurements for the FEL pulses and thus for the user experiments.

5.2 Machine Studies

5.2.1 Arrival Time Dependency on Injector Settings

The arrival time of the electron bunches at the entrance of the first bunch compressor is mainly determined by the arrival time of the injector-laser pulses on the cathode material and by the phase of the RF field in the 1½ cell cavity of the gun. The combination is not simply a composition of both contribution in equal parts, instead the proportion is depending on the RF gun phase. The RF settings of the injector have large influence not only on the arrival time, but also on the bunch length and bunch charge, since the electrons are not ultra-relativistic up to the first cavity of ACC1, the first accelerating module.

The beam dynamics of the injector, which are governed by space charge forces, had been investigated by simulations only before a bunch arrival time monitor (BAM) had been available in front of the first bunch compressor. From the simulations values for the weights G_i had been estimated, which determine the accumulated timing change of the electron bunches $\delta t_{\mathrm{bunch}}$ in the injector, see [Lö9]. A mathematical representation of the combined effect is,

$$\delta t_{\mathrm{bunch}} = G_{\mathrm{gun}} \cdot \delta t_{\mathrm{gun}} + G_{\mathrm{laser}} \cdot \delta t_{\mathrm{laser}} + \delta t_{\mathrm{ACC1}} \tag{5.6}$$

where the factors G_i define the fractional part of timing change from the RF gun and the photo-injector laser. Since the combined timing change of the laser and the gun must cause an equal timing shift of the whole machine, both factors G_i have to add up to unity. This is still valid for additionally regarding effects from gun amplitude variations and from timing jitter caused in the first cavity of ACC1.

$$1 \equiv G_{\mathrm{gun}} + G_{\mathrm{laser}} \tag{5.7}$$

This condition is equivalent to the statement, that the timing change per degree phase change have to add up to 2.1368 ps/deg for an RF frequency $f_{\mathrm{RF}} = \omega_{RF}/2\pi$ of 1.3 GHz, where the individual contributions are given by

$$\delta t_{\mathrm{gun}} = \frac{\delta\Phi_{\mathrm{gun}}}{2\pi f_{\mathrm{RF}}} \qquad \text{and} \qquad \delta t_{\mathrm{laser}} = \frac{\delta\Phi_{\mathrm{laser}}}{2\pi f_{\mathrm{RF}}} \tag{5.8}$$

The time duration between two 1.3 GHz buckets amounts to 0.769 ns, corresponding to 360 deg phase advance, therefore a phase change of $\delta\Phi = 1$ deg results in

$$\frac{\delta\Phi\,[\mathrm{deg}]}{360\,[\mathrm{deg}] \cdot 1.3 \times 10^9 \mathrm{Hz}} \equiv 2.1368\,[\mathrm{ps}]$$

To verify these results, measurements at two different RF gun phases had been performed where both the laser phase and the RF gun phase had been changed by small amounts. The initial settings are shown in table 5.3. The normal operation point of the gun is determined by first performing a phase scan to identify the zero-crossing point where no charge escapes the gun and then shifting the phase by −38 deg w.r.t. the zero-crossing [LSM+10].

Table 5.3: Overview of initial settings of accelerator modules before starting the systematic measurements of the injector timing. The nominal operation point of the gun is 0 deg according to the phase scan as shown in fig. 5.10.

	INJ laser	Gun	ACC1
gradient [MV]	--	3.7	164.0
phase [deg]	−71.9	−1.0	−1.0
on-crest phase [deg]	--	0.0	−1.0

Figure 5.10 shows a gun phase scan during which the charge is monitored by the first toroid, 3GUN. The scan was performed at at medium charge, where space charge effects are reduced. The machine had been set-up with 30 bunches per macro pulse at a bunch spacing of 100 kHz and a bunch charge of 0.5 nC, at which BAM.1UBC2 had a shot-to-shot resolution of 10 fs. For each scan step the measured arrival times had been averaged over 20 macro pulses. In each case the individual scan steps had been automatically set with a pause of 10 seconds between sending the new set-point and reading the data of 20 successive macro pulses.

Figure 5.11 shows an arrival time slope across the bunch train, as it prevailed during the measurements, for five different laser phase offsets. The slope is not affected by the phase change, it rather causes a parallel translation in time. The mean arrival time across the macro pulse had been evaluated

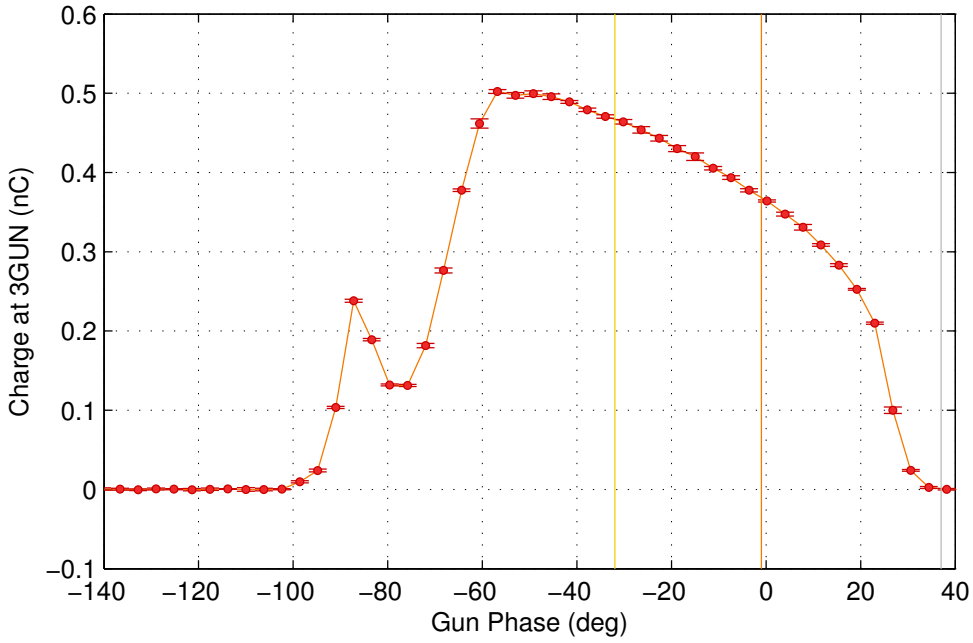

Figure 5.10: Dependency of measured charge at toroid 3GUN for a medium charge of up to 0.5 nC. The normal operation point of the gun is at about −1 deg in this case (orange line).

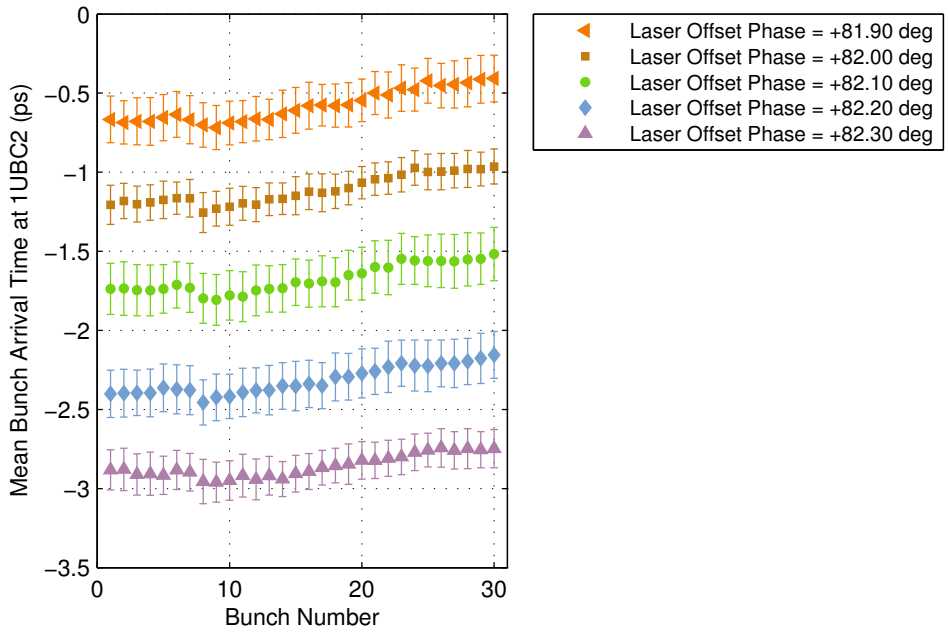

Figure 5.11: Measured arrival time slope across the bunch train, for five different laser phase offset values.

in dependence of the phase offsets for two different cases regarding the RF lock of the photo injector laser system (IL2). Normally the laser is synchronised in a PLL with reference to the machine timing system based on an RF master oscillator (MO). The intra-cavity phase and hence the timing of the laser pulse train is controlled with an EOM at 1.3 GHz and operated with a vector modulator (VM).

In the first step of the injector-timing investigation, the phase lock had been exceptionally established with reference to an LO signal generated from the optical timing system. For this purpose, the MLO pulse train provided via an optical fibre in the injector-laser hutch had been converted to an RF frequency comb using a 10 GHz PD, a bandpass filter and an LNA. The sixth harmonic of the MLO fundamental mode, i.e. 6 × 216 MHz was used to drive the EOM. The laser phase offset is the phase shift of the oscillator pulse train with respect to the 1.3 GHz (for details refer to [Sch11b]).

Figure 5.12(a) shows the result of the first two scans performed at the nominal operation point of the RF gun, in this case at −1 deg. The laser timing contributes with about 75 % to the electron bunch arrival time at BAM.1UBC2. The combined timing change amounts to 2.09 ps/deg, which deviates from the expected value by only 2.3 %.

In the next step, the RF gun phase had been set to a value at −31.0 deg off from the nominal operation point, where the influence of the gun on the electron bunch timing is excepted to be nearly zero, which could be verified by a gun phase scan, as shown in figure 5.12(b). In this case, the arrival time at BAM.1UBC2 is totally governed by the arrival time of the IL2 pulses on the photo cathode.

In the third step, the scans had been repeated at the same gun phase set-point but with the PLL of IL2 switched back to the RF timing reference. As can be seen in figure 5.12(c) the timing change corresponds to the expected value of 2.14 ps/deg within an error range of 2 % and is caused by the laser pulse timing only.

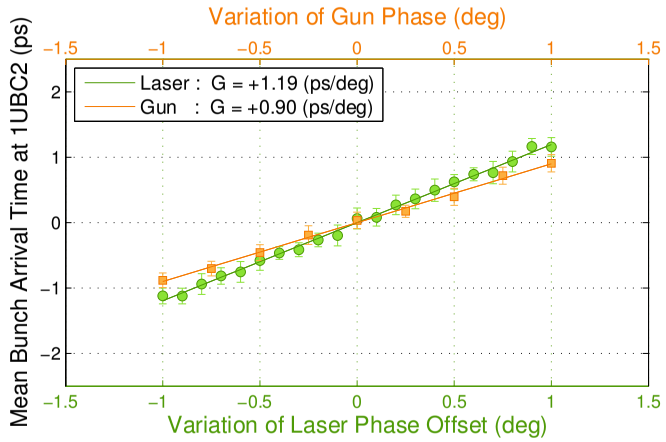

(a) Injector laser locked to optical timing reference. RF gun at nominal operation point.

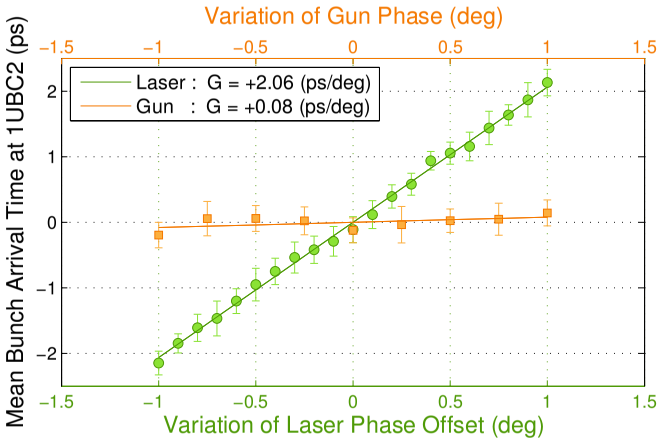

(b) Injector laser locked to optical timing reference. RF gun −31.0 deg off from nominal operation point.

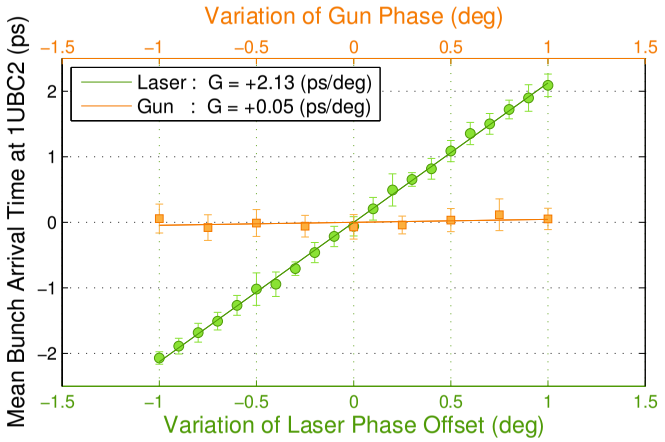

(c) Injector laser locked to RF timing reference. RF gun −31.0 deg off from nominal operation point.

Figure 5.12: Averaged arrival times across the macro pulse, evaluated for two different cases of the RF lock of the IL2

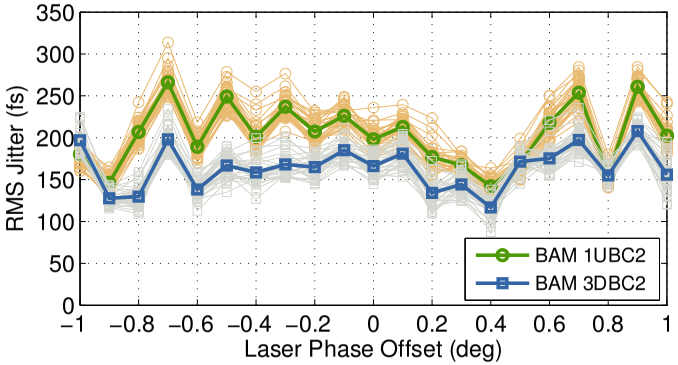

(a) Injector laser locked to optical reference.

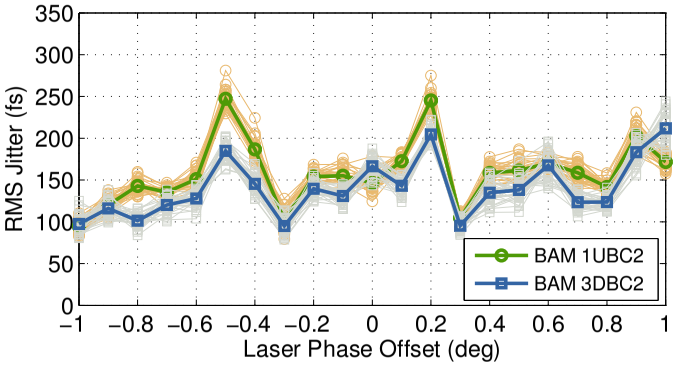

(b) Injector laser locked to RF machine reference.

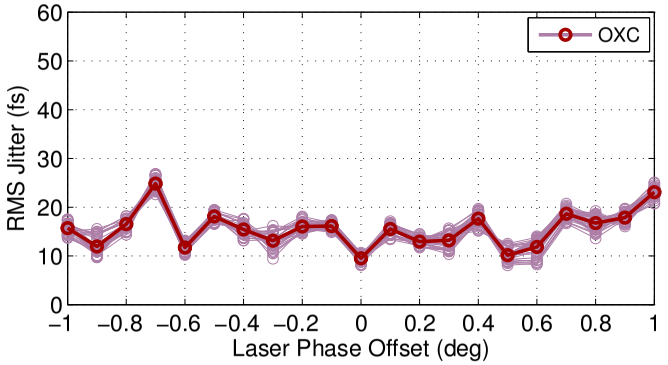

(c) Injector laser locked to optical reference. Nominal laser phase operation point is +82.9 deg at 1.3 GHz.

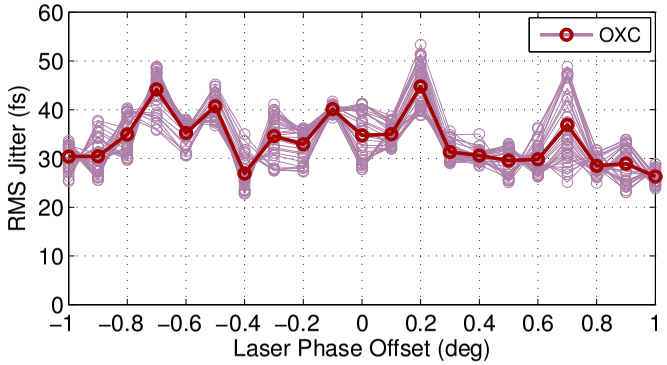

(d) Injector laser locked to RF machine reference. Nominal laser phase operation point is −70.6 deg at 1.3 GHz.

Figure 5.13: Evolution of arrival-time jitter while changing the laser phase-offset. The RF gun phase was set to a point of zero influence on the electron bunch arrival time. Plot 5.13(a) and 5.13(b) show the arrival-time jitter of electron bunches during 20 macro pulses. The 30 overlaid curves (in lighter color) correspond to 30 electron bunches per macro pulse. Plot 5.13(c) and 5.13(d) show the rms arrival-time jitter of 30 laser oscillator pulses during the same scans, measured with the OXC.

Figure 5.2.1 shows the change in RMS arrival-time jitter during the performed laser phase-offset scans, for both laser oscillator pulses (lower row) and electron bunches (top row). Those evaluations were done with the gun set to a phase of zero influence on the electron bunch arrival time. The arrival time of the infra-red (IR) laser pulses of IL2 was measured relative to the optical reference by use of an optical cross-correlator (OXC) (details can be found in [Sch11b]). It is worth to mention, that the arrival time of the IL2 oscillator pulse train does not necessarily determine the arrival time of the UV laser pulses on the photo cathode, since the oscillator is followed by three stages of laser amplifiers and a wavelength-conversion stage (details on the injector-laser system can be found in [WTSS11]). Especially the wavelength-conversion stage is likely to show a large influence on the laser pulse arrival time, which could not be measured directly up to now. For this purpose, a second OXC operating in the UV spectral range is required.

The OXC offered the possibility of an out-of-loop detection of the laser-to-RF (L2RF) lock of the injector laser. Although, there is no strong correlation between the measured arrival-time jitter values of IL2 pulses and electron bunches, there are some distinctive features visible. Nevertheless, those oscillatory structures and peaks observed in both, laser pulse and electron bunch arrival time, compare figure 5.13(a) and figure 5.13(b), are most probably caused by random fluctuations and have no significance. During the same scan repeated with IL2 locked to the RF reference the mean arrival time jitter of the laser pulses is increased by a factor of 2. In this case, no clear dependence on laser pulse and electron bunch timing jitter is visible (figure 5.13(c) and figure 5.13(d)). Note that the phase offset values around which the scans were performed are different for both PLL configurations. The normal operation points of the laser phase offset controlled by the VM differ by 153.5 deg between RF and optical timing reference.

Even though the IL2 pulse jitter, measured out-of-loop with the OXC could be remarkably decreased by locking the injector laser to the optical reference, the arrival time jitter of the electron bunches is not decreased as well. Instead, the arrival time jitter measured at BAM.1UBC2 is larger when the injector laser is locked to the optical reference (figure 5.13(a)) and it is lowered by about 100 fs when the injector laser is locked directly to the RF MO (figure 5.13(b)). This effect can be explained by the following: the RF reference is distributed from the MO to the optical master laser, the injector laser, the gun and all other accelerator components. The MLO is locked in narrow-band to the RF MO and delivers the stabilised optical reference to the BAM and the OXC. In the normal operation mode both the injector laser and the gun are locked to the RF reference and common mode drifts and jitter between both subsystems are excluded. But when the injector laser is locked to the optical reference there is an additional chain in between, containing the MLO, its RF-lock to the MO and the distribution from the optical reference to the injector laser. In this signal chain timing drifts and jitter occur which are not in common mode with the RF-lock of the gun. This additional timing jitter is visible in the arrival time measurement behind the gun.

5.2.2 Influence of Piezo-Tuner in First Cavity of ACC1

As mentioned in the section 5.2.1 before, the simulations on the influences of the electron bunch timing in the injector of FLASH had only indicated a small contribution of ACC1, by about 6 % [Lö9]. Lately, measurements have been performed revealing an unexpected large effect from the amplitude and phase tuning of the first cavity of module ACC1 (C1.ACC1). For the measurement, the gradient and phase during the flat-top time of the RF field was adjusted by use of a piezoelectric actuator. This actuator excites mechanical vibrations of the cavity shortly before the RF field is filled in, allowing for a fine tuning of the resonance frequency and, therefore, influencing the phase and gradient slopes. For details compare section 1.3 and section A.1.

The voltage of C1.ACC1-piezo had been varied from 0 to 20 V during a closed-loop operation, i.e. the vector sum of the phases and amplitudes from all cavities remained constant. Figure 5.14 shows the change of amplitude and phase at 1.3 GHz in this cavity during the scan. The value has been recorded at the temporal position of bunch number 1 and had been averaged over 20 macro-pulses. Before the scan, the phase of the accelerating RF field was set to 11 deg off-crest with a nominal gradient of 19.49 MV/m. The total change in energy as function of the piezo-voltage is calculated from the vector sum, regarding the total cavity length of 1.038 m:

$$\Delta E(V) = \left[A_0 \cos\left(2\pi \frac{\Phi_0}{360}\right) - A(V) \cos\left(2\pi \frac{\Phi(V)}{360}\right) \right] \cdot 1.038 \tag{5.9}$$

The first unforeseen observation is, that the tuning of the cavity C1.ACC1 not only influences the energy gain of the electron bunches, as expected, but also has a large impact on the beam orbit. This might happen if the symmetry axis of the cavity is not aligned to the reference axis of the beam line, but is slightly tilted. If the accelerating RF field amplitude changes this could cause a kick on the electron bunches.

The effect had been observed at different locations of FLASH, compare figure 5.15 where the orbit variation for the first bunch averaged over 20 macro pulses is shown. The largest effect in both transverse planes is measured directly behind ACC1. At position 2UBC2, i.e. behind module ACC39 the orbit change in x is as large as in front of this module, but with opposite sign. The BPM.2UBC2 is located only about 1 m behind the first BAM, i.e. BAM.1UBC2. Further downstream the effect of orbit change is less pronounced but still up to ±100 µm depending linearly on the piezo-actuator voltage. In the vertical plane the orbit change directly behind ACC1 is about twice as large as in the horizontal plane, but further downstream the orbit variations are less pronounced. At position 2UBC2, the change of beam position during the piezo scan is stronger in x than in y. In the latter case, there is only a weak linear dependency on the piezo-voltage of C1.ACC1.

To point this out, in figure 5.18 the orbit change in x (lower row) and y (upper row) during the voltage scan is shown for BPM.3GUN on the left hand side and for 2UBC2 on the right hand side. In this illustration it is clearly seen that the orbit change in y is more pronounced than in x near the position of BAM.1UBC2. Furthermore, it can be seen, that the beam position is changing equally across the macro pulse, i.e. the curves are displaced parallel. Figure 5.17 shows the measured arrival times of the macro pulses during the performed piezo-scan. Also here, the slope across the macro pulse does not change, but the curves are displaced parallel, depending on the actuator voltage set-point.

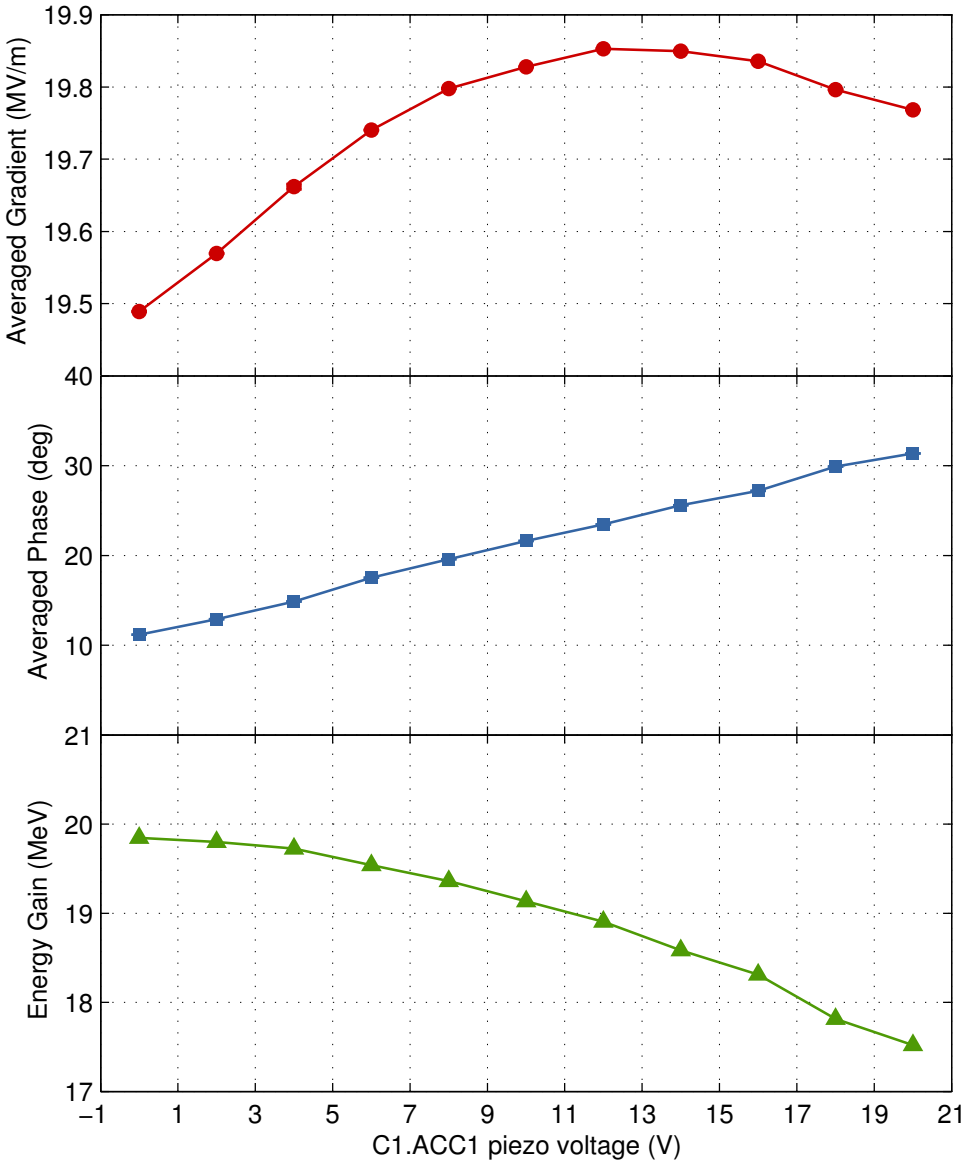

Figure 5.14: Measurement of the amplitude and phase in cavity C1 of ACC1 during the piezo-actuator scan. The plot in the lowermost row shows the calculated energy gain in cavity C1.

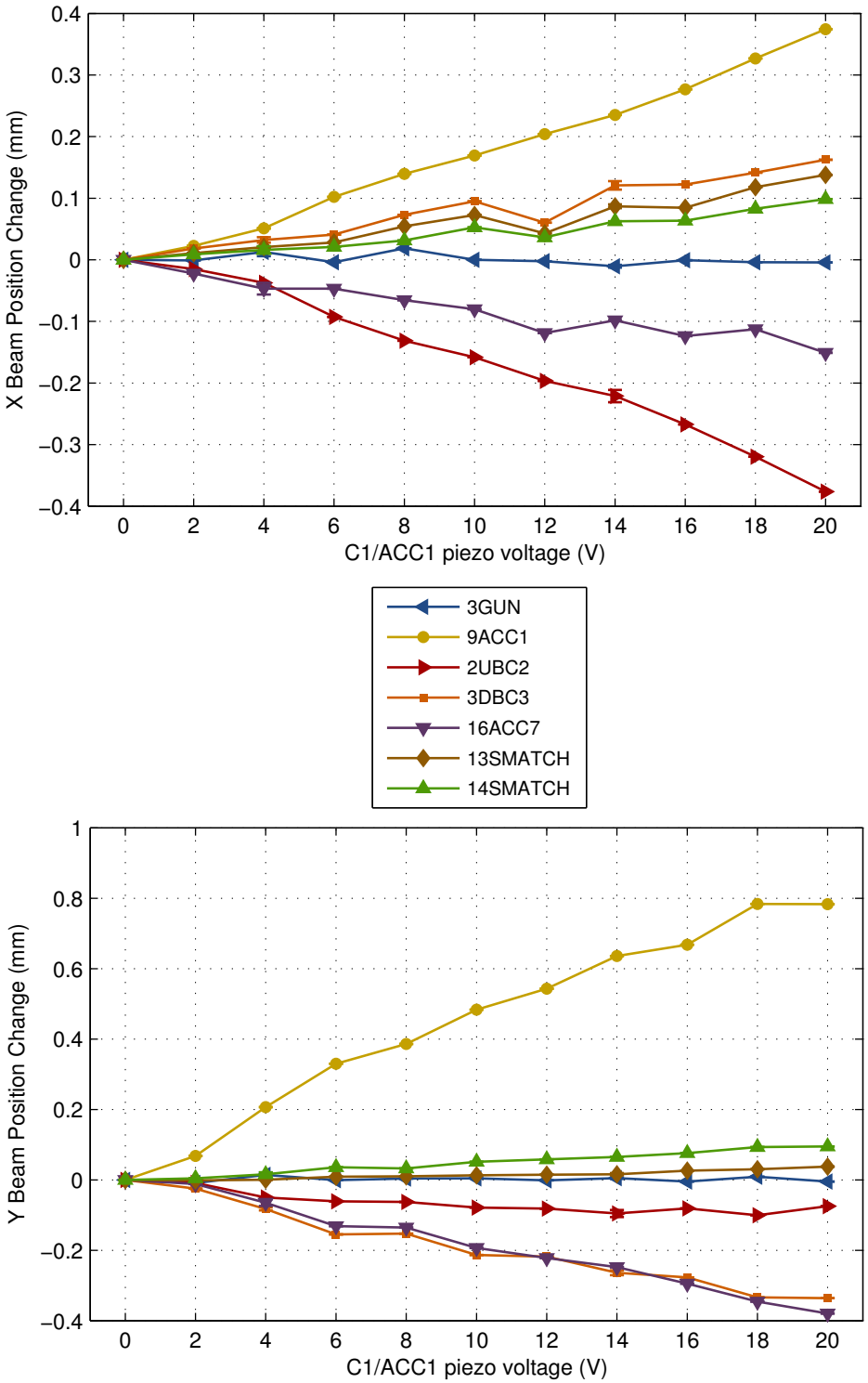

Figure 5.15: Beam orbit changes in x and y during the piezo-actuator scan, measured with different BPMs at those locations denoted by the caption entries. (the names describe the positions of the monitors at FLASH, compare illustrations 1.2 and 1.3 on pages 4 f.)

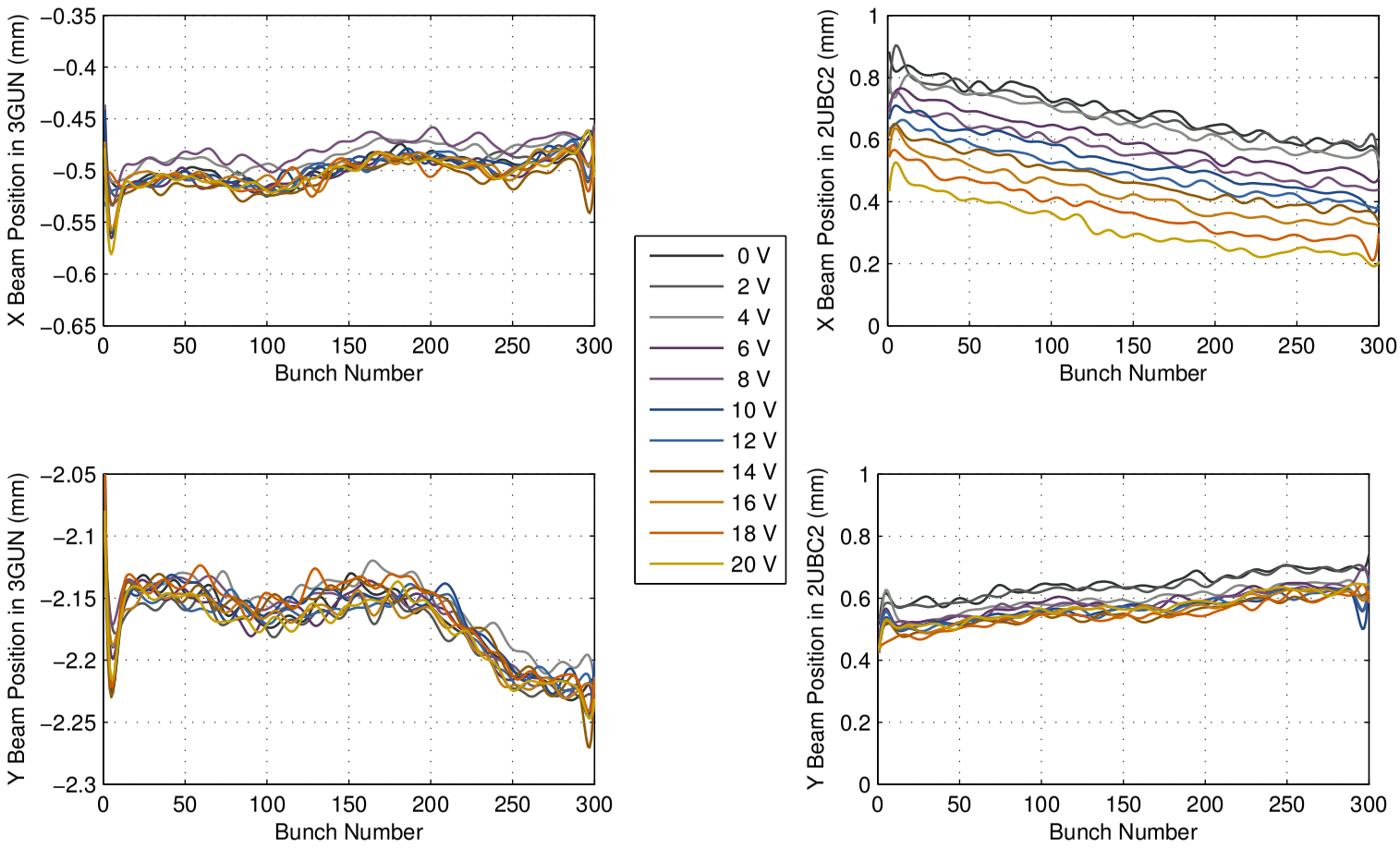

Figure 5.16: Beam position change in horizontal and vertical plane during the piezo-voltage scan of the actuator in cavity C1.ACC1. Comparison between the initial beam orbit at BPM.3GUN, i.e. in front of ACC1 and the beam orbit at BPM.2UBC2, i.e. behind BAM.1UBC2.

Although the resolution of the BAM had been relatively low with 30 fs only, the effect of timing shift during the cavity tuning is with $\Delta t_{\mathrm{BAM1}} \approxeq 1\,\mathrm{ps}$ significantly large. In figure 5.18 the effect is shown for the mean arrival time of the macro pulse. A linear fit of the measured data delivers the following slope:

$$\begin{aligned} \delta t &= a_1 \cdot \frac{E - \langle E \rangle}{\sigma_E} - a_0 \\ \text{with} \quad \langle E \rangle &= 18.99\,\mathrm{MeV} \quad \text{and} \quad \sigma_E = 0.81\,\mathrm{MeV} \\ a_0 &= 0.382\,\mathrm{ps} \quad \text{and} \quad a_1 = -0.266\,\mathrm{ps/MeV} \end{aligned} \tag{5.10}$$

When calculating the total effect, the timing change across the total scan range amounts to 1.16 ps. In recent studies the orbit dependency of the arrival time measurement has been investigated, compare figure 4.6 of section 4.2.2 on page 112. But in case of BAM.1UBC2, those measurements revealed no correlation for horizontal orbit changes and a clear linear dependence in the vertical plane. Since in the case of the piezo scan the beam position changes at 2UBC2 were most pronounced in the horizontal plane, this effect cannot explain the observed arrival time change at 1UCB2. A possible explanation of this observation is related to the fact, that the electron bunches are not yet relativistic when entering C1.ACC1. Therefore, changes in the energy gain do have an effect on the actual gain in velocity which causes arrival time changes in cavity C1.ACC1 and further downstream of the module. To verify these results, the measurements should be repeated after the shut-down work at FLASH in 2012.

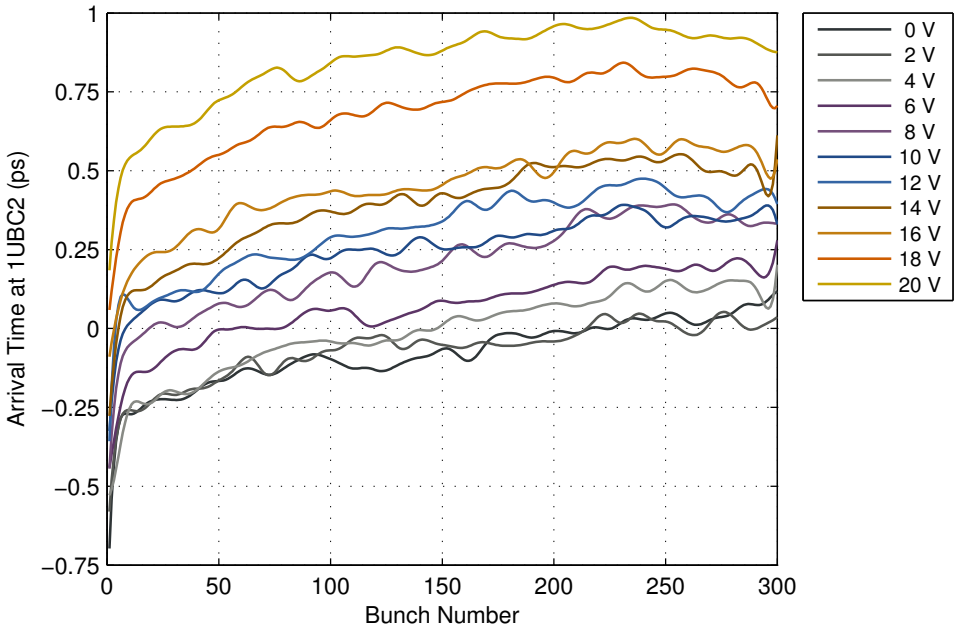

Figure 5.17: Measured arrival times during the piezo-actuator scan in C1.ACC1. Values are averaged over 20 macro pulses.

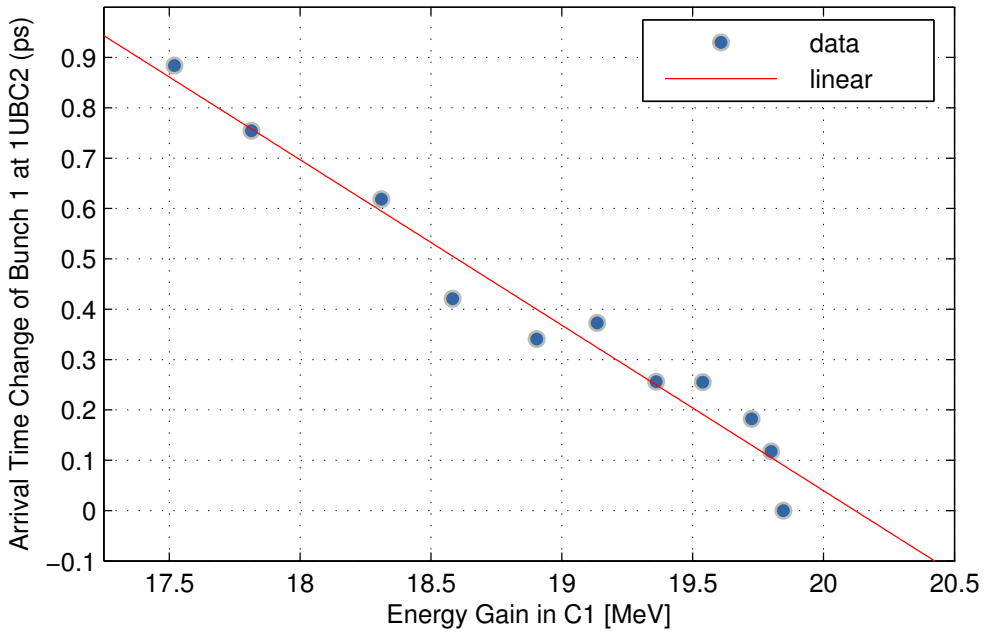

Figure 5.18: Change of the mean arrival time of the macro pulse at BAM.1UBC2 in dependency of the energy gain in C1.ACC1 during the piezo-actuator voltage scan.

5.2.3 Long-term Stability Studies

In this section, an excerpt from the enormous amount of arrival time data is presented. It has been collected during a user experiments period in 2011. In a few shifts an arrival time stabilisation of the free-electron laser (FEL) pulses, and therefore, of the electron bunches has been specially enquired. These occasions have provided beneficial opportunities to test and further develop the beam based feedback (BBF) algorithms. In those shifts, the feedback has been applied to either only compensate for slow drifts or to regulate solely on intra-train fluctuations or both in combination. The *slow* and *fast* BBF systems are introduced in chapter 1, section 1.3 on page 15 ff. In the following, three examples for the mentioned feedback applications are given. The data has been analysed under two aspects: first, to evaluate the long-term stability of the BAMs themselves, and second, to evaluate the long-term stability of the feedback systems.

2011, 3rd to 4th of July: slow arrival time feedback

In the beginning of July in 2011, a slow feedback has been added which regulates the amplitude set-point of ACC1, to stabilise the bunch arrival time measured by BAM.3DBC2, behind the first bunch compressor. The MATLAB™ GUI provides an adjustment of the arrival time set-point and the proportional feedback gain. To prevent the controller from applying too large amplitude changes, strict set-point limits and an averaging of the arrival time data from 20 successive pulses is included. Although the feedback is currently written in a MATLAB™ environment, it can be handled by the machine operators from the normal control system panels.

A short-term evaluation during the course of 1 hour, before and after commissioning the new slow feedback (FB) yielded the results as shown in table 5.4. During both measurements, all other

Table 5.4: Statistical evaluation showing the benefit of the slow arrival time feedback regulating the amplitude set-point of ACC1. The out-of-loop data was measured with BAM.18ACC7 during a course of 1 hour, before and after switching on the feedback. The values given, are the calculated peak-to-peak and rms variations during one hour each.

	FB off		FB on	
BAM	Pk-Pk [fs]	RMS [fs]	Pk-Pk [fs]	RMS [fs]
3DBC2	640	83.00	390	52.57
18ACC7	940	151.4	480	72.1

slow FBs have been switched on, i.e. the phase stabilisation of ACC1 and ACC23 as well as the stabilisation of beam energy with module ACC45. The first quick evaluation of the additional amplitude stabilisation in ACC1 showed a significant improvement of the electron bunch timing stability. Both, the peak-to-peak variation of the arrival time and the RMS arrival time jitter at BAM.18ACC7 have been reduce by a factor of two. By mid of July in 2011, a clone of the described slow arrival time FB has been adapted to regulate the amplitude of ACC23. For this purpose, the information from either BAM.4DBC3 or BAM.18ACC7 can be used, since both are located in the straight section behind BC3.

The data presented here has been recorded for 19 hours between the 3rd and the 4th of July. During this period four slow feedbacks had been switched on, regulating on the following modules and parameters:

1. ACC1 phase relative to the bunch compression measured with a BCM behind BC2
2. ACC1 amplitude relative to the bunch arrival time at BAM.3DBC2
3. ACC23 phase relative to the bunch compression measured with a BCM behind BC3
4. ACC45 amplitude relative to the bunch energy, measured behind ACC67

Table 5.5 gives an overview on the initial settings of the acceleration modules. Figure 5.19 shows the arrival time of the macro pulse, measured with BAMs No. 1, 2 and 4, i.e. BAM.1UBC2, BAM.3DBC2 and BAM.18ACC7. The first monitor is located in front of BC2. The bunch arrival time at this location is in general not influenced by amplitude and phase adjustments of the field vector sum in ACC1. It rather reflects the timing (in)stability of the injector, i.e. injector laser and RF gun.

During the whole time, an out-of-loop timing stability of about 55 to 65 fs (RMS) for each of the 30 bunches has been maintained, calculated in a sliding window of 10 s with the data from BAM.18ACC7. The RMS jitter of the mean macro pulse arrival time has been measured to be about 37 fs, in a sliding window of 10 s. The machine operators reported, that the SASE level has been quite stable without the need for manually tuning any machine settings. During the presented time period,

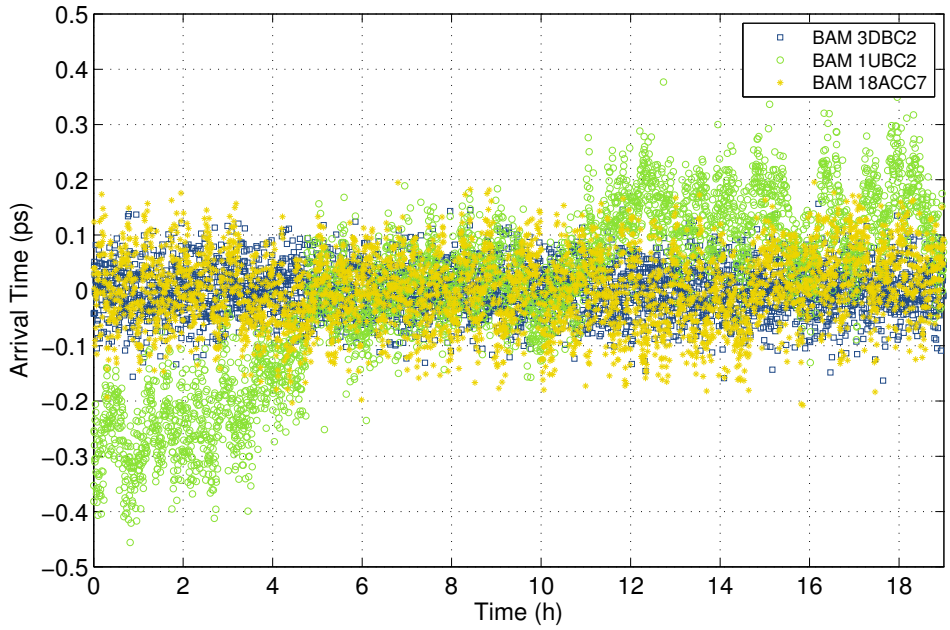

Figure 5.19: Figure showing the arrival time of the macro pulse during 19 hours, recorded between the 4rd and the 5th of July. During the user experiment shift four individual, slow feedbacks had been switched on, regulating on RF amplitudes and phases of different modules. The bunch arrival time has been measured at three locations with BAM No. 1, 2 and 4, i.e. BAM.1UBC2, BAM.3DBC2 and BAM.18ACC7.

the FEL had been set to an energy of 681.2 MeV delivering SASE light at ~ 13.74 nm with 50 to 60 µJ.

Another incident has been observed in the data, which is most probably not related to the slow feedback implementation. Figure 5.20 shows a statistical evaluation of the amplitude and phase stability across the bunch train containing 30 bunches, of the RF Gun and all powered modules except for ACC23. Data from a time frame of 30 min is picked out randomly, but is representative for the total time period of 19 hours. The RMS fluctuations shown here, are typical values which can be achieved by the normal field-probe based LLRF controller, compare table 5.6. Only for ACC1 at irregular occasions and for a limited fraction of all bunches, a temporal increase in RMS flucations is observed, compare plot (b). At these incidents, the mean value of both amplitude an phase devi-

Table 5.5: Overview of initial settings of accelerator modules during the slow arrival time FB shift.

	Gun	ACC1	ACC39	ACC23	ACC45	ACC67
gradient [MV]	3.744	163.7	18.9	330.6	219.9	0.0
phase [deg]	−1.24	+3.08	−14.65	+23.22	+9.3	–
on-crest phase [deg]	−2.0	0.0	−3.0	−1.0	1.0	–

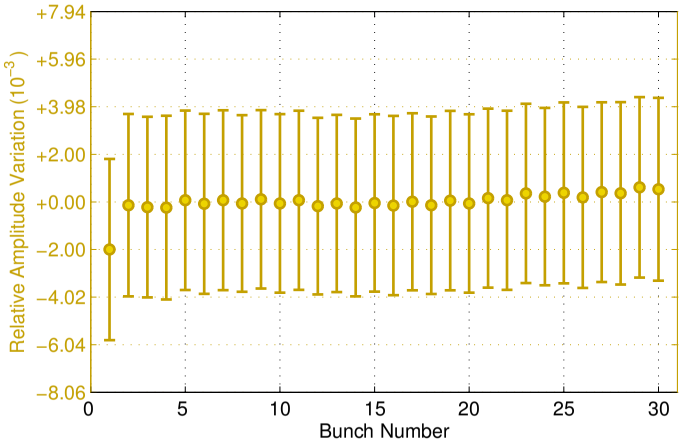

(a) RF Gun - amplitude

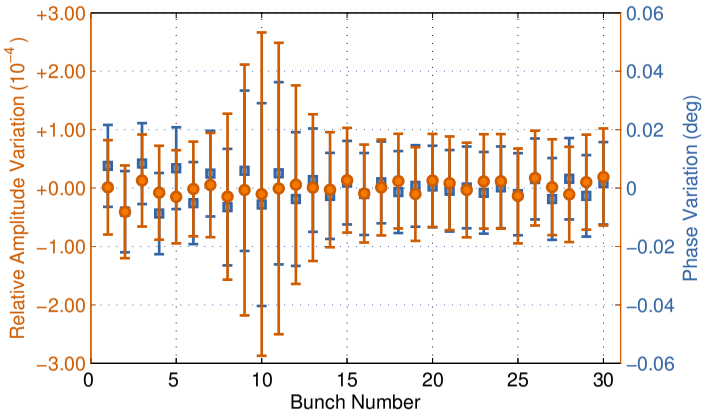

(b) ACC1 - amplitude (orange circles) and phase (blue squares)

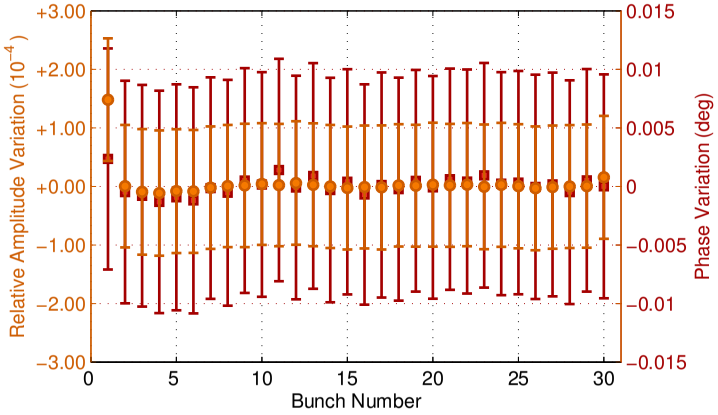

(c) ACC39 - amplitude (orange circles) and phase (red squares)

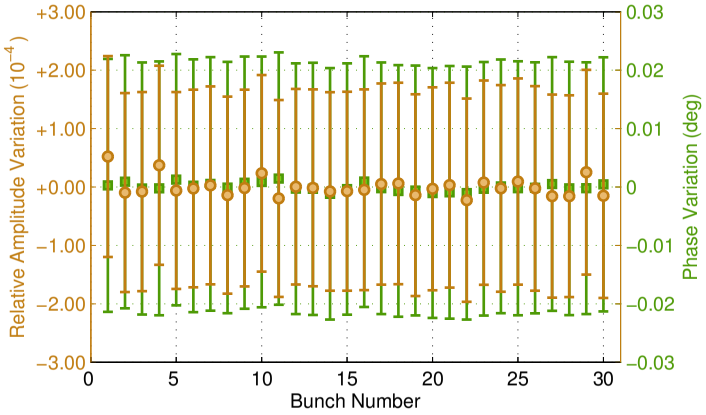

(d) ACC45 - amplitude (light brown circles) and phase (green squares)

Figure 5.20: Relative amplitude and phase variations. For ACC1 two individual slow feedbacks had been regulating the phase and amplitude. The phase was stabilised for constant compression and the amplitude for constant arrival time after BC2. The amplitude of ACC45 had been stabilised by a slow energy feedback. In each case, the mean and RMS values for 15 000 events (30 min duration) are plotted.

Table 5.6: Overview of the field vector sum stability in different acceleration modules. The RMS values for 15 000 events (30 min duration) have been calculated.

	Gun	ACC1	ACC39	ACC45
gradient [rel. units] $\times 10^{-4}$	39.8	0.95	1.1	1.7
phase [deg]	–	0.018	0.009	0.022

ates by small amounts, also resulting in a temporary increase of arrival time offset for the affected bunches by a maximum of about 100 to 200 fs. Both, the extent over neighbouring bunches as well as the location within the bunch train is not the same for all incidents. This region rather migrates back and forth during the flat-top duration of the RF field in the cavity. During the whole 19 hours a deviation of more than 5.0×10^{-4} in RF amplitude is observed for about 17.5 percent of all events.

This effect is probably related to short-term instabilities of the learning feed forward (LFF). Before evaluating the presented bunch-resolved data, this effect has not been identified yet. Though, it is a hint at which part of the complex combination of feed forward and feedback algorithms spontaneous instabilities can appear, which have the potential to deteriorate the overall systems stability, especially during fast BBF applications.

2011, 12$^{\text{th}}$ to 14$^{\text{th}}$ of June: intra-train longitudinal feedback

During this featured time frame, FLASH had been set up to 30 bunches at 250 kHz bunch repetition rate and 0.2 nC bunch charge. During a course of 35 hours in a row, the arrival time data from all four BAMs had been recorded, compare figure 5.21. The arrival time of bunch No. 15 is shown for every 200$^{\text{th}}$ macro pulse. The solid lines are mean values, calculated over a sliding window of 10 s. Besides three slow FBs, the intra-train arrival time feedback on ACC1 has been switched on:

1. ACC1: slow FB on RF phase set point
2. ACC1: fast FB on RF amplitude and phase shape
3. ACC23: slow FB on RF phase set point
4. ACC45: slow FB on RF amplitude set point

Since by that time, the BAM-server sent erroneous data to the DAQ system, a thorough analysis was required to filter out the corrupt fractions. In a first step, all macro pulses, or events, have been excluded, at which the arrival time data from at least one BAM was missing. In a second step, all events have been identified, which showed successively identical arrival time data. For those incidents, only the first event has been kept, the subsequent, identical events have been filtered out. Finally, only those events have been considered for which data from all of the four BAMs has been available after the preceding filtering. Due to this, up to 60 % of the total amount of stored events were lost. By mid of June 2011 this software fault has been removed completely, so that the BAM-server has been sending only trustworthy data to the DAQ ever since. Only a small fraction of events, i.e. typically below

2.5 %, is lacking. The BAM-server checks at the beginning and at the ending of each data processing run, if the particular general event numbers are identical. If this is not the case, the arrival time data is not sent to the DAQ.

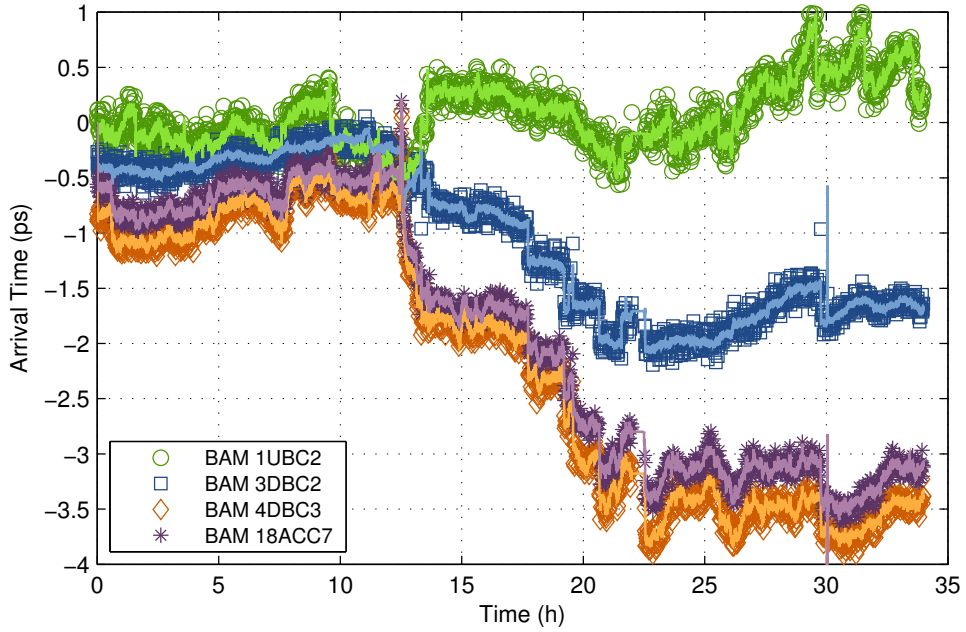

Figure 5.21: Arrival time data from all four BAMs during the course of 35 hours in a row. The arrival time of bunch No. 15 for every 200th macro pulse is plotted. The solid lines depict the mean values, calculated over a sliding window of 10 s.

During the one and a half days with continuously running feedbacks, at several occasions amplitude and phase set-points of different modules have been adapted to compensate for a slow drift in SASE intensity. Especially the RF gun amplitude and phase, as well as the phase of ACC1, have the largest impact on the achieved SASE level. For example, after 12.5 h (on 2011-06-13 at around 08:30 am), both the bunch charge and the ACC1 slow FB set point had been slightly changed to compensate for a decreasing SASE level. Obviously, the change in bunch charge had large impact on the arrival time downstream of both bunch compressors. Any set-point adjustments inside of the injector, i.e. in front of ACC1, are visible in the arrival time measured at BAM No. 1. Depending on the location and extent of adjustment, this also affects all other RF settings of the acceleration modules further downstream. Within the mentioned time frame, there is clear anti-proportional behaviour between the arrival time measured at BAM.1UBC2 and at BAMs No. 3 and 4. Despite the continuously operated FBs, a repeated, manual tuning of the machine settings had been necessary to maintain a SASE level of about 11 µJ during the 1.5 days.

All of those set-point adjustments are clearly seen in the presented data (fig. 5.21) in form of fast, pronounced steps in the arrival time, downstream of the according module. Nevertheless, after a manual set-point adaptation, the combined FBs re-established stable conditions. Those are visible as short, temporal islands of flat arrival time, especially inside of the in-loop signal of BAM 2. The

out-of-loop measured arrival times at BAM No. 3 and 4 are less stable. This is related to the fact, that with the RF module and bunch compressor additional timing jitter sources are located between BAMs No. 2 and 3. In BC3, the strong longitudinal compression of the bunches was controlled with a slow set-point adaptation of the RF phase in the preceding module. The data clearly shows, that the complicated interplay of beam dynamics cannot be controlled by individual, separated feedback systems. Any set-point change in the front part of the linac affects set points further downstream.

In the following, some aspects concerning the functionality and performance of the bunch arrival time monitors are shortly discussed. Already from figure 5.21 it is visible, that the difference between arrival times measured with BAM.4DBC3 and BAM.18ACC7 is not constant over time. Between both monitors, no dispersive sections, but only four RF acceleration modules are located. Since the electron bunches are already ultra-relativistic at this location, the modules can be viewed as drift section. Any change in bunch energy does not significantly affect the electron velocity.

The BAMs can only measure relative arrival times, i.e. relative to the optical reference. Therefore, at any location, one can add or subtract an arbitrary offset from the determined arrival time, without constraints. This offset has to be constant and equal for the whole data set. If choosing the arrival time offsets for BAM No. 3 and No. 4 such, that the mean value of the determined arrival time is the same for both monitors, the difference signal between both should be zero, in principle. Due to uncorrelated errors in the signal detection and processing chain in both BAMs, the difference signal is expected to show a normal distribution around zero with a certain RMS range. This value would then be a worst case measure for the actual accuracy with which the arrival time at two different locations of the linac can be determined.

Figure 5.22 shows the difference signal, or rather the error signal, between BAM.4DBC3 and BAM.18ACC7 from the data spanning over 34 hours. The same data is illustrated in two distinct ways: figure 5.22(b) contains the time-domain plot of the error signal during the total time span. Figure 5.22(a) shows a cumulative distribution of the difference between both monitors for each of the 30 bunches. If only random, uncorrelated error sources would contribute to the error signal the distribution would be simply Gaussian-shaped. But since the curve in this illustration rather resembles a superposition of many normal distributions, one can conclude, that there has to be a systematic error source within the arrival time detection. On short time-scales, this systematic failure does not appear. Its existence has been suspected earlier, but has not been demonstrated clearly before the long-term arrival time data from the DAQ had been available. When comparing figures 5.22(b) and 5.21, the variations in the difference signal are partly correlated to slow and small bunch arrival time changes, but not strictly.

As mentioned above, the RMS value of the difference signal can be used as an estimation of the overall resolution of the arrival time detection process. This is depending on the time frame used for the statistical evaluation, since over shorter time scales less fluctuations are accounted for. Figure 5.23 shows the calculated RMS fluctuations of the determined difference signal between BAMs No. 3 and 4. Different time frames from 2.5 min to about 60 min are shown. To get a measure of the detection resolution, the values have to be divided by $\sqrt{2}$, since one can assume, that both monitors are independent from each other. Nevertheless even over a few minutes, the resolution does not reach values below 17.5 fs. This is in contrast to the measurements performed by Florian Löhl four years ago, where he could show a resolution of below 6 fs over 9 min [Lö9]. To explain this

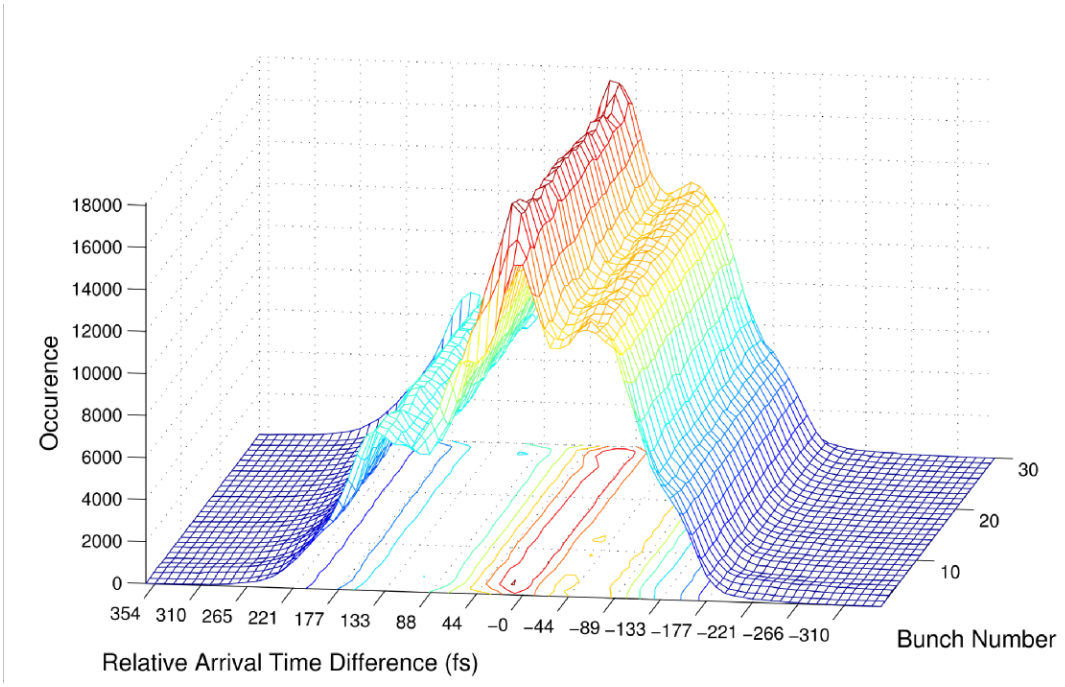

(a) Histograms showing the cumulative distribution of the difference signal between BAMs No. 3 and 4, for each of the 30 bunches.

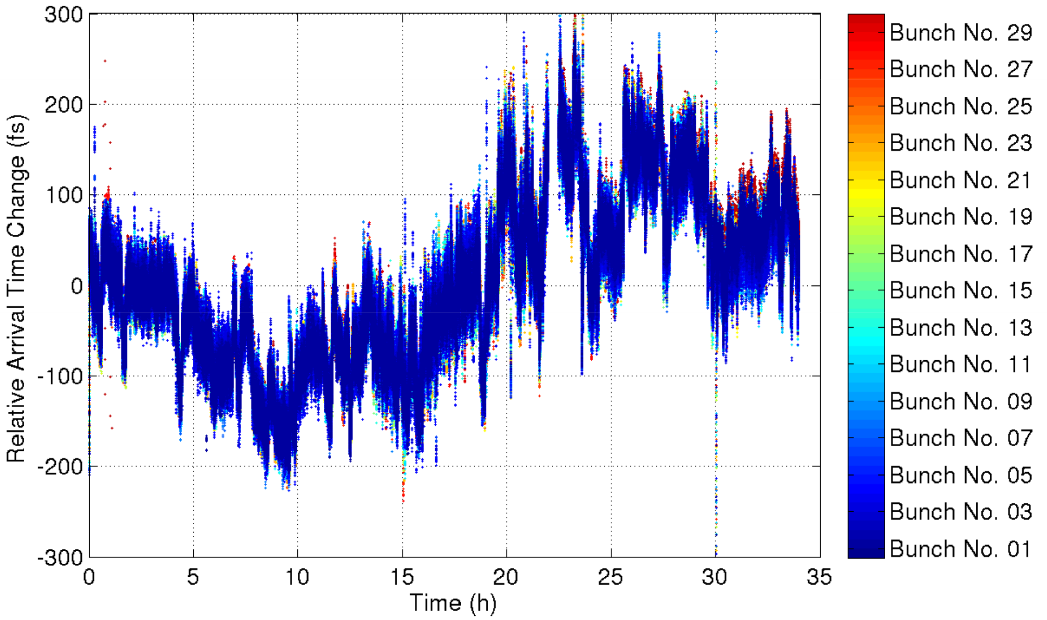

(b) Time domain plot, showing the difference signal between BAMs No. 3 and 4. The various bunches are colour coded.

Figure 5.22: Difference signal between BAM No. 3 and 4 during 34 hours of operation in two distinct illustration types.

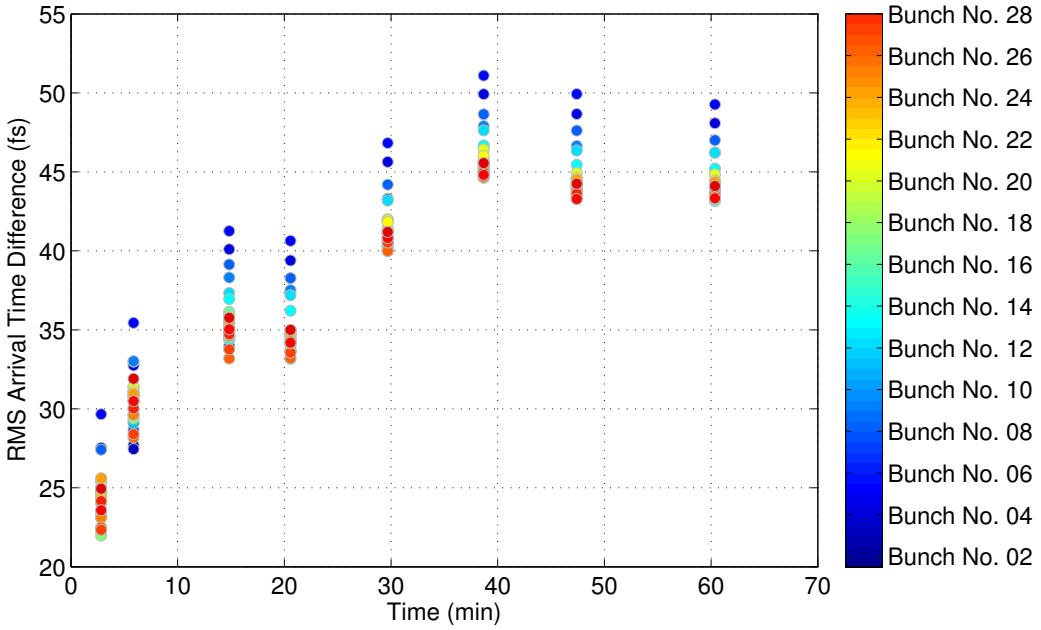

Figure 5.23: Calculated RMS fluctuations of the determined difference signal between BAMs No. 3 and 4, determined for different time frames. To obtain an upper limit for the accuracy of the arrival time measurement at each BAM, the RMS values have to be divided by $\sqrt{2}$.

massive deviation, one has to account for a variety of possible reasons:

- Compared to the earlier investigations which involved only two individual fibre links and the two, first BAM prototypes, all of the four current BAMs are an integral part of the complex, more comprehensive LbSyn system. Since the latter is still in the development phase, an unwanted and complicated interplay or cross-talk between the optical signals within one link or between two or more links can possibly deteriorate the overall system performance.
- Especially BAM.4DBC3 and BAM.18ACC7 are more than four years old. A decreased performance might indicate first effects from components ageing.
- Most likely error sources are failures and deficiencies from the read-out electronics, which do not yet comply with the specifications, for example regarding instabilities of the internal clock generation. The tests performed by Florian Löhl which revealed a much better BAM performance, had not been carried out with the present ACB electronics; instead the early tests involved an external clock generation.

The latter possible error source is related to the construction of the ACB, which is applied for all BAMs. A detailed description can be found in section 3.1.4 on page 79 ff. Inside of the electronic board, first a 108 MHz signal is generated from the unmodulated laser pulses, which are split inside of the BAM box in front of both detection channels. For the purpose of a clock generation, the 216 MHz laser pulses are detected by a narrow-bandwidth photodiode and converted to a rectangular signal at half the frequency using standard, digital electronics. The rising slope of this signal is

resynchronised to the external 10 Hz machine trigger, to be synchronous to both the general event (macro pulse) and to every second laser pulse arriving at the 108 MHz ADCs. Most probably, this clock resynchronisation is the weakest part in the detection chain. Failures can appear, since the detection and clock signal generation is very sensitive to the optical power level and to EMI from the surrounding electronics. Just lately, it was suspected, that within the fibre link transmission line unwanted ghost signals propagate with the wanted link pulses. Those could in principle be transmitted from the link ending through the total fibre-optics of the BAM up to the read-out electronics. There, those ghost signals could affect the electronic synchronisation of the detection process. This requires further thorough investigations.

2011, 15th of July: slow and fast arrival time feedback

In this section, an exemplary excerpt of arrival time data is presented, measured during a machine operation which used all available slow and fast feedbacks:

1. ACC1: slow FB on RF phase set point
2. ACC1: slow FB on RF amplitude set point
3. ACC1: fast FB on RF amplitude and phase shape
4. ACC23: slow FB on RF phase set point
5. ACC23: slow FB on RF amplitude set point
6. ACC23: fast FB on RF amplitude shape
7. ACC45: slow FB on RF amplitude set point

Table 5.7: Overview of initial settings of accelerator modules during the combined slow & fast arrival time FB shift.

	Gun	ACC1	ACC39	ACC23	ACC45	ACC67
gradient [MV]	3.76	164.4	18.5	329.0	332.7	165.0
phase [deg]	−5.70	+3.70	−12.20	+22.50	4.0	2.0
on-crest phase [deg]	−3.0	0.0	0.0	0.0	0.0	0.0

The regulation range of the fast, intra-train arrival-time feedback is restricted to very narrow limits, to avoid instabilities in the regulation chain. But due to those restrictions, the fast BBF in the current implementation cannot compensate for a slow drift of the average RF amplitude and phase vector sums. For this purpose, the slow FBs had been included, to allow for a long-term operation of the fast FB, e.g. over more than 8 hours.

The initial machine settings are given in table 5.7. Figure 5.24 shows the arrival time data from all four BAMs for bunch No. 50, during a time frame of 30 min. During this time, FLASH had been

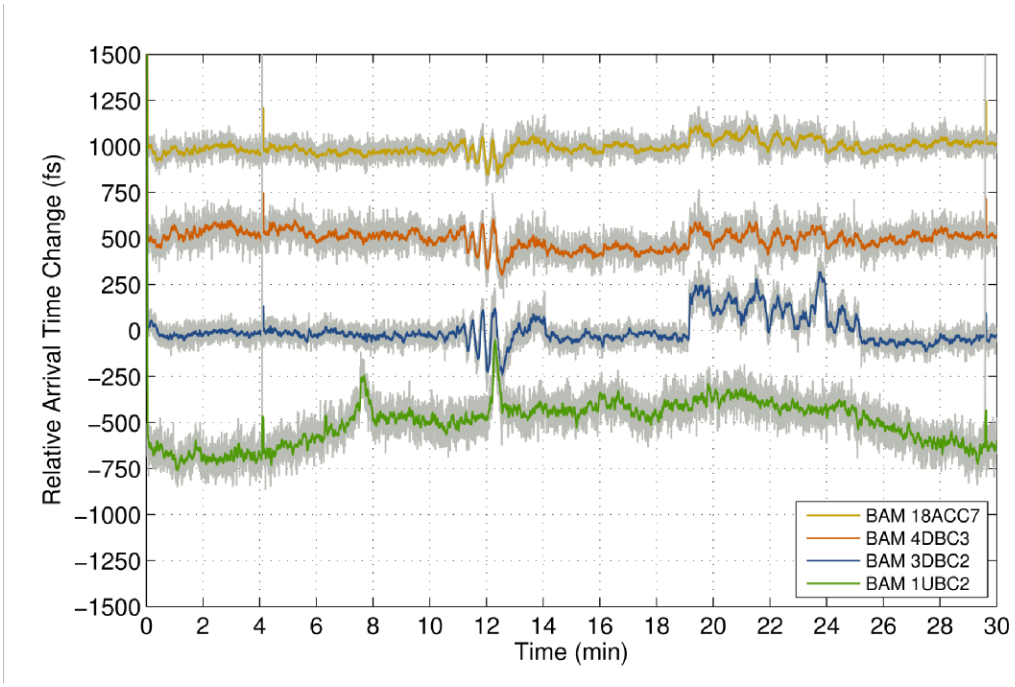

Figure 5.24: Arrival time data from all of the four BAMs for bunch No. 50 out of 300, during a time frame of 30 min. During this time a total of seven feedbacks had been applied. Four of the feedbacks are meant to stabilise the bunch arrival time at two different locations of FLASH.

operated with 300 bunches at a bunch repetition rate of 1 MHz. The charge has been set to 0.37 nC and the total bunch energy had been 955.94 MeV.

The incident between about 11 and 12 min is due to a temporary cutting of the long bunch train from a total of 300 bunches down to a minimum of 3. This action was caused by the toroid protection system (TPS) which should protect the machine from increased charge loss. A toroid (charge monitor) which is set to a very high sensitivity can spuriously trigger the protection system, even though no harmful beam loss is detected at any site of the accelerator. Since at the time of bunch length cutting-off the BBF systems were already active, the controller became unstable and oscillated for a short time. It reached its initial stable state again, after the re-established long bunch train. After about 19.5 min there is a step visible in the arrival time at BAM.3DBC2 and less pronounced further downstream of the linac, at BAMs No. 3 and 4. This step was caused by an RF phase set-point change in ACC1 with running FBs. Afterwards, the initial state was slowly recovered automatically by the response of the fast BBF.

During the data analysis, another fact became visible, which had already been observed earlier. Figure 5.25 shows the mean and RMS arrival time jitter of every third bunch, measured with BAM.1UBC2. The statistical values were calculated from a total time frame of 30 min. Interestingly, there is a clear and stationary offset between the mean arrival times of odd and even numbered bunches. Although the offset is only about 22 fs, this effect can be observed unaltered during the total long-bunch train operation.

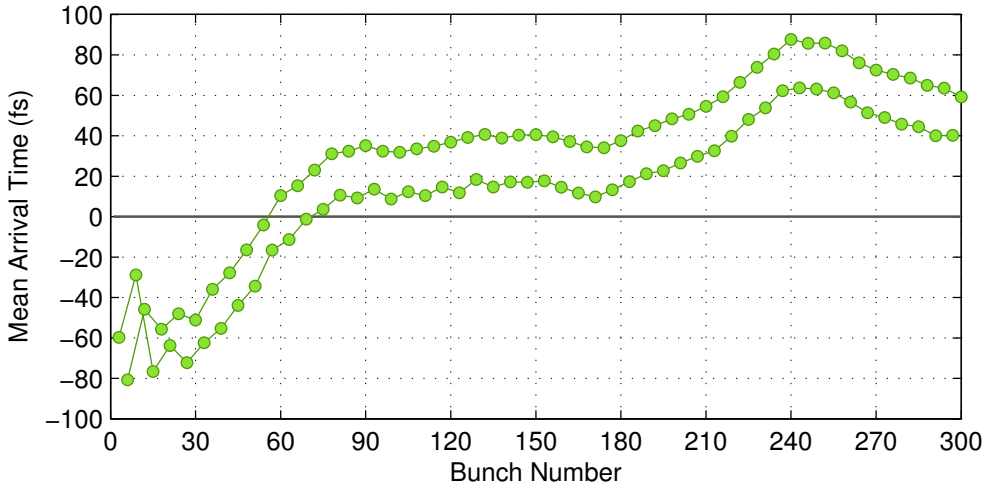

Figure 5.25: Mean values of the arrival time data from BAM.1UBC2 over 30 min. The statistical values are shown for every third bunch from No. 1 to 300. The nearly constant offset between the mean values of odd and even bunches is about 22 fs.

For evaluating the performance of the combined feedback operation, the RMS arrival time jitter for each of the 300 bunches had been calculated for different time frames. Figure 5.26(a) shows the result when evaluating the data for the total duration of 30 min. The arrival time jitter measured at BAM No. 1 is nearly the same for all bunches. At the end of the linac, at BAM No. 4, the arrival time jitter is reduced to about half the initial value for the first 130 bunches, whereas the later bunches show an increased timing jitter, though it is still less than in the injector. The oscillatory shape has been introduced in the first acceleration module, i.e. ACC1, due to the short periods in which the BBF regulation became unstable. This effect is very pronounced in the in-loop timing signal, measured by BAM No. 2.

In contrast to this, when picking out a stable region from the data, for example between 15 and 19 minutes, the beneficial effect of the arrival time regulation system is clearly visible across the whole bunch train. Figure 5.26(b) shows the RMS arrival time jitter at all four BAMs, calculated for a time window of 2.5 min during the mentioned stable region. The minimum achieved arrival time jitter at BAM No. 4 is 28 fs, which is less than half of the value measured in the injector. One can also see the typical effect of the BBF of an initial slow decrease of arrival time jitter during the first few bunches until a stable and uniform behaviour for all following bunches is reached. In 2011, the best result achieved for an arrival time stabilisation had been an out-of-loop RMS jitter of less than 22 fs for 85 out of 100 bunches within a time period of 8 min, measured with BAM 4, for details see [SBP+11].

In the previous section, pg. 149 ff., the meaning of the residual difference signal between BAM No. 3 and 4 has been discussed in detail. Also the difficulties of evaluating the effective measurement resolution through correlations between two BAMs, have been pointed out. With the current read-out electronics and data processing chain, the calculated RMS arrival time difference on short time scales of e.g. 5 min is limited to a range of 25 fs to 30 fs. This analysis has also been applied to an excerpt of 30 min from data gathered during the BBF shift. Figure 5.27(a) shows the difference signal

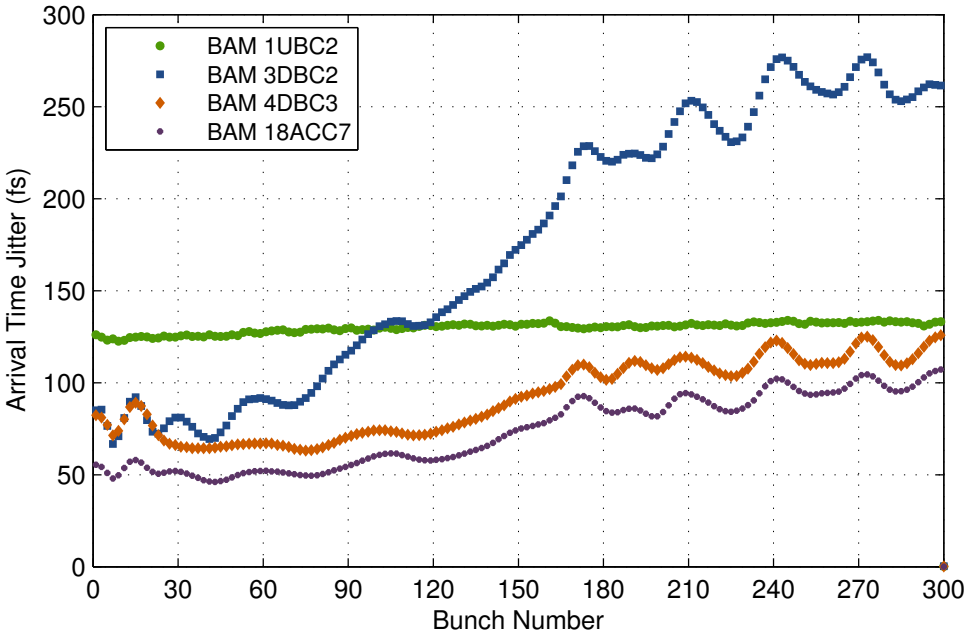

(a) Calculated rms arrival time jitter of all 300 bunches, for total duration of 30 min

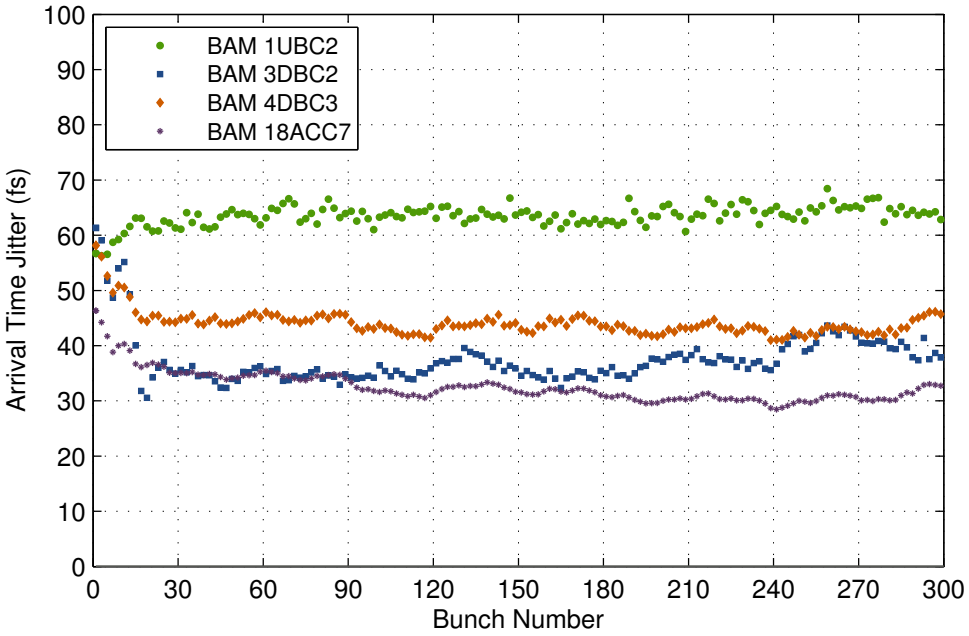

(b) Calculated rms arrival time jitter of all 300 bunches, for total period of 2.5 min. The lowest arrival time jitter measured out-of-loop at BAM No. 4 (BAM.18ACC7) is about 28 fs.

Figure 5.26: Calculated RMS arrival time jitter of all 300 bunches in two different time periods, i.e. 30 min and 2.5 min. The lowest arrival time jitter measured out-of-loop at BAM No. 4 (BAM.18ACC7) is about 28 fs during 2.5 min.

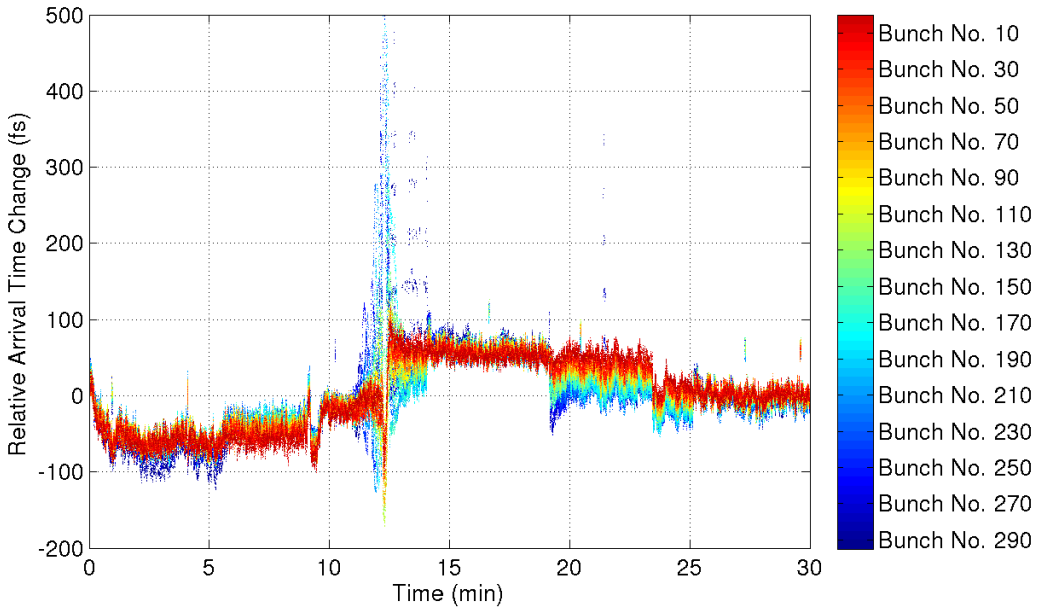

(a) Difference signal between BAM No. 3 and 4, as measured during the total 30 min and for all 300 bunches. The large deviation after about 13 min has happened by the time of a temporary cutting of the long bunch train from a total of 300 bunches down to a minimum of 3, triggered by the TPS.

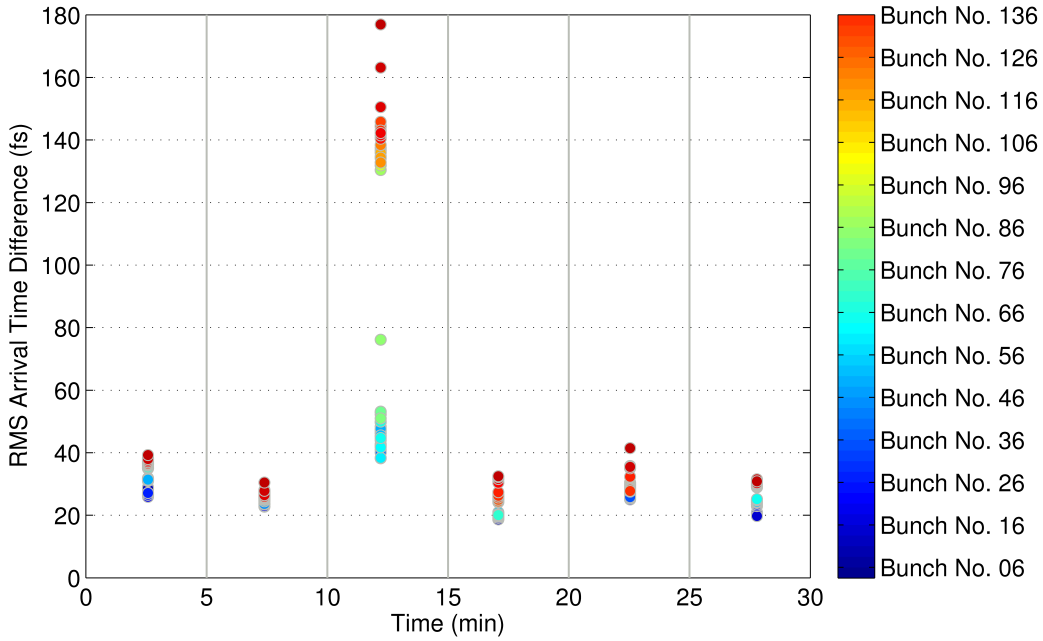

(b) Calculated RMS timing jitter of the difference signal between BAM No. 3 and 4, for all 300 bunches, in intervals of 5 min. The RMS values have been divided by $\sqrt{2}$ to obtain the residual single-BAM resolution.

Figure 5.27: Difference signal of the measured arrival times at BAM.4DBC3 and BAM.18ACC7, for all 300 bunches (a) and the calculated single-BAM resolution (b).

between BAM No. 3 and BAM No. 4 for all 300 bunches of the long pulse train. The large deviations in the time frame between 12 and 14 min has been measured during the temporary cutting of the long bunch train, which has been triggered by the TPS. Figure 5.27(b) shows the RMS value of the difference signal, calculated over time intervals of 5 min, as indicated by the vertical separations in the plot. Except for the middle part, the residual RMS arrival time difference takes values of 20 fs to 40 fs. With dividing by the factor of $\sqrt{2}$, one obtains the statistical single-BAM resolution of about 14 fs to 28 fs, which confirms the result from the previous section on page 149 ff.

The future developments, partly already started, for improving the electric BAM front-end is a key effort. A reliable estimation of the actual resolution of any bunch arrival time monitor can only be obtained through correlation measurements between two independent monitors, which can be considered as measuring, in principle, the same arrival time.

Summary & Outlook

In the course of this thesis two major components of the laser-based synchronisation (LbSyn) system at the Free-Electron Laser in Hamburg (FLASH) have been optimised in many aspects of their design and performance. The main focus has been the installation and characterisation of two bunch arrival time monitors (BAMs), which have been assembled and commissioned in 2009 and 2010. The two monitors are installed at the entrance and exit of the first bunch compressor. Together with the two older prototypes, which had been installed before 2008 downstream of the second bunch compressor, in total four optical arrival time monitors are now available to measure the electron bunch arrival times with femtosecond resolution relative to the optical timing reference. The main focus of attention has been the optimisation of the opto-mechanical design, which is one of the three subcomponents of the bunch arrival time monitor system. Although the first prototypes already proved the functionality of the general BAM detection and measurement principle, the actual operation of such a monitor as a standard diagnostics device makes high demands on the long-term stability and the possibility of automation.

Since the BAM is an integral part of the LbSyn system, which is being developed at DESY, the performance quality of the BAMs is intimately connected with the quality of the optical reference, which is provided at the location of each BAM via individual, length-stabilised fibre links. The further developments and improvements of the opto-mechanical BAM front-end has therefore run in parallel to intense improvements of the reliability and performance of the fibre links.

The systematic redesign and evaluation of both, the opto-mechanics of the BAM and the opto-mechanics of the links, are two major achievements of this thesis. In the process of commissioning and operation survey, design errors and performance limitations have been identified and solved. The newest BAM design allowed for the transition of a prototype used in proof-of-principle measurements to a standard diagnostic tool, which is used during routine machine operation.

Length-stabilised fibre links

Since the laser-based synchronisation system is still, though in an advanced, development phase, the seven currently installed links differ not only in their opto-mechanical design, but especially in their performance. A view on the distinctive features of all employed link module shows the sequence of continuous improvements, which have been applied since 2008.

Not only the target of a uniform system layout, but also the performance limitations from design errors necessitated the repeated revision of the link opto-mechanics, albeit the basic concept has in principle not changed compared to the first prototypes. The following list gives an overview on the achieved improvements connected to the systematic design studies, which have been performed during this thesis:

- All required optical components have been rearranged on the given limited space of the mount-

ing plate. In particular, one critical and profound design flaw has been removed, which is connected to the location of the optical delay line (ODL) within the round trip path of the laser pulses through the link.

- The mechanical stability of the motorised delay stage, as employed in the optical delay line ODL, has been significantly improved. Furthermore, the adjustment range of the optical path length has been doubled (up to ±125 mm) while keeping to the limited space in the link chassis. This makes the design suitable for future applications in the European XFEL.

- The alignment of the free-space optics has been optimised with regard to effectiveness and providing additional degrees of freedom, where it is necessary.

- The Gaussian beam properties of the laser pulses propagating through the free-space optic of the link has been systematically optimised in a comprehensive design study, in order to increase the incoupling efficiency of the laser pulses into a fibre collimator and to improve its stability during optical path length changes of the ODL. This allows to use lower power levels, thus reducing non-linear effects in the optical fibres, which can otherwise deteriorate the performance of the link itself and also the performance of the connected end stations.

- As a key issue, the perturbing amplitude noise, which has reproducibly been observed at different positions along the link, has been reduced significantly to a measured relative intensity noise (RIN) of below 0.09 % by choosing a modified arrangement of critical, optical components. The existence of pronounced amplitude noise, especially at the link ending, averted the allocation of a timing stability below 30 fs for bandwidths of less than 10 MHz.

The overall design revision improved the operation of the links enormously. Especially, a major contribution to the observed, problematic amplitude noise has been identified and suppressed. Due to the overall lower noise levels, the extensively redesigned opto-mechanics paved the way for future improvements. Furthermore, the older links presently installed at FLASH will be exchanged by the revised design, to achieve a uniform system.

Bunch arrival time monitors

Not only the assembly, installation, commissioning and characterisation of the two newest BAMs behind the injector of FLASH, but especially the improvements in their opto-mechanical design have been key subjects of this thesis. The further developments of the opto-mechanical subsystem have been mainly aimed at an improved performance, but at the same time were also focussed on the effectiveness and simplification of the assembly and commissioning. The latter are two critical points with regard to the viability of the BAM as a standard diagnostic tool at FLASH and the upcoming beamline FLASH II, as well as for the planned European XFEL.

Due to the vast experience, which has been gained during the course of this thesis, several constrictions of the performance have been investigated and solved for the most part. Regarding the opto-mechanical front-end, the following advancements have been achieved:

- The fibre and cabling management of the current fibre-optical layout has been improved.

- A first implementation of a temperature regulation for the fibre-optic components in the BAM chassis has been included. Since the first simple approach did not fulfil the required RMS temperature stability of a few 10 mK and less over long periods, an enhanced layout has been successfully tested, with regard to the upcoming installation of a fifth BAM at FLASH.
- In parallel to the reduced optical power requirements, the overall optical fibre length has been shortened, reducing possible performance penalties caused by drifts. The lower optical power requirements in the BAM even allowed for further decreasing the intra-link optical power level.
- The weak points of the ODL design, which has been employed in the BAM since the first prototypes, has been solved in a revised ODL design for the next BAM generation.

Besides the progress in the opto-mechanical BAM front-end, also errors and shortcomings in the server of the electrical front-end have been identified and removed. A major improvement of the long-term operability of all existing BAMs has been achieved through an automated polarisation control of the laser pulses at the critical electro-optical components in the BAM detection scheme. This required a comprehensive programme, currently implemented in a MATLAB™ environment. Moreover, critical, statistical and systematic errors, especially related to the BAM read-out electronics, have been identified, which deteriorated the overall systems accuracy. Those issues have to be addressed in the on-going developments in connection with a completely new layout of the electronic front-end, based on a Micro Telecommunications Computing Architecture (uTCA) system.

Naturally, also the performance of the RF front-end has been thoroughly investigated during the course of this thesis. The resolution of the arrival time measurement is expected to depend linearly on the bunch charge. The systematic measurement showed, that this linear behaviour is suppressed for bunches with more than 200 pC, resulting in a resolution in the order of 10 fs and better, which is nearly uncorrelated with the bunch charge. Only for short bunches with charges below the threshold of 200 pC, the resolution decreases strongly. Nevertheless, the BAMs are still operational even at bunch charges as low as 50 pC, but with reduced performance. Those measurements delivered valuable information for the initiation of a design revision of the RF front-end in cooperation with a group at the *Technical University of Darmstadt*, in which the pick-up signal bandwidth is enlarged by a factor of four to achieve a higher detection accuracy at small signals, and therefore at lower bunch charges [APJ+11].

Furthermore, the orbit dependency of the current RF front-end has been investigated in systematic beam orbit scans at the location of each BAM RF pick-up. The observed strong quadratic dependency of the arrival time detection on the beam orbit cannot be explained until now, but at least can be compensated for with an algorithm incorporated to the BAM server, as measurements proved.

Since the performance and reliability of the bunch arrival time monitors have been enormously enhanced, the monitors enabled thorough investigations on the properties of specific accelerator subsystems in dedicated machine studies. In this conjunction, the BAMs proved to be a valuable diagnostic tool for several applications, which make use of the arrival time information. Those include:

- A non-invasive measurement of the on-crest RF phase of specific acceleration modules, using the BAMs, which are located behind dispersive, magnetic chicanes. The measurement has sev-

eral advantages compared to the usual technique, which involves optical transition radiation (OTR) screens in the straight sections of the chicane.

- A determination of relative energy deviations of the first two acceleration modules, using time-of-flight measurements between the two BAMs which have been installed around the first bunch compressor. The resolution of this measurement is as high as 4.8×10^{-5} and is nearly independent on the compression factor of the electron bunches, in contrast to the synchrotron radiation monitor (SRM), which has been used in a comparative study.
- The incorporation of the BAMs into a system of slow and fast, longitudinal feedbacks, which target an arrival time stabilisation of below 20 fs at the end of the linac during routine machine operation.

Outlook

For the near future, several tasks are foreseen to upgrade the current LbSyn system at FLASH.

- Exchanging the existing old fibre-link opto-mechanics by the new design to obtain a uniform system with improved performance.
- The two oldest BAM front-ends have to be exchanged with a new version as soon as it is available, in order to guarantee a reliable, long-term stable performance.
- The revised electro-optical front-end, being currently under development, will be tested in conjunction with an additional BAM. The latter is scheduled to be installed at FLASH during 2012.
- The upgraded RF front-end, which will be capable of measuring with high resolution at low bunch charges, will be tested in the beam line of FLASH.

Bunch arrival time monitors with an increased operative range are not only crucial for the low bunch charge operation at FLASH, which is increasingly demanded, but has also significant relevance for the upcoming expansion FLASH II and for the planned European XFEL.

Appendix

A Regulation & Limitations of the Beam Stability

A.1 LLRF System at FLASH

The radio frequency (RF) power is generated in a klystron and distributed through a wave-guide system to the main couplers at each cavity of an acceleration module. The RF field amplitude and phase are monitored by use of pick-ups in each cavity. The signals are digitised and sent to a low-level radio frequency (LLRF) controller, which provides a real-time correction on the input driving the klystron. For a simplified illustration compare figure A.1. Not only the RF field, but other properties like the expected bunch charge and bunch number are accounted for. Those multiple input parameters are evaluated and used to regulate the RF field through a complex but coordinated system involving feedback and adaptive feed forward loops.

The tuning of the superconducting cavities to the resonant frequency of 1.3 GHz is done in a coarse adjustment of the cavity length using a stepper-motor and in a fine adjustment with piezo-electric actuators, which are used to excite pre-detuned mechanical oscillation modes in a frequency range $\Delta\omega_m$ of a few 100 Hz. Those induced oscillations interfere with the mechanical oscillations generated by the loaded high-frequency RF field. By this, the phase and amplitude gradient can be controlled during the flat-top duration. A detailed description of the system can be found in [Sch11a].

Fluctuations in the RF field, especially at off-crest operation, where an intended energy chirp is imprinted onto the electron bunches, lead to variations in the rate of energy chirp. This causes bunch arrival time jitter and fluctuations of the electron peak current, which is critical for the SASE process in the undulators. At the injector of FLASH the amplitude and phase stability has to be about 10^{-4} and 0.01 deg, respectively, to restrict peak current variations to below 1 % [GBH+11].

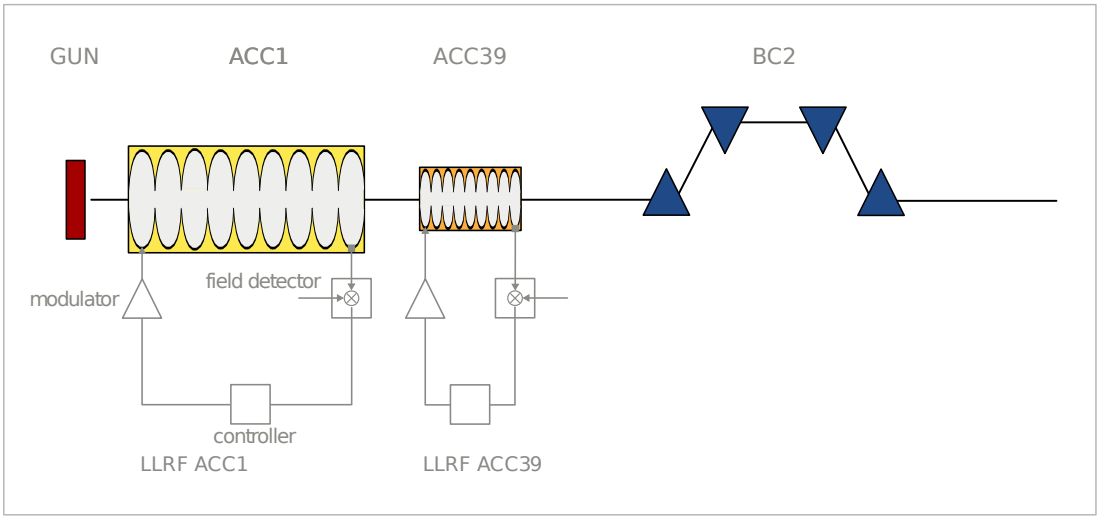

Figure A.1: A simplified illustration of the LLRF feedback control loop for stabilising the amplitude gradient and phase of the RF field in the cavities. Only one cavity per module is shown here.

A.2 Beam Energy Calculation & Measurement

The beam energy in BC2 can be calculated from the vector sums of the detected fields in the acceleration modules ACC1 and ACC39. The energy of electrons at a longitudinal position z inside of the bunch, where $z = 0$ coincides with the bunch centre, results from

$$E = E_{\mathrm{GUN}} + A_1 \cos\left(k_{\mathrm{RF}} z + \Phi_1\right) + A_3 \cos\left(3k_{\mathrm{RF}} z + \Phi_3\right) \tag{A.11}$$

with $k_{\mathrm{RF}} = {}^{\omega_{\mathrm{RF}}}/_{c}$, where the indices 1 and 3 denote ACC1 and ACC39, respectively. For the centre of the bunch, this reduces to

$$E = E_{\mathrm{GUN}} + A_1 \cos\left(\Phi_1\right) + A_3 \cos\left(\Phi_3\right) \tag{A.12}$$

Assuming, that the initial beam energy imprinted by the RF gun is constant, any deviation in E is a combination of statistically independent amplitude and phase fluctuations in both acceleration modules in front of the bunch compressor. Therefore, the energy deviation ΔE can be written as

$$\Delta E = \sqrt{\left(\frac{\partial E}{\partial A_1}\,\sigma_{A_1}\right)^2 + \left(\frac{\partial E}{\partial \Phi_1}\,\sigma_{\Phi_1}\right)^2 + \left(\frac{\partial E}{\partial A_3}\,\sigma_{A_3}\right)^2 + \left(\frac{\partial E}{\partial \Phi_3}\,\sigma_{\Phi_3}\right)^2} \tag{A.13}$$

with standard deviations σ_{A_i} and σ_{Φ_i} of amplitude and phases. Using equation A.12, one obtains for the relative energy deviation ${}^{\Delta E}/_{E}$:

$$\frac{\Delta E}{E} = \frac{\sqrt{\left(\cos(\Phi_1)\,\sigma_{A_1}\right)^2 + \left(A_1 \sin(\Phi_1)\,\sigma_{\Phi_1}\right)^2 + \left(\cos(\Phi_3)\,\sigma_{A_3}\right)^2 + \left(A_3 \sin(\Phi_3)\,\sigma_{\Phi_3}\right)^2}}{E_{\mathrm{GUN}} + A_1 \cos(\Phi_1) + A_3 \cos(\Phi_3)} \tag{A.14}$$

A.2.1 Relative energy calibration with dipole magnets

In a relative beam energy measurement using the synchrotron radiation monitor (SRM) and two bunch arrival time monitors (BAMs), as described in section 5.1.2 on page 122 ff., the effect of an energy fluctuation ${}^{\Delta E}/_{E}$ on the monitor signals has to be calibrated first. For the purpose of generating a defined energy change ΔE, one can use the dipole magnets of the chicane. In first approximation, one obtains a linear relation between magnet current change and beam position inside of the bunch compressor.

For relativistic electron bunches any energy deviation in front of BC2 is translated into a beam position change, governed by the linear, horizontal dispersion of the chicane:

$$\Delta x = R_{16} \frac{\Delta E}{E} + \mathcal{O}\left(\frac{(\Delta E)^2}{E^2}\right) \tag{A.15}$$

A similar relation, but with the longitudinal dispersion, relates relative energy fluctuations with arrival time changes behind the chicane:

$$\Delta t = R_{56} \frac{1}{c_0} \frac{\Delta E}{E} + \mathcal{O}\left(\frac{(\Delta E)^2}{E^2}\right) \tag{A.16}$$

These equations are explained in more detail in the next section, A.3.

The monitor signal of the SRM is given by the ratio of radiation intensities measured by two PMTs:

$$\Delta s = \frac{I_1 - I_2}{I_1 + I_2} \tag{A.17}$$

Within the linear range of the monitor, the signal change Δs is directly proportional to a position change Δx of the electron bunches, which is connected to a relative change in beam energy through eq. A.15:

$$\Delta s = \mathcal{C}_x \Delta x = \mathcal{C}_x R_{16} \frac{\Delta E}{E} \tag{A.18}$$

$$\Delta s = \mathcal{C}_E \frac{\Delta E}{E} \tag{A.19}$$

with calibration constants $\mathcal{C}_E = \mathcal{C}_x R_{16}$, expressed in terms of position and relative energy change, respectively.

The magnetic field B in the dipole is related to the beam energy E and the bending radius R through:

$$B = \frac{E}{R} \tag{A.20}$$

The field strength B of the electromagnet is controlled by the current J. Although the core of the dipole is magnetically soft, in general the hysteresis curve follows a third order polynomial in dependency of the current:

$$B = a_0 + a_1 J + a_2 J^2 + a_3 J^3 \tag{A.21}$$

In a linear approximation for only small current changes ΔJ around the nominal operation point, one obtains

$$\frac{\Delta B}{B} = \frac{\Delta J}{J} \left(1 - \frac{1}{1 + \frac{a_1}{a_0} J} \right) \tag{A.22}$$

The denominator of the last term contributes with only about 2 % and can therefore be neglected. Using equation A.20, a determined relative energy change in the chicane BC2 can be generated through small changes ΔJ of the first dipole magnetic.

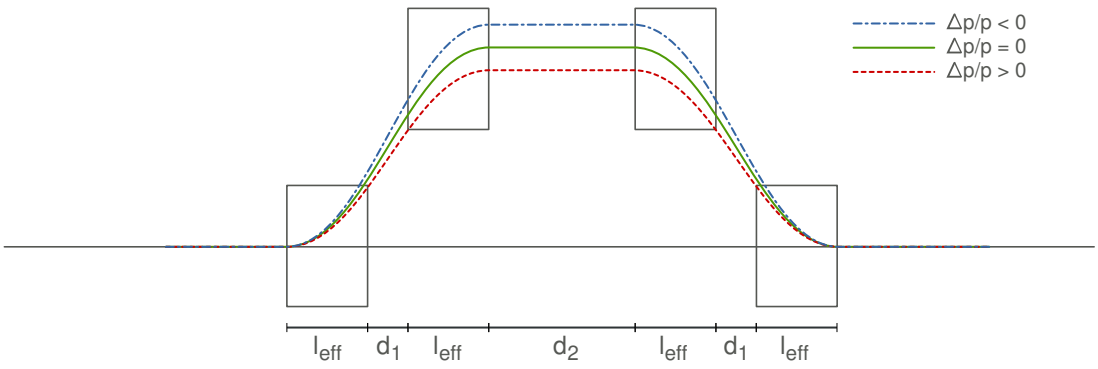

Figure A.2: Illustration of the momentum dependent orbit through a magnetic chicane. Bunch compressor BC2 of FLASH complies with this trapeze-like structure. (Figure adapted from Florian Löhl [Lö9])

A.3 Sources of Bunch Arrival Time Jitter

The arrival time behind magnetic chicanes is governed by the time-of-flight through the structure. The latter is directly related to the path length of the dispersive orbit of the electron beam, determined by their momentum. In the following, this relation is briefly described for the example of BC2. The bending radius of the beam orbit inside of a dipole magnet is connected to the particle momentum p and magnetic field B, through

$$\frac{1}{r} = e_0 \frac{B}{p} \tag{A.23}$$

The effective dipole length can be defined by use of the bending radius r and the bending angle α, which is introduced by the magnetic field strength:

$$l_{\text{eff}} = r \sin(\alpha) \tag{A.24}$$

Figure A.2 shows the structure of the first bunch compressor, BC2, at FLASH. According to the notation as used in the illustration, the path length through this chicane amounts to [Lö9],

$$l_{\text{BC2}}(p) = \frac{4p \arcsin\left(\frac{l_{\text{eff}} e_0 B}{p}\right)}{e_0 B} + \frac{2d_1}{\sqrt{1 - \left(\frac{l_{\text{eff}} e_0 B}{p}\right)^2}} + d_2 \tag{A.25}$$

When considering a bunch with many electrons, there will only be a few which have the nominal energy and momentum. Most of the electrons deviate in momentum by Δp and therefore take a different orbit through the chicane. For relativistic electrons the relative momentum deviation is proportional to energy deviations, introduced by the acceleration modules in front of the bunch compressor:

$$\frac{\Delta E}{E} = \frac{\Delta p}{p} \tag{A.26}$$

For small deviations of the relative momentum change $\Delta p/p$, equation A.25 can be approximated by a TAYLOR expansion. The dispersive change in path length l_{BC2} through the chicane is then given by,

$$\begin{aligned} l_{\mathrm{BC2}}\left(p+\frac{\Delta p}{p}\right) &= l_{\mathrm{BC2}}(p)+p\frac{\partial l_{\mathrm{BC2}}(p)}{\partial p}\frac{\Delta p}{p}+\dots \\ &\quad \frac{1}{2}p^2\frac{\partial^2 l_{\mathrm{BC2}}(p)}{\partial^2 p}\left(\frac{\Delta p}{p}\right)^2+\dots \\ &\quad \frac{1}{6}p^3\frac{\partial^3 l_{\mathrm{BC2}}(p)}{\partial^3 p}\left(\frac{\Delta p}{p}\right)^3+\mathcal{O}\left(\frac{(\Delta p)^4}{p^4}\right) \end{aligned} \tag{A.27}$$

which can also be written as

$$l_{\mathrm{BC2}}\left(p+\frac{\Delta p}{p}\right) = l_{\mathrm{BC2}}(p)+R_{56}\frac{\Delta p}{p}+T_{566}\left(\frac{\Delta p}{p}\right)^2+U_{5666}\left(\frac{\Delta p}{p}\right)^3+\mathcal{O}\left(\frac{(\Delta p)^4}{p^4}\right) \tag{A.28}$$

The coefficients R, T, and U are functions of the magnetic field and the effective length of the magnet structure. Neglecting higher order terms, which only become important for long bunches and large deviations $\frac{\Delta p}{p}$, the first coefficient R_{56} is given by [Lö9]:

$$R_{56} = -\frac{4l_{\mathrm{eff}}}{\sqrt{1-\left(\frac{l_{\mathrm{eff}}e_0B}{p}\right)^2}}-\frac{2d_1}{\left[1-\left(\frac{l_{\mathrm{eff}}e_0B}{p}\right)^2\right]^{\frac{3}{2}}}\left(\frac{l_{\mathrm{eff}}e_0B}{p}\right)^2+\frac{4p}{e_0B}\arcsin\left(\frac{l_{\mathrm{eff}}e_0B}{p}\right) \tag{A.29}$$

Typical values of R_{56} for FLASH range between 140 mm and 228 mm. The indices of the TAYLOR coefficients are related to the transfer matrix formalism which is a convenient way to describe the movement of particles through a the magnet lattice of an accelerator. A detailed description of this formalism is found in [Wie98] and a well-structured summary is published in [Lö9]. Here, the basic relations are shortly explained. Any particle propagating along the ideal trajectory s is represented by a six-dimensional vector $\vec{X}(s)$, in the form of

$$\vec{X}(s) = \begin{pmatrix} x \\ x' \\ y \\ y' \\ \zeta \\ \frac{\Delta p}{p} \end{pmatrix}$$

where x and y denote the transverse position, and the derivatives x' and y' describe the divergences dx/ds and dy/ds. $\frac{\Delta p}{p}$ is the already introduced relative momentum deviation from the nominal value and ζ is the longitudinal displacement from the reference particle. The particle trajectory through a magnet lattice can then be described by an inhomogeneous, linear equation of motion which has sine and cosine like solutions S and C. The latter are functions of the longitudinal coordinate s and

contain parameters which describe the magnetic devices, like bending radii and gradients of the magnetic field. Those solutions are given by transfer matrices for each of the n elements, like dipoles, quadrupoles and drift sections, composing the lattice.

$$\overrightarrow{X_n} = \mathcal{R}_n \overrightarrow{X_{n-1}} \tag{A.30}$$

Each six-dimensional transfer matrix $\mathcal{R}_n$ can be written in the form:

$$\begin{pmatrix} x_n \\ x'_n \\ y_n \\ y'_n \\ \zeta_n \\ \left(\frac{\Delta p}{p}\right)_n \end{pmatrix} = \begin{pmatrix} C_{n,x} & S_{n,x} & 0 & 0 & 0 & R_{n,16} \\ C'_{n,x} & S'_{n,x} & 0 & 0 & 0 & R_{n,26} \\ 0 & 0 & C_{n,y} & S_{n,y} & 0 & R_{n,36} \\ 0 & 0 & C'_{n,y} & S'_{n,y} & 0 & R_{n,46} \\ R_{n,51} & R_{n,52} & R_{n,53} & R_{n,54} & R_{n,55} & R_{n,56} \\ 0 & 0 & 0 & 0 & 0 & 1 \end{pmatrix} \begin{pmatrix} x_{n-1} \\ x'_{n-1} \\ y_{n-1} \\ y'_{n-1} \\ \zeta_{n-1} \\ \left(\frac{\Delta p}{p}\right)_{n-1} \end{pmatrix} \tag{A.31}$$

For instance, the parameters R_{16} and R_{36} are measures for the horizontal and vertical dispersion. Timing fluctuations of electrons at the exit of BC2, due to energy deviations introduced by amplitude or phase variations of the first acceleration module ACC1, are connected to the parameter R_{56} of the chicane:

$$\Delta t_{\mathrm{BC2}} = \frac{\Delta E_{\mathrm{ACC1}}}{E_{\mathrm{ACC1}}} \frac{R_{\mathrm{BC2},56}}{c_0} \tag{A.32}$$

The energy dependent path length change Δl inside of the chicane is given by

$$\Delta l_{\mathrm{BC2}} = \frac{\Delta E_{\mathrm{ACC1}}}{E_{\mathrm{ACC1}}} R_{BC2,56} \tag{A.33}$$

The value R_{56} has the dimension of length, $[R_{56}] = \mathrm{m}$.

$$R_{56} = \frac{\partial l}{\partial \left(\frac{\Delta p}{p}\right)} \tag{A.34}$$

If it is normalised to the total length of the nominal orbit through the magnetic chicane, one obtains the momentum compaction factor of the bunch compressor.

The compression factor $\mathcal{C}$ is defined as ratio of the RMS bunch lengths before and after longitudinal compression:

$$\mathcal{C} \equiv \frac{\sigma_i}{\sigma_f} \tag{A.35}$$

Assume an electron bunch in a co-moving coordinate system, which centre is located at the nominal position $z_{\mathrm{nom}} = 0$ of the reference particle. After traversing a bunch compressor (BC), the bunch centre is in general shifted to a new position $z_{\mathrm{ref}} \neq 0$. The energy and energy gain of an electron depends on its longitudinal position within the bunch. An electron at z_i with energy $E(z_i)$ will change its position relative to the co-moving coordinate system, due to the energy dependent path

length through a bunch compressor. The position offset is then given by the path length difference between the considered electron and the ideal reference particle with energy E_{nom}.
The final position is then given by:

$$z_f = z_i + \left(l_{\mathrm{BC}}\left(E(z_i)\right) - l_{\mathrm{BC}}\left(E_{\mathrm{nom}}\right)\right) \tag{A.36}$$

This can be written as:

$$z_f = z_i \cdot \left(1 + \frac{\Delta l_{\mathrm{BC}}(z)}{\Delta z}\right) \qquad \text{with} \qquad \Delta z = z_i - z_{\mathrm{nom}} \tag{A.37}$$

A variation of the initial position z_i causes a change in z_f by

$$\frac{\partial z_f}{\partial z_i} = \left(1 + \frac{\partial l_{\mathrm{BC}}}{\partial E}\frac{\partial E}{\partial z}\right) \tag{A.38}$$

where the path length l_{BC} is a function of the energy E, as given by equation A.28. According to this, the path length through the chicane can be approximated for small energy deviations by use the first order Taylor coefficient, which is the R_{56} of the chicane. Therefore, with regard to eqs. A.28 and A.26, the energy dependent path length for small offsets from the nominal energy, $\Delta E = E - E_{\mathrm{nom}}$, is equal to:

$$l_{\mathrm{BC}}(E) \approx l_{\mathrm{BC}}\left(E_{\mathrm{nom}}\right) + R_{56}\frac{E - E_{\mathrm{nom}}}{E} \tag{A.39}$$

The partial derivative of this for E = E_{nom} is given by:

$$\frac{\partial l_{\mathrm{BC}}(E)}{\partial E} = R_{56}\frac{1}{E_{\mathrm{nom}}} \tag{A.40}$$

Using this result, equation A.38 becomes:

$$\frac{\partial z_f}{\partial z_i} = \left(1 + R_{56}\frac{1}{E_{\mathrm{nom}}}\frac{\partial E}{\partial z}\right) \tag{A.41}$$

Finally, the inverse compression factor $\mathcal{C}^{-1}$ can be approximated for the case of a linear compression by use of expression A.41:

$$\frac{1}{\mathcal{C}} = \frac{\sigma_f}{\sigma_i} \approx \frac{\partial z_f}{\partial z_i} = 1 + R_{56}\frac{1}{E_{\mathrm{nom}}}\frac{\partial E}{\partial z} \tag{A.42}$$

The last factor, $\partial E/\partial z$, is the bunch energy chirp. Fluctuations and fast jitter of RF amplitudes and phases of the acceleration modules, generate slow and fast fluctuations of the energy and energy chirp, which are imprinted onto the electron bunch. Through the longitudinal dispersion of the chicane, those fluctuations are converted to arrival time variations of the electrons behind the bunch compressor. But due to the relation between the energy chirp and the compression factor, the arrival time jitter of electron bunches is compressed as well, to a certain extent.

According to [Hac10], the arrival time jitter σ_t^2 behind a chicane and for a linearly compressed bunch can be described approximately as a function of amplitude and phase jitter from the preceding acceleration module with the following expression:

$$\sigma_{t_f}^2 \approx R_{56}^2 \frac{1}{c^2} \cdot \left(\frac{\sigma_A}{A}\right)^2 + \left(\frac{\mathcal{C}-1}{\mathcal{C}}\right)^2 \cdot \left(\frac{\sigma_\Phi}{\Phi}\right)^2 + \left(\frac{1}{\mathcal{C}}\right)^2 \cdot \sigma_{t_f}^2 \tag{A.43}$$

where σ_{t_f} is the arrival time jitter behind the chicane and σ_{t_i} is the initial arrival time jitter when entering the module.

The energy dependent arrival time fluctuation and jitter accumulates, when traversing through multiple acceleration modules. For example, the energy deviations in the acceleration stage ACC23 accumulate the amplitude or phase variations of the module itself and energy deviations due to timing discrepancies of electrons arriving from BC2. The RMS arrival time jitter depends primarily on the stability of the accelerating RF field. For instance, the arrival time jitter σ_t behind the second bunch compressor, is given in a comprehensive expression, which regards the main contributions from ACC1 and ACC23, but for the special case of an on-crest operation of ACC23:

$$\begin{aligned} \sigma_t^2 \quad = \quad & \frac{1}{c_0^2}\left[\left(R_{56,\mathrm{BC2}} + \frac{E_{\mathrm{BC2}}}{E_{\mathrm{BC3}}} R_{56,\mathrm{BC3}}\right)\frac{\sigma_{A,\mathrm{ACC1}}}{A_{\mathrm{ACC1}}}\right]^2 + \ldots \\ & \frac{1}{c_0^2}\left[R_{56,\mathrm{BC3}} \cdot \frac{E_{\mathrm{BC3}} - E_{\mathrm{BC2}}}{E_{\mathrm{BC3}}}\frac{\sigma_{A,\mathrm{ACC23}}}{A_{\mathrm{ACC23}}}\right]^2 + \left[\frac{\sigma_{\Phi,\mathrm{ACC1}}}{k_{\mathrm{RF}}}\right]^2 \end{aligned} \tag{A.44}$$

with $k_{\mathrm{RF}} = {}^{\omega_{\mathrm{RF}}}/_{c}$ wave number of the RF fundamental mode in the cavity. This relation has first been published in [SAL+05]. A detailed derivation is given in [Hac10].

B Optics

B.1 Gaussian Beam Propagation

In the following, the matrix analysis method for thick lenses and analytical ray-tracing is shortly described. The ray vectors r_i and r_t denote the initial and transformed rays at a transition surface of an optical element, e.g. the curved surface of a lens.

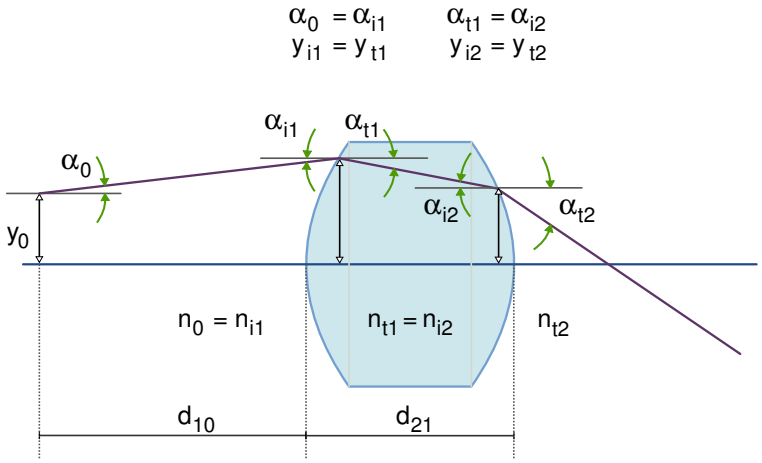

Figure B.1: Geometry and parameter definitions as used for the ray-tracing calculations. The index i indicates the initial states and t denotes the transformed vectors at each interface. The parameters d_{kj} describe the geometrical distances between the optical elements k and j, measured on the optical axis.

The ray vector consists of the transverse displacement y from the optical axes and the according divergence angle α at each point z of the optical path, compare figure B.1. For example, the ray vectors at the left interface of the lens can be written in the form of [Heco2]:

$$r_{i1} \equiv \begin{bmatrix} y_{i1} \\ \alpha_{i1} \end{bmatrix} \quad \text{and} \quad r_{t1} \equiv \begin{bmatrix} y_{t1} \\ \alpha_{t1} \end{bmatrix} \tag{B.45}$$

A 2×2 refraction matrix $\mathcal{R}$ transforms the ray r_{i1} from the left hand side of the interface into the ray r_{t1}:

$$\mathcal{R}_1 \equiv \begin{bmatrix} 1 & 0 \\ -\frac{\mathcal{D}_1}{n_{t1}} & \frac{n_{i1}}{n_{t1}} \end{bmatrix} \tag{B.46}$$

with $\mathcal{D}$ containing the radius of curvature ROC of the interface and the refractive indices on both sides of it:

$$\mathcal{D}_1 = \frac{n_{t1} - n_{i1}}{\text{roc}_1} \tag{B.47}$$

The transformation can then be written in the terms of:

$$r_{t1} = \mathcal{R}_1 \, r_{i1} \tag{B.48}$$

Another transfer matrix $\mathcal{T}$ describes the propagation of a ray inside of a medium with a refractive index n and thickness d. According to the example above, the ray is transferred through the medium of the lens with optical thickness $d_{21}^{\text{opt}} = d_{21}/n_t$ and index of refraction n_t by

$$\mathcal{T}_{21} \equiv \begin{bmatrix} 1 & d_{21}^{\text{opt}} \cdot n_t \\ 0 & 1 \end{bmatrix} \tag{B.49}$$

The total path of the ray can be described by a simple matrix multiplication:

$$r_{t2} = \mathcal{R}_2 \cdot \mathcal{T}_{21} \cdot \mathcal{R}_1 \, r_{i1} \tag{B.50}$$

For calculating the propagation of a Gaussian beam inside of the link optics, up to 30 transfer matrices are necessary to describe the total optical path comprising concave, convex and perpendicular surfaces as well as drift sections. To achieve a matched estimation of the optical path length not only lenses, but also the waveplates, beam cubes and the isolator have been included into the calculation.

To find an optimum lens configuration for a maximum incoupling efficiency into the output collimator, up to seven free parameters have been available, i.e. up to three lenses, two radii of curvature ROC and a thickness d for each lens, as well as the distance d_L of two of those lenses used in a Galilean telescope. The mismatch factor MF can be used as a measure for the quality of coupling a Gaussian beam into a given collimator. In the following, the definitions used for simulating the beam propagation and for optimising the mismatch factor inside of the link optics is shortly described.

The initial Gaussian beam parameters can be written in form of a matrix $\mathcal{B}$ with coefficients being determined by the geometry of the collimators:

$$\mathcal{B}(0) = \begin{pmatrix} \beta_G(0) & -\alpha_G(0) \\ -\alpha_G(0) & \gamma_G(0) \end{pmatrix} \tag{B.51}$$

Since the beam is collimated in its initial state, the value $\alpha_G(0)$ is zero. Along the optical path, the parameter α_G is a dimensionless quantity taking on positive (divergent beam) and negative (convergent beam) values. The parameter β_G consists of the beam radius w_G and the emittance ε_G, as defined by

$$\beta_G(0) = \frac{w_G(0)^2}{\varepsilon_G} \tag{B.52}$$

$$\varepsilon_G \equiv \frac{\lambda}{\pi} \tag{B.53}$$

with wavelength $\lambda = 1.56\,\mu\text{m}$ in case of the links. The Rayleigh range of the collimated beam can be calculated from:

$$z_{\mathcal{R}}(0) = \frac{\pi w_G(0)^2}{\lambda} \tag{B.54}$$

It is the distance over which the beam's cross-sectional area doubles [Heco2], $w_G(z_{\mathcal{R}}) = \sqrt{2} w_G(0)$. The beam radius w_G is defined as half of the width at which the intensity distribution of the Gaussian beam is decreased by a factor of $1/e^2$. The beam diameter at the output surface of the employed

collimators from *OZ Optics*[1] is specified with 1.2 mm, therefore $w_G(0) = 0.6\,\text{mm}$. The initial position of the beam waist coincides with the position of the collimator's lens centre, $z(0) = 0$.

The third parameter, γ_G, is a composition of α_G and β_G:

$$\gamma_G = \frac{1 + \alpha_G^2}{\beta_G} \tag{B.55}$$

This can also be written in the form of $1/(\theta_G \cdot z_\mathcal{R})$. As a descriptive interpretation γ_G is the inverse radius of the beam at a distance of $z_\mathcal{R}$ from the beam waist. The parameter θ_G describes the half angle of divergence around a beam waist depending on the longitudinal position z. Its initial value is calculated through

$$\theta_G(0) = \frac{w_G(0)}{z_\mathcal{R}(0)} \tag{B.56}$$

Typical values of θ_G in the link optics vary between 0.4 mrad and 1.4 mrad. This should not be confused with θ_{DA}, which is the full divergence angle for $z \gg z_\mathcal{R}$. For fibre optical collimators it is given by

$$\theta_{DA}[\text{mrad}] = \frac{a[\mu\text{m}]}{f[\text{mm}]} \tag{B.57}$$

with the fibre core diameter a and the focal length f of the collimator lens. In case of the *OZ Optics* SMF-collimators with a 9 µm fibre core and a focal length of about $f_b = 6.34\,\text{mm}$, the full divergence angle amounts to $\theta_{DA} = 1.42\,\text{mrad}$. The beam diameter BD which is specified with 1.2 mm in that case, is calculated from the focal length and the numerical aperture of the fibre:

$$\text{BD}\,[\text{mm}] = 2 \cdot f\,[\text{mm}] \cdot \text{NA} \tag{B.58}$$

A commonly used geometric definition of the numerical aperture NA for step-index fibres is:

$$\text{NA} = \sin(\theta_{DA}/2) = \sqrt{n_1^2 - n_2^2} \tag{B.59}$$

comparing the refractive indices of the core (n_1) and of the cladding (n_2). A typical value of NA for SM-fibres is 0.14.

Taking all of the predefinitions into account, the beam parameters at any point along the optical path can be calculated by a simple matrix formalism using the beam matrix $\mathcal{B}$ and the matrices describing the optical elements $\mathcal{M}$:

$$\mathcal{B}_j = \mathcal{M}_j \cdot \mathcal{B}_{j-1} \cdot \mathcal{M}_j^T \tag{B.60}$$

The beam parameters at any position z can then be recovered from matrix $\mathcal{B}$ using the following

[1] OZ Optics Limited 1985 – 2011, 219 Westbrook Rd, Ottawa, Ontario, KoA 1L0, Canada

equations:

$$w_G(z) = \sqrt{\mathcal{B}(1,1)(z)\,\varepsilon_G} \tag{B.61}$$

$$\theta_G(z) = \sqrt{\mathcal{B}(2,2)(z)\,\varepsilon_G} \tag{B.62}$$

$$\alpha_G(z) = -\mathcal{B}(1,2) \tag{B.63}$$

The mismatch factor MF is defined to be a measure for the transverse overlap of two beams at a certain position. For the calculation concerning the optimisation of the link optics, the input beam from the first collimator, i.e. the forward directed link pulses, are compared to the returning link pulses at the position of the output collimator, which is of the same type as the input collimator. Therefore, the initial beam parameters of the input beam are compared to the final parameters after propagating through the free-space link optics. The mismatch factor MF is calculated through

$$\begin{aligned} \xi &= \frac{1}{2}\left(\beta_{G,i}\,\gamma_{G,f} - 2\alpha_{G,i}\,\alpha_{G,f} + \beta_{G,f}\,\gamma_{G,i}\right) \\ \mathrm{MF} &= \xi + \sqrt{\xi^2 - 1} \end{aligned} \tag{B.64}$$

The factor MF takes values of $\geqq 1$.

B.2 Electro-Optics

B.2.1 Linear electro-optic effect

In specific anisotropic crystals, the electro-optic (EO) effect permits to control properties of optical signals, like phase, amplitude, frequency or the state of polarisation (SOP) through application of external electric fields. The propagation of normal modes in this type of crystals is governed by the refractive index ellipsoid. In its simplest form, the surface of the index ellipsoid can be written as [YY02]:

$$\frac{x^2}{n_x^2} + \frac{y^2}{n_y^2} + \frac{z^2}{n_z^2} = 1 \tag{B.65}$$

The properties $1/n_i^2$ are the principal values of the impermeability tensor η_{ij}. In presence of an electric field $\vec{E}$, the ellipsoid changes size and orientation, specified by the following coefficients, using the Einstein summation convention,

$$\Delta\eta_{ij} = r_{ijk}\,E_k + s_{ijkl}\,E_k\,E_l + \mathcal{O}(E^3) \tag{B.66}$$

where the parameters r_{ijk} describe the linear dependency (or Pockels effect) and s_{ijkl} describe the quadratic dependency (or Kerr effect) on the electric field strength. In some materials under special circumstances even higher order non-linear effects, like the quadratic Kerr effect have to be taken into account. With an applied electric field the index ellipsoid is given by

$$\eta_{ij}(\vec{E})\,x_i\,x_j = 1 \tag{B.67}$$

Taking only the linear effect into account, the tensor r_{ijk} has 27 independent elements, though when regarding rotational symmetries of the crystal orientations it can be simplified.

The EO material which is used for sampling fast electro-magnetic field transients in the bunch arrival time monitors (BAMs) is Lithium Niobate ($LiNbO_3$). This trigonal, non-centrosymmetric crystal has a ditrigonal pyramidal system structure and belongs to the point group $3m$ (according to Hermann-Maugin symbols), having a three-fold rotational symmetry [SS10]. For a descriptive model of a ditrigonal pyramidal crystal structure, follow the instructions in figure B.2.

Using a contracted indices notation with

$$r_{1k} = r_{11k} \tag{B.68}$$
$$r_{2k} = r_{22k} \tag{B.69}$$
$$r_{3k} = r_{33k} \tag{B.70}$$
$$r_{5k} = r_{13k} = r_{31k} \tag{B.71}$$

and $k = 1, 2, 3$, the linear electro-optic coefficients of $LiNbO_3$ reduce to [YY02]:

$$\begin{pmatrix} 0 & -r_{22} & r_{13} \\ 0 & r_{22} & r_{13} \\ 0 & 0 & r_{33} \\ 0 & r_{51} & 0 \\ r_{51} & 0 & 0 \\ -r_{22} & 0 & 0 \end{pmatrix} \tag{B.72}$$

For symmetry reasons all other indices, $r_{23k} = r_{32k}$ and $r_{12k} = r_{21k}$ are zero. Thus, $LiNbO_3$ has only four independent non-zero elements of the linear electro-optic tensor. With an electric field applied along the crystal axis c, the equation of the surface of the index ellipsoid can be written as

$$\left(x^2 + y^2\right)\left(\frac{1}{n_o^2} + r_{13}E\right) + z^2\left(\frac{1}{n_e^2} + r_{33}E\right) = 1 \tag{B.73}$$

with the ordinary n_o and extraordinary n_e indices of refraction. Therefore, an applied electric field changes the index ellipsoid axes by

$$n_x = n_o - \frac{1}{2}n_o^3 r_{13}E \tag{B.74}$$

$$n_y = n_o - \frac{1}{2}n_o^3 r_{13}E \tag{B.75}$$

$$n_z = n_e - \frac{1}{2}n_e^3 r_{33}E \tag{B.76}$$

Although in presence of an electric field, the anisotropic crystal keeps the direction of the uniaxial symmetry. For example, the change in index of refraction for an x-propagating optical signal amounts to

$$n_z - n_y = (n_e - n_o) - \frac{1}{2}\left(n_e^3 r_{33} - n_o^3 r_{13}\right)E \tag{B.77}$$

Since the application possibilities for devices made from $LiNbO_3$ depend on the direction of crystal cuts, the coordinate system in which the physical tensor properties are usually described in is shortly explained.

The conventional hexagonal unit cell [Kito5] of $LiNbO_3$ shows a three-fold rotational symmetry about the c axis. Three equivalent axes a (a_1, a_2, a_3) in the plane normal to c are seperated by 120 deg. The alternative structural characterisation is done by using a rhombohedral unit cell. The according crystal lattice parameter can be deduced from the hexagonal dimensions c and a_H.

In contrast to this, the common coordinate system to describe the physical properties of $LiNbO_3$ is neither hexagonal nor rhombohedral, but rather Cartesian. According to the convention [IRE49] the z axis is chosen to be parallel to the crystal axis c and the x-axis coincides with any of the equivalent a_H axes. The y-axis is then chosen such to sustain a right-handed coordinate system[2]. For commercial applications the crystals are commonly processed as wafers with x-cut, y-cut and z-cut

[2] 3.1 *Coordinate System for Tensor Properties* taken from [WG85]

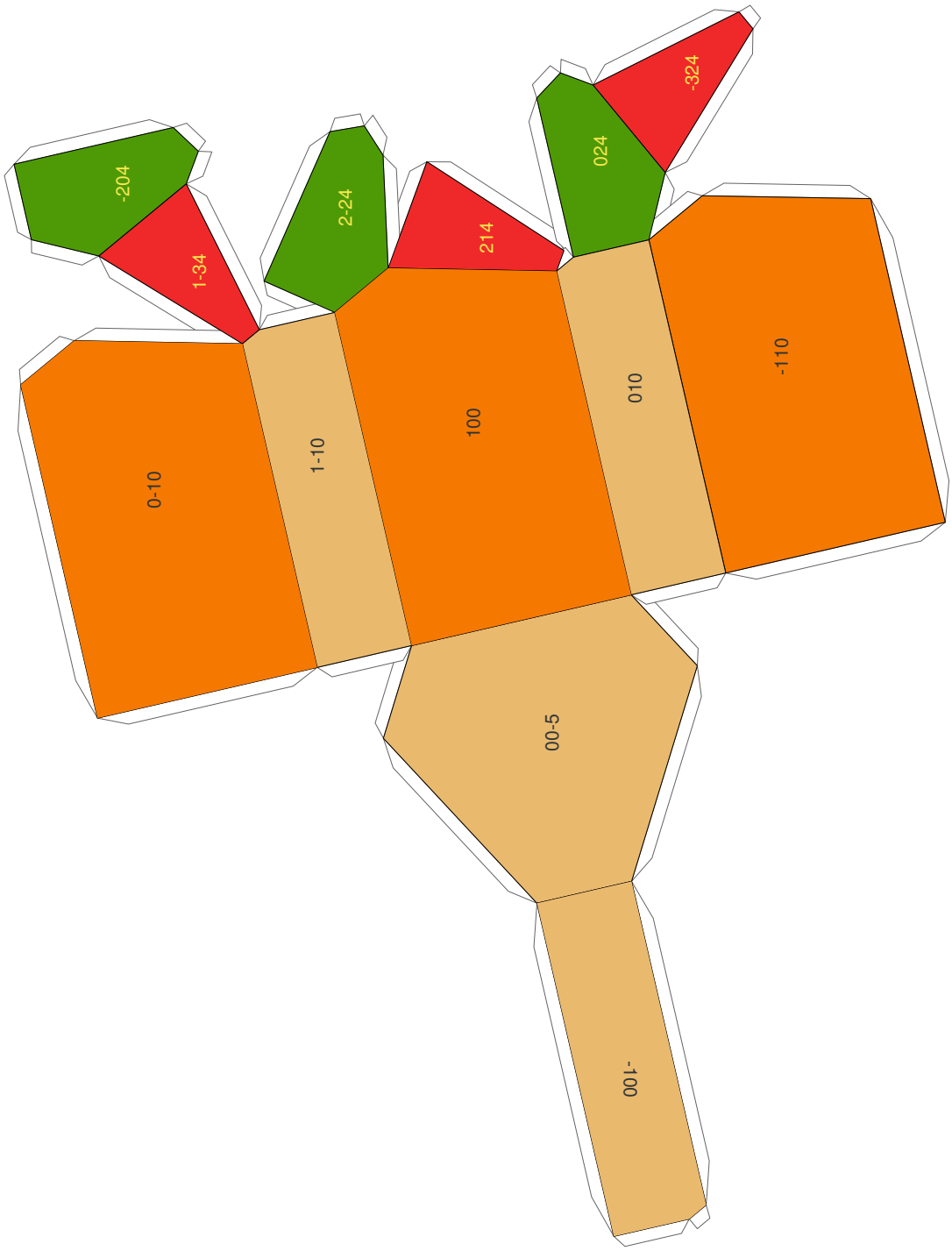

Figure B.2: Model of a ditrigonal pyramidal crystal, as found on web page [Web11e]. Instructions:
1. (scan page if not digitally available), print on heavy paper, card stock for best results
2. cut along lines, fold and crease tabs and crystal faces
3. test folding crystal to check if it fits
4. apply white glue on tabs, one pair at a time using toothpick and hold tabs together until dry
5. repeat for each tab.

respectively, corresponding to the large area surfaces oriented normal to the x,y and z axes. Details on the crystal structure and electric properties of $LiNbO_3$ can be found in [WG85] and [SS10].

B.2.2 Integrated optics devices

The fibre-coupled electro-optic modulator (EOM) as used in the bunch arrival time monitor (BAM) is an integrated optics device. Similar to an optical fibre, the light is guided through a channel structure where the total internal reflection at the transition of a high-index core and a lower-index cladding is used for the confinement of the propagating light wave. In a single-mode wave guide the dimensions are small enough, that only one bound mode for each polarisation state is existing. The phase evolution of an electro-magnetic field along the longitudinal axis is governed by the propagation constant β

$$\beta = \frac{2\,\pi\,n_1}{\lambda} \cdot \sin\theta \tag{B.78}$$

where θ is the enclosed angle between the axis with refractive index n_1 and the propagation direction. In case of the non-linear crystal $LiNbO_3$ the high-index core is usually produced by impurity indiffusion or implantation leading to a graded index profile. Such a graded refractive index structure can be described approximately by use of the *effective index method* [Tam90]. A 3-dimensional channel wave guide is sequentially simulated with a 2-dimensional structure by separating the lateral dimension into a multilayer where each layer has a homogeneous index of refraction. The field in each of those layers as a solution of Maxwell's equations is proportional to $e^{\vec{k_\mathrm{m}} \cdot \vec{r}}$ with the wave propagation factor $|\vec{k_\mathrm{m}}| = 2\pi\,n_\mathrm{m}/\lambda$ for each complex index of refraction n_m. The mode field amplitude ε_m in the general case for each homogeneous layer m can be written as

$$\varepsilon_\mathrm{m} = \left[a_\mathrm{m} e^{iq_\mathrm{m} y} + b_\mathrm{m} e^{-iq_\mathrm{m} y}\right] e^{i\beta_z} \tag{B.79}$$

where $q_\mathrm{m} \equiv \left[(2\pi\,{}^{n_\mathrm{m}}/\lambda)^2 - \beta^2\right]^{1/2}$. This general solution can be reduced to a superposition of a transverse electric (TE) and a transverse magnetic (TM) field [Tam90], where each solution has only one component of the field pointing in the direction y parallel to the multi-layers and perpendicular to the propagation direction z. The TE and TM modes have different propagation constants, i.e. the wave guide exhibits birefringence.[3]

Once the modes of a wave guide structure are known, other physical properties of interest can be calculated, for example, the phase evolution, group velocity $v_g = \left[\partial\beta/\partial\omega\right]^{-1}$ and the coupling of light between wave guides of different components with different modal structure or between parallel wave guides of one component, by applying the *coupled-mode theory* [Tam90]. For example, the energy efficiency η of coupling an injected field ε_i at the input surface of a wave guide into a particular TE mode ε_m is given by[4]

$$\eta = \frac{\left|\int \varepsilon_\mathrm{m}^*(y)\varepsilon_i(y)dy\right|^2}{\int |\varepsilon_\mathrm{m}(y)|^2 dy \cdot \int |\varepsilon_i(y)|^2 dy} \tag{B.80}$$

[3] [Bas10], chapter 21: *Integrated Optics*, page 5
[4] [Bas10], chapter 21: *Integrated Optics*, page8

In the following, two examples for applications of the electro-optic effect are discussed, namely the phase modulator and the intensity modulator. Even though the principle of operation is quite different for bulk material and optical integrated circuit (OIC) devices the following short description is helpful to understand the function of the integrated-optics EOM which is employed in the BAMs.

B.2.3 Phase modulator

In bulk modulators the anisotropic crystal is embedded between two electrodes and is therefore modelled as capacitor [Bas95]. One distinguishes between the transverse and longitudinal configuration, depending on the orientation of the electric field lines in relation to the light wave propagation.

An ideal phase modulator when combined with an input polariser will only change the phase of the light wave without affecting its intensity or the state of polarisation (SOP). This configuration is also known as dynamic phase retarder. If the polariser is aligned parallel to a principal axis of the EO crystal, so that the light propagates along a principal axis of the index ellipsoid, the electro-optic effect can be described by the electric field vector $\vec{E}$ rather than the displacement vector $\vec{D}$. In a uniaxial crystal, like $LiNbO_3$ the principal axes will not be rotated by the applied voltage. For light propagating along z the optical output of a transverse modulator at $z = L$ is then given by [Bas95],

$$E_{\mathrm{opt},f}(t) = \left|E_{\mathrm{opt},i}\right| \cos(\omega t - \phi) \tag{B.81}$$

with $E_{\mathrm{opt},i}$ being the input electric field of the light wave. For light polarised along x the total phase shift ϕ consists of the constant phase ϕ_0 and the induced phase shift $\Delta\phi_x$:

$$\phi = \phi_0 + \Delta\phi_x = \frac{2\pi}{\lambda}\left(n_x + \Delta n_x\right) L \tag{B.82}$$

In a simple capacitor configuration the perpendicular electrical field between the electrodes depends only on the applied voltage and on the separation of the electrodes d, i.e. $E_{\mathrm{mod}} = {}^{V_{\mathrm{mod}}}/_{d}$. For an electric field which is stationary but varying sinusoidal over time, i.e. $E_{\mathrm{mod}} = E_{\mathrm{mod},m}\sin(\omega_m t)$, the total phase shift at $z = L$ becomes

$$\phi = \frac{2\pi}{\lambda}\left(n_x - \frac{1}{2}n_x^3 r_{13} E_{\mathrm{mod},m}\sin(\omega_{\mathrm{mod},m} t)\right) L \tag{B.83}$$

Which reduces to

$$\phi = \frac{2\pi}{\lambda} n_x L - \Psi\sin(\omega_{\mathrm{mod},m} t) \tag{B.84}$$

with

$$\Psi = \frac{\pi}{\lambda} n_x^3 r_{13} E_{\mathrm{mod},m} L = \pi\frac{V_{\mathrm{mod},m}}{V_\pi} \tag{B.85}$$

where the half-wave voltage V_π is defined to induce a phase advance of $\Delta\phi_x = \pi$.

B.2.4 Intensity modulator

Based on the operating mechanism of the EO phase modulator, an intensity modulator can be realised in several configurations [Bas95]:

- a dynamic phase retarder with a pair of crossed polarisers
- a dynamic phase retarder with a pair of parallel polarisers
- a phase modulator inside of one branch of a MACH-ZEHNDER interferometer
- phase modulators in both branches of a MACH-ZEHNDER interferometer with push-pull electrodes

The first two are single-channel modulators while both mentioned MACH-ZEHNDER interferometers are two-channel modulators. The latter configuration is applied in the commercial, travelling-wave EOM as an OIC-device which is used in the BAMs. Therefore the following considerations concentrate on the MACH-ZEHNDER type modulator.

The general principle of this device is to use an external electric field to generate a path length difference between two coherent optical signals propagating in two separate paths in order to introduce a phase shift which is proportional to the applied voltage. When recombining both optical signals into a common output port the phase difference is then transformed into an amplitude modulation by interference.

In application of an OIC device, the input light wave is coupled from a single mode fibre (SMF) into a single-mode wave guide which only supports the propagation of the lowest order modes. The wave-guide is then divided symmetrically into two branches. This can either be done by use of a Y-junction or with a 3 dB directional coupler. If required, the coupling ratio can be controlled with external electrodes which are deposited along the guides of the junction. In this case the electro-optic effect is used to vary the index of refraction in one branch of the junction to steer the light wave since it tends to propagate into the direction of the higher refractive index.

For modulating the index of refraction in one or both branches of the MACH-ZEHNDER interferometer, external electrodes are placed above or beside the wave-guides, depending on the crystal orientation. If the applied voltage is just the half-wave voltage V_π, so that the phase difference between the optical waves at the output of the two branches is an odd multiple of π, the electro-magnetic fields will interfere destructively. Correctly speaking, the field distribution is such that at the output only higher order modes are excited which are cut-off depending on the dimensions of the output wave-guide and irradiate into the substrate. If the output guide is widened no total cancellation will occur [Hun09]. By switching the applied voltage V_π on and off the device will switch the optical power on and off. Related to the application of an EOM as an optical switch, V_π is also called drive voltage of the modulator. At any intermediate voltage the intensity at the output port of the MACH-ZEHNDER interferometer is given by [Hec02]

$$I_{\text{out}} = \frac{I_{\text{in}}}{2}\left(1 + \cos(\Gamma)\right) \tag{B.86}$$

with the input intensity I_{in} and the total phase difference Γ between the two branches of the interferometer. To control the operation point of the modulator, i.e. a constant phase shift Γ_0 at zero external modulation voltage, a fixed DC bias voltage can be applied using an additional electrode in one of the two branches of the interferometer. Using the half-wave voltage V_π as introduced in eq. B.85, the

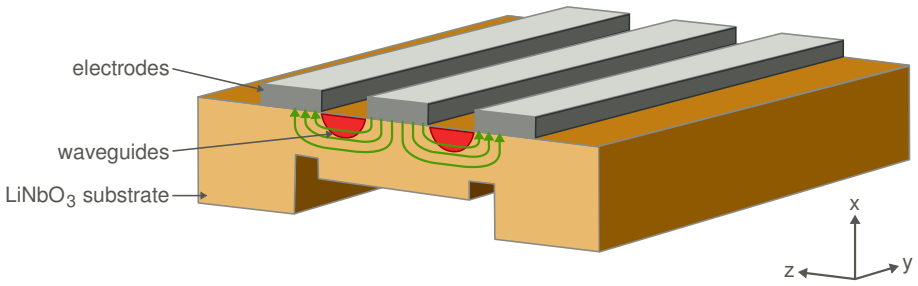

(a) x-cut $LiNbO_3$

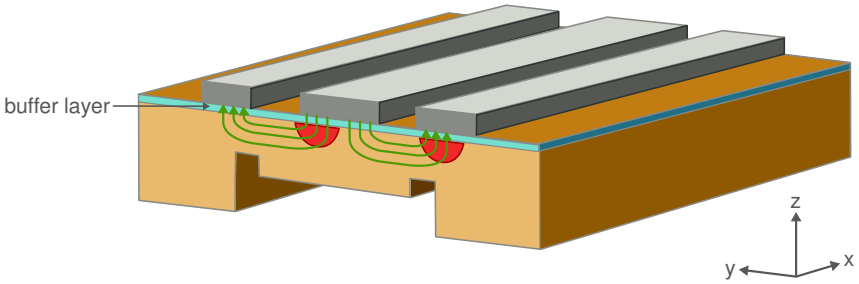

(b) z-cut $LiNbO_3$

Figure B.3: Co-planar electrode structure on x-cut (a) and z-cut (b) $LiNbO_3$ [Hun09]. The curved arrows denote the direction of the electrical field lines when applying an external voltage between the central conductor and the two grounded electrodes.

output intensity I_{out} can also be written as

$$I_{\text{out}} = I_{\text{in}} \cos^2\left(\frac{\Gamma_0}{2} + \frac{\Gamma_{\text{mod}}}{2}\right) \quad \text{with} \quad \Gamma_{\text{mod}} = \pi \frac{V}{V_\pi} \tag{B.87}$$

For a sinusoidal modulation voltage $V = V_m \sin(\omega_m t)$ the output intensity results in [Bas95]

$$I_{\text{out}} = I_{\text{in}} \cos^2\left(\frac{\Gamma_0}{2} + \frac{\Gamma_m}{2} \sin(\omega_m t)\right) \tag{B.88}$$

introducing the intensity modulation index Γ_m as defined by

$$\Gamma_m = \pi \frac{V_m}{V_\pi} \tag{B.89}$$

In practice, OIC modulators are fibre coupled. Any elliptically polarised light from the fibre will excite both TE and TM modes in a rectangular wave guide. In $LiNbO_3$ the linear electro-optical coefficients are different for the individual crystal axes (compare page 180). Because of this, the effect of optical polarisation modes on the modulation efficiency has to be considered.

For example, figure B.3 (a) shows an x-cut $LiNbO_3$ crystal with external electrodes located between the wave-guides aligned in y direction. With an external voltage applied the electric field lines

align parallel to the z axis near the region of the wave-guides. If a TE_0 mode is launched into the wave-guide with a polarisation along z, the external electric field lines will be parallel to the optical electric field lines, so that the refractive index change is dominated by r_{33}. On the other hand, if a TM_0 mode is launched into the same wave-guide with its polarisation along x, the external and optical electric field lines will be perpendicular to each other, so that the dominant EO-effect is given by r_{13} which is about only one third of r_{33} [Huno9].

Thus, in this configuration, it is more efficient to use only TE modes. If one wants to increase the efficiency for TM modes in x-cut $LiNbO_3$ one has to place the electrodes on top of the wave-guides to align the external electric field lines in parallel to the optical field. On the contrary, in z-cut $LiNbO_3$ (figure B.3 (b)) the electrodes have to be placed on top of the wave-guides if x-propagating TE_0 modes (polarised along the z axis) are used for exploiting the linear EO-coefficient r_{33}. In any case, for this configuration an additional buffer layer has to be placed between wave guide and electrode to suppress optical absorption losses in the metal.

Bulk material EOMs can be constructed in a way to be polarisation insensitive by placing two pairs of electrodes in both configurations behind each other, so that the applied voltage first modulates only the TE and then only the TM modes. In case of the travelling wave EOMs this is not possible so that the unwanted polarisation mode has to be filtered out by using a clean-up polariser like it is implemented in most commercial modulators at the input or output of the device. But for maximum efficiency the polarisation of the input light has to be controlled by use of polarisation maintaining fibre (PMF) and a slow polarisation feedback.

The bandwidth of frequency response of a bulk material modulator is mainly limited by the transit time τ required for the optical signal to pass the crystal of length L:

$$\tau = \frac{nL}{c} \tag{B.90}$$

where n is the refractive index seen by the light [Bas95]. For modulation frequencies $\omega_m > {}^{2\pi}/_{\tau}$ the bandwidth is influenced by τ. In crystals of lengths

$$L > \frac{2\pi c}{\omega_m}\sqrt{\varepsilon_{\text{eff}}} \tag{B.91}$$

with the effective microwave dielectric constant ε_{eff} (taking a value of 35.8 for $LiNbO_3$), the optical phase is no longer following the time varying index of refraction adiabatically. The bandwidth of bulk modulators is limited to typically 1 GHz [Huno9].

For higher bandwidth applications modulators with a travelling wave structure have to be considered, where the applied microwave signal propagates collinearly with the optical signal. By carefully choosing the material properties and geometry the phase velocities of the optical and electrical signals can be matched over the interaction length. The drive voltage and the transit time can further be decreased when constructing the Mach-Zehnder modulator in a push-pull electrode configuration, compare figure B.4. In both branches of the interferometer a phase modulator is located with the same modulation voltage applied but with opposite polarity. The commercial EOM as used in the BAMs complies with this design[5].

[5] Zero-Chirp Intensity Modulator Mach-10™056 from Covega, compare section C on page 191

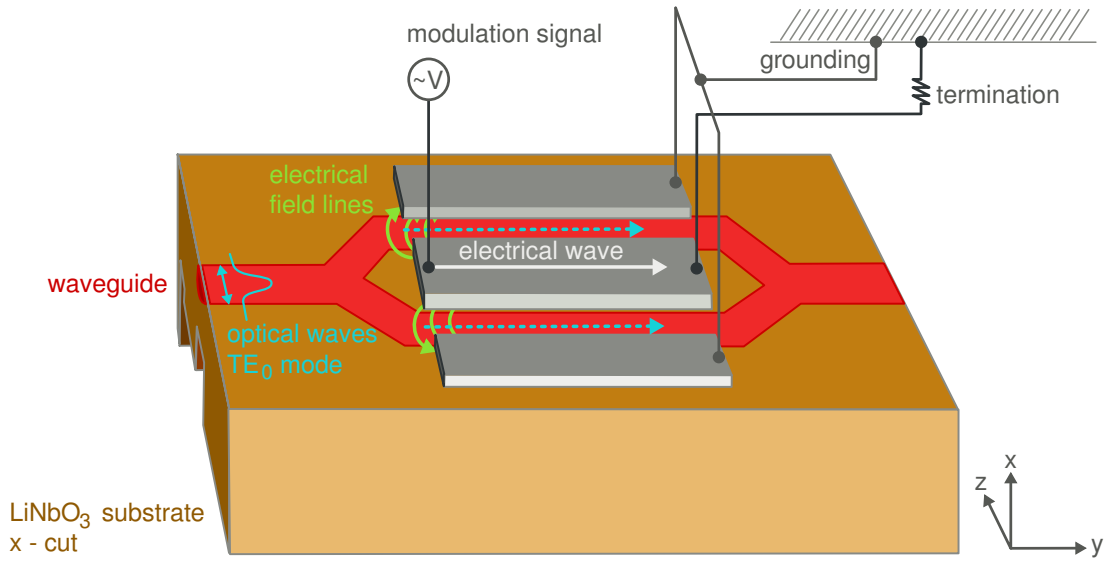

Figure B.4: Co-planar electrode structure on x-cut Lithium Niobate with y-propagating optical and electrical signals. A TE_0 optical mode with polarisation parallel to z is launched into the wave guide. The travelling wave electrodes are placed in push-pull configuration, so that the electrical field lines of the travelling modulation signal are parallel and anti-parallel to the z axis in each interferometer branch, respectively. Thus, the EO effect is dominated by the r_{33} component. The induced phase shift is equal but with opposite sign in the two branches (according to [Nog07])

Consider a RF signal with modes m travelling along the y-axis, i.e. collinearly with the optical signal. The electrical field varies along the z-axis, with

$$E_{\mathrm{RF}}(t, y) = E_m \sin(\omega_m t - k_m y) \tag{B.92}$$

where $k_m = {\omega_m}^{n_m}/_c$ is the wave vector and n_m is the refractive index as seen by the modulating RF signal, with $n_m = \sqrt{\varepsilon_{\mathrm{eff}}}$. A velocity mismatch of

$$v_{\mathrm{tw}} = \frac{c}{Ln}\left(1 - \frac{\sqrt{\varepsilon_{\mathrm{eff}}}}{n}\right) \tag{B.93}$$

between the RF modulation wave and the optical wave leads to a reduction of the intensity modulation index Γ_m by a factor of δ_{tw} depending on the difference in effective refractive indices for electrical and optical fields and on the crystal length:

$$\Gamma_{\mathrm{tw}} = \Gamma_m \delta_{\mathrm{tw}} \tag{B.94}$$

A detailed derivation can be found in [YY02]. According to [Bas95], the reduction factor δ_{tw} inside of an uni-axial crystal can be written as

$$\delta_{tw} = \frac{\sin\left(\frac{\omega_m}{2c_0}\left[n - n_m\right]L\right)}{\frac{\omega_m}{2c_0}\left[n - n_m\right]L} \tag{B.95}$$

The modulation speed is depending on the electrode impedance and on the propagation loss, but also on the difference between the group velocity of the optical signal and the phase velocity of the RF signal. In Lithium Niobate the effective refractive index for the RF electrical wave is about $n_m = 4.2$, which is twice as large as the extraordinary refractive index of $n_e = 2.15$ for micrometer optical waves. The effective electrical modulation bandwidth B at the electrical 3 dB point depends on this difference and on the interaction length L [Nog07],

$$B = \frac{1.4c}{\pi L \left(n_m - n_e\right)} \tag{B.96}$$

According to this, for a modulation bandwidth of more than 40 GHz the index difference has to be less than 0.16 for an interaction length of $L = 2\,\text{cm}$. From this, it follows that a smaller length is preferable for high modulation speeds, but it has the disadvantage that the drive voltage increases with shorter lengths. Therefore, in the fabrication of high-speed modulators there always has to be a trade-off between those two critical properties.

The configuration using push-pull electrodes allows for lowering the drive voltage and has an additional advantage when considering thermally induced birefringence drifts in the substrate. The unwanted birefringence drifts are compensated because the applied electrical field affects the optical wave propagation symmetrically in both branches of the interferometric modulator but with opposite sign. Thermal drifts are thus compensated and the intended birefringence change is doubled compared to a configuration with electrodes in only one branch.
Limitations in the signal quality can also be related to strain acting on the substrate. Since $LiNbO_3$ is also piezoelectric the electrical signals applied for a refractive index modulation can also induce vibrations which in turn act on the optical signal due to the elasto-optical effect [WG85]. However, since in $LiNbO_3$ the piezoelectric constants are quite weak this effect is negligible for many applications, but can become problematic for mechanical vibrations between 1 and 10 MHz [Web11a].

In the following some commonly used terms are introduced which are needed to describe the functionality of an intensity modulator (compare [Bas95]). The crucial parameter is the transmission T, i.e. the ratio of output to input intensity. Taking eq. B.88 into account, the transmission is given by

$$T = \frac{I_{\text{out}}}{I_{\text{in}}} = \cos^2\left(\frac{\Gamma_0}{2} + \frac{\Gamma_m}{2}\sin\left(\omega_m t\right)\right) \tag{B.97}$$

The modulation depth η is defined as

$$\eta = \frac{I - I_0}{I} \qquad \text{for} \qquad I > I_0 \tag{B.98}$$

$$\eta = \frac{I - I_{\max}}{I_{\max}} \qquad \text{for} \qquad I > I_{\max} \tag{B.99}$$

with I being the intensity at the operation voltage, I_0 the transmitted intensity with zero modulation voltage and $I_{\max}$ the transmitted intensity at maximum applied modulation voltage. The maximum achievable modulation depth, $\eta_{\max}$, also named extinction ratio of the modulator, can be described

using the transmission T:

$$\eta_{\max} = \frac{T_{\max}}{T_{\min}} \tag{B.100}$$

In general, the maximum possible transmission $T_{\max}$ is < 1 due to absorption, internal reflections and scattering. At the same time, the minimum achievable transmission $T_{\min}$ is always > 0 due to residual crystal birefringence, crystal inhomogeneity, non-uniform spatial distribution of the electric field or polariser misalignment.

The modulation efficiency takes into account which electrical power consumption is required to achieve a maximum intensity modulation factor of $\Gamma_m = {}^{\pi V_m}/_{V}$:

$$\kappa = \frac{\Gamma_m^2}{P} \tag{B.101}$$

with $P = {}^{V_m^2}/_{2R}$ where R is the impedance of the resonant modulator circuit.

For a wave guide modulator which is operated at $\Gamma_0 = 0$, i.e. in which the modulation voltage tends to increase the transmitted signal, the insertion loss IL is defined by the ratio ${}^{I_t}/_{I_{\max}}$, where I_t is the optical intensity which would be transmitted by the wave guide if the modulator was absent and $I_{\max}$ is the optical intensity which is transmitted by the wave guide with the modulator in place and with maximum electrical signal applied. Commonly stated in decibels, the insertion loss is given by [Hun09]

$$\mathrm{IL} = 10 \log\left(\frac{I_t}{I_{\max}}\right) \tag{B.102}$$

If the modulator is operated at $\Gamma_0 = \pi$, the insertion loss is defined according to the intensity I_0 at zero applied modulation voltage:

$$\mathrm{IL} = 10 \log\left(\frac{I_t}{I_0}\right) \tag{B.103}$$

The isolation ISO between the input and the output port of the modulator is equal to the maximum modulation index and commonly stated in decibels:

$$\mathrm{ISO} = 10 \log\left(\frac{I_{\max}}{I_0}\right) \tag{B.104}$$

C Components

C.1 Electro-Optical Modulator

Table C.1: SELLMEIER equation coefficients for $LiNbO_3$ at 293 K. [Bas10, SRE77]

SELLMEIER coefficients	ordinary	extraordinary
A	4.9048	4.5820
B	−0.11768	−0.099169
C	−0.04750	−0.044432
D	−0.027169	−0.021950

Table C.2: Overview of the following properties :
(1) temperature variation of refractive indices and for λ = 1.0 µm to 4.0µm, [SRE77]
(2) electro-optic coefficients r at λ = 0.633 µm, [KT71]

temperature variation of refractive index	ordinary	extraordinary
$dn_{o,e}/dT$ [$\times 10^{-6}$/K]	3.3	37

electro-optic coefficient r [pm/V]	unclamped and tension-free (T)		clamped and strain-free (S)
r^T_{13}	10.	r^S_{13}	8.6
r^T_{22}	6.8	r^S_{22}	3.4
r^T_{33}	32.2	r^S_{33}	30.8
r^T_{51}	32.	r^S_{51}	28.

$LiNbO_3$ is one of the most important ferro-electric materials and has widespread applications because of its electro-optic, elasto-optic, piezo-electric and dieletric properties. It is a uniaxial, birefringent crystal whose index of refraction is described by the wavelength-dependent extraordinary (TE-mode) and ordinary indices (TM-mode), n_e and n_o which comply with the SELLMEIER equation

$$n^2_{o,e}(\lambda) = A_{o,e} + \frac{B_{o,e}}{\lambda^2 + C_{o,e}} + D_{o,e}\lambda^2$$

with wavelength λ given in µm. The coefficients A,B,C and D as given in table C.1 are valid in a wavelength range between 0.8 µm and 4.8 µm. In table C.2 further constants and coefficients are given describing the optical and electro-optical properties of Lithium Niobate.

For a wavelength of 1.56 µm the SELLMEIER equation delivers the value 2.2109 for the ordinary index n_o and 2.1378 for the extraordinary index n_e. Furthermore, those indices exhibit a temperature dependence where the variation constant $^{dn}/_{dT}$ in a wavelength range of $\lambda = 1.0\,\mu m$ to $4.0\,\mu m$ is about one order of magnitude larger for the extraordinary index than for the ordinary one, compare table C.2

Polarised light propagates through a Lithium Niobate crystal in such a way, that an extraordinary mode is supported for a polarisation along the optical axis z and an ordinary polarisation mode is supported in the x-y plane. For different applications, the devices are made from either x-, y- or z-cut wafers. Typically, devices for phase modulation, fibre gyro-scopes and MACH-ZEHNDER interferometers are fabricated on x-cut, y-propagating wafers. Through an in-diffusion with Titanium , both the ordinary and extraordinary indices of refraction are increased locally, so that for any crystal orientation TE and TM modes are supported [Bas10].

C.1.1 Properties of the Zero-Chirp Intensity Modulator Mach-10™056 from Covega

The electro-optic modulator (EOM) used for the BAMs is made from Titanium (Ti)-indiffused x-cut Lithium Niobate ($LiNbO_3$).

Table C.3: Data sheet of EOM Mach-10™056 from Covega [Web11d].

parameter	symbol	unit	min.	typ.	max.
operating case temperature	T_{CASE}	°C	0.		70.
operating wavelength	λ	nm	1525.		1605.
optical insertion loss (connectorised)	IL	dB		4.0	5.0
insertion loss variation (EOL)	ΔIL	dB	−0.5		0.5
modulator chirp parameter	α		−0.1		0.1
optical return loss	RL	dB	40.		
optical on/off extinction ratio (@ DC)	ER	dB	20.		
optical extinction ratio (PRBS)	ER	dB	13.		
bit rate frequency	f_{BR}	Gbit/s	9.95		12.
E bandwidth (−3 dB with linear fit)	$f_{c-3\,dB}$	GHz	10.		
O bandwidth (−3 dB with linear fit)	$f_{c-3\,dB}$	GHz	12.		
scattering parameter (DC to 10 GHz)	S_{11}	dB		−12.	−10.
RF drive voltage (PRBS)	V_{PRBS}	V		5.5	6.
V_π bias port (@ DC)		V			8.
DC bias voltage	V_{PRBS}	V		5.5	6.
PD responsivity (ref. to output power)		mA/mW	0.1		0.5
output optical power monitoring range		dBm	−5.		10.
output monitor variation		dB	−0.5		0.5
monitor photodiode reverse bias voltage		V	−5.5		−3.0

C.2 Components Listing: BAM system

Table C.4 gives an overview on components required for read-out and control electronics based on *Beckhoff* terminals. Table C.5 contains a summary of the optical, mechanical and electrical components needed for assembling one opto-mechanical front-end of the bunch arrival time monitor. The prices given are estimates based on the price lists from 2009, when previous orders had been placed.

Table C.4: Electrical components for read-out and control of devices built into the opto-mechanical front-end of the BAM (Generation 3).

component	article number	amount	application
RTD bus terminal	BC9000	2	
stepper motor terminal	KL2531	2	24 VDC, 1.5 A
power supply terminal	KL9505	2	5 V
Heidenhain encoder read-out	KL5051-0010	2	
digital input terminal	KL1124	1	5 V
digital input terminal	KL1404	2	24 V, 4 channels
feed-in terminal	KL9210	1	24 V
digital output terminal	KL2104	2	24 V
ADC, 12 bit	KL3464	1	+/ – 10 V
DAC, 12 bit	KL4034	1	+/ – 10 V
RTD 3-wire	KL3203-0028	2	2 channels
bus end terminal	KL9010	2	

Table C.5: Components for an opto-mechanical front-end of the BAM (Generation 3).

component	supplier	article number	amount	[k€]/piece	total [k€]
absolute position encoder	Heidenhain	LC 483	1	0.83	0.83
ACB 2.1	in-house production		1	2.50	2.50
BAM and electronics chassis	in-house production		1	3.0	3.0
Beckhoff electronics	Beckhoff	diverse	1	2.0	2.0
collimator holder (2 axis)	Newport	HVM-.5	2	0.12	0.24
collimator holder (5 axis)	Newport	LPV-1	2	0.23	0.46
EOM	Covega	Mach-10 056-12-P-A-A-NL-STL	2	1.2	2.4
high-precision linear stage	Owis	LIMES 80-130-HSM	1	2.3	2.3
mechanics	in-house production		1	1.0	1.0
Peltier elements	Thorlabs	TEC3-6	4	0.03	0.12
PMF collimator	Lightel	LPC-02-1550-8/125-P-0.9-3.9AS-60-X-3-1	3	0.15	0.45
PMF coupler (50/50)	Lightel	PMC-S-12-5050-1550-1-L-0	1	0.11	0.11
precision linear stage	Owis	LTM 80F-100-MSM	1	1.06	1.06
RF power limiter	Agilent	N9356C	1	0.35	0.35
SMF collimator	Lightel	LPC-02-1550-9/125-S-0.9-3.9AS-60-X-3-1	1	0.12	0.12
SMF coupler	Lightel	SWC-12-P-9010-1550-H-1-L-0	1	0.07	0.07
temperature controller board	Wavelength Electronics	PT10K-CH	1	0.30	0.30
10 kΩ thermistor	Thorlabs	TH10K	1	0.01	0.01
				total	17.32

C.2.1 Photographs of BAM – Generation 2

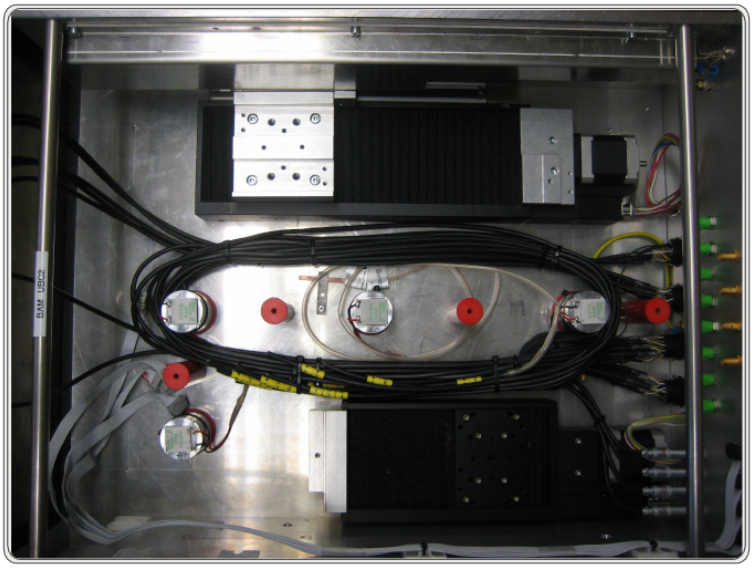

(a) Bottom layer of BAM box: isolated aluminium posts with PELTIER elements. Both high-precision, motorised delay stages are mounted already. The longer one carries an absolute position encoder (between stage and wall of the BAM box).

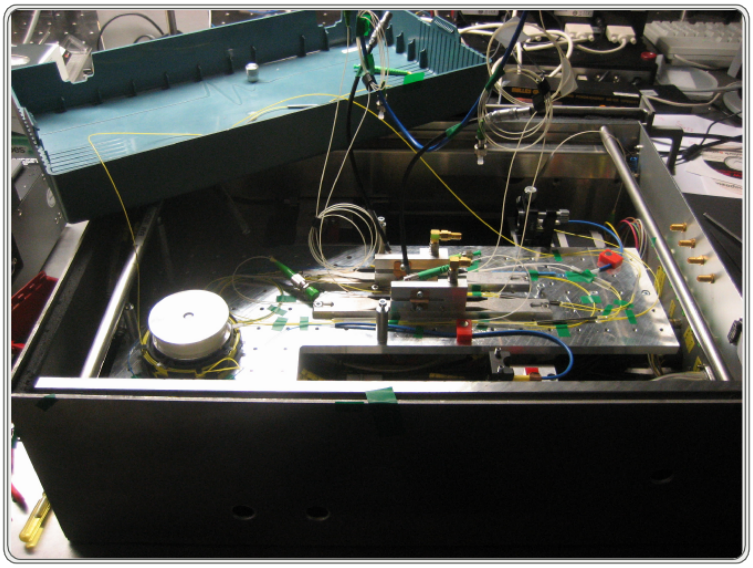

(b) BAM box with temperature stabilised aluminium plate, two motorised linear stages and two EOMs: The picture has been taken during the assembly of fibre-optical components. The last few fusion splices have to be made with parts of the fibre section already fixed.

Figure C.1: Photographs showing the (a) ground plate and (b) the middle layer with fibre-optical components during the assembly.

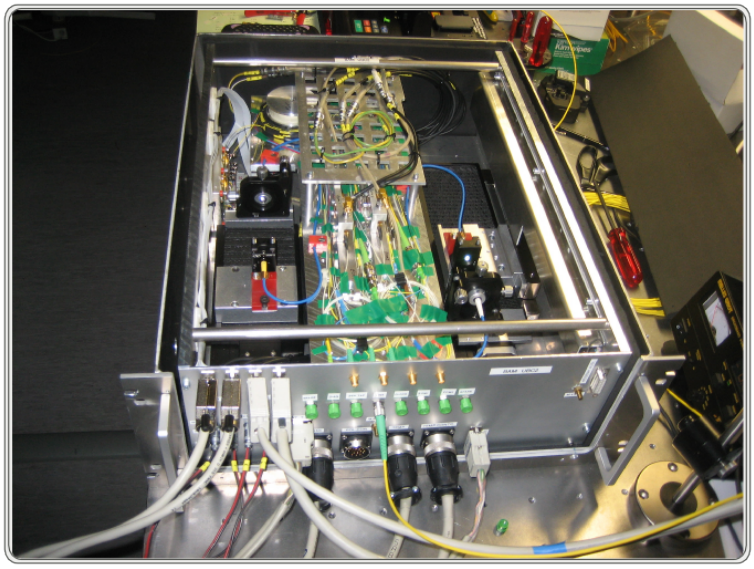

(a) Completely assembled BAM box: In the laboratory, final tests of electronics (comprising laser diodes, EOM bias voltage, motor stages, an absolute position encoder and temperature read-out) as well as the alignment of the optical delay lines are carried out.

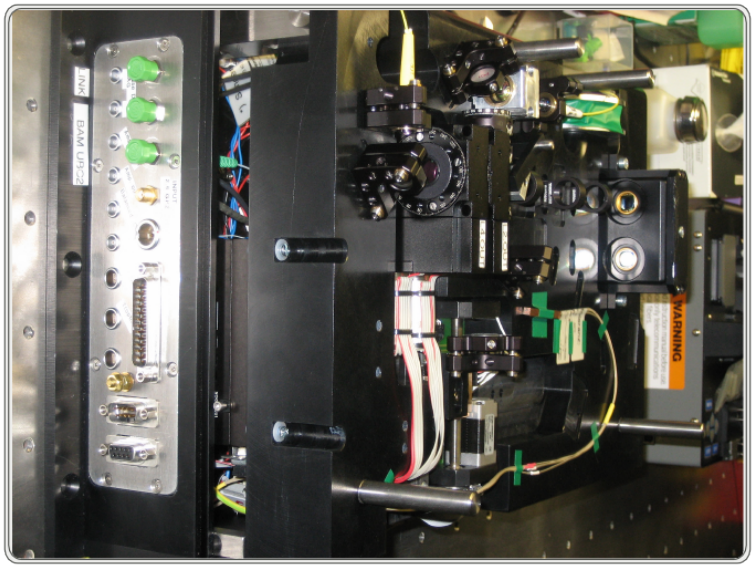

(b) (rotated by 90 ° clockwise). Fibre-link box of version 1.1 (Link 09), belonging to BAM.1UBC2.

Figure C.2: Photograph (a) shows the completed opto-mechanical front-end of BAM.1UBC2. After the assembly, the electronics (motor control, EOM bias voltage, etc.) are finally tested. The free-space optics of both optical delays are aligned, before the BAM can be transported to its destination inside of the accelerator tunnel. Photograph (b) shows the according fibre-link box, Link.09, which comprises the old design version 1.1, during its assembly.

C.3 Components Listing: Fibre-Link Unit

The fibre-links as a complex system consist of three major parts: the mechanics, optics (including fibre-optics) and the electronics. Table C.6 gives a general cost overview for a complete link unit. Table C.7, C.8 and C.9 give a more detailed listing of the required components for a link of opto-mechanics design version 3.0.

Table C.6: Cost overview for a complete Link-unit. (Version 3.0)

component	amount	[k€]/piece	total [k€]
mechanics and chassis	1	2.60	2.60
optics incl. fibre-optics	1	8.31	8.31
electronics (without LDD)	1	10.93	10.63
EDFA	2	2.23	4.46
		total	26.00

Table C.7: Electrical and fibre-optical components required for one EDFA.

component	supplier	article number	amount	[k€]/piece	total [k€]
Er-doped gain fibre	Thorlabs	Er110-4/125	0.6 m	0.03	0.03
laser diode driver (LDD)	in-house	–	1	1.00	1.00
laser diode mount	Thorlabs	LM14S2	1	0.29	0.29
pump laser diode 980 nm	Oclaro	LC96-AA74-20R	1	0.8	0.8
pump termination	in-house	–	1	0.01	0.01
WDM	Lightel	WDM4-12-P-1-L-0	2	0.05	0.1
				total	2.23

Table C.8: Electrical components required for a fibre-link unit of the latest design version (3.0).

component	supplier (manufacturer)	article number	amount	[k€]/piece	total [k€]
ADC (2 out of 8 channels)	in-house	–	0.25	1.2	0.3
amplifier (2.6 GHz)	Municom (Mini-Circuits)	ZX60-33-LN-S+	1	0.07	0.07
amplifier, low-noise (LNA)	in-house	–	2	0.10	0.20
balanced detector	Thorlabs (Newfocus)	Model 2307	1	0.77	0.77
DSP (dual) regulation system	in-house	–	0.5	4.00	2.00
filter, band-pass (2.6 GHz)	IMC	IDBP60-2600-33-4-0-A10-D-C-T17-S1	1	0.20	0.20
filter, low-pass (1.9 GHz)	Municom (Mini-Circuits)	SLP-1.9+	2	0.03	0.06
linear delay stage (motorised)	in-house	LMS-Vers10.2-Type3	1	2.30	2.30
motor driver, 3 channels	in-house (Beckhoff)	–	1	0.70	0.70
piezo driver	in-house	–	1	0.45	0.45
phase detector	in-house	AD8302	1	0.07	0.07
photodiode (1550 nm)	EOT	ET-3010	2	0.26	0.52
power splitter (6 dB, resistive)	Municom (Mini-Circuits)	ZX10R-14-S+	1	0.05	0.05
rotation table	OWIS	DMT 40-D20-HiSM	2	1.30	2.60
temperature sensor (Pt100)	ABB	SensyTemp SF R	2	0.07	0.14
voltage regulator/divider	in-house	–	1	0.20	0.20
				total	10.63

Table C.9: Opto-mechanical, fibre-optic and optical components required for a fibre-link unit of the latest design version (3.0).

component	supplier (manufacturer)	article number	amount	[k€]/piece	total [k€]
collimator, SMF (1.2 mm)	AMS (OZ Optics)	LPC-02-1550-9/125-S-1.2-6.2AS-60-X-3-1	2	0.13	0.26
collimator, SMF (0.9 mm)	AMS (OZ Optics)	LPC-02-1550-9/125-S-0.9-3.9AS-60-X-3-1	2	0.13	0.26
corner cube retro-reflector	Altechna	N-BK7, AR 1550 nm, OD 15 mm, 180° ± 10″	1	0.15	0.15
coupler, SMF (95/05)	AMS (Lightel)	SWC-22-P-9505-H-1-L-0	1	0.02	0.02
DCF fibre (no module)	OFS	LLWB 70m 0921500700xx, 2x splice 1m SMF	0.5	0.28	0.14
FRM (90/10)	Opternus (Lightel)	500-61272-14-1	1	0.32	0.32
goniometer	Thorlabs	GN05M	1	0.11	0.11
isolator (free-space)	Lightel	polarisation dependent, 1550 nm	1	0.50	0.50
lens, achromatic doublet	Thorlabs	AC064-013-C	2	0.04	0.08
lens, bi-concave	Altechna	N-BK7, AR 1550 nm, OD 12.7 mm, f −194 mm	1	0.03	0.03
lens, plano-convex	Altechna	N-BK7, AR 1550 nm, OD 12.7 mm, f +34 mm	1	0.03	0.03
lens, plano-convex	Altechna	N-BK7, AR 1550 nm, OD 12.7 mm, f +84 mm	1	0.03	0.03
lens holder, w stop angle	Thorlabs	LMR05/M	1	0.02	0.02
lens holder, w/o stop angle	Thorlabs	SMR05/M	3	0.02	0.06
lens mount, adjustable	Thorlabs	SM05V05	3	0.03	0.09
mirror, Ag-coated	Thorlabs	PF05-03-P01	1	0.03	0.03

continued on next page ...

Table C.9: (continued) Opto-mechanical, fibre-optics and optical components required for a fibre-link unit of the latest design version (3.0).

component	supplier (manufacturer)	article number	amount	[k€]/piece	total [k€]
mirror, Ag-coated, D-shaped	Thorlabs	PFD05-03-P01	1	0.03	0.03
mirror, dichroic	MSO Jena	ST800-1550 OD 12.5 mm x 1.5 mm	1	0.05	0.05
mirror, dielectric	Thorlabs	BB05-E04	6	0.07	0.42
mirror mount, fixed	Thorlabs	DMM05/M	1	0.05	0.05
mirror mount, kinetic	Thorlabs	KM05/M	9	0.04	0.36
patchcords, SMF	PFP	(diverse lengths)	3	0.05	0.15
piezo-stretcher (SMF, 3-layer)	Optiphase	PZ2-SM2-O-155	1	0.90	0.90
polarising beam cube	Altechna	12.7 mm, AR 1550 nm, optically contacted	2	0.21	0.42
PPKTP crystal, AR/HR coated	Raicol	period 46.2 µm, dim. 1x2x4 mm^3	1	0.88	0.88
right-angle prism	Altechna	N-BK7, AR 1550 nm, AxBxC = 7x7x7 mm	1	0.06	0.06
rotation mount, for waveplates	Thorlabs	RSP05/M	6	0.06	0.36
wavplate, $\lambda/2$	Soliton (Meadowlark)	NH-050-1550	3	0.50	1.5
wavplate, $\lambda/4$	Soliton (Meadowlark)	NQ-050-1550	2	0.50	1.0
				total	8.31

C.3.1 Photographs of recent link design: Version 3.0

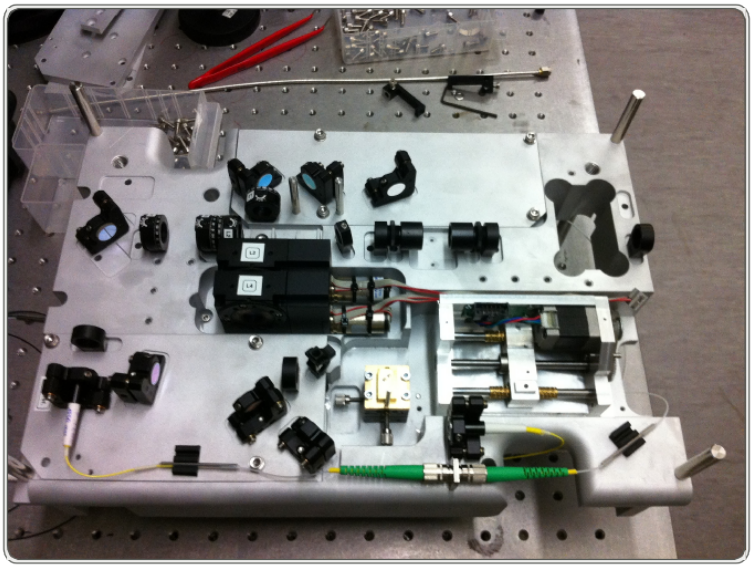

(a) top layer: free-space optics

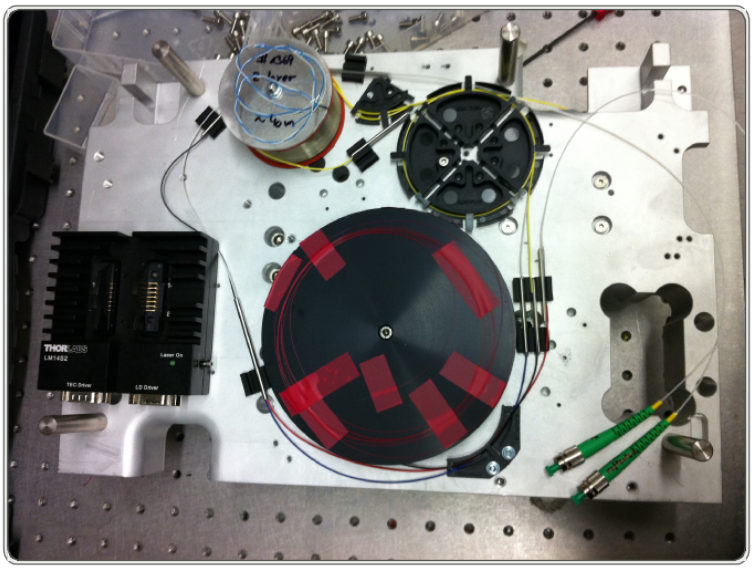

(b) middle layer: optical fibre assembly

Figure C.3: Photographs showing the (a) top and (b) middle layer of the link opto-mechanics, latest design version 3.0. The pictures where taken during the assembly.

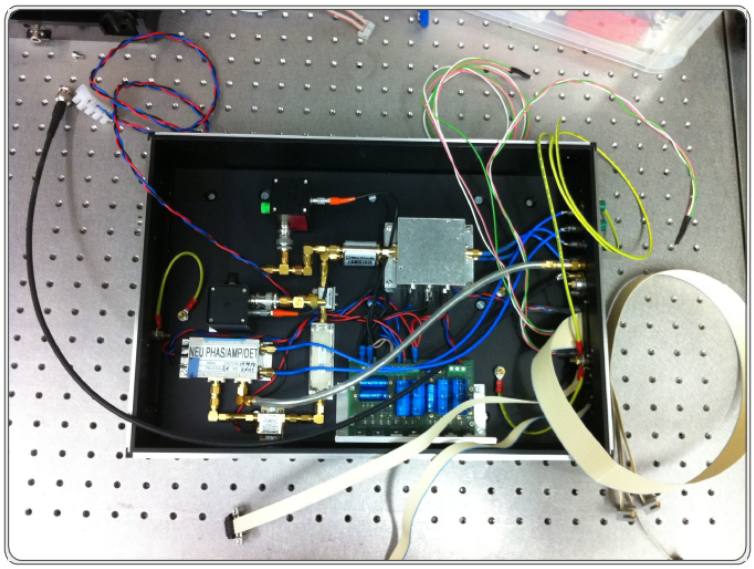

(a) bottom layer: electronics

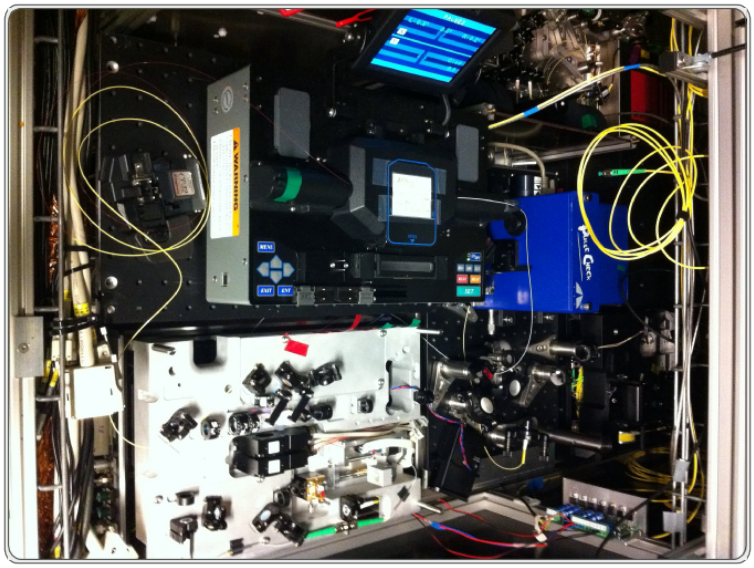

(b) (rotated by 90 ° clockwise) during commissioning of the link in the synchronisation hutch

Figure C.4: Photograph (a) shows the bottom layer of the link opto-mechanics, latest design version 3.0. The lower picture was taken during the commissioning of the link in the synchronisation hutch. Here, the link is surrounded by other optical components of the LbSyn system and by hardware and diagnostics, required for the commissioning process, like fusion splicer and auto-correlator.

D Principal Component Analysis

The principal component analysis (PCA) is a standard tool for statistical data analysis and is related to the mathematical technique of singular value decomposition. This technique is used to find the most meaningful basis to re-express a data set [Shl05]. In the context of data analysis for this thesis the PCA was used as a trustworthy method to distinguish between the correlated variance (signal variance) and uncorrelated variance (system noise). The uncorrelated noise can thus be filtered out from the data set and is used as a measure for the precision of two independent detectors measuring the same variable. First, the mathematical method of PCA is shortly discussed, followed by an overview of the implementation in MATLAB™.

general discussion

In order to apply the PCA to a data set, some assumptions have to be fulfilled. First, it is assumed that there exists a *linear transformation* **P** between the originally observed data **X** and the new representation of it, **Y**, such that

$$\mathbf{Y} = \mathbf{P}\,\mathbf{X} = \begin{pmatrix} \overrightarrow{p_1} \\ \overrightarrow{p_2} \\ \vdots \\ \overrightarrow{p_m} \end{pmatrix} \begin{pmatrix} \overrightarrow{x_1} & \overrightarrow{x_2} & \cdots & \overrightarrow{x_n} \end{pmatrix} \tag{D.105}$$

with **X** being a $m \times n$ matrix where each of the n columns contains m values of the measured variable from m individual detectors. Geometrically, **P** describes a transformation which rotates and stretches the coordinate system in which **X** has been measured into a new coordinate system in which the **X** transforms into **Y**. The new basis vectors for expressing the columns of **X** are then given by the rows of **P**. For each data column $\overrightarrow{y_i}$ this can be written as

$$\overrightarrow{y_i} = \begin{pmatrix} \overrightarrow{p_1} \cdot \overrightarrow{x_i} \\ \overrightarrow{p_2} \cdot \overrightarrow{x_i} \\ \vdots \\ \overrightarrow{p_m} \cdot \overrightarrow{x_i} \end{pmatrix} \qquad i = 1, \ldots, n \tag{D.106}$$

hence, the data vectors $\overrightarrow{x_i}$ are projected onto the row vectors of **P**, which are the principal components of **X**.

Another assumption besides the linearity concerns the noise of the measurement. When using PCA, one assumes that the data set shows low noise, i.e. the *redundancy of the data set is as high as possible*. Otherwise no bijective principal components can be identified. The high precision is indicated by a signal-to-noise ratio (SNR) $\gg 1$, calculated from

$$\mathrm{SNR} = \frac{\sigma^2_{\mathrm{signal}}}{\sigma^2_{\mathrm{noise}}} \tag{D.107}$$

The direction of the highest SNR and thus the largest signal variance $\sigma^2_{\mathrm{signal}}$ will then be identified as

the most probable principal axis, i.e. the axis along which the measured variable is changing linearly.

In case of a 2-dimensional data set, i.e. comparing the same measured variable from two individual detectors, the direction of the largest signal variance corresponds to the best-fit line to the data cloud. In the general case of an n-dimensional data set the principal axes can be found by determining the covariance of the data vectors $\vec{x_i}$. The covariance is a measure for the linear relationship between variables and its absolute magnitude is a measure for the degree of redundancy [Shl05]. The covariance matrix $\mathbf{C_Y}$ is determined by

$$\mathbf{C_Y} = \frac{1}{n}\mathbf{Y}\,\mathbf{Y}^T \tag{D.108}$$

Using equation D.105 this can also be written as

$$\mathbf{C_Y} = \mathbf{P}\left(\frac{1}{n}\mathbf{X}\,\mathbf{X}^T\right)\mathbf{P}^T = \mathbf{P}\,\mathbf{C_X}\,\mathbf{P}^T \tag{D.109}$$

with $\mathbf{C_X}$ being the covariance of the initial data set $\mathbf{X}$. The rows of $\mathbf{P}$ are the principal components of $\mathbf{X}$, i.e. each row $\vec{p_i}$ is an eigenvector of $(1/n)\ \mathbf{X}\,\mathbf{X}^T$.

If a matrix $\mathbf{P}$ exists which fulfils eq. D.109 the following statements are valid:

- $\mathbf{P}$ diagonalises the matrix $\mathbf{C_Y}$
- the row vectors $\vec{p_i}$ are orthonormal
- the off-diagonal terms of $\mathbf{C_X}$ are the covariances between the different detectors
- the matrix $\mathbf{C_X}$ includes the covariances between all possible pairs of measured values
- the diagonal values of $\mathbf{C_Y}$ are the variances of $\mathbf{X}$ along the axes $\vec{p_i}$ for $i = 1, \ldots, n$
- the off-diagonal terms of $\mathbf{C_Y}$ are zero

The latter means, that the data set is decorrelated.

2-d PCA in MATLAB™

The PCA for a 2-dimensional case has been implemented in a simple MATLAB™ function, compare [Shl05]. In the context of this thesis it was applied for evaluating the correlation between 2-dimensional data sets of

1. arrival times measured with two different BAMs
2. time-of-flight measurements done with two BAMs at bunch compressor (BC)2 in comparison with relative energy measurements performed with a BCM

In addition to this, the correlation tests according to Pearson and Spearman are calculated in the MATLAB™ script (see below). For a 2-dimensional data set $\left[\vec{\mathbf{x_1}}, \vec{\mathbf{x_2}}\right]$ with n individual samples, the Pearson's sample correlation is defined by [RK04]

$$\rho_P = \frac{\sum_{i=1}^{n}\left(\mathbf{x_{1,i}} - \bar{\mathbf{x}}_\mathbf{1}\right)\left(\mathbf{x_{2,i}} - \bar{\mathbf{x}}_\mathbf{2}\right)}{\sqrt{\sum_{i=1}^{n}\left(\mathbf{x_{1,i}} - \bar{\mathbf{x}}_\mathbf{1}\right)^2 \sum_{i=1}^{n}\left(\mathbf{x_{2,i}} - \bar{\mathbf{x}}_\mathbf{2}\right)^2}} \tag{D.110}$$

with mean values $\bar{\mathbf{x}}$. When using the standard deviations $\sigma_{\mathbf{x}}$, an equivalent expression is

$$\rho_P = \frac{1}{n-1} \sum_{i=1}^{n} \left(\frac{x_{1,i} - \bar{x}_1}{\sigma_{x_1}} \right) \left(\frac{x_{2,i} - \bar{x}_2}{\sigma_{x_2}} \right) \tag{D.111}$$

When replacing the data $\left[\vec{\mathbf{x_1}}, \vec{\mathbf{x_2}}\right]$ by their bivariate ranks $\left[\vec{\mathbf{R_1}}, \vec{\mathbf{R_2}}\right]$ equation D.110 yields the SPEARMAN's rank correlation ρ_S [RK04], which can also be written as

$$\rho_S = 1 - \frac{6 \sum_{i=1}^{n} \left(\mathbf{R_{1,i}} - \mathbf{R_{2,i}}\right)^2}{n^3 - n} \tag{D.112}$$

The MATLAB™ code of the "correlation function" is given below:

```
%
% Correlate Function
% input:    two data vectors
% output:   two data vectors normalised to the mean value,
%           covariance matrix diagonalised,
%           SPEARMAN's and PEARSON's rho - correlation coefficients
%

function [stats] = Correlate(data1, data2)

  %data statistics:
   orig_dat = [data1, data2];
   [M,~] = size(orig_dat);

  %subtract mean in each dimension
   mean_val = mean(orig_dat,1);
   norm_dat = orig_dat' - repmat(mean_val',1,M);
   cov_mat = cov(orig_dat);

  %find eigenvectors and eigenvalues
   [PC, V] = eig(cov_mat);

  %extract diagonal of matrix as vector
   V = diag(V);

  %sort variances in decreasing order
   [~, rindices] = sort(-1*V);
   V = V(rindices);
   PC = PC(:, rindices);

  %project the original data set
    projected_dat = PC' * norm_dat;

  %Pearson's correlation
    [R,~,~,~]=corrcoef(orig_dat);

  %Spearman's rho:
    X = orig_dat;
    Y = sort(X);
```

```
40    Z = zeros(size(X,1), size(X,2));
41    for col = 1:size(X,2)
42      for row = 1:size(X,1)
43         Z(X(:,col) == X(row,col),col) = mean(find(Y(:,col) == X(row,col)));
44      end
45    end
46   [rho, ~, ~, ~] = corrcoef(Z);
47
48   stats.normalised_data    = norm_dat;
49   stats.projected_data     = projected_dat;
50   stats.covariance_mat     = PC;
51   stats.Pearsons_rho       = R(1,2);
52   stats.Spearmans_rho      = rho(1,2);
53   stats.sigma_signal       = sqrt(V(1));
54   stats.sigma_noise        = sqrt(V(2));
55   stats.SNR                = V(1)/V(2);
56
57 end
```

E Matlab Code: Polarisation Adjustment

This section contains the MATLAB™ code of the automatised polarisation control, which has been written and implemented in the beginning of 2011. Through regular, e.g. hourly, adjustments of the intra-link waveplates an optimised signal quality of all three optical outputs of each bunch arrival time monitor (BAM) is assured. This has been an essential contribution to the longterm failsafe operation of the BAMs.

The programme consists of three files: in a main file a *timer* object is defined. Here, one can choose for which BAM the optimisation should be active. Furthermore, one can decide if the programme should adjust to a maximised signal in one of the ADCs of the advanced carrier board (ACB) or if the signal should be stabilised to a specified value. The second file comprises a listing of the relevant DOOCS addresses, and the third file contains the actual algorithm for the adjustment of the waveplates, including additional auxiliary functions. The also included exception handling, as well as callbacks to the user interface have been commented out and are not shown here, in order to cut the source code short.

Main file:

```
%
% automatic polarisation adjustment of any specified Link endstation
%
% the according monitor-ADCs have to declared in:
%  GLOBAL_ADDRESSES (in /home/ttflinac/user/mkbock/GLOBAL/)
%
% when running this m-file a timer object is created, named 'PolAdjust_Timer'
% options:
%  stop(PolAdjust_Timer)        : stops the timer without removing it
%  start(PolAdjust_Timer)       : restarts 'PolAdjust_Timer'
%  delete(PolAdjust_Timer)      : obvious
%  clear PolAdjust_Timer        : obvious
%
%--------------------------------------------------------------------------
% uses the function 'Callback_PolAdjust_Timer'
%
% author:           M.K. Bock
% date of begin:    20.04.2011

clear all

addpath('/home/ttflinac/user/mkbock/GLOBAL/');
address = GLOBAL_ADDRESSES;
%%
%-------------------------------- EDIT ------------------------------------
% cell list of devices:
def.DEV.name = {'1UBC2','3DBC2','4DBC3','18ACC7'};

% coarse stepsize for optimisation procedure for each device
% fine stepsize will be half of this value
% e.g. 4 degree
%----------------------
```

```
def.DEV.stepsize = 5;

% number of iterative waveplate adjustments per optimisation run
% has to be defined for each device
% integer 0, 1, 2 or higher; normaly 1 repetition is enough
%----------------------
def.DEV.iterate = 0;

% polarisation with using only L2 or only L4 or both
%----------------------
def.DEV.L2 = 1;
def.DEV.L4 = 0;

% list of target values for optimisation in order of device
% if def.opt_target == NaN value will be optimised to maximum
%----------------------
def.DEV.target = [NaN NaN 10000 NaN];

%----------------------
tdelay = 0;        % time to wait until start
tperiod = 60;      % time between starts of callback fct. in minutes
hours = 12;        % time to run in No. of hours
days = 1;        % time to run in No. of days

%%
%--------------------------- NOT TO EDIT --------------------------------
% total number of callbacks witin one run
ttasks = (hours + days*24)/(tperiod/60)+1;
%------------------------------------------------------------------------
 PolAdjust_Timer = timer( 'StartDelay', tdelay, ...
            'Period', tperiod*60, ...
            'TasksToExecute', ttasks, ...
            'ExecutionMode', 'fixedRate', ...
            'Name', 'timer_polarisation_adjust');

 startstring = sprintf(['Timer for Polarisation Adjustment started.\n', ...
                        'Time between executions of Timer callback function: %s
                            minutes.\n', ...
                        'Repetition of Timer: %s callbacks.'], ...
                        num2str(get(PolAdjust_Timer, 'Period')/60),
                            num2str(get(PolAdjust_Timer, 'TasksToExecute')));

 stopstring = sprintf('Timer for Polarisation Adjustment stopped.');

 errorstring = sprintf('Unexpected Error occured. Restart Timer.');
 set(PolAdjust_Timer, 'StartFcn', 'disp(startstring)');
 set(PolAdjust_Timer, 'StopFcn', 'disp(stopstring)');
 set(PolAdjust_Timer, 'ErrorFcn', 'disp(errorstring)');
 set(PolAdjust_Timer, 'TimerFcn', 'Callback_PolAdjust_Timer(def, address)');
 start(PolAdjust_Timer)
```

File containing the relevant DOOCS addresses:

```
% m-file with global address list for DOOCS server and properties

function [address] = GLOBAL_ADDRESSES

  %BAM DOOCS adresses and properties
  BAMcell = cell(1,4);
  address.BAM =  cell2struct(BAMcell, 'name');

  %--------------------------
  % BAM No.1
  address.BAM(1).name = '1UBC2';
  address.BAM(1).link_number = 9;
  address.LINK(9).name = address.BAM(1).name;
  address.LINK(9).monitor =
      ['TTF2.SYNCH/','BAM.ADC/',address.BAM(1).name,'/ADC2'];
  %--------------------------
  % BAM No.2
  address.BAM(2).name = '3DBC2';
  address.BAM(2).link_number = 11;
  address.LINK(11).name = address.BAM(2).name;
  address.LINK(11).monitor =
      ['TTF2.SYNCH/','BAM.ADC/',address.BAM(2).name,'/ADC2'];
  %--------------------------
  % BAM No.3
  address.BAM(3).name = '4DBC3';
  address.BAM(3).link_number = 1;
  address.LINK(1).name = address.BAM(3).name;
  address.LINK(1).monitor =
      ['TTF2.SYNCH/','BAM.ADC/',address.BAM(3).name,'/ADC2'];
  %--------------------------
  % BAM No.4
  address.BAM(4).name = '18ACC7';
  address.BAM(4).link_number = 3;
  address.LINK(3).name = address.BAM(4).name;
  address.LINK(3).monitor =
      ['TTF2.SYNCH/','BAM.ADC/',address.BAM(4).name,'/ADC2'];
  %--------------------------

  %Link DOOCS addresses and properties
  for n = 1:16
    %--------------------------
    address.LINK(n).name = sprintf('LINK%02i', n);
    address.LINK(n).motor = sprintf('TTF2.SYNCH/LINK.MOTOR/LINK%02.0f', n);
    %--------------------------
  end
```

Algorithm with subfunctions:

```
%
% file:           m-file with auxiliary functions
% parent:         'Polarisation_Adjustment.m'
% author:         M.K. Bock
% date of begin: 20.04.2011
%
function Callback_PolAdjust_Timer(def, address)

%% Identification of Links
param.lnum = 0;
for k = 1:size(def.DEV.name,2)
  param.iterate(k) = def.DEV.iterate(k);
  for i = 1:size(address.LINK,2)
      if strcmp(address.LINK(i).name, def.DEV.name{k}) ~= 0
    param.lnum = [param.lnum, i];
      end
  end
end

%% Definitions --------------------
param.opt_trains = 10;
param.Badc = [-1 50 5 10]'; %[-1 50 150 10]'
param.Rate = 10;
param.waveplate_type = ['L4';'L2'];
param.L = [def.DEV.L4 def.DEV.L2];

for i = find(param.lnum)
  param.name(i-1,:) = address.LINK(param.lnum(i)).name;
  param.address(i-1).adc = address.LINK(param.lnum(i)).monitor;
  param.address(i-1).waveplate(:,1) = [address.LINK(param.lnum(i)).motor,'.L4'];
  param.address(i-1).waveplate(:,2) = [address.LINK(param.lnum(i)).motor,'.L2'];
  param.target_value(i-1) = def.DEV.target(i-1);
  param.step(i-1) = def.DEV.stepsize(i-1);

  ifnum = param.lnum(i);
  if ifnum == 1 || ifnum == 3 || ifnum == 9 || ifnum == 11
      param.target_dim{i-1} = 'bits';
  else
      param.target_dim{i-1} = 'V';
  end
end

%% Initiate Optimisation functions
for i = length(param.target_value)
  if ~isnan(param.target_value(i))
    Optimise_SpecialTarget(param, i)
  else
    Optimise_Maximum(param, i)
  end
end

```

```
%% helper functions
%
% function Optimise_Maximum
% sub-routine for optimising until the maximum ADC-level is reached
%
function Optimise_Maximum(param, num)
  i = num;
  %-----------------
  clear ADC LINK
  %----Initial Values----
  LINK.val = [];
  LINK.val.([param.waveplate_type(1,:),'_start']) =
      ttfr([param.address(i).waveplate(:,1)','/FPOS']);
  LINK.val.([param.waveplate_type(2,:),'_start']) =
      ttfr([param.address(i).waveplate(:,2)','/FPOS']);

  [adc_mean, adc_std] = SUBFCNT_Iterationstep(param.address(i).adc, param.Badc,
      param.opt_trains, param.Rate);
  ADC.val.adc_start_mean = adc_mean;
  ADC.val.adc_start_std = adc_std;

  %----Start Optimisation to maximum value----
  for m = 1:param.iterate(i) +1
    for n = find(param.L>0)
      %-------------------------------------------------------------------
      clear LX_act adc_mean adc_std
      clear LX_act_initial
      %-------------------------------------------------------------------
      randomdir = randi([-1 1], 1,1);
      while randomdir == 0
        randomdir = randi([-1 1], 1,1);
      end
      sgn = randomdir;

      LX_act_initial= ttfr([param.address(i).waveplate(:,n)', '/FPOS']);
      [adc_mean, adc_std] = SUBFCNT_Iterationstep(param.address(i).adc,
          param.Badc, param.opt_trains, param.Rate);
      adc_old = adc_mean;
      adc_old_std = adc_std;

      % first step = start position + param.step(i)
      [~,LX_act, err]=SUBFCNT_Set_LXMotorpos(LX_act_initial +
          sgn*param.step(i), param.address(i).waveplate(:,n)');
      [adc_mean, adc_std] = SUBFCNT_Iterationstep(param.address(i).adc,
          param.Badc, param.opt_trains, param.Rate);

      if adc_mean < adc_old || adc_mean + adc_std < adc_old + adc_old_std
        sgn = -sgn;
      end

      adc_old = adc_mean;
      adc_old_std = adc_std;

```

```
99        %OPTIMISATION PROCEDURE
100       while adc_mean >= adc_old || adc_mean - adc_std >= adc_old - adc_old_std
101         adc_old = adc_mean;
102         adc_old_std = adc_std;
103         % one step to the right:
104
105         [~,LX_act, err]=SUBFCNT_Set_LXMotorpos(LX_act + sgn*param.step(i),
                param.address(i).waveplate(:,n)');
106         [adc_mean, adc_std] = SUBFCNT_Iterationstep(param.address(i).adc,
                param.Badc, param.opt_trains, param.Rate);
107       end
108
109       % now moving back in small steps
110       sgn = -sgn;
111
112       adc_old = adc_mean;
113       adc_old_std = adc_std;
114       param.halfstep = param.step(i)/2;
115
116       [~,LX_act, err]=SUBFCNT_Set_LXMotorpos(LX_act + sgn*param.halfstep,
              param.address(i).waveplate(:,n)');
117       [adc_mean, adc_std] = SUBFCNT_Iterationstep(param.address(i).adc,
              param.Badc, param.opt_trains, param.Rate);
118       LX_set = LX_act;
119
120       while adc_mean >= adc_old || adc_mean + adc_std >= adc_old + adc_old_std
121         adc_old = adc_mean;
122         adc_old_std = adc_std;
123
124         [~,LX_act, err]=SUBFCNT_Set_LXMotorpos(LX_act + sgn*param.halfstep,
                param.address(i).waveplate(:,n)');
125         [adc_mean, adc_std] = SUBFCNT_Iterationstep(param.address(i).adc,
                param.Badc, param.opt_trains, param.Rate);
126         LX_set = LX_act;
127       end
128       [~,~, err]=SUBFCNT_Set_LXMotorpos(LX_set -sgn*param.halfstep,
              param.address(i).waveplate(:,n)');
129     end
130
131     LINK.val.([param.waveplate_type(n,:),'_stop']) =
            ttfr([param.address(i).waveplate(:,n)','/FPOS']);
132   end
133 return
134
135 %
136 % function Optimise_SpecialTarget
137 % sub-routine for optimising until a predefined ADC-level is reached
138 %
139 function Optimise_SpecialTarget(param, num)
140   i = num;
141   %-----------------
142   clear ADC LINK
143   %-----------------
```

```
144   if isnan(param.target_value(i)) || isempty(param.target_value)
145       disp('No target value for optimisation specified.');
146       return
147   else
148   %----Initial Values----
149   LINK.val.L4_start = ttfr([param.address(i).waveplate(:,1)','/FPOS']);
150   LINK.val.L2_start = ttfr([param.address(i).waveplate(:,2)','/FPOS']);
151
152   [adc_mean, adc_std] = SUBFCNT_Iterationstep(param.address(i).adc, param.Badc,
          param.opt_trains, param.Rate);
153   ADC.val.adc_start_mean = adc_mean;
154   ADC.val.adc_start_std = adc_std;
155
156   %----Start Optimisation to target value----
157   for m = 1:param.iterate(i)+1
158     for n = find(param.L>0)
159       %--------------------------------------------------------------------
160       clear LX_act adc_mean adc_std adc_old adc_old_std
161       clear LX_act_initial offset_initial offset_min
162       %--------------------------------------------------------------------
163       randomdir = randi([-1 1], 1,1);
164       while randomdir == 0
165         randomdir = randi([-1 1], 1,1);
166       end
167       sgn = randomdir;
168
169       param.halfstep = param.step(i)/2;
170
171       LX_act_initial = ttfr([param.address(i).waveplate(:,n)', '/FPOS']);
172       [adc_mean, ~] = SUBFCNT_Iterationstep(param.address(i).adc, param.Badc,
            param.opt_trains, param.Rate);
173       adc_old = adc_mean;
174
175       % first step = start position + param.step(i)
176       [~,LX_act, err]=SUBFCNT_Set_LXMotorpos(LX_act_initial +
            sgn*param.step(i), param.address(i).waveplate(:,n)');
177       [adc_mean, ~] = SUBFCNT_Iterationstep(param.address(i).adc, param.Badc,
            param.opt_trains, param.Rate);
178
179       %OPTIMISATION PROCEDURE
180       offset_initial = param.target_value(i) - adc_old;
181
182       if abs(param.target_value(i) - adc_mean) <= abs(offset_initial)
183         offset_min = param.target_value(i) - adc_mean;
184         LX_set_min = LX_act;
185         widthfactor = 1;
186       else
187         sgn = -sgn;
188         widthfactor = 2;
189         offset_min = offset_initial;
190         LX_set_min = LX_act_initial;
191       end
192
```

```
193         % one step further
194         [~,LX_act, err]=SUBFCNT_Set_LXMotorpos(LX_act +
                sgn*widthfactor*param.step(i), param.address(i).waveplate(:,n)');
195         [adc_mean, ~] = SUBFCNT_Iterationstep(param.address(i).adc, param.Badc,
                param.opt_trains, param.Rate);
196
197         while abs(param.target_value(i) - adc_mean) <= abs(offset_min)
198           offset_min = param.target_value(i) - adc_mean;
199           LX_set_min = LX_act;
200           [~,LX_act, err]=SUBFCNT_Set_LXMotorpos(LX_act + sgn*param.step(i),
                  param.address(i).waveplate(:,n)');
201           [adc_mean, ~] = SUBFCNT_Iterationstep(param.address(i).adc, param.Badc,
                  param.opt_trains, param.Rate);
202         end
203         %-------------------------
204         % now moving back in small steps
205         sgn = -sgn;
206
207         [~,LX_act, err]=SUBFCNT_Set_LXMotorpos(LX_act + sgn*param.halfstep,
                param.address(i).waveplate(:,n)');
208         [adc_mean, ~] = SUBFCNT_Iterationstep(param.address(i).adc, param.Badc,
                param.opt_trains, param.Rate);
209
210         while abs(param.target_value(i) - adc_mean) < abs(offset_min)
211           offset_min = param.target_value(i) - adc_mean;
212           LX_set_min = LX_act;
213           [~,LX_act, err]=SUBFCNT_Set_LXMotorpos(LX_act + sgn*param.halfstep,
                  param.address(i).waveplate(:,n)');
214           [adc_mean, ~] = SUBFCNT_Iterationstep(param.address(i).adc, param.Badc,
                  param.opt_trains, param.Rate);
215         end
216         %-------------------------
217         [~,~, err]=SUBFCNT_Set_LXMotorpos(LX_set_min,
                param.address(i).waveplate(:,n)');
218       end
219     end
220   return
221
222   %
223   % function SUBFCNT_Iterationstep
224   % sub-routine for reading out the ADC
225   %
226   function [adc_mean, adc_std] = SUBFCNT_Iterationstep(ADC_Address, Buffer_Array,
        Opt_Trains, Sample_Rate)
227
228     if size(ADC_Address,1) == 2
229       adc_actual=zeros(2,Opt_Trains);
230       for j=1:Opt_Trains
231         tic
232         adc_actual(1,j)= mean(ttfr_iiii(ADC_Address(1,:), Buffer_Array));
233         adc_actual(2,j)= mean(ttfr_iiii(ADC_Address(2,:), Buffer_Array));
234         pause(1/Sample_Rate -toc)
235       end
```

```
236     adc_mean = mean(adc_actual(1,:)) - mean(adc_actual(2,:));
237     adc_std  = mean([std(adc_actual(1,:)) std(adc_actual(2,:))]);
238
239   elseif size(ADC_Address,1) == 1
240     adc_actual=zeros(1,Opt_Trains);
241     for j=1:Opt_Trains
242       tic
243       adc_actual(j)= mean(ttfr_iiii(ADC_Address, Buffer_Array));
244       pause(1/Sample_Rate -toc)
245     end
246     adc_mean = mean(adc_actual(:));
247     adc_std  = std(adc_actual(:));
248   else
249     disp('DOOCs address of monitor ADC not defined well.')
250     return
251   end
252 return
253
254 %
255 % function Set_LXMotorstep
256 % sub-routine for setting a new Waveplate angle
257 %
258 function [Flag,Lx_act, err]=SUBFCNT_Set_LXMotorpos(Lx_target,motor_address)
259   Flag  =0;
260   jmotor=0;
261   jwarn =7;
262   jerr  =jwarn+3;
263   err = 0;
264
265   % apply new value
266   [~] = ttfw(Lx_target,[motor_address,'/FPOS.SET']);
267   pause(0.5);
268   % start motor
269   [~] = ttfw(1,[motor_address,'/CMD']);
270   pause(5);
271
272   % loop checking when motor has reached new target value
273   Lx_act = ttfr([motor_address,'/FPOS']);
274   while abs(Lx_target-Lx_act)>0.1
275     jmotor=jmotor+1;
276     if jmotor<=jwarn
277       fprintf('Target value again applied ');
278       [~] = ttfw(Lx_target,[motor_address,'/FPOS.SET']);
279       pause(0.5);
280       ttfw(1,[motor_address,'/CMD']);
281       pause(3)
282     end
283     while jmotor<jerr && jmotor>jwarn
284       jmotor=jmotor+1;
285       [~] = ttfw(Lx_target,[motor_address,'/FPOS.SET']);
286       pause(0.5);
287       ttfw(1,[motor_address,'/CMD']);
288       pause(5)
```

```
289         Lx_act = ttfr([motor_address,'/FPOS']);
290       end
291       if jmotor==jerr
292         disp(['Motor ',motor_address(end-1:end),' does not reach position']);
293         err =1;
294         break;
295       end
296         Lx_act = ttfr([motor_address,'/FPOS']);
297     end
298     fprintf('Motor position: %2.2f\n', Lx_act);
299 return
```

Bibliography

[APJ+11] A. Angelovski, et al., *Pickup Design for High Resolution Bunch Arrival Time Monitor for FLASH and XFEL*, Proceedings of DIPAC'10, Hamburg, Germany, 2011, pp. 122–124.

[Bab11] N. Baboi, DESY, private communication, August 2011.

[Bas95] M. Bass, *Handbook of Optics*, second ed., vol. II, McGraw-Hill, 1995.

[Bas10] ———, *Handbook of Optics*, third ed., vol. I, McGraw-Hill, 2010.

[BBC+10a] W. A. Barletta, et al., *Free electron lasers: Present status and future challenges*, Nuclear Instruments and Methods in Physics Research Section A **618** (2010), no. 1-3, 69–96.

[BBC+10b] J. Blau, Y. H. Bae, K. Cohn, W. B. Colson, and J. M. Wittrock, *Free Electron Lasers in 2010*, Proceedings of FEL 2010, Malmö, Sweden, 2010, pp. 33–37.

[BCH+07] N. Baboi, et al., *Beam Position Monitor Calibration at the FLASH Linac at DESY*, Proceedings of PAC 2007, Albuquerque, N.M., USA, 2007, pp. 3937–3939.

[BDG+08] B. Beutner, W. Decking, O. Grimm, M. Hüning, M. Krasilnikov, T. Limberg, and M. Vogt, *Velocity Bunching at FLASH*, Proceedings of EPAC 2008, Genoa, Italy, 2008, pp. 112–114.

[BEJ83] L. A. Bergmann, S. T. Eng, and A. R. Johnston, *Temperature Stability of Transit Time Delay for a Single-Mode Fibre in a Loose Tube Cable*, Electronics Letters **19** (1983), 865–866.

[BG10] C. Behrens, and C. Gerth, *Measurements of Sliced-Bunch Parameters at FLASH*, Proceedings of FEL 2010, Malmö, Sweden, 2010, pp. 131–134.

[BSWN10] C. Behrens, B. Schmidt, S. Wesch, and D. Nicoletti, *Upgrade and Evaluation of the Bunch Compression Monitor a the Free-Electron Laser in Hamburg (FLASH)*, Proceedings of IPAC'10, Kyoto, Japan, 2010, pp. 912–914.

[CAB+10] F. Curbis, et al., *Characterization of Seeded FEL Pulses at FLASH: Status, Challenges and Opportunities*, Proceedings of FEL 2010, Malmö, Sweden, 2010, pp. 298–301.

[EBH10] H. Edwards, C. Behrens, and E. Harms, *3.9 GHz Cavity Module for Linear Bunch Compression at FLASH*, Proceedings of LINAC 2010, Tsukuba, Japan, 2010, pp. 41–45.

[FBA+10] B. Faatz, et al., *FLASH II: A Seeded Future at FLASH*, Proceedings of IPAC'10, Kyoto, Japan, 2010, pp. 2152–2154.

[FBG+10] M. Felber, et al., *RF-based Synchronization of the Seed and Pump-Probe Lasers to the Optical Synchronisation System at FLASH*, Proceedings of FEL 2010, Malmö, Sweden, 2010, pp. 544–547.

[Fel10] J. Feldhaus, *FLASH—the first soft x-ray free electron laser (FEL) user facility*, Journal of Physics B: Atomic, Molecular and Optical Physics **43** (2010), no. 19, 194002.

[Fr9] L. Fröhlich, *Machine Protection for FLASH and the European XFEL*, Ph.D. thesis, University of Hamburg, Germany, 2009.

[GBF+10a] P. Gessler, M. K. Bock, M. Felber, K. E. Hacker, W. Koprek, F. Ludwig, H. Schlarb, B. Schmidt, and S. Schulz, *Longitudinal Bunch Arrival Time Feedback at FLASH*, Proceedings of FEL 2010, Malmö, Sweden, 2010, pp. 578–580.

[GBF+10b] P. Gessler, et al., *Real-Time Sampling and Processing Hardware for Bunch Arrival Time Monitors at FLASH and XFEL*, Proceedings of FEL 2010, Malmö, Sweden, 2010, pp. 585–587.

[GBH+11] C. Gerth, M. K. Bock, M. Hoffmann, F. Ludwig, H. Schlarb, and C. Schmidt, *Beam Energy Measurements in the FLASH Injector using Synchrotron Radiation and Bunch Arrival Monitors*, Proceedings of FEL 2011, Shanghai, China, 2011, pp. 489–492.

[Ger07] C. Gerth, *Synchrotron Radiation Monitor for Energy Spectrum Measurements in the Bunch Compressors at FLASH*, Proceedings of DIPAC 2007, Venice, Italy, 2007, pp. 150–152.

[Hac10] K. E. Hacker, *Measuring the Electron Beam Energy in a Magnetic Bunch Compressor*, Ph.D. thesis, University of Hamburg, Germany, September 2010.

[Hec02] E. Hecht, *Optics*, fourth ed., Addison Wesley, 1301 Sansome St., San Francisco, CA 94111, 2002.

[Hun09] R. G. Hunsperger, *Electro-Optic Modulators*, Springer New York, 2009, http://dx.doi.org/10.1007/b98730_9.

[IRE49] IRE, *IRE Standards on Piezoelectric Crystals*, vol. 37, 1949, pp. 1378–1949.

[Kam11] R. Kammering, DESY, private communication, November 2011.

[KBB+10] W. Koprek, et al., *Intra-Train Longitudinal Feedback for Beam Stabilisation at FLASH*, Proceedings of FEL 2010, Malmö, Sweden, 2010, pp. 537–543.

[KCCK08] J. Kim, J. A. Cox, J. Chen, and F. X. Kaertner, *Drift-free femtosecond timing synchronization of remote optical and microwave sources*, Nature Photonics **2** (2008), 733 – 736.

[Kit05] C. Kittel, *Introduction to solid state physics*, fifth ed., John Wiley & Sons, Inc., 2005.

[KT71] I. P. Kaminow, and E. H. Turner, *Handbook of Lasers*, Chemical Rubber Co., Cleveland, Ohio, 1971.

[Lö9] F. Löhl, *Optical Synchronization of a Free-Electron Laser with Femtosecond Precision*, Ph.D. thesis, University of Hamburg, Germany, September 2009.

[LAF+10] F. Löhl, et al., *Electron Bunch Timing with Femtosecond Precision in a Superconducting Free-Electron Laser*, Phys. Rev. Lett. **104** (2010), 144801.

[Lam10] T. Lamb, *Femtosecond Stabilization of Optical Fiber Links Based on RF Power Detection*, Diploma thesis, University of Magdeburg, Germany, November 2010.

[LHSS06] F. Ludwig, M. Hoffmann, H. Schlarb, and S. Simrock, *Phase Stability of the Next Generation RF Field Control for VUV- and X-Ray Free Electron Laser*, Proceedings of EPAC 2006, Edinburgh, Scotland, 2006, pp. 1453–1455.

[LNBR07] J. Lund-Nielsen, N. Baboi, and W. Riesch, *Button Beam Position Monitors For FLASH*, Proceedings of DIPAC 2007, Venice, Italy, 2007, pp. 201–203.

[LSM+10] S. Lederer, S. Schreiber, P. Michelato, L. Monaco, and D. Sertore, *Photocathode Performance at FLASH*, Proceedings of IPAC'10, Kyoto, Japan, 2010, pp. 2155–2157.

[Neu11] R. Neumann, DESY, private communication, August 2011.

[Nog07] K. Noguchi, *Ultra-high-speed $LiNbO_3$ modulators*, Ultrahigh-Speed Optical Transmission Technology (H.-G. Weber, and M. Nakazawa, eds.), Optical and Fiber Communications Reports, vol. 3, Springer Berlin Heidelberg, 2007, http://dx.doi.org/10.1007/978-3-540-68005-5_4, pp. 89 – 101.

[OES+10] J. Osterhoff, E. Elsen, F. Stephan, R. J. D. Miller, K. Floettmann, B. Schmidt, and R. Brinkmann, *Prospects of Plasma Acceleration at DESY*, 470. WE-Heraeus-Seminar on Particle Accelerators and High Intensity Lasers, Bad Honnef, Germany, 2010, http://fla.desy.de/publications/2010/index_eng.html.

[Pen11] A. Penirschke, Technical University of Darmstadt, private communication, November 2011.

[RASA+11] H. Redlin, A. Al-Shemmary, A. Azima, N. Stojanovic, F. Tavella, I. Will, and S. Düsterer, *The FLASH pump–probe laser system: Setup, characterization and optical beamlines*, Nuclear Instruments and Methods in Physics Research Section A: Accelerators, Spectrometers, Detectors and Associated Equipment **635** (2011), no. 1, S88–S93.

[RK04] E. Rödel, and W. Kössler, *Linear rank tests for independence in bivariate distributions—power comparisons by simulation*, Computational Statistics & Data Analysis **46** (2004), no. 4, 645 – 660.

[SAL+05] H. Schlarb, V. Ayvazyan, F. Ludwig, D. Nölle, B. Schmidt, S. Simrock, A. Winter, and F. Kärtner, *Next Generation Synchronization System for the VUV-FEL at DESY*, Proceeding of FEL 2005, Stanford, California, USA, 2005, pp. 118–121.

[SBP+11] C. Schmidt, M. K. Bock, S. Pfeiffer, H. Schlarb, W. Koprek, and W. Jałmużna, *Feedback Strategies for Bunch Arrival Time Stabilization at FLASH Towards 10* fs, Proceedings of FEL 2011, Shanghai, China, 2011, pp. 531–534.

[Sch10] J. R. Schneider, *FLASH—from accelerator test facility to the first single-pass soft x-ray free-electron laser*, Journal of Physics B: Atomic, Molecular and Optical Physics **43** (2010), no. 19, 194001.

[Sch11a] C. Schmidt, *RF System Modeling and Controller Design for the European XFEL*, Ph.D. thesis, Technical University of Hamburg, Germany, June 2011.

[Sch11b] S. Schulz, *Implementation of the Laser-Based Femtosecond Precision Synchronization System at FLASH*, Ph.D. thesis, University of Hamburg, Germany, May 2011, to be published.

[SDR08] P. Schmüser, M. Dohlus, and J. Rossbach, *Ultraviolet and Soft X-Ray Free-Electron Lasers*, first ed., Springer, Berlin, 2008.

[SFF+10a] S. Schreiber, B. Faatz, J. Feldhaus, K. Honkavaara, and R. Treusch, *FEL User Facility FLASH*, Proceedings of IPAC'10, Kyoto, Japan, 2010, pp. 2149–2151.

[SFF+10b] S. Schreiber, B. Faatz, J. Feldhaus, K. Honkavaara, R. Treusch, M. Vogt, and J. Rossbach, *FLASH Upgrade and First Results*, Proceedings of FEL 2010, Malmö, Sweden, 2010, pp. 198–201.

[Shl05] J. Shlens, *A Tutorial on Principal Component Analysis*, Tech. report, Systems Neurobiology Laboratory, Salk Insitute for Biological Studies, December 2005.

[SRE77] S. D. Smith, H. D. Riccius, and R. P. Edwin, Optics Communications **17, 20** (1976, erratum 1977), 332 – 335, 188.

[SS10] S. Sanna, and W. G. Schmidt, *Lithium niobate X-cut, Y-cut, and Z-cut surfaces from ab initio theory*, Phys. Rev. B **81** (2010), 214116.

[SWB+10] S. Schulz, et al., *Performance of the FLASH Optical Synchronization System with a Commercial SESAM-based Erbium Laser*, Proceedings of FEL 2010, Malmö, Sweden, 2010, pp. 571–584.

[Tam90] T. Tamir (ed.), *Guided-Wave Optoelectronics*, second ed., Springer, 1990.

[Web11a] *Application Note 2: Practical Uses and Applications of Electro-Optic Modulators*, http://www.newport.com/New-Focus-Application-Note2-Practical-Uses-and-Ap/919642/1033/content.aspx, November 2011.

[Web11b] *Corning® 28e™ Optical Fiber with NexCor® Technology: Product Information*, http://www.corning.com/docs/opticalfiber/pi1463.pdf, December 2011.

[Web11c] *Fiber Collimators & Focussers - Product Description and Specification Sheet*, http://www.ozoptics.com/archived/collimators_focusers.pdf, December 2011.

[Web11d] *Mach-10™ 056: Zero-Chirp Intensity Modulator with integrated Photo-Diode*, http://www.covega.com/Products/pdfs/Mach-10%20056%20Rev%20D.pdf, September 2011.

[Web11e] *Mineralogy Database: Ditrigonal-Pyramidal crystal structure, class 3M*, http://webmineral.com/crystal/Trigonal-DitrigonalPyramidal.shtml, November 2011.

[Web11f] *PTC10K-CH temperature controller from Wavelength Electronics Inc.*, http://www.teamwavelength.com/downloads/datasheets/ptcxk-ch.pdf#page=1, November 2011.

[Web11g] *PZ2 High-efficiency Fiber Stretcher - 2 layer SMF - from Optiphase, Inc.*, http://www.optiphase.com/data_sheets/PZ2_Data_Sheet_Rev_E5.pdf, November 2011.

[Web12] *Absolute linear position encoders with high positioning accuracy and traversing speed.*, http://www.heidenhain.com/fileadmin/pdb/media/img/571_470-24.pdf, January 2012.

[Wen01] M. Wendt, *BPM Read-Out Electronics Based on the Broadband AM/PM Normalisation Scheme*, Proceeding of DIPAC 2001, ESRF, Grenoble, France, 2001, pp. 63–65.

[WG85] R. S. Weis, and T. K. Gaylord, *Lithium niobate: Summary of physical properties and crystal structure*, Applied Physics A: Materials Science & Processing **37** (1985), 191–203, 10.1007/BF00614817.

[Wie98] H. Wiedemann, *Particle Accelerator Physics I*, second ed., vol. I, Springer, Berlin, 1998.

[Win08] A. Winter, *Fiber Laser Master Oscillators for Optical Synchronization Systems*, Ph.D. thesis, University of Hamburg, Germany, April 2008.

[WTD+10] A. Willner, et al., *High Repetition Rate Seeding of a Free-Electron Laser at DESY Hamburg*, Proceedings of FEL 2010, Malmö, Sweden, 2010, pp. 2158–2160.

[WTSS11] I. Will, H. I. Templin, S. Schreiber, and W. Sandner, *Photoinjector drive laser of the FLASH FEL*, Opt. Express **19** (2011), no. 24, 23770–23781.

[YY02] A. Yariv, and P. Yeh, *Optical Waves in Crystals*, John Wiley & Sons, Inc., 2002.

Acknowledgements

This work would not have been possible without the support of many people. My warmest gratitude goes to the group leader of the accelerator devision at the University of Hamburg, Professor Jörg Rossbach, and to the head of the research group on linear accelerator technology, Docent Bernhard Schmidt, for giving me the chance to pursue my doctoral thesis at DESY.

Grateful thanks go to the official reviewers Professor Eckhard Elsen and Professor Jörg Rossbach. I am deeply grateful to my supervisors Bernhard Schmidt and Holger Schlarb, who suggested the topic of this study and had trust in my capability to complete the work.

My deep gratitude is also owed to all members of the laser-based synchronisation system for the inspiring teamwork and support. Special thanks go to Sebastian Schulz, for sharing his rich experience and expertise and, moreover, for his friendship. Sincere thanks are given to Christian Schmidt and Sven Pfeiffer for their teamwork and for the pleasurable times spend together in the control room working on the beam-based feedback, to Matthias Felber, Thorsten Lamb and Cezary Sydlo for assistance in the laser lab and for fruitful discussions.

I thank Florian Löhl and Kirsten Hacker, whose research created the basis for my work on improving the performance and operation of bunch arrival time monitors and fibre links.

Many thanks go to the members of the machine control group, in particular to Siegfried Schreiber, Katja Honkavaara, Bart Faatz and Mathias Vogt, for giving me many opportunities to perform measurements and to realise installations at FLASH and for giving me the chance to gain pratical experience on the work as machine operator.

I am indebted to Patrick Gessler, Jaroslaw Szewinski and Robert Meyer for support with understanding the BAM electronics and DOOCS servers as well as for pushing the BAM electronics to their limits. My thank goes to Philip Pototzki for prompt and valuable help with the Beckhoff electronics, to Gerhard Schlesselmann and Thomas Bruns for helping to overcome obstacles with DOOCS servers and VME crates, and to Raimund Kammering for his great helpfulness to solve many smaller and larger problems concerning the control system.

My warmest appreciation goes to many colleagues for their support during machine studies, namely to Christopher Gerth, Christopher Behrens and Stephan Wesch for their help with other beam diagnostics like SRM, BCM and LOLA, and to Nicoletta Baboi and Reinhard Neumann for sharing their expertise on BPMs and toroids.

I would like to show my gratitude to all technical engineers and technicians for realising the mechanical constructions, namely to Katharina Jähnke, Kai Ludwig and Bernd Beyer, to Matthias Hoffmann, Albert Schleiermacher, Karol Dlugolecki and Wolfgang Reinsch.

My thank is due to all former and present colleagues at FLA and MSK, also to those not explicitly mentioned here, for a good working relationship and for a nice and friendly atmosphere.

I could not have succeeded without my precious family and husband. I am much obligded to their whole-hearted support and great patience.